Investigating the influence of contact area on carpal bone motion

Sirkett, Daniel M.

Award date:
2004

Awarding institution:
University of Bath

Investigating the Influence of Contact Area on Carpal Bone Motion

Submitted by Daniel M Sirkett
For the degree of PhD
of the University of Bath
29 April 2004

Supervised by: Prof. A. W. Miles and Dr. G. Mullineux

ProQuest LLC
789 East Eisenhower Parkway
P.O. Box 1346
Ann Arbor, MI 48106-1346

Acknowledgements

Firstly, I am grateful to the patient of Mr. Giddins who saw fit to donate his left arm to medical research after it was amputated following an accident. Due to patient confidentiality, his identity was not revealed to me. Without his wrist, however, there would be no CARPAC model.

Thanks also to Tony Miles who has been consistently encouraging, positive and optimistic about this work over the last three years. Without his objectivity, I fear there were times when my own occasionally negative outlook could have jeopardised the entire project. Thanks also for finding the money for my trip to Glasgow to do the bone scanning. Without Prof. Miles' encouragement, I would probably never have considered submitting this and other work to the conferences I have been to in Rhodes, Istanbul, New Orleans and San Francisco.

Next, I must thank my other supervisor, Glen Mullineux for all his help with SWORDS, C++ and the various computational problems I encountered. I am especially grateful for Glen's work on the finite helical axis program. Also thanks for the surface-to-solid conversion program and for suggesting the idea for collision detection by looking at the intersection perimeter.

For his boundless enthusiasm and ideas, I must also thank Grey Giddins from the Royal United Hospital in Bath. Grey provided a substantial input to the work by supplying and dissecting the human forearm from which the three-dimensional computer bone models were created.

In addition to his surgical expertise, Grey is a tremendous ideas-man. On many occasions when the CARPAC model was giving poor results, he made insightful suggestions. Specifically, thanks for the separation distance idea, which prevented bones drifting apart. Grey was also responsible for securing the grant from the BSSH to fund an MR study of the wrist at Exeter University. This will help immensely with the continuation of this work.

Thanks to Chris Bowen from the Department of Engineering and Applied Science at the University of Bath. Chris showed me how to use the Proscan laser profilometer that was

used to scan a trapezium bone. Thanks too at this point to our Biomechanics lab technician, Richard Weston, for making the jig that was used for the scanning.

Thanks too must go to Jeroen Snel and Cornelius Grimbergen from the Technical University of Delft in The Netherlands. At the start of the project when I was desperate to lay my hands on a detailed set of carpal bone models, Jeroen kindly allowed me to use the data he had obtained during his PhD, which ended as mine was just beginning. He also included a copy of his thesis and a CD ROM of animations for which I am very grateful.

I would also like to thank Nigel Johnston and Adrian Bowyer from Mechanical Engineering. Nigel's "Introduction to C++" undergraduate course notes and various other tips helped my knowledge of C++ programming go from zero to adequate. I picked Adrian's brains on several occasions when geometric modelling problems arose and he produced some physical models of the wrist bones for me on the rapid prototyping machine. From the Department of Electronic Engineering at Bath, I would like to thank Iliana Portugues who gave me the computer on which some of this thesis was written.

From the Department of Physics at Exeter University, thanks to Ian Summers, who showed me around the Magnetic Resonance Imaging laboratory and explained how MR scanners work. Thanks also to Ilana Langdon who took me to look at wrists and other body parts at the dissection room at Bristol Medical School. To Chris Budd from the department of Mathematical sciences at Bath, thanks for taking the time to discuss the optimisation problems I was having and for suggesting a genetic algorithm might be worth a try. From the University of East London, I would like to thank Tom Mallard for providing the CAD model of the prototype biaxial wrist joint which was used to test the CARPAC model.

Thanks to Jez Clements, Simon Dodd, Matt Jones, Mark Schmitz and Hazel Turner from the office, for putting-up with my bouts of manic behaviour, which increased in frequency during the writing of this thesis!

I would like to acknowledge the help of the Engineering and Physical Sciences Research Council for providing my research grant. Thanks also to the Royal Academy of Engineering and the Institution of Mechanical Engineers whose travel grants helped me attend two international conferences during the course of this work.

No law or ordinance is mightier than understanding.

- Plato (427 BC - 347 BC)

A prudent question is one half of wisdom.

- Sir Francis Bacon (1561 - 1626)

Investigating the Influence of Contact Area on Carpal Bone Motion

Daniel M Sirkett PhD Thesis 2000-2003

Abstract

The wrist has been described as the most complex joint in the human body and is essential for optimal hand function. Despite numerous experimental studies, the joint is poorly understood and there is still no satisfactory explanation of the factors governing the complex movements of the carpal bones. This lack of understanding is hindering progress in joint replacement technology for which, in the wrist as with other smaller joints, there is now a growing demand.

The purpose of the work described in this thesis was to test a new hypothesis on wrist kinematics. The basis of the hypothesis was that the bones of the wrist move in such a manner as to maximise total contact area in the joint, thereby minimising contact stress.

Using a geometric constraint modeller, a computer model was created to test the hypothesis. Three dimensional computer models were created using data obtained from laser digitisation of bones dissected from a cadaveric wrist. A computer program was written to calculate the contact area between the bone models. Rotation in the radial-ulnar deviation plane was applied in 1.0° increments to four interlocked bones defining the overall posture of the wrist, and an optimisation algorithm was used to maximise the contact area by adjusting the positions and orientations of the remaining bones.

The results of the work are very encouraging because certain known characteristics of carpal behaviour were clearly predicted by the model. The movement of the scaphoid bone in particular showed good agreement with experimental results. The out-of-plane rotation of this bone was in the correct direction and of a similar magnitude to results reported in the literature in both radial and ulnar deviation.

Content

1 INTRODUCTION

Introduction

The wrist has been described as the most complex joint in the human body (Linscheid, 1986) and is essential for optimal hand function. Despite numerous experimental studies, the joint is poorly understood in comparison to other joints and there is still no satisfactory explanation of the factors governing the complex movements of the carpal bones (Crisco *et al.*, 1999; Patterson *et al.*, 1998; Youm and Flatt, 1980). A thorough understanding of wrist function is essential for surgeons and researchers investigating joint injuries and arthritic conditions that may result in abnormal kinematics.

1.1 Arthritis

Arthritis is a general term for a range of pathological conditions in which the structure and function of the joints are damaged, resulting in pain, inflammation and debilitation. A growing elderly population has resulted in an increasing prevalence of the condition, although it can affect all ages. In 2000, 8.9 million UK adults sought help from their GP for an arthritis or related condition and more than 79000 hip and knee-replacements were performed (Arthritis Research Campaign, 2003).

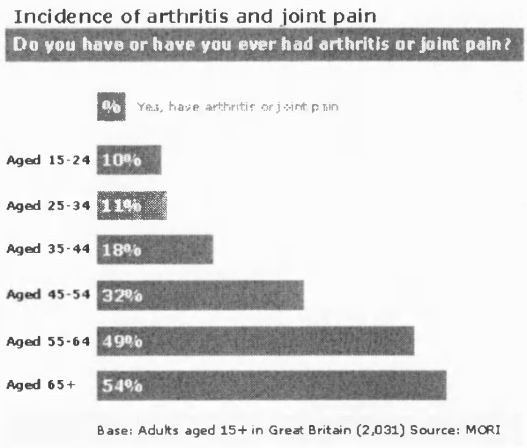

Figure 1 Incidence of arthritis and joint pain in the UK 2000 (www.arc.org).

Arthritis covers a spectrum of around two hundred specific conditions, the most common of which are osteoarthritis (4.4 million UK adults) and rheumatoid arthritis (387,000 UK adults). Osteoarthritis is one of the oldest and most common types of arthritis. It is characterised by the breakdown of cartilage on the joint surfaces. Cartilage breakdown causes bones to rub against each other, causing pain and loss of movement. Rheumatoid arthritis is an autoimmune condition characterised by the inflammation of the membrane lining the joint. The inflamed joint lining, the synovium, can invade and damage bone and cartilage. The involved joint can lose its shape and alignment, resulting in pain and loss of movement.

1.1.1 Arthritis in the Hand and Wrist

Generally, the first and most common complaint associated with arthritis in the hand is swelling at the knuckles. Swelling also occurs in the wrist. The swollen tissue may destroy the ligaments that hold the joints together, and damage cartilage and bone. This can result in certain deformities due to instability. The wrist may turn toward the thumb side of the hand, causing "ulnar drift" of the fingers.

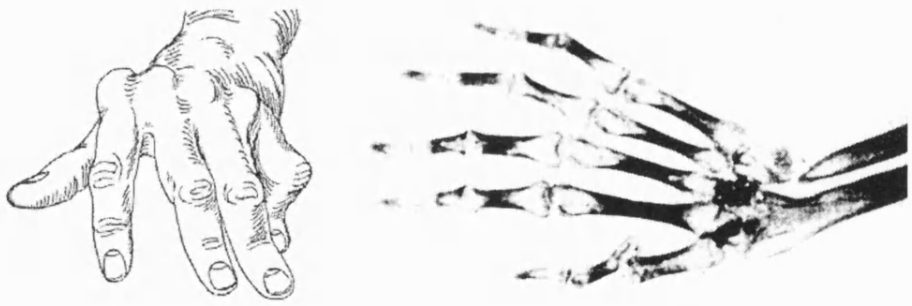

(a) (b)

Figure 2 (a) Rheumatoid arthritis results in characteristic ulnar drift of the hand (www.hand-surg.org) . (b) Radiograph showing dorsal view of right hand (Inglis, 1982).

1.2 Treatments for Arthritis of the Wrist

There are two treatments commonly used for arthritis of the wrist. Total joint replacement can relieve pain and increase functionality while joint fusion can provide excellent long-term pain relief at the expense of a loss of joint function.

1.2.1 Total Joint Replacement

Replacement of the larger joints is one of the success stories of modern medicine. In 2000, over 79000 total hip and knee replacement operations were performed in the UK (Arthritis Research Campaign, 2003). The published results suggest that for hip implants, the revision rate is around ten percent at ten years (Malchau *et al.*, 2000). By contrast, joint replacement for the wrist is still an emerging technology due to the many challenges it presents. The revision rate for one of the most widely used prosthesis, the Biax, is around forty percent at 6 years (Cobb and Beckenbaugh, 1996). The joint is small, which means that there is a lower tolerance for alignment errors. The kinematics of the joint are complex and not easily replicated artificially. There are ten tendons crossing over the wrist to operate the hand, which adds to the complexity of the procedure. Consequently, the preferred treatment is often joint fusion.

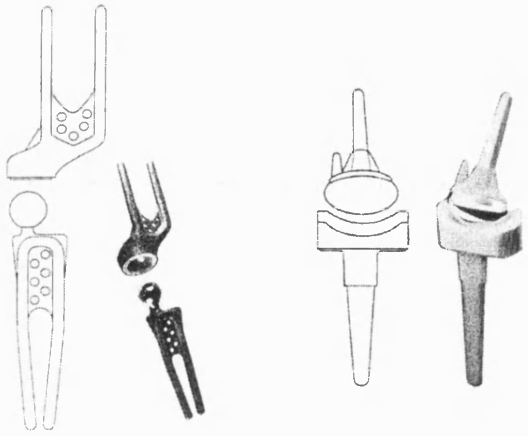

(a) (b)

Figure 3 Two wrist joint replacements. (a) Meuli MWP III. (b) Biaxial.

1.2.2 Total Joint Fusion

The pain associated with the arthritic wrist may be relieved through fusion of all of the bones of the wrist in a procedure known as arthrodesis. The articular surfaces are removed to allow bone-on-bone contact. The spaces between bones are then packed with morcelised bone graft taken from the hip to encourage fusion. To assist the process, the wrist is immobilised by implanting a metal plate across the joint (Figure 4). While pain-relief is achieved, this comes at the expense of wrist mobility. However, postoperative functionality of the hand as a whole has been shown to be adequate for many activities of daily living (Lorei *et al.*, 1997).

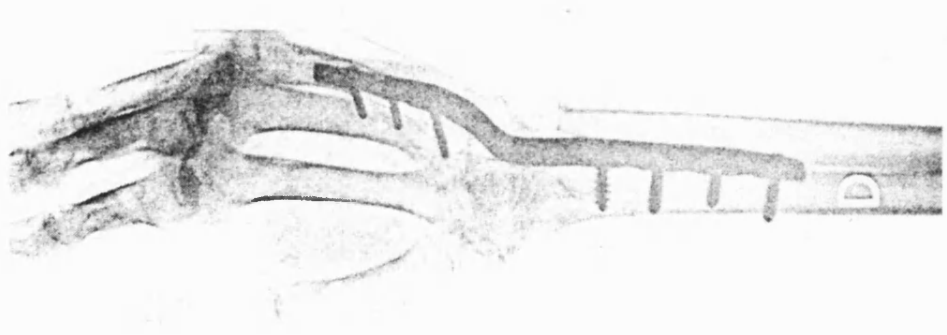

Figure 4 Arthrodesis of the wrist provides relief from pain but total loss of joint-function.

1.2.3 Partial Joint Fusion

A compromise that allows pain relief and maintains some degree of joint function is partial joint fusion. This is where two or more of the bones of the wrist are joined together and is suitable for localised arthritis. Since this kind of surgery is tailored to the individual requirements, it is not always easy to determine what effect it will have on the kinematics of the joint.

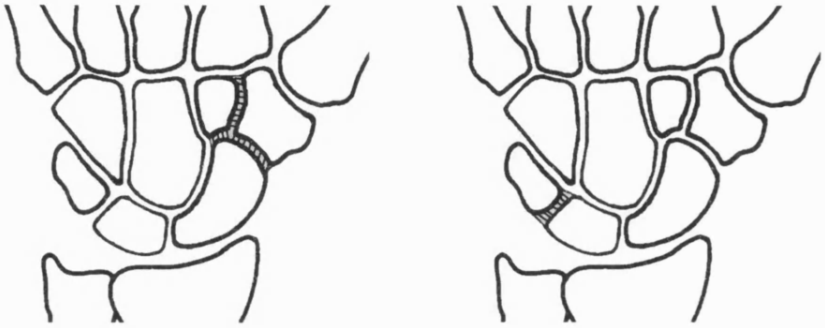

(a) (b)

Figure 5 (a) Scaphoid-trapezium-trapezoid fusion. (b) Lunate-triquetrum fusion. (http://www.pncl.co.uk/~belcher/wristoa.htm).

1.3 The Wrist Group at Bath

The wrist joint is one of the most complex joints in the human body and wrist joint disorders affect millions of sufferers of arthritis throughout the world. Unlike the large joints such as the hip and knee, replacement of small joints such as the wrist and ankle have largely been unsuccessful. In the Bone and Joint Decade 2000-2010 consensus statement small joint replacement has been singled out as an area in need of attention. It is against this background that a Wrist Joint Biomechanics Group has been initiated within the newly formed University Research Centre for Orthopaedic Biomechanics at Bath. This group is a multidisciplinary team drawn from both clinical and engineering perspectives. The group now numbers some 16 people including Orthopaedic Consultants and Registrars, Industrialists, Engineers and Mathematicians. The group is involved in diverse projects relating to the wrist joint including replacement prostheses, the development of a wrist joint simulator and fundamental studies of wrist joint forces and functions associated with daily living activities in normal and pathological subjects. This relatively recent grouping has been funded by start up grants from ARC, Wishbone, The Royal College of Surgeons, Action Research and a DTI Teaching Company Programme with Osteotec a company specialising in Orthopaedic Devices for the Extremities.

The contribution of the work described in this thesis to the activity of the Wrist Group was a new insight into the detailed kinematic function of the wrist.

Despite being the most complex joint in the body, there is relatively little research being carried out on the wrist in comparison to the larger joints. A search on Pub-Med, a widely-used database for searching medical literature, revealed just 14 publications from 2003 (as of 10th October) having the words "wrist" and "kinematics" in the title or abstract. The figures for kinematics of the other joints of the body were: 85 for the knee, 37 for the hip, 37 for the ankle, 27 for the shoulder, 22 for the elbow and 21 for the spine. The only joint having fewer results than the wrist was the thumb, with three publications.

1.4 Purpose of the Study

The purpose of the work described in this thesis was to test a new hypothesis of wrist kinematics. The question being addressed is: Why do the bones move in the way they do?

The underlying premise was that the shapes of the carpal bones and the way they move, in common with many other natural processes, are governed by a minimum energy principle. If the minimum energy principle does govern the form and function of the joint, then it is reasonable to assume that the quantity of material (bone, ligament, muscle etc.) is kept to a minimum. This is due to the high "cost", in terms of metabolic energy, of creating and maintaining these materials from dietary constituents. Given that this assumption holds true, then it is necessary to inquire as to the factors that influence the amount of construction material required, and investigate the strategies adopted by the body to minimise their effect.

In the case of the wrist, it was assumed that the factor governing the amount of material required to construct and maintain the carpal bones is the level of contact stress occurring at the joint surfaces. The contact stress may be minimised by maximising the area over which the contact loads are applied. Therefore, the hypothesis relates to whether the carpal bones move in such a way as to maintain maximum possible contact area throughout the total range of motion of the joint.

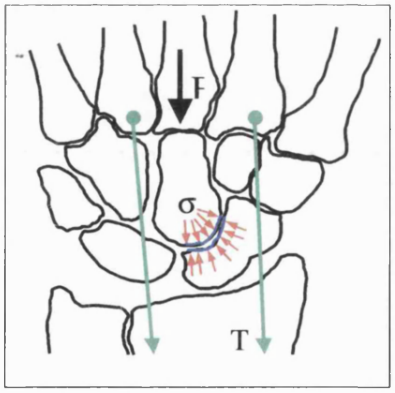

Figure 6 External loads (F) and tension in tendons passing across the wrist (T) results in contact stress (σ) at the joint interfaces. Do the bones move so as to minimise σ?

The work was carried out using SWORDS (Mullineux, 2001), a geometric constraint modeller created at the University of Bath. SWORDS contains a solid modeller for creating and editing three-dimensional objects, a graphics display and numerical optimisation algorithms for generating solutions to multi-variable problems. SWORDS has previously been used to assist in the design of complex mechanical systems and this project was its first application to a biological joint.

Since a literature search has not revealed any predictive model of the wrist that fully explains the laws governing its function, the work described in this thesis represented fundamental research that yielded valuable insight into this poorly understood joint.

1.5 Thesis Structure

Section 2 provides a glossary of terms. Essential background material pertaining to the engineering, mathematical, computational, geometrical and anatomical concepts embraced by the study is presented in section 3. Sections 3.1 to 3.9 contain basic information on anatomy of the wrist and a literature review covering studies of wrist kinematics, wrist kinetics and wrist morphology. Relevant computational background to the work, including optimisation techniques, packing theory and geometric modelling is provided in sections 3.11 to 3.13.

The aims and objectives of the project are presented in section 4.

Section 5 contains the methods used to achieve the stated objectives. Sections 5.2 to 5.5 are concerned with the various approaches that were tried in order to obtain the three-dimensional computer models of the wrist bones. Sections 5.6 to 5.11 describe the processes involved in writing a computer program to assess the closeness of packing of the carpal bones. Every effort has been made to explain processes in sufficient detail that the work could be reproduced by someone having a reasonable grasp of geometrical concepts and C++ programming. The process of maximising the contact area using optimisation techniques is described in sections 5.13 to 5.15, while sections 5.16 to 5.18 are concerned with testing the complete algorithm. A summary of the method is provided in section 5.20.

Results are presented in section 6. The purpose of this section was to show the progress made in improving the performance of the algorithm. Consequently, there is a large amount of information in this section. The animations described in this section are presented on a CD ROM included on the inside back cover of this document. Section 7 contains the analysis of the best sets of results from all the trial runs presented in section 6.

The method and outcome of the work is discussed in section 8. Acquisition of the three-dimensional bone models is discussed in section 8.1. Section 8.2 discusses the anatomical considerations in relation to assumptions and approximations that were made. Section 8.3 to 8.4 cover aspects of the optimisation process. Kinematic considerations are discussed in section 8.5.

Conclusions and recommendations for further work are given in section 9.

2 GLOSSARY

Glossary

ACIS	A geometrical modeller used within SWORDS (Spatial Technologies Inc.).
AutoCAD	Three-dimensional computed-aided design software application (Autodesk Inc.)
Bounding box	The smallest orthogonally aligned cuboid volume into which an object fits.
CARPAC	Name given to the macro script written to control the operation of SWORDS. *Car*pal *Pac*king.
CIEP	Contact and Intersection Evaluation Program.
Convex hull	The smallest convex three-dimensional shape into which an object fits.
Cost function	Mathematical expression whose result describes the fitness of a trial-solution obtained during an optimisation process.
DSP file	A file containing a three-dimensional surface-facetted model that is read by SWORDS (DiSPlay file).
Facet	A planar region constructed between three or more vertices in order to represent a region on the surface of a three-dimensional computer model.
FFRP	Far-away Facet Removal Program.
FHA	Finite Helical Axis.
Genetic Algorithm	A method of optimisation based upon Darwinian selection.
Macro	Text-based script written to control an application.
Model space	Three-dimensional region of space contained within world space having its own coordinate system and which contains geometric entities and other model spaces.
Points2Polys	Freeware application for triangulating/manipulating point-cloud data (Paraform Inc.)
RAMdisk	Random Access Memory disk – using part of the system-memory as a virtual hard-disk.

SAT file	A file containing a three-dimensional solid model that is read by ACIS.
SWORDS	Geometric constraint modeller created by colleagues at the University of Bath.
TFCC	Triangular fibrocartilage complex. A structure at the distal-end of the ulna whose primary purpose is to limit extremes of wrist deviation.
Voxel	Three-dimensional volume element.
World space	Three-dimensional region of space whose coordinate system does not move relative to the world.

3 BACKGROUND

Background

The work described in this thesis was multi-disciplinary and contained aspects of mathematics, computer programming, engineering, geometric modelling, anatomy and joint kinematics. The purpose of this section is to introduce these topics and to critically review the relevant literature.

Topics covered in this section are:

- Anatomy of the hand and forearm
- Wrist kinematics
- The Minimum Energy Principle
- Packing theory
- Geometric modelling
- Optimisation

3.1 Anatomy of the Hand and Forearm

The wrist is mechanically the most complicated joint in the body. It consists of eight mobile bones that articulate against one another and against the radius bone of the forearm. Bones glide against each other on patches of articular cartilage. Movement of the wrist is primarily controlled by six muscles. There are three extensors and three flexors (Figure 8).

Conventionally, the eight carpal bones are divided into two rows, proximal and distal. The bones of the distal row – the trapezium, trapezoid, capitate and hamate – constitute a relatively immobile transverse unit that articulates with the metacarpals to form the carpometacarpal joints. All four bones in the distal row fit tightly against each other and are held together by stout interosseous ligaments. The more mobile proximal row, composed of the lunate and the triquetrum, articulates with the radius to form the radiocarpal joint. The scaphoid spans both rows anatomically and functionally. The eighth carpal bone, the pisiform, functions as a sesamoid bone that enhances the mechanical advantage of the wrist's most powerful motor, the flexor carpi ulnaris, and forms its own small joint with the triquetrum. For the purposes of this study, the pisiform bone was omitted, since it is not one of the main load-bearing bones of the wrist.

Between the proximal and distal rows of carpal bones is the midcarpal joint, and between adjacent bones of these rows are the intercarpal joints. The distal radius and the ulnar carpal bones (lunate and triquetrum) articulate with the distal ulna through a ligamentous and cartilaginous structure, the ulnocarpal complex (Nordin and Frankel, 1989).

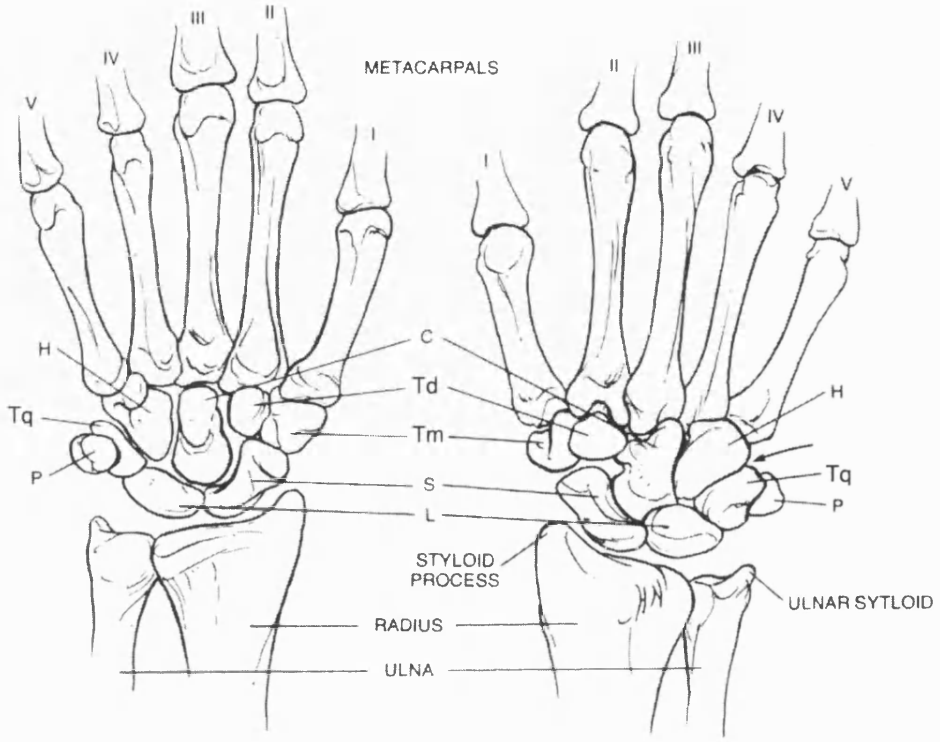

Figure 7 Schematic drawing of the bones of the hand. Palmar view (left), dorsal view (right) of the right hand. H, hamate; C, capitate; Td, trapezoid; Tm, trapezium; Tq, triquetrum; P, pisiform; L, lunate; S, scaphoid (Nordin and Frankel, 1989).

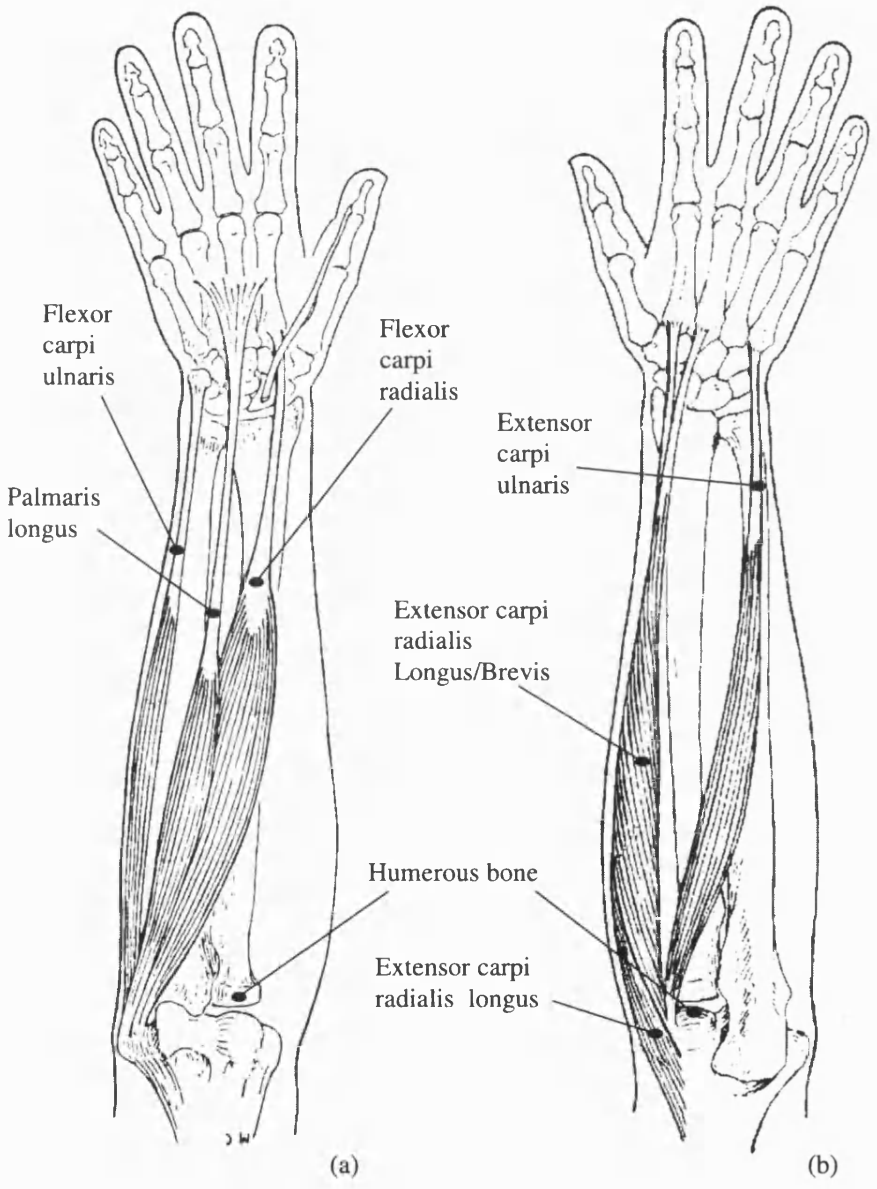

Figure 8 The six main muscles controlling wrist motion. (a) Palmar view. (b) Dorsal view of right hand (Luttgens *et al.*, 1992).

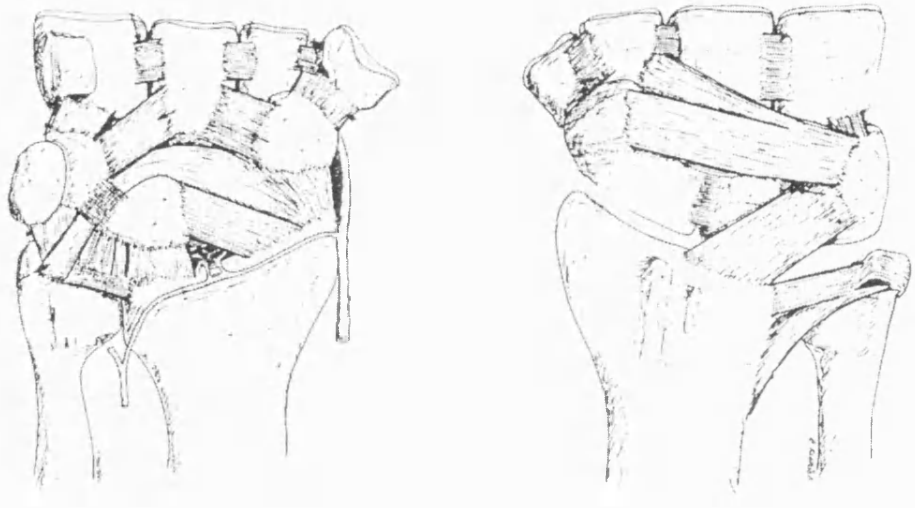

Figure 9 The carpal bones are held together by a complex network of 21 ligaments (Berger, 2001). (a) Palmar view. (b) Dorsal view of right hand.

3.2 Wrist Kinematics and Morphology

This section presents an overview of the various studies of wrist kinematics. Studies are discussed in five broad categories:

- Overall movements of the wrist
- Variation in joint kinematics
- Variations in joint morphology
- Quantification of kinematic properties for the wrist as a whole
- Quantification of kinematics of individual bones

3.2.1 Flexion-Extension Motion

The Normal wrist range is 85 to 90 degrees of flexion, 75 to 80 degrees of extension although this can vary widely among individuals. Owing to a slight palmar tilt of the distal radial plates, flexion exceeds extension by an average of 10 degrees. In flexion, the wrist functions as a two hinge joint, with rotation occurring between the lunate and radius, and between the capitate and lunate (Nordin and Frankel, 1989).

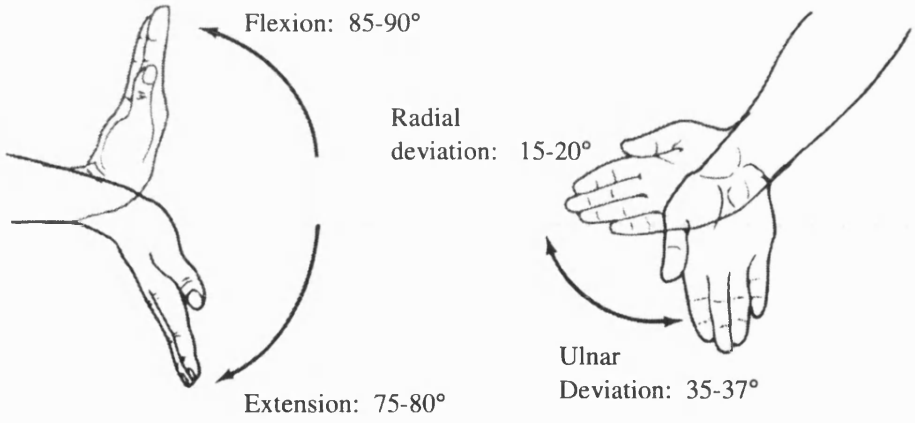

Figure 10 The four principal wrist motions (Luttgens *et al.*, 1992).

3.2.2 Radial-Ulnar Deviation

The total arc of radial-ulnar deviation is approximately 50 degrees. This is split between 15 to 20 degrees radially and 35 to 37 degrees ulnarly (Youm *et al.*, 1978). While the elements of flexion-extension can be easily apportioned between the radiocarpal and mid carpal joints, analysis of radial-ulnar deviation is more complex. With radial deviation of the hand, the proximal carpal row moves ulnarly while the distal carpal row is displaced radially. These diametric shifts in proximal and distal carpal rows are reversed with ulnar deviation (Figure 11) (Volz *et al.*, 1979).

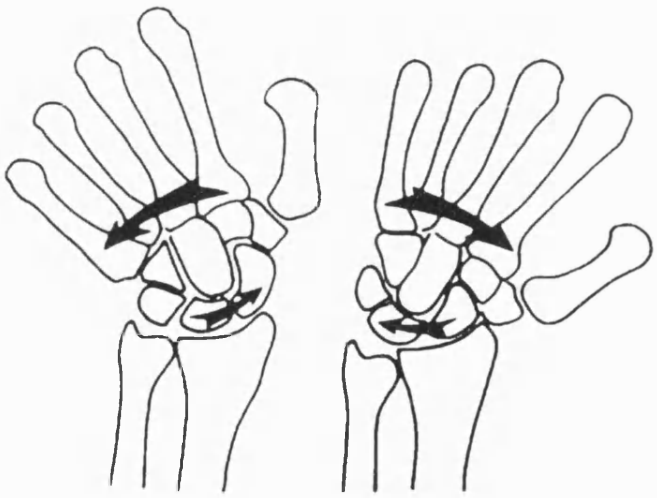

Figure 11 Movement of the carpal bones during radial (a) and ulnar (b) deviation. Palmar view of right hand (Volz *et al.*, 1979).

3.3 Studies of Overall Joint Kinematics

Many studies have been carried out with the aim of quantifying the overall kinematic properties of the wrist joint (Youm *et al.*, 1978; Moore *et al.*, 1993; Brumbaugh *et al.*, 1982; Andrews and Youm, 1979). It is generally accepted that the joint behaves like a two-hinge system, with the axis of radial-ulnar deviation (RUD) is slightly distal to the flexion-extension (FE) axis and located in the proximal pole of the capitate.

Youm placed the axis of rotation for radial-ulnar deviation slightly to the ulnar side of the longitudinal axis of the capitate at a point located one quarter of the total length of the capitate distal to its proximal end (Youm *et al.*, 1978). The axis of rotation for flexion-extension motion was located on the longitudinal axis of the captiate just distal to its proximal cortex.

Andrews reached a similar conclusion to Youm. The wrist joint was shown to behave like a simple hinge joint in both flexion-extension motion and radial-ulnar deviation (Andrews and Youm, 1979). Both RUD and FE axes were shown to pass through the capitate bone with the RUD axis 5mm distal to the FE axis.

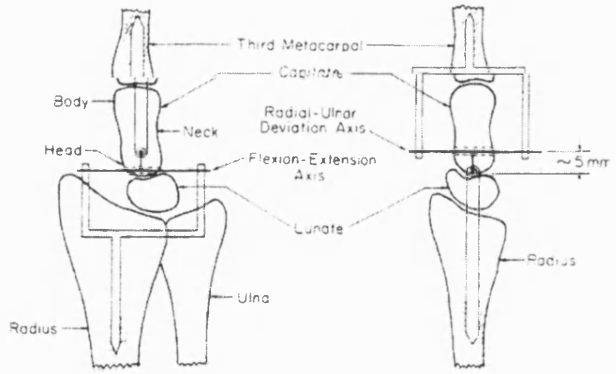

Figure 12 Andrews proposed an offset universal joint as the mechanical analogue of the wrist Dorsal view (left), lateral view (right) of right hand.

Brumaugh showed that the hinge axes were not orthogonal but skewed. The FE axis was shown to lie perpendicular to the x-axis and rotated by –10° about the y-axis. The RUD

axis was shown to lie parallel to the yz plane and is skewed by 12° about the x-axis (Brumbaugh *et al.*, 1982) (Figure 13).

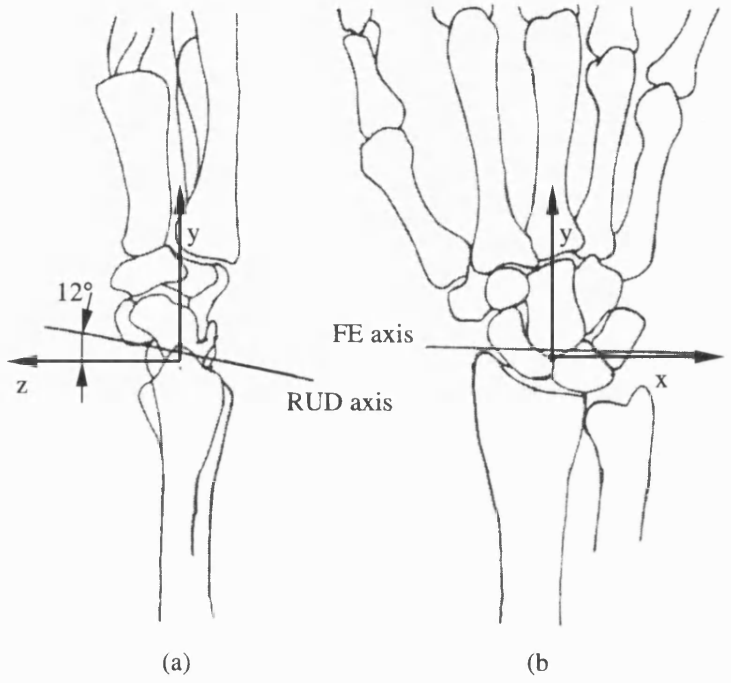

Figure 13 Brumbaugh measured the orientations of the axes. (a) Medial view and (b) dorsal view of right hand.

3.4 Variations in Kinematics

A radiographic study of 52 wrists showed that the movement characteristics of the scaphoid bone varied from one individual to another and between males and females (Craigen and Stanley, 1995). The findings were based upon the level of shortening of the scaphoid bone and its translation as observed in an anterior-posterior radiograph as the wrist is moved from ulnar to radial deviation in neutral flexion-extension (Figure 14, Figure 15).

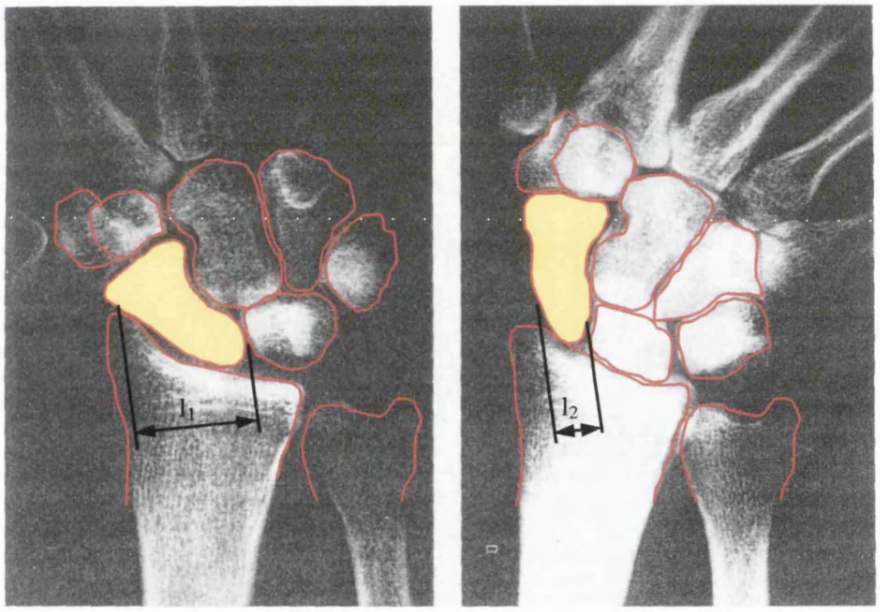

Figure 14 Shortening of the scaphoid as the wrist moves from radial (left) to ulnar (right) deviation (Craigen and Stanley, 1995).

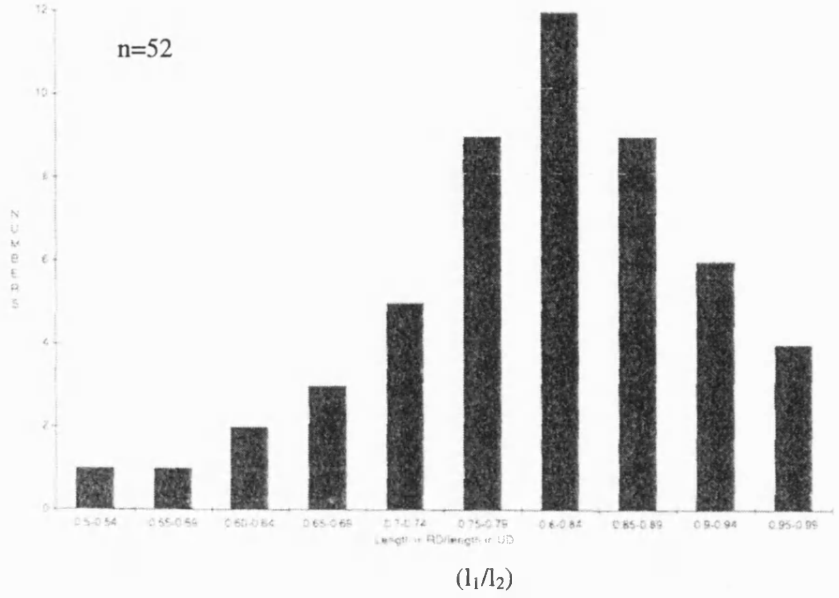

Figure 15 Distribution of scaphoid shortening ratios (Craigen and Stanley, 1995).

A second radiographic study of thirty four subjects suggested that there were two types of wrist motion, classified according to the level of rotation of the lunate during flexion and extension in neutral radial-ulnar deviation (Ferris *et al.*, 2000).

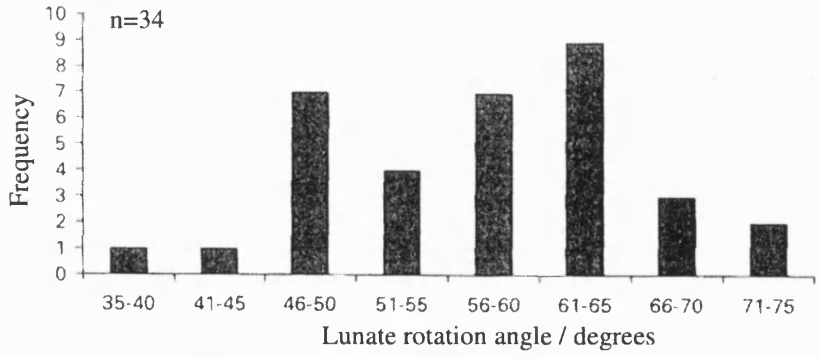

Figure 16 Variation in the total range of lunate movement shows a bi-modal distribution (Ferris *et al.*, 2000).

The two studies discussed above maintain that there are subtle differences in the ways in which the carpal bones move during deviation of the joint. However, they do not propose any significant reasons for the variations other than possibly the sex of the subject. It would have been interesting to compare the three-dimensional morphology of the bones to see whether variation in their surface shape was in part responsible for the variation in scaphoid movement patterns.

3.5 Variations in Morphology

The purpose of this section is to briefly demonstrate the variations that are present in the morphology of the wrist.

3.5.1 Variation in Bone Morphology

A 2001 study demonstrated clearly the variations in morphology of the carpal bones (Viegas, 2001). Two different types of lunate were described (Figure 17). Type I does not have a medial facet and type II has a medial facet that articulates with the hamate. The width of the medial facets in a type II lunate was shown to vary from 1mm to 9mm.

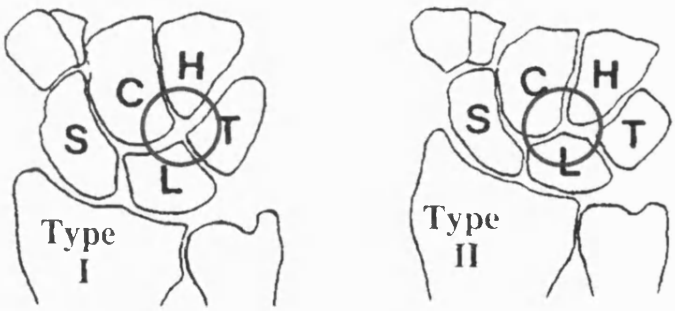

Figure 17 Viegas identified two types of lunate (L) bone. Type I does not have a medial facet for articulation against the hamate (H). Type II has a medial facet whose depth ranges from 1 to 9 mm (Viegas, 2001).

3.6 Variations in Ligament Morphology

A second study by Viegas *et al.* in 1999 revealed that variations were present in the ligaments of the wrist in addition to the bones. Four different kinds of dorsal intercarpal ligament were observed from a study of 45 wrists. The greatest variation was found in the distal radio-carpal ligament (see Figure 18). The kinematics of these wrists was not investigated in this study and so the effect of the morphological variations was not quantified.

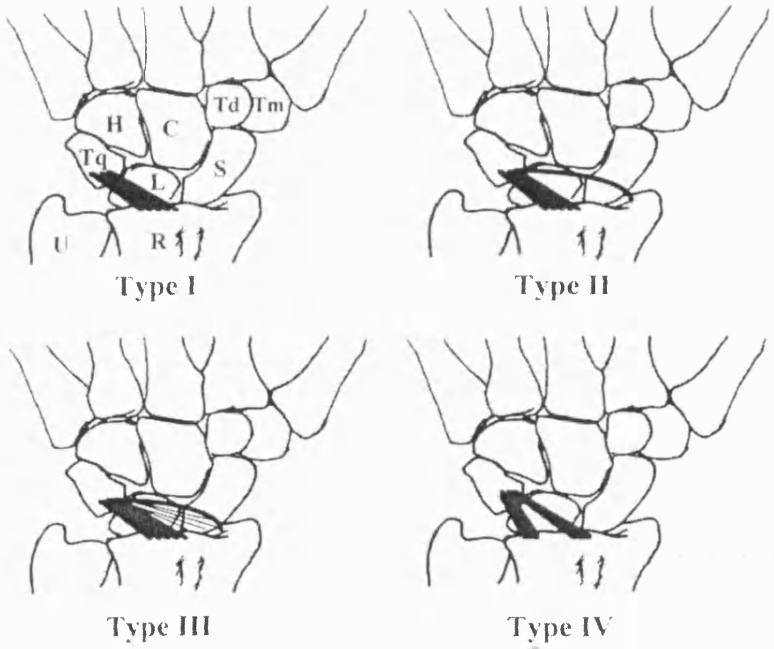

Figure 18 Naturally occurring variation in the morphology of the distal-radiocarpal ligament from a study of 45 wrists (Viegas *et al.*, 1999).

3.7 Relationship between Morphology and Kinematics

While the studies described in section 3.5 clearly demonstrated the differences in the morphology of the bones and ligaments, they did not establish a link between bone shapes and their kinematic behaviour. However, several authors have suggested that there may be a link between surface shape and kinematics. The hamate has a helicoid or screw shaped surface and it has been suggested that this is well suited to provide rotational control (Weber, 1984). In agreement to the hypothesis of the present work, two further studies conclude that the geometries of the carpal bones govern their movements:

> *"...This implies that mechanical behaviour of the wrist is predominantly determined by articular geometry, and not by ligament constraints."* (Savelberg *et al.*, 1992)

> *"...we are able to conclude that the geometries of the carpal bones are responsible for the characteristic articulations in the wrist joint."* (Kooloos *et al.*, 1994)

One author has drawn attention to the positions of ligaments of the wrist in relation to the overall axes of motion (Kapandji, 1982). The attachment points of the anterior and posterior ligaments on the carpus were shown to coincide with the approximate location of the axis of radial-ulnar deviation. Similarly, the medial and lateral ligaments were anchored at the entry and exit points of the flexion-extension axis. This suggests that these ligaments stabilise the carpus under load, rather than influencing its movement.

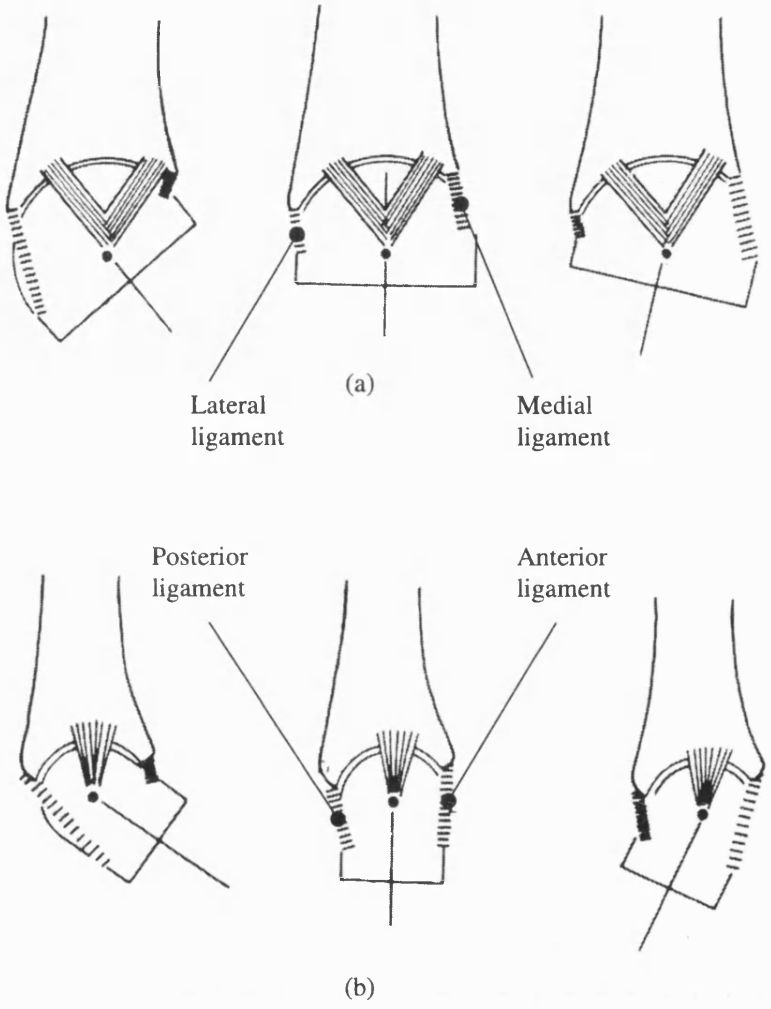

Figure 19 Kapandji drew attention to the fact that certain ligaments have their attachment points near to the entry and exit points of the axes of rotation. (a) In Radial-ulnar deviation. (b) in flexion and extension.

3.8 Studies of Individual Bone Kinematics

This section will describe the various methods used by researchers to quantify the movement of individual carpal bones. The studies will be discussed in order of increasing sophistication.

3.8.1 Stereoradiographic Studies

Early attempts at studying individual carpal bone motion used stereoradiographic techniques with radio-opaque pellets implanted in the bones of cadaveric specimens. This approach was adopted for a study of five cadaveric forearms (Savelberg *et al.*, 1991). Tantalum markers were implanted in each of the carpal bones. The tendons acting on the hand were loaded using springs and the hand was moved passively by guiding a Steinman pin inserted into the third metacarpal. Radiographs were taken in two planes at four-degree increments of flexion and extension and radial-ulnar deviation. Stereophotogrammetric principles were employed to reconstruct the 3D positions of the tantalum pellets for each wrist position. The sequential positions were used to determine the six degree of freedom motion behaviour of each bone.

It was shown that in flexion of the hand, there was very little out-of-plane movement of the carpals. However, in deviation, the lunate and scaphoid were shown to have a notable out-of-plane (flexion) component. For all movements, the four bones comprising the distal row (trapezium, trapezoid, capitate and hamate) displayed very little out-of-plane movement during both flexion and deviation. These findings agree with a further study of wrist kinematics using CT imaging (Moojen *et al.*, 2002a), whose results are illustrated in Figure 20.

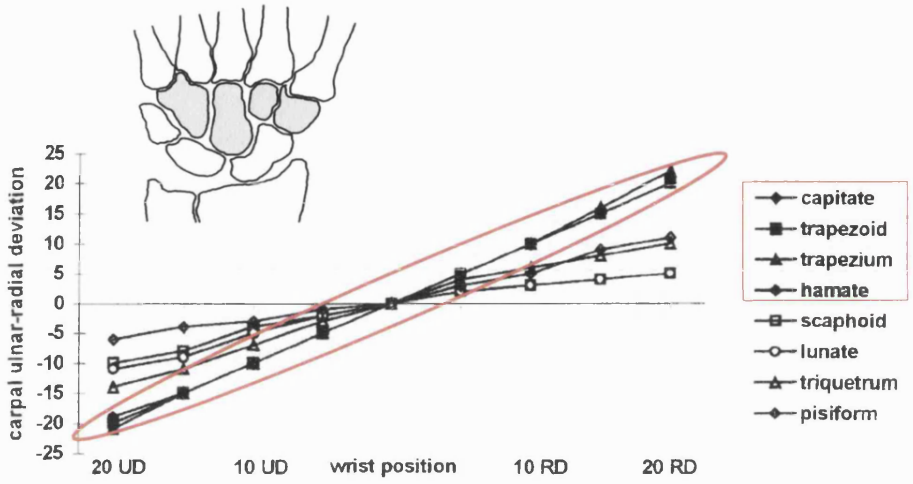

(a)

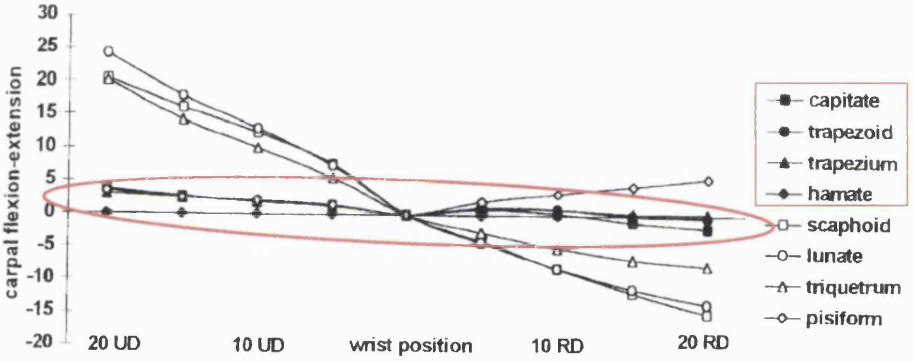

(b)

Figure 20 Graphs showing that there is relatively little relative movement between the bones of the distal row (Moojen *et al.*, 2002a). (a) Deviation of the carpals during radial-ulnar deviation. (b) Out-of-plane movement of the carpals during radial-ulnar deviation.

3.8.2 Motion Capture Techniques

A study was performed to measure carpal kinematics using motion capture techniques (Patterson *et al.*, 1998). The study was again performed on cadaveric wrists using markers implanted in each of the carpal bones. However, moving image video capture methods were used instead of radiographs to assess kinematic behaviour. Only flexion and extension movements were investigated. The results were displayed as an animation of three-dimensional bone models. In this study, the bone models were obtained by reconstruction of serial 2D computed tomographic image slices. The contribution of the radiocarpal and midcarpal joints to the total arc of flexion were found. It was shown that the midcarpal joint contributes more to flexion and the radiocarpal joint contributes more to extension. Further, it was shown that the third metacarpal and capitate are rigid with respect to one another. The average difference between capitate and third metacarpal angles with respect to the radius was just 1.1°. Hence, the capitate-third metacarpal joint may be considered rigid. If the angle of the third metacarpal is indicative of overall hand posture, then this result allows the capitate to be considered the "output" bone of the wrist. These results will be referred to when considering the design of the computer model.

3.8.3 In Vivo Studies

While the studies discussed so far produced accurate results describing carpal movement, they were limited to cadaveric specimens and relied upon implanting markers in the bone. Recent advances in medical imaging and computer graphics technologies have made feasible the non-invasive study of carpal kinematics in live subjects. Furthermore, the results of the studies are by nature three-dimensional models, allowing the most complete visualisation of the movements.

A kinematic analysis of a single normal live wrist was performed using computed tomographic imaging and reconstruction (Crisco *et al.*, 1999). The method used comprised four stages. First, a series of 2D cross sectional scans was taken for each increment of wrist motion. Image processing techniques were then manually applied to extract the outlines of the bone shapes from the images. The outlines were then stacked and surfaced to create the three-dimensional models. The centroid and principal axes of inertia for each bone model were calculated at each increment of wrist motion in order to calculate the

rotation matrix and translation vector for movement from one position to the next. The translation vector and rotation matrix were converted to the finite helical axis (FHA) form (Woltring *et al.*, 1985; Spoor and Veldpaus, 1980). The FHA describes an axis in space about which an object rotates and along which it translates in order to move from one position to the next. FHAs are described in more detail in section 5.17.

A principal aim of the Crisco study was to assess errors in calculating carpal movements. This was achieved by applying the method to a cadaveric specimen with the wrist fixed in known positions. The analysis yielded an error of +/-2° of rotation and 1mm of translation along a helical axis of motion. Movement patterns of the carpal bones showed flexion of the lunate and scaphoid during neutral to radial deviation which agrees with Patterson's marker based video capture study.

The main source of error and variability in Crisco's *in vivo* study of carpal kinematics was the requirement for user intervention in the segmentation of the carpal outlines on the 2D slice images. A study in 2000 demonstrated a fully automated, non-invasive method of investigating 3D carpal kinematics (Snel *et al.*, 2000). The methodology was essentially the same as that used in Crisco's work except an algorithm was developed to automate the segmentation process thereby eliminating inter-operator errors. Furthermore, x-ray dosage was reduced by using regular dosage scans to obtain good surface description of the bones and low dosage scans giving a level of detail sufficient to allow registration in order to track the positions of the bones for extraction of kinematic data. The study was performed on eleven live subjects.

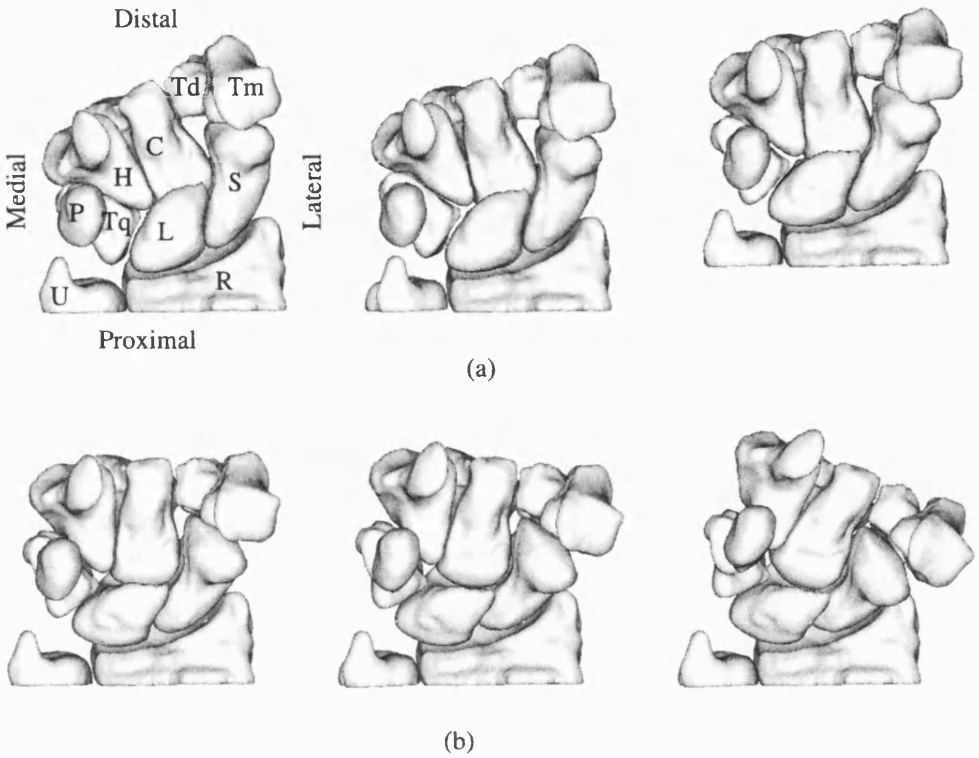

Figure 21 Six frames from an animation of radial-ulnar deviation produced by a multi-position CT reconstructive study (Snel *et al.*, 2000). Palmar view of right wrist. (a) Ulnar deviation (bone abbreviations as per Figure 7.) (b) Radial deviation. The animation is included on the CD ROM accompanying this thesis.

Since the results of the work by Snel *et al.* will be used to qualitatively assess the outcome of the present study, some key observations from Figure 21 are now summarised:

3.8.3.1 Movement of the Proximal Row

The carpus can be seen to slide bodily up and down the inclined surface of the radius. When moving into ulnar deviation, the carpus slides up towards the lateral side of the radius (see Figure 22). When moving into radial deviation, the carpus slides down the slope towards the medial side nearest the ulna.

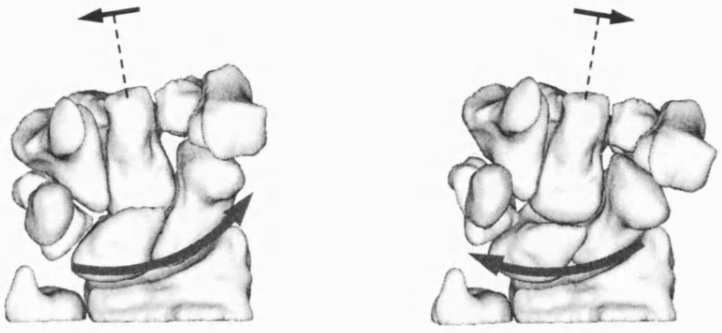

(a) (b)

Figure 22 Movement of the proximal row. (a) The carpus slides in a medial-to-lateral direction up the face of the radius during ulnar deviation and (b) slides down in a lateral-to-medial direction during radial deviation (Snel *et al.*, 2000).

3.8.3.2 Movement of the Distal Row

There is little or no movement between the capite-hamate-trapezoid complex throughout the range of movement. The trapezium can be seen to alter its orientation very slightly with respect to the trapezoid, but this only occurs at the extremes of motion. This result agrees with the generally held view that the distal row moves as a single unit, with the remaining bones (lunate, triquetrum, scaphoid) undergoing greater excursions.

3.8.3.3 Movement of the Scaphoid

Of all the bones, the scaphoid is observed to undergo the greatest change in attitude. In addition to sliding up and down the radius with the carpus, the bone exhibits out-of-plane movement. The scaphoid is seen to rotate into the page (extend) as the wrist moves ulnarward (see Figure 23). During radial deviation, the scaphoid rotates out of the page (flexes) to lie closer to the surface of the radius.

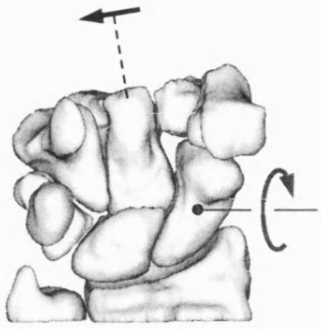

Figure 23 The scaphoid extends during ulnar deviation so that the distal pole rotates into the plane of the page (Snel *et al.*, 2000).

3.8.3.4 Movement of the Lunate

The lunate bone also exhibits out-of-plane rotation, but to a lesser extent than the scaphoid. As the wrist moves into ulnar deviation, the lunate follows the scaphoid and rotates into the page (extends), to curl over the proximal pole of the capitate. In radial deviation, the lunate slides up the slope of the radius and tilts into flexion.

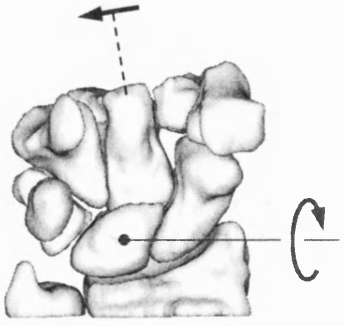

Figure 24 The lunate extends as the wrist moves into ulnar deviation (Snel *et al.*, 2000).

3.8.3.5 Movement of the Triquetrum

Throughout the cycle of movement, the proximal surface of the triquetrum is seen to remain in close contact with the lunate but its lateral surface slides against the hamate. The lateral surface slides up the medial surface of the hamate as the wrist moves into ulnar deviation and slides down the surface in radial deviation

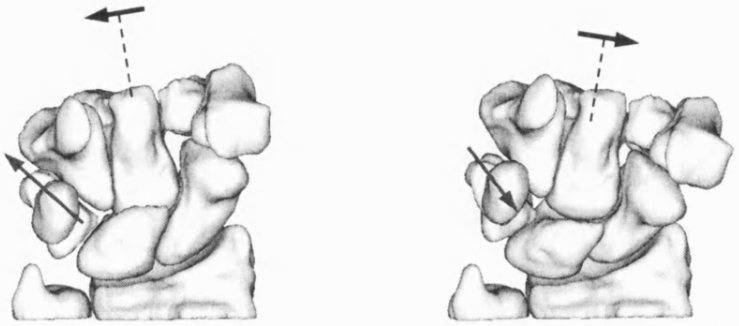

(a) (b)

Figure 25 The triquetrum slides up the medial surface of the hamate as the wrist moves into ulnar deviation (a), and slides down during radial deviation (b) (Snel *et al.*, 2000).

3.8.3.6 Triangular Fibrocartilage Complex

The triangular fibrocartilage complex (TFCC) is a soft-tissue structure located at the distal tip of the ulna. It acts as an ingenious buffer to limit extremes of motion in both radial and ulnar deviation. In radial deviation, the TFCC is compressed from the lateral direction as the lunate slides off the radius. In extreme ulnar deviation, the TFCC is compressed by the triquetrum approaching from a distal direction. In the neutral position, the TFCC also plays a small role in transmitting force from the wrist into the arm. Approximately 12% of wrist load is transferred in this way (Genda and Horii, 2000).

The TFCC is a deformable structure. Its stiffness is estimated as 25% that of articular cartilage (Genda and Horii, 2000). Since one of the limitations of the SWORDS model was the difficulty of modelling deformable objects, the TFCC was excluded from the present study.

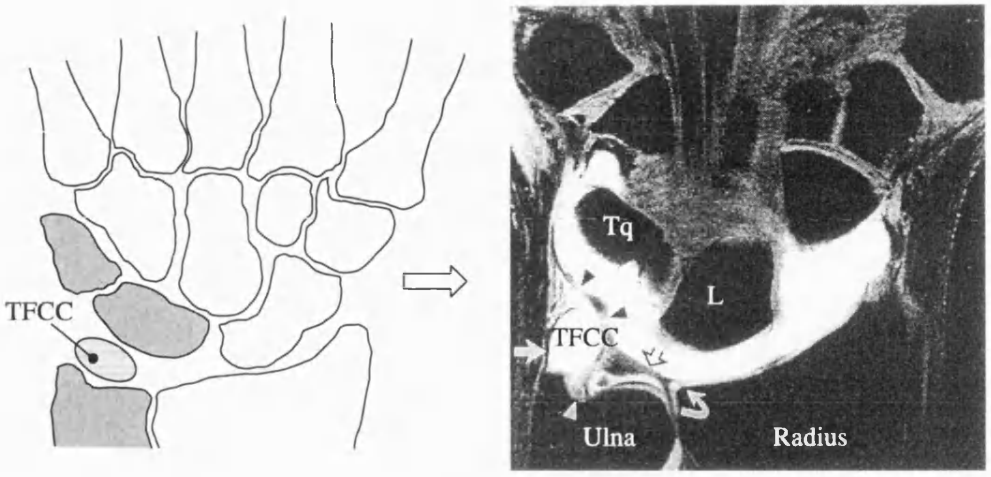

Figure 26 Coronal MR image of the wrist showing the triangular fibrocartilage complex (TFCC) (Chung *et al.*, 2001). Tq=triquetrum, L=lunate. Palmar view of right wrist.

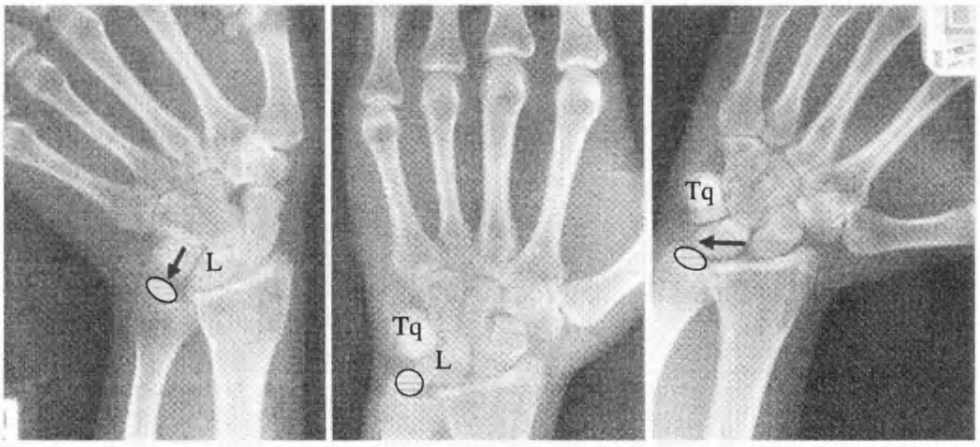

(a) (b) (c)

Figure 27 The TFCC acts as an ingenious buffer to limit extremes of movement (adapted from Nordin & Frankel, 1989). (a) In extreme ulnar deviation, the complex is compressed from above by the triquetrum (Tq). (b) In neutral deviation, the TFCC bears around 12% of the load transmission into the forearm. (c) In extreme radial deviation, the complex is compressed from the side by the lunate as it slides off the radius.

3.9 Studies of Wrist Kinetics

Several authors have created kinetic models of the wrist using rigid-body spring methods (Schuind *et al.*, 1995; Horii *et al.*, 1990; Iwasaki *et al.*, 1998; Manal *et al.*, 2002).

The aim of studies of this kind is to establish a theoretical model of the force distribution throughout the normal carpus. The anatomy used in the model can then be modified to simulate surgical procedures, to reveal the effects on load distribution.

The bones are represented as two or three-dimensional rigid bodies whose shapes are obtained by digitisation of anterior-posterior radiographs (Schuind *et al.*, 1995; Manal *et al.*, 2002) or reconstructed from serial CT images (Horii *et al.*, 1990; Iwasaki *et al.*, 1998) . The bones are interconnected by compressive springs representing the articular cartilage and tensile springs representing ligaments. Loads are applied axially through the metacarpals to simulate a grasping action with the wrist in the neutral position and resultant displacements and contact forces are calculated.

The models were used to simulate the effect of partial joint fusion (Horii *et al.*, 1990; Iwasaki *et al.*, 1998), and to investigate force transmission through the juvenile arthritic wrist (Manal *et al.*, 2002).

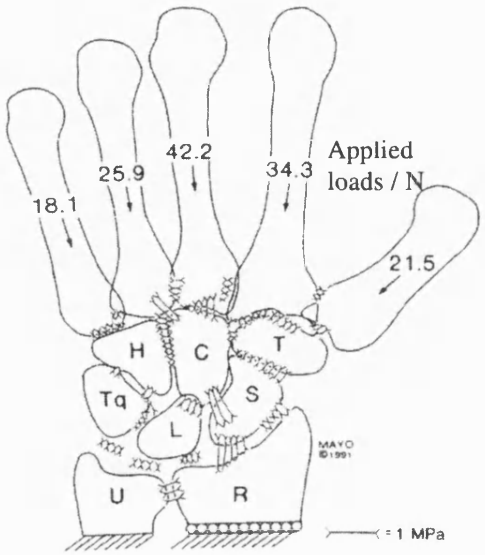

Figure 28 Predictive models of wrist force distributions have been created using rigid body spring techniques (Schuind *et al.*, 1995).

For the normal case, the models consistently showed that the greatest contact force occurred at the radio-scaphoid and radio-lunate interfaces. The proportion of total force transmitted through the wrist was found to be 55% and 35% respectively by Schuind *et al.*, 46% and 32% respectively by Horri *et al.* and 49% and 23% respectively by Manal *et al.*

While work of this kind has proved successful in simulating the effects of surgical procedures on the forces acting in the wrist, there is little in the literature to suggest that models have been developed that can simulate alterations of the movement patterns of the bones that may arise from surgical intervention. Furthermore, while kinetic models such as these require information about the positions and properties of the ligaments in addition to the shapes of the bones, the goal of the present study is to investigate whether it is possible to predict the kinematics *independently of the ligaments*.

3.10 Minimum Energy Principle

The key assumption underlying the hypothesis is that the kinematic behaviour of the carpal bones is governed by the minimum energy principle. Also known as the Principle of Least Action, it was formulated in 1746 and is one of the greatest generalisations in all physical science (Maupertuis, 1746). Maupertuis arrived at the conclusion that natural motions must be such as to make some quantity a minimum. It was only necessary to find that quantity, and this he proceeded to do. The quantity was the product of the duration (time) of the movement and twice what we now call its kinetic energy. Having found the quantity that tends to a minimum, Maupertuis regarded the principle as all-inclusive:

> *"The laws of movement and of rest deduced from this principle being precisely the same as those observed in nature, we can admire the application of it to all phenomena. The movement of animals, the vegetative growth of plants... are only its consequences; and the spectacle of the universe becomes so much the grander, so much more beautiful, the worthier of its Author, when one knows that a small number of laws, most wisely established, suffice for all movements"*

3.10.1 Bone Remodelling

It is not solely natural *motions* that are governed by the minimum energy principle. It also applies to natural *processes*. A pertinent example can be found in Wolff's Law of Functional Adaptation. In his 1870 paper *The Law of Bone Remodelling*, German anatomist Julius Wolff established a connection between the internal structure of bone and the loading conditions to which it is subjected (Wolff *et al.*, 1986). He observed that the bone microstructure within mal-unioned fractures at the femoral neck changed in response to what must have been altered loading. Wolff also suggested that bone adapted *optimally* to change in stress, attaining maximum strength with minimum material. This ties the idea of optimisation to bone adaptation.

Based on these ideas, Wolff generated the famous postulate that is named after him as Wolff's law:

> *"Every change in the form and the function of a bone or of their function alone is followed by certain definite changes in their internal architecture, and equally definite secondary alterations in their external confirmation, in accordance with mathematical laws"*

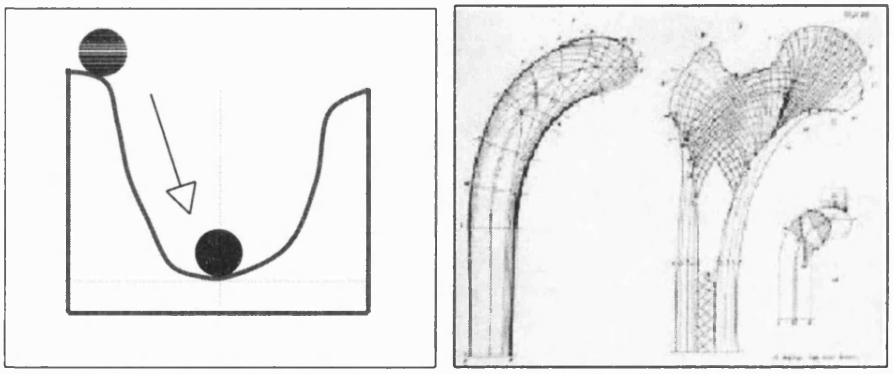

(a) (b)

Figure 29 The minimum energy principle can be used to predict (a) the resting position of a ball rolling into a valley. It is also likely that the principle governs the internal structure of load-bearing bones in accordance with Wolff's Law.

3.10.2 Applying the Minimum Energy Principle to the Wrist

It was assumed for this study that, in the case of the wrist, the minimum energy principle relates to the amount of energy required to *construct and maintain* the carpal bones. It is possible that the ligaments and muscles are arranged in such a manner that the energy requirements of *moving* the joint are minimised as well, but that was *not* the objective of this study.

Creation and construction of the carpal bones from dietary constituents requires metabolic energy. Therefore, if the minimum energy hypothesis holds, it would seem reasonable to assume that the body uses the minimum of construction material to make the joint.. It was assumed that the factor governing the amount of material required to construct and maintain the carpal bones is the level of contact stress occurring at the joint surfaces. This relates to Wolff's Law, which states that bone is laid down adaptively in response to the loads that are present. Since pressure = force / area (see Figure 30), the contact stress may be minimised by maximising the area over which loads are applied. Therefore, the hypothesis considered in this thesis relates to whether the carpal bones move in such a way as to maintain maximum possible contact area throughout the total range of motion of the joint.

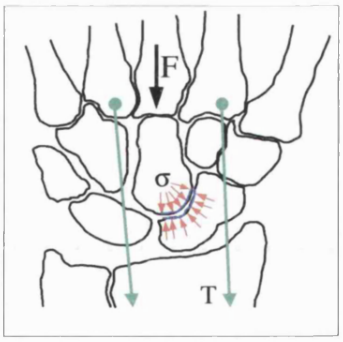

Figure 30 External loads (F) and tension in tendons passing across the wrist (T) results in contact stress (σ) at the joint interfaces. Do the bones move so as to minimise σ?

3.11 Packing Theory

Optimisation of the arrangement of the bones in the wrist to maximise contact has much in common with a "packing problem." The Packing Problem is defined as:

> *"Given a set of three-dimensional objects of arbitrary geometry and an available space (possibly the space of a container), find a placement for the objects within the space that achieves the design objectives, such that none of the objects interfere (i.e. occupy the same space) while satisfying optional spatial and performance constraints on the objects."*
>
> (Szykman and Cagan, 1997).

Packing theory has many applications in for example the loading of containers, job scheduling, stock cutting and rapid prototyping. The increased complexity of the three-dimensional problem over the two dimensional case means that exact solutions are unlikely to be effective (Downsland and Downsland, 1992). Only heuristics which can find a solution close to the optimum have been developed. To date, several approaches have been developed. These include genetic algorithms (Ikonen, 1997), simulated annealing (Szykman and Cagan, 1997) and pattern search (Yin and Cagan, 2000).

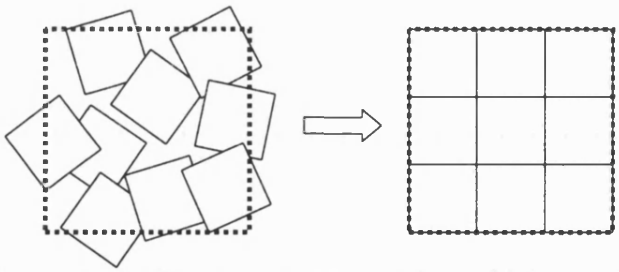

Figure 31 The objective of a packing algorithm is to pack objects together as tightly as possible so that they fit into a fixed size container.

3.12 Packing Problems

This section discusses some of the approaches used in solving the three-dimensional packing problem. Note that these studies are not exactly the same as the wrist problem because they involve the additional constraint of packing objects into a fixed size container and not simply maximising their packing density. However, aspects of each that may be applicable to the present study are discussed.

Every packing algorithm contains three essential features. A fitness function is needed to assess the suitability of each trial solution. A penalty function is required to lower the fitness of the solution if any constraints are violated. The penalty is related to the degree of interference between neighbouring objects and between objects and the container into which they are packed. The computational difficulties associated with the latter requirement are considerable.

The algorithm also requires an optimisation scheme (see section 3.13.2) to control the iterative improvement process.

3.12.1 Packing Regular-Shaped Objects

A packing algorithm in which 3D objects are represented mathematically using parametric equations is described (Udy *et al.*, 1988). Interference evaluation involves solving equations to see whether any part of one object occupies the same space as another. If interference is detected then further calculations are used to quantify the intersection distance. If interference is not detected then the clearance distance is determined.

In this case, the objective is to fit several objects into a container. The cost function is defined as the sum of the squared clearances between each object and the base of the container. A steepest gradient descent type optimisation method is used. While this approach is acceptable for regular-shaped engineering objects whose surfaces can be described mathematically, it is less suitable for the wrist problem. This is because the complex freeform surfaces of the carpal bones cannot be easily expressed mathematically, unless NURBS representation is implemented (see section 8.1.5).

3.12.2 Spatial Decomposition Method

A packing method was developed whose efficiency was improved using the octree (Meagher, 1982) spatial decomposition technique. (Dai *et al.*, 1994). Octrees are data structures in which the workspace is subdivided into a hierarchy of world axis-aligned cubic volumes. Their use allows for faster location of sites of interference, since large regions of the search volume may be discarded with a minimum of calculations.

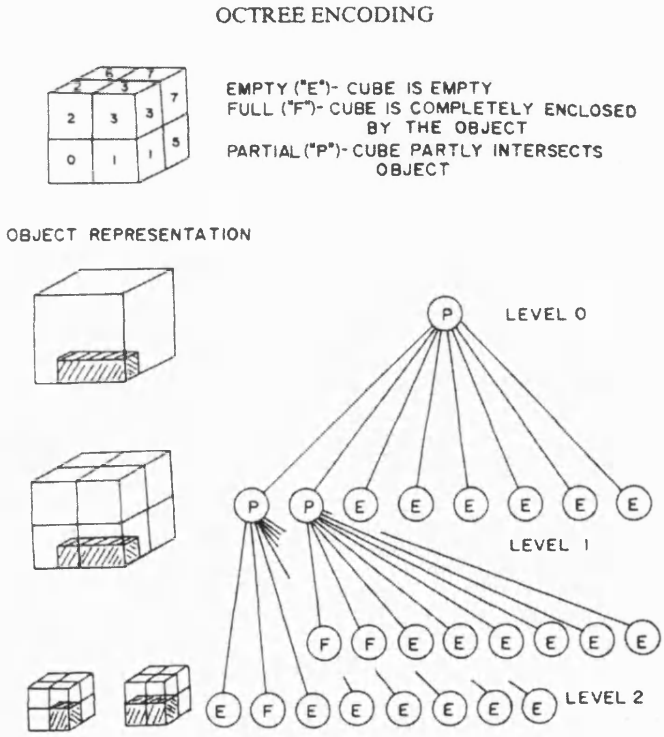

Figure 32 Octree representation of an object. The object is subdivided into cubes whose contents are classified as Empty (E), full (F) or partial (P) (Meagher , 1982).

Interference evaluation was achieved by comparing the contents of sub-cubes of the octree data structure. The optimisation algorithm utilised a serial approach to packing. Objects are placed one at a time into the container. The order in which they are placed into the container is dependent upon the volume of the holding cube and the number of empty sub-

cubes in the holding cube. Objects are then moved to maximise the remaining space in the container.

The serial packing methodology described in this paper is unsuitable for packing the bones of the wrist because a reasonably good starting position already exists. It is not necessary to remove and re-pack all the bones; the bones need only be perturbed slightly from their initial positions. Furthermore, while it is appropriate for this particular method, the octree method of spatial decomposition may be unsuitable for the wrist project. The method is ideally suited for applications where gross adjustments in object positions are made. Here, the regions of intersection change appreciably at each iteration, and an efficient "narrowing down" of the search space is required. Since there will be a good initial configuration of the carpal bones, it is only necessary to use small perturbations at each iteration. Therefore, the regions of surface in which intersection occurs will not change significantly. Consequently, the computational expense and storage requirements of re-generating the octree hierarchy at each iteration will outweigh the benefits that it can afford. An alternative approach that is more suitable for the present study is described in section 5.12.2.

3.12.3 Genetic Algorithm Method

A genetic algorithm (Goldberg, 1989) was used to tackle the packing problem (Ikonen *et al.*, 1997). Genetic algorithms are described in section 8.4.3. Unlike those discussed previously, this packing algorithm is able to cope with non-convex objects and objects having holes. The algorithm is used to arrange 3D objects within a cylindrical container to maximise material usage during rapid prototyping by selective laser sintering.

Three-dimensional objects are represented as a series of points on the surface to which a mesh of triangular facets is fitted. The advantage of this approach over a mathematically defined surface is that complex freeform surfaces can be easily represented. Interference evaluation is achieved by comparison of triangles on parts (Figure 33). This is an efficient method but the final answer is not the actual intersection *volume* between the two objects.

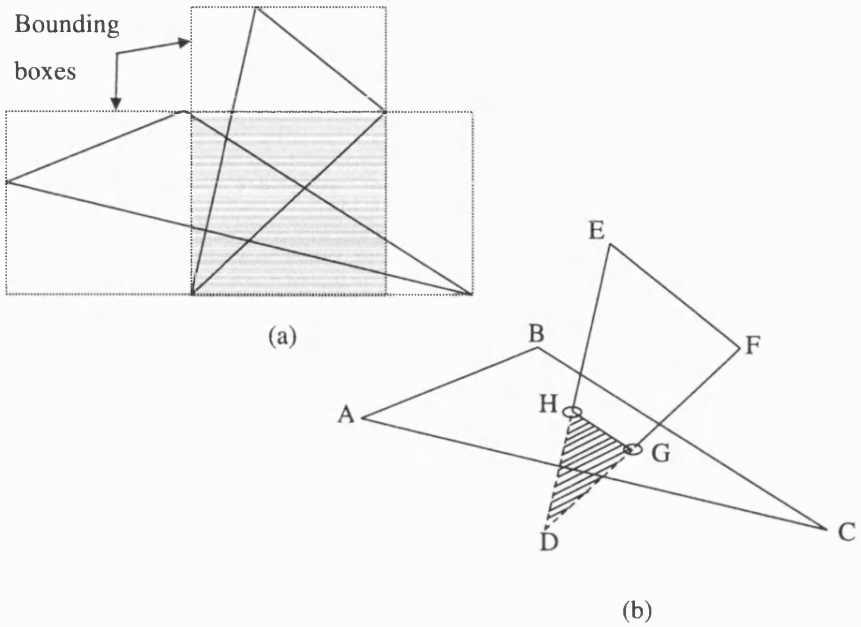

Figure 33 Pair-wise comparison of triangles to evaluate intersection between geometric models. (a) Checking for overlap between bounding boxes. (b) Checking edge-facet intersections to find points H and G.

The face-vertex method of 3D object display is ideally suited to representing the irregular shapes of the carpal bones. Furthermore, the pair-wise triangle intersection test is straightforward to implement for face-vertex models.

3.12.4 Simulated Annealing Method

A simulated annealing (Kirkpatrick *et al.*, 1983) optimisation method combined with a variation of octree encoding to solve the general 3D layout problem was developed (Cagan *et al.*, 1998). The hierarchical nature of the octree data structure allows the resolution of the model to be varied according to the level of accuracy required. Rough analyses are performed using a low-resolution model for initial iterations while a higher resolution model allows more refined analysis towards the end of the algorithm.

Interference evaluation is achieved by summing the overlapping volume between cubes whose contents are entirely solid at a given level in the hierarchy. The degree of accuracy is controlled by the hierarchy level at which the overlap is calculated. This is an elegant method and it is likely that the ACIS solid modeller within SWORDS utilises a similar approach to finding the Boolean intersection of two objects.

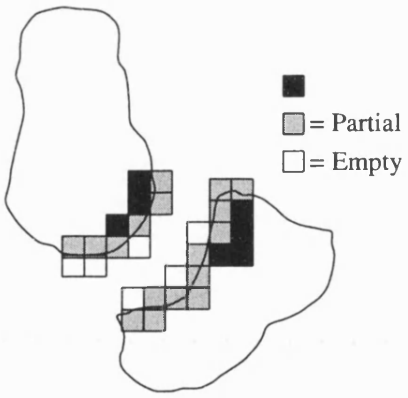

Figure 34 When objects are represented using Octree encoding, intersection evaluation is achieved by calculating the overlapping volume of all "full" boxes. To increase accuracy of the result, the boxes may be sub-divided.

3.13 SWORDS Constraint Modeller

The SWORDS constraint modeller is a piece of software created in the Department of Mechanical Engineering at the University of Bath by G. Mullineux and A. J. Medland (Mullinuex, 2001). This section briefly describes its function.

3.13.1 Geometric Modeller

SWORDS contains a three-dimensional geometric modeller, called ACIS. This allows solid objects to be created from a set of geometrical primitives (cones, cylinders, cubes) using Boolean operations (addition, subtraction, intersection). Three-dimensional solid models may also be imported to SWORDS in the form of SAT files from Computer Aided Design (CAD) programs such as AutoCAD. The modeller can also define objects using triangular facets, and these may be imported in the form of DSP files. However, Boolean operations may not be performed on such models since only the surface is defined.

3.13.2 Optimisation Method

SWORDS is equipped with three optimisation methods.. These are as follows:

1. Powell's method (old)
2. Hooke and Jeeves method
3. Powell's method (new)

3.13.2.1 Hooke and Jeeves' Method

The Hooke and Jeeves method (Hooke and Jeeves, 1961) is one of the most widely used direct search methods (direct search means that it is not necessary to calculate derivatives in order to minimise the cost function). It attempts in a simple though ingenious way to find the most profitable search directions. The method advances towards the minimum through a series of *exploratory* and *pattern moves*. Exploratory moves involve evaluating magnitudes of changes in the solution for a one step-length change in each variable in turn. An exploratory move that reduces the solution is termed a success; otherwise, it is termed a failure. Once a successful search direction has been found, the process is repeated with the step-lengths halved until some desired level of accuracy is reached. A pattern, or leapfrog,

move attempts to speed up the search by using information already acquired about the cost function. Typically, a leapfrog move will be made in the same direction as the last successful exploratory move, but the magnitude of the leap may be large in comparison to the initial step-length, thereby taking the process into hitherto un-explored regions of the search-space. Pattern moves are an attempt to prevent the method converging to local minima. The process is illustrated in Figure 35.

3.13.2.2 Powell's Method (old)

Powell's method (Powell, 1964) is very similar to Hooke and Jeeves' method except for the way the search directions are chosen. Unlike the Hooke and Jeeves method, in which exploratory moves are always made in orthogonal directions, Powell's method allows the search to proceed in directions perpendicular to the pattern move. In this way, the algorithm "learns" about the shape of the cost-function.

3.13.2.3 Powell's Method (new)

New Powell's method is essentially the same as Powell's method except the computer code was reworked and minor differences were introduced.

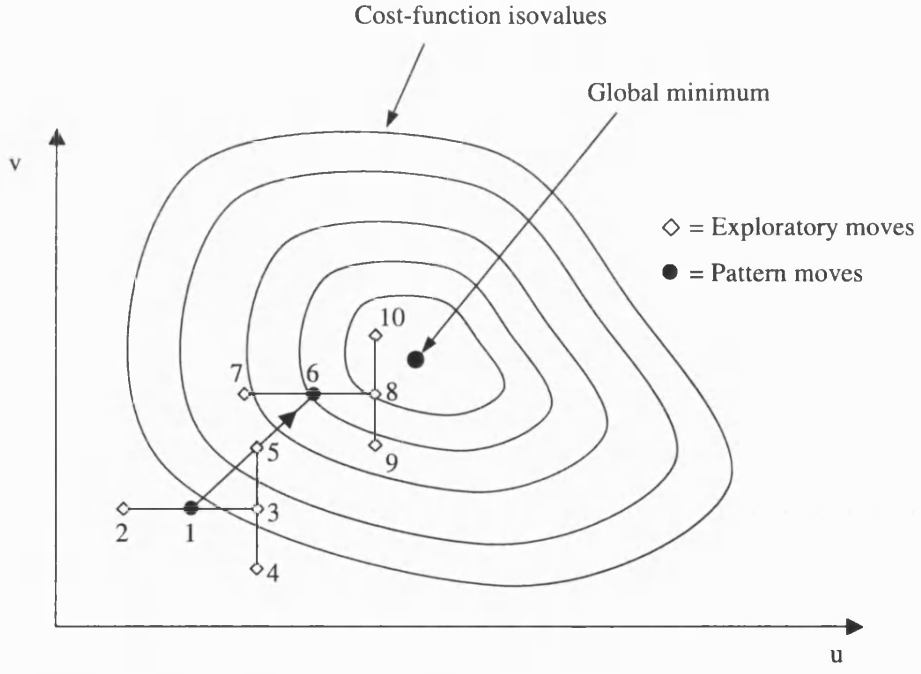

Figure 35 Optimisation progress for Hooke and Jeeves direct-search with two degrees of freedom. Exploratory moves are always made in orthogonal directions.

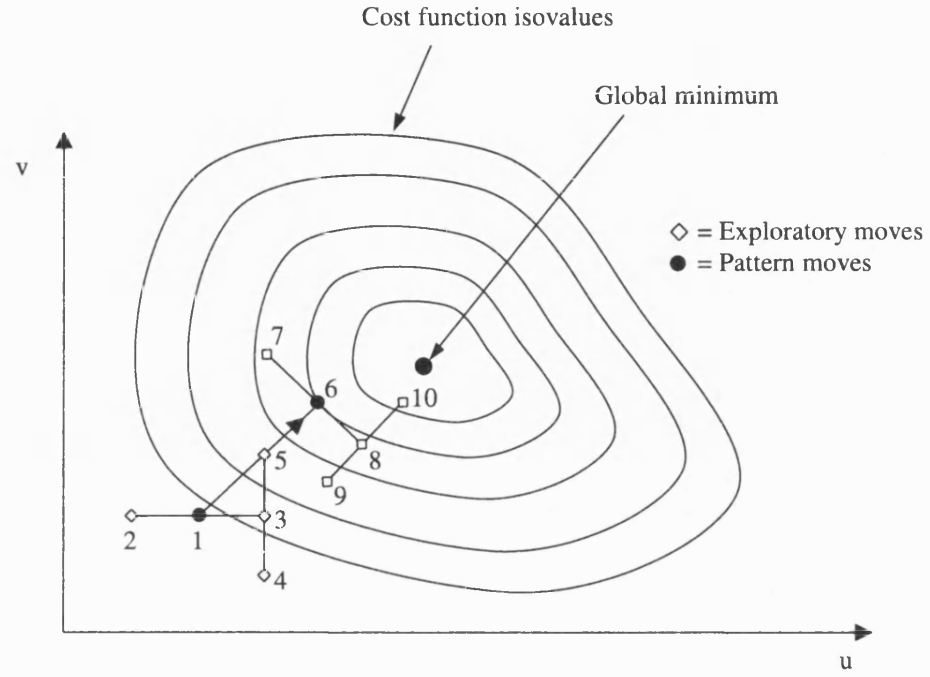

Figure 36 Powell's method allows exploratory moves to be made perpendicular to pattern moves.

3.13.3 Controlling SWORDS

To control the modeller, commands are entered at a prompt. For convenience, commands may be written in the form of a text-file, which is read by SWORDS. Such a file is referred to as a "macro".

The program displays visual output in a graphics window, and error messages and text output in a status window (Figure 37). Three-dimensional objects may be viewed from any angle in either shaded or wireframe mode. The SWORDS window contains buttons to control view angle, position and zoom. There is also a region reserved for user-defined buttons, which are created in the macro.

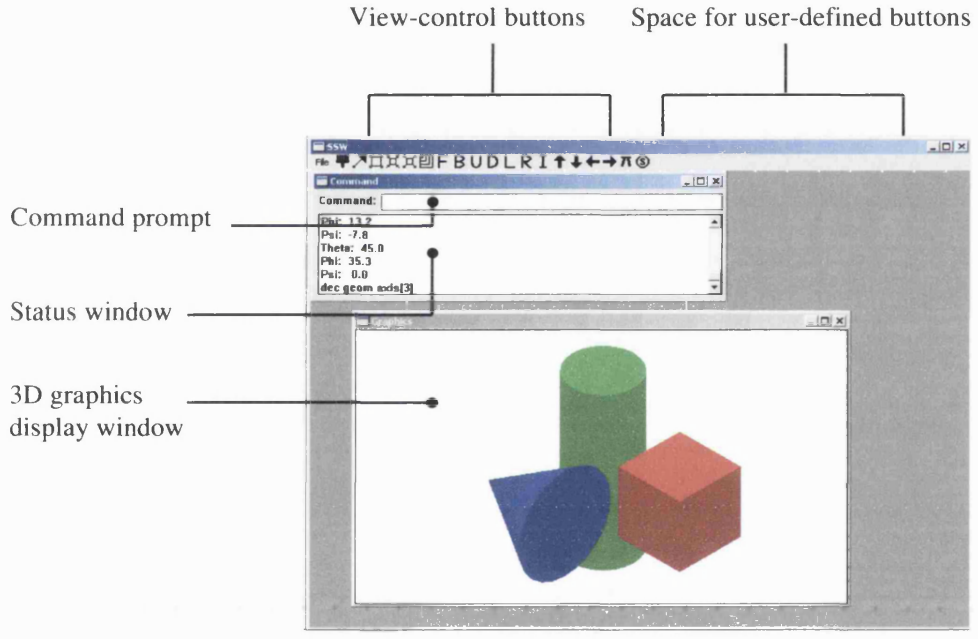

Figure 37 The appearance of SWORDS.

4 AIMS AND OBJECTIVES

4.1 Overall Aim

The aim of the work was to investigate whether it is possible to predict the characteristic movement patterns of the carpal bones by maximising the total contact area occurring between selected pairs of contacting articular surfaces. The work was carried out using the SWORDS geometric modeller with support from external programs where appropriate.

4.2 Objectives

The specific objectives were as follows:

1. Obtaining Three-Dimensional Computer Models of the Carpal Bones

It was necessary to start with three-dimensional models because the complex out-of-plane movements of the bones means that very little useful information could be gleaned from a two-dimensional approximation.

2. Calculation of Total Surface Contact Area

A method of estimating the contact area between joint surfaces was required.

3. Collision Detection and Evaluation

When moving objects in a virtual environment, it is necessary to have some means of avoiding the situation where two or more objects occupy the same region of space. The need for a method of collision detection and evaluation was therefore of fundamental importance for this study.

4. Movement Prediction

The final objective was to combine all the elements encompassed by the three statements above and use an optimisation scheme to determine the movement of the bones for increments of overall hand position in radial and ulnar deviation.

5 METHODS

Methods

This section describes the methods used to achieve the stated objectives. There were many difficult problems to solve and frequently several alternative approaches were available. Where possible in these cases, experiments were performed in order to determine the most appropriate direction in which to proceed. In cases where this was not possible, every effort is made to justify the decisions that were taken.

In several cases, time was invested into solving a problem, with no justification other than the desire to explore. While these experiments occasionally succeeded, this section also covers some of the inevitable failures that resulted. The useful knowledge learned from these experiments is presented where possible.

This section includes the following:

- Obtaining and manipulating three-dimensional models of the carpal bones
- Methods of evaluating contact area between joint surfaces
- Methods of evaluating level of interference between bone models
- Moving the bones in three-dimensions
- Run-time considerations and methods used to increase speed of computation
- Optimisation techniques
- Animating and quantifying the predicted movement

In order to maintain readability of this section, calculations longer than a single equation have been placed in appendix section 11.1.

Unless stated otherwise, the convention adopted for symbols in equations is as follows:

Scalar variables:	Italic type, lower-case, not bold e.g. p
Matrices:	Italic type, upper-case, not bold e.g. R
Vectors:	Upright type, lower-case, bold e.g. $\mathbf{u}$

Rotations in 3D follow the right-hand thumb convention.

5.1 Coordinate System

The origin of the coordinate system was placed on the distal-most tip of the ulnar styloid of a right wrist. The ulnar styloid was chosen as the origin as it is a prominent and easily identifiable landmark.

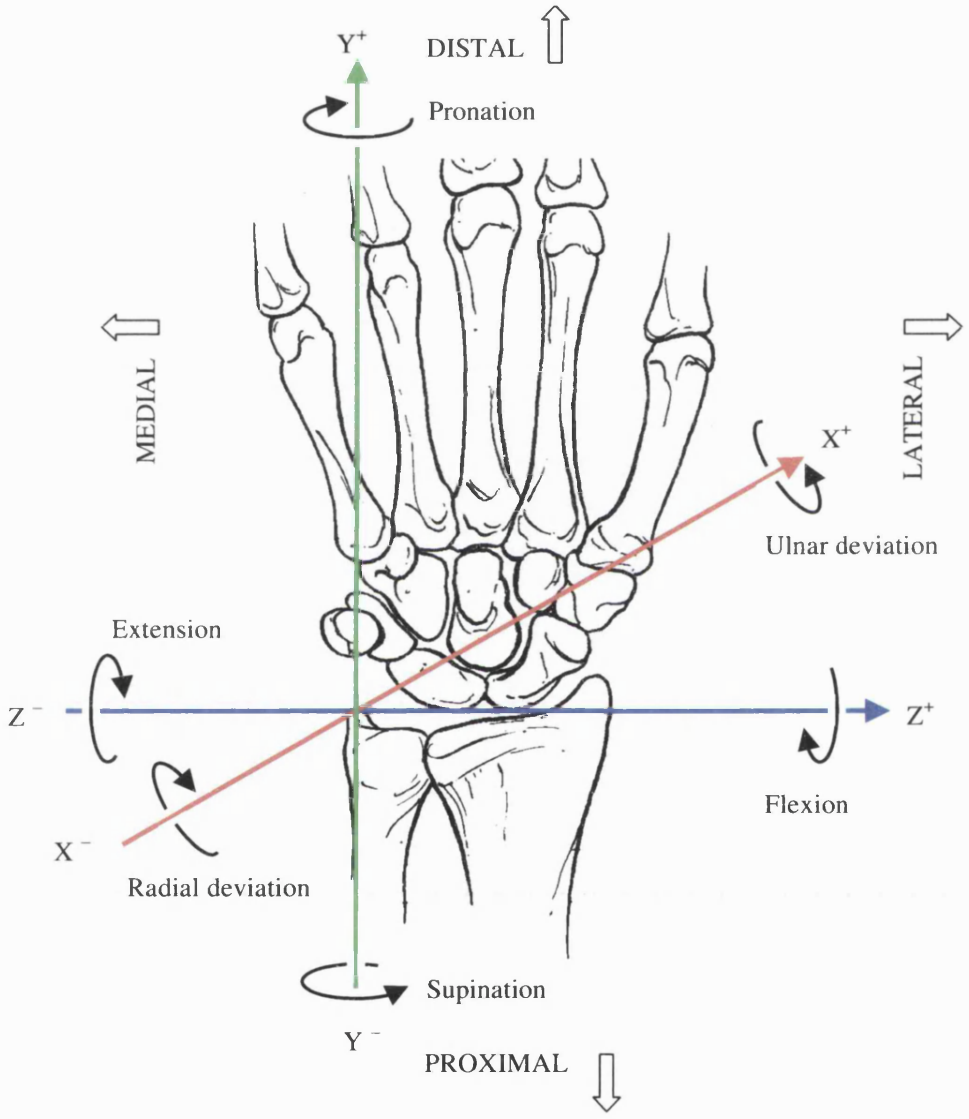

Figure 38 Coordinate system. Palmar view of right wrist. (Adapted from Nordin & Frankel, 1989).

5.2 Obtaining Computer Models from a Computed Tomographic Study

The authors of a study of carpal kinematics (Snel *et al.*, 2000) kindly agreed to donate a set of three-dimensional models of the carpal bones. The bones were obtained by reconstructing a series of cross sectional CT images recorded at 0.3mm longitudinal intervals. A single right male wrist, oriented in the neutral position was recorded. The average number of facets in each bone was around 5000, resulting in a surface resolution of approximately 0.5mm.

5.2.1 Mesh Resolution Reduction

Initial experiments showed that the computational expense of performing repetitive operations on the bones was too high unless the number of facets could be reduced. A fifty percent reduction was achieved using "Points2Polys" (Paraform Inc.), a freeware point-cloud triangulation/manipulation application.

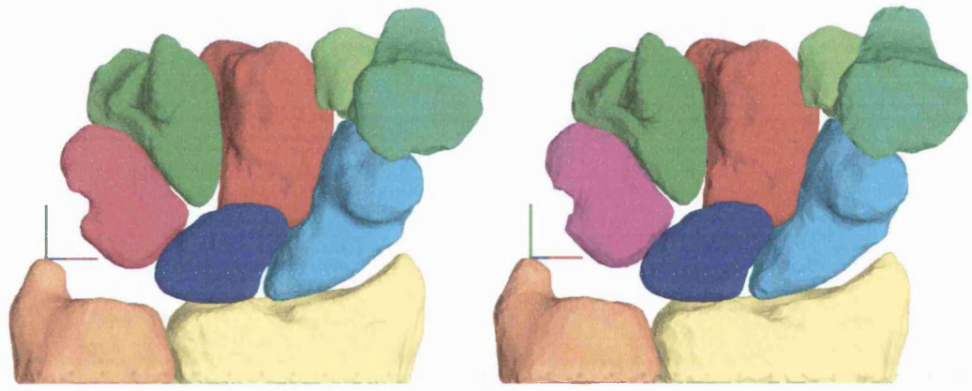

(a) (b)

Figure 39 Three-dimensional models of the wrist bones from reconstructed CT slice images: (a) original resolution (b) resolution reduced by 50%.

5.2.2 Conversion of Models to Solid Format

The bone models were supplied in a surface mesh format. The 3D modeller within SWORDS is capable of displaying both surface and solid models. However, Boolean operations (union, intersection, subtraction etc.) may only be performed on solid models. During the initial stages of the work, it was envisaged that collision detection could be performed within SWORDS by evaluating the volume of the solid formed from the Boolean intersection of adjacent bones. Therefore, it was necessary to convert the surface models to solids.

A C++ computer program was written by G. Mullineux to perform the conversion.

5.2.3 Investigation of separation distance between bone models

Since the bone models were obtained using CT imaging, they did not include the articular cartilage covering. Therefore, there were air spaces between the bones. The distribution of facet separation distances, in the "as supplied" i.e. neutral, position of the wrist, was investigated so that the articular cartilage thickness could be inferred (Figure 41-Figure 44). Separation was defined as the distance along the surface normal from the centroid of one facet to the piercing point on the nearest facet on the opposite surface. The separation values obtained in this way (marked with dotted lines on the graphs) were used to specify minimum/maximum thresholds for points of closest approach between two models in the optimisation algorithm and are summarised in Table 1. This is discussed in more depth in section 5.7.

It is interesting to note the variation in separation between the joint surfaces. The greatest gap, around 2.0mm was found to occur between those bones in contact with the radius, i.e. lunate and scaphoid. This reflects the fact that the radial surface has a greater thickness of articular cartilage than the carpals since it is subject to the resultant of all forces transmitted through the various load paths of the wrist. This agrees with the findings of a study of force transmission through the wrist (Schuind *et al.*, 1995), in which the greatest forces were found at the radio-scaphoid and radio-lunate joints (see Figure 40).

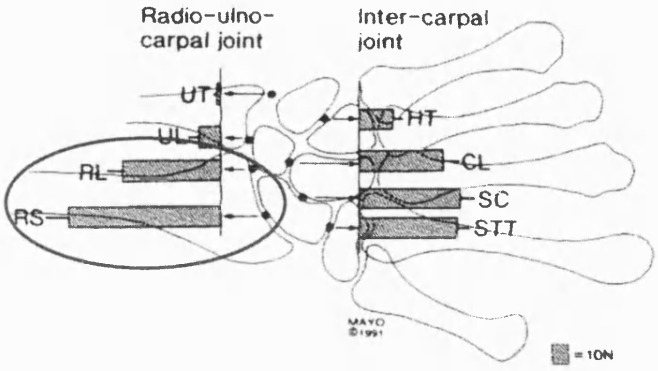

Figure 40 Resultant force distribution in the wrist shows the greatest forces exist at the radio-lunate and radio-scaphoid interfaces. where the cartilage thickness is greatest (Schuind *et al.*, 1995).

Similarly, the smallest gap occurred between the scaphoid and lunate. This interface is perpendicular to the principal loading planes of the wrist, so presumably contact stresses are lower and the cartilage thickness does not need to be as great. These two observations reinforce the notion that materials used to make the joint are kept to a minimum.

5.2.4 Summary

This section has described how models of the bones in a wrist were obtained from a CT reconstructive study and processed for use in this study. The bones were supplied in the form of surface models and these were converted to solid form to allow Boolean operations to be performed within SWORDS. Since the articular surfaces were absent, the separation distances between the bones was investigated as a means of estimating the average cartilage thickness.

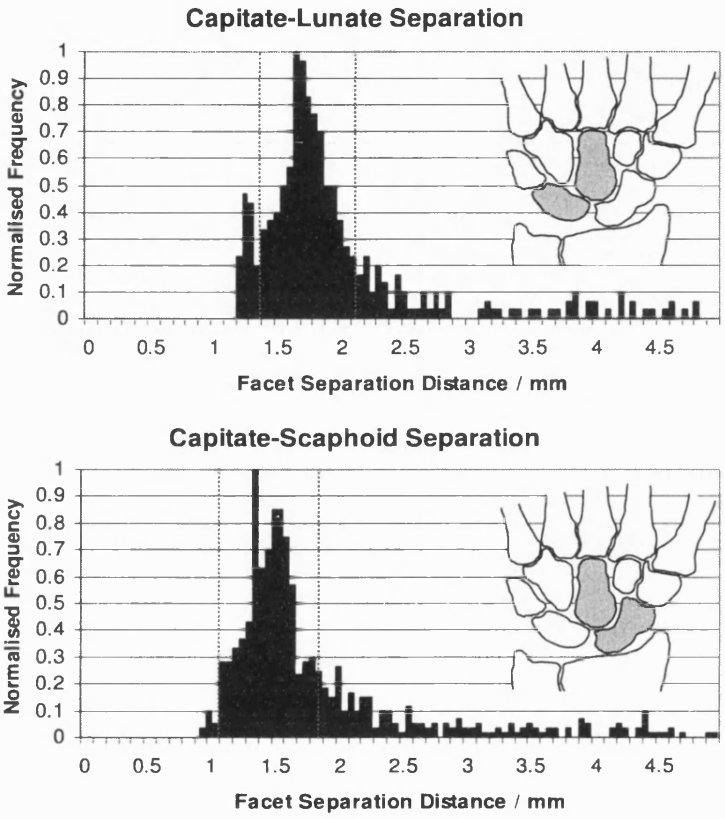

Figure 41 Separation distance between bones of the wrist (1/4). Dotted lines indicate the minimum/maximum distance threshold values that were used when running the predictive computer program (see section 6.2).

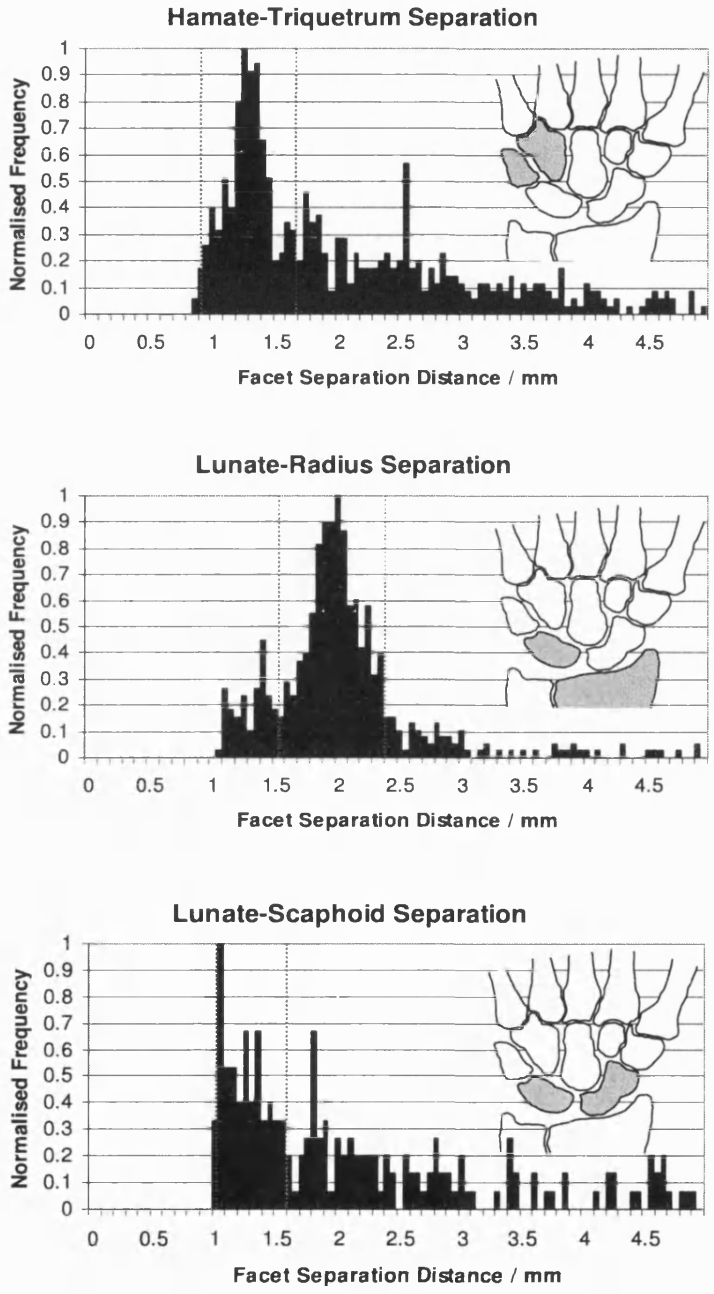

Figure 42 Separation distance between bones of the wrist (2/4).

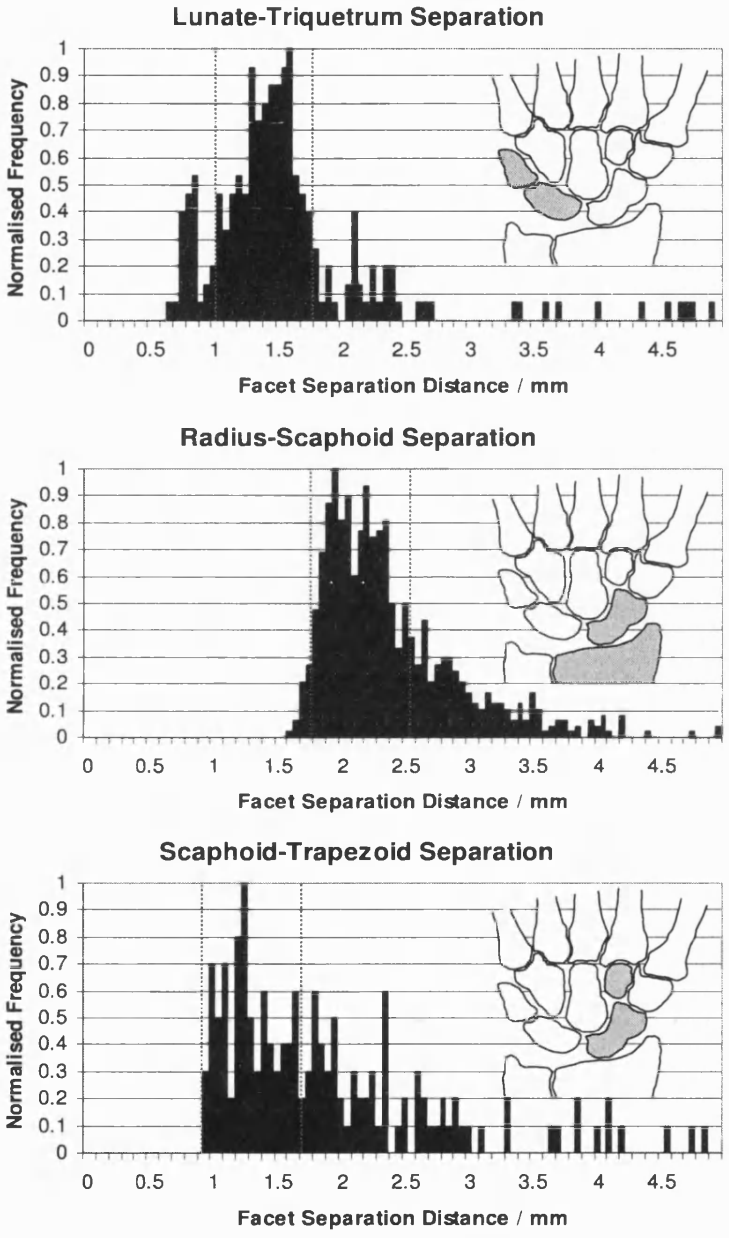

Figure 43 Separation distance between bones of the wrist (3/4).

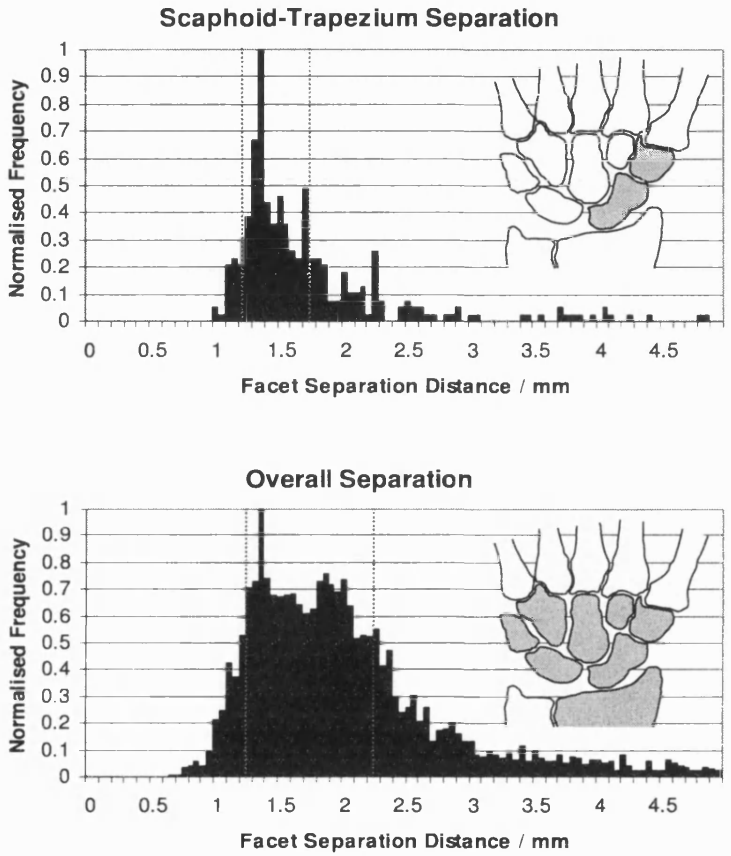

Figure 44 Separation distance between bones of the wrist (4/4).

Bone Pair	Min / mm	Max / mm
Capitate-Lunate	1.35	2.05
Capitate-Scaphoid	1.05	1.85
Hamate-Triquetrum	0.85	1.65
Lunate-Radius	1.50	2.35
Lunate-Scaphoid	1.00	1.55
Lunate-Triquetrum	1.05	1.75
Radius-Scaphoid	1.75	2.50
Scaphoid-Trapezoid	0.85	1.65
Scaphoid-Trapezium	1.15	1.70
All Pairs	**1.20**	**2.20**

Table 1 Summary of separation distance thresholds derived from graphs of Figure 41-Figure 44.

5.3 Laser Surface Profilometer Experiments

Since this study is concerned with calculating contact area between joint surfaces, ideally a set of bone models that include the articular cartilage is required. Due to the variability of cartilage thickness between different bones and over the surface of the same bone, the thickness estimation outlined in section 5.2.3 was considered unsatisfactory. Furthermore, the results of predicted movements using these models bore little resemblance to known movement patterns (see section 6.2). Therefore, ways of obtaining cartilage-inclusive bone models were investigated. The first method tested was direct surface digitisation using a laser profilometer in the department of Engineering and Applied Science at the University of Bath.

The laser profilometer consists of a platen that can move in the x-y direction and a visible light laser probe. The system calculates the perpendicular height above an x-y datum plane of points on the surface of an object. Its primary purpose is to measure surface roughness at the level of microns. However, the system is supplied with an additional probe that can record variations in height in the range of zero to 8mm, but at lower resolution. This probe was used to test the feasibility of using the system to obtain models of the carpal bones.

5.3.1 Scanning Jig

In order to record the entire surface, it was necessary to scan the object in several different orientations. Further, a means of registering the mosaic of scans was required. To meet these requirements, a special jig was created (Figure 45). This consisted of a 1mm diameter skewer onto which the object to be scanned was mounted, indexing devices at either end which allowed the skewer to be rotated in increments of exactly 90°, and two cylinders mounted on the shaft at either side of the bone to provide axial registration.

5.3.2 Testing on Trapezium Bone

The system was tested on a dissected human trapezium bone. The bone had been removed due to eburnation of the joint surface at the interface with the hamate. Full patient consent was granted. The bone was scanned in four rotational positions. Then the skewer was removed and re-inserted through the centre of the bone but at right angles to its original orientation to allow the ends of the bone to be scanned. To provide additional alignment cues, eight marker-pins (four at each end) were inserted into the bone.

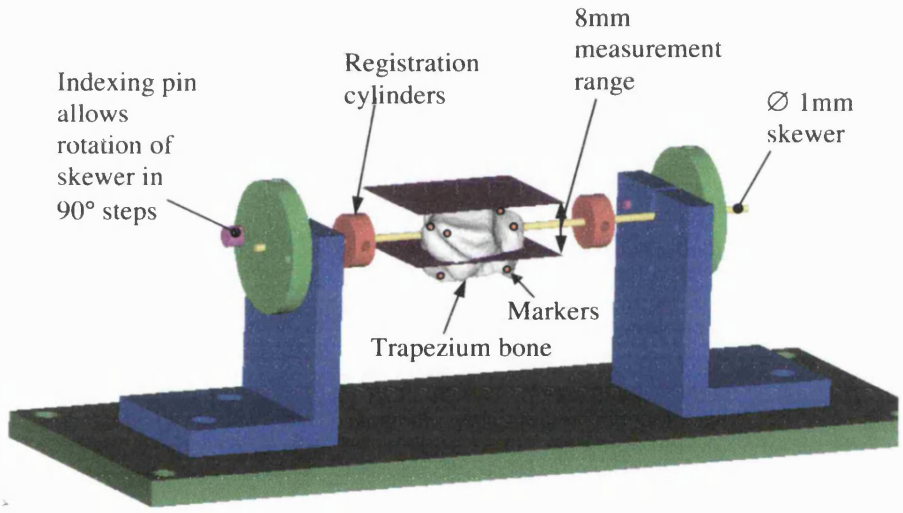

Figure 45 A jig was created to allow a bone to be scanned in four rotational positions.

5.3.3 Surface Treatment

Initial trials showed that the translucency and reflectivity of the articular cartilage was problematic for the system and consequently null readings were returned for several regions of the surface (Figure 48). It is presumed that this occurred because the laser light was scattered throughout the depth of the cartilage, causing multiple reflections to be returned, thereby confusing the system. Consequently, it was decided to spray-paint the bone matt grey. This procedure solved the null reading problem and allowed the full surface detail to be recorded (Figure 50).

5.3.4 Mesh Alignment

The spray-painted bone was scanned at a resolution of 0.2mm. The time taken to scan each of the six partial surfaces used for the bone was approximately three minutes. The partial surfaces were aligned using AutoCAD (Figure 51). The surfaces of the registration cylinders at each end of the bone were identified and used to determine the location of the skewer axis. Once the axis was determined, each partial surface was rotated about this axis into the correct orientation. Any regions of overlap between adjoining partial surfaces were removed by manually erasing individual facets. Fitting of the two partial surfaces of the ends of the bone was more problematic. In order to align these, the positions of four marker pins inserted into each end of the bone were matched. Despite manual repositioning of the scans, it was difficult to achieve matching of all markers to accuracy greater than 1mm (see Figure 51).

The realignment procedure was extremely labour-intensive, and matching errors persisted in the finished model despite the measures taken to ensure proper alignment. Furthermore, due to the limited measurement range, the method was not suitable for scanning bones having any part of the surface further than 8mm from the skewer axis.

5.3.5 Summary

The profilometer method was ultimately rejected as a means of obtaining carpal bones. However, the experiments yielded information that would prove useful for future work.

There were several reasons why the method was deemed unsatisfactory. Firstly, the alignment and editing of the sections of mesh proved to be a very laborious task. Ideally, it should only have been necessary to rotate each mesh section through 90° and adjust translation in one direction in order to align mesh segments. However, due to mechanical imperfections and alignment problems, it was necessary to apply manual adjustments. Once the mesh sections were aligned, the removal of overlapping facets was another time-consuming task.

Another disadvantage of the method was that the height measurement range was limited to 8mm. While this range was sufficient for the trapezium bone, it would have been difficult to scan bones having high levels of curvature in a single pass, as some regions of the surface would have been beyond measurable limits (Figure 46).

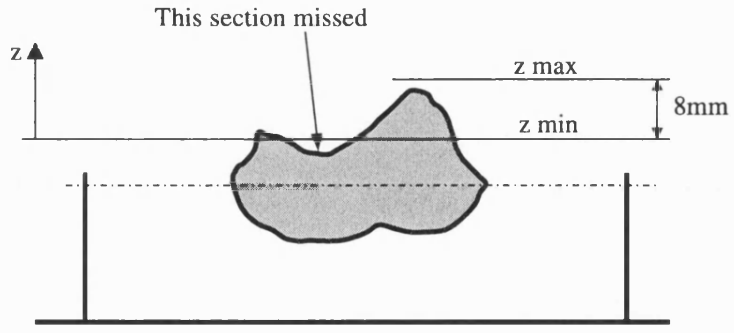

Figure 46 An 8mm measurement range means it is difficult to use the profilometer to scan bones having high curvature, e.g. the scaphoid.

Despite the shortcomings of the method, some valuable lessons were learned. When the un-painted bone was scanned, it became apparent that the articular cartilage de-hydrated rapidly when exposed to the air. Hence, it was decided that for future procedures of this kind (see section 5.5), the bones would be stored in saline to maintain hydration and only removed immediately prior to scanning. Further, the experiments revealed a problem with laser scanning of translucent materials, which was solved by spray-painting the surface. It is possible that this procedure also partially seals the surface, thereby reducing evaporative dehydration.

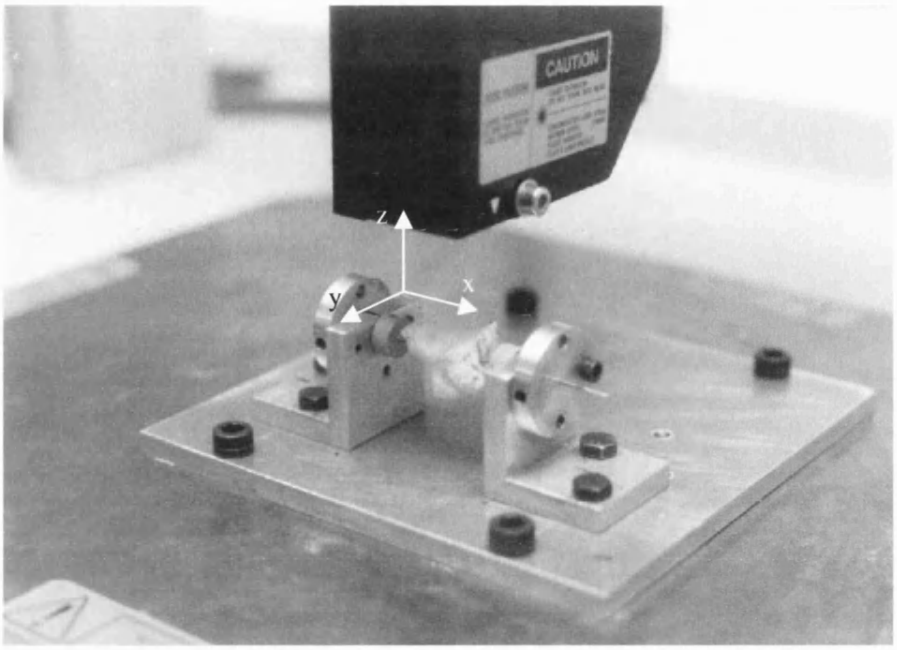

Figure 47 Scanning a trapezium bone using a laser surface profilometer. Note diffusion of laser-spot.

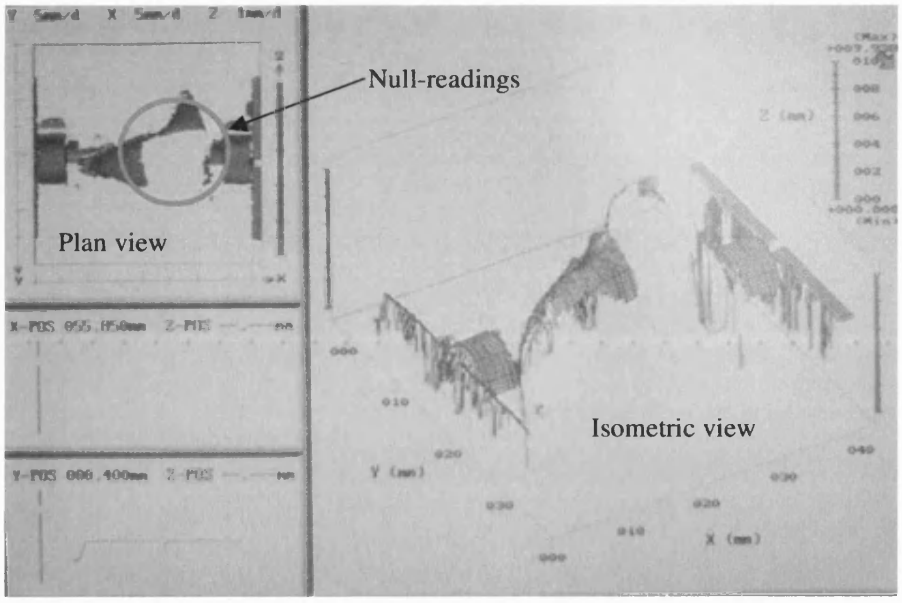

Figure 48 Screen-image from the acquisition software showing large areas of null readings due to cartilage translucency.

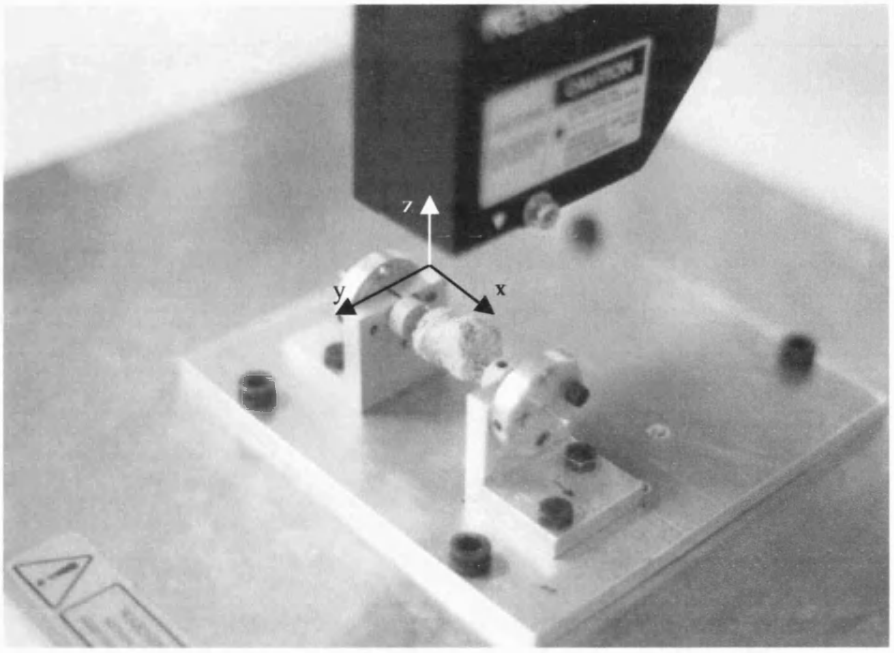

Figure 49 Scanning of the trapezium following matt-grey spray-painting. The laser-spot is less diffuse.

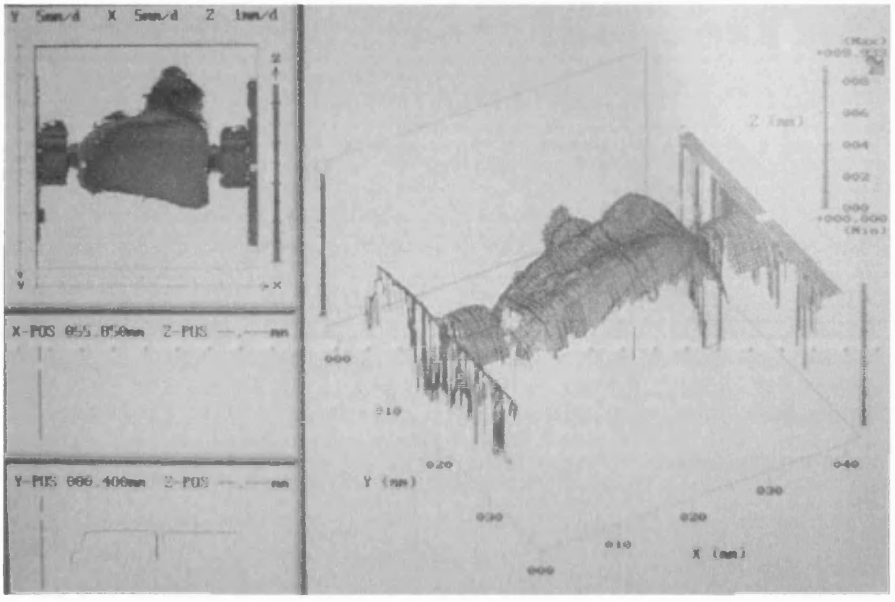

Figure 50 Screen-image from the acquisition software showing improved results for the painted surface.

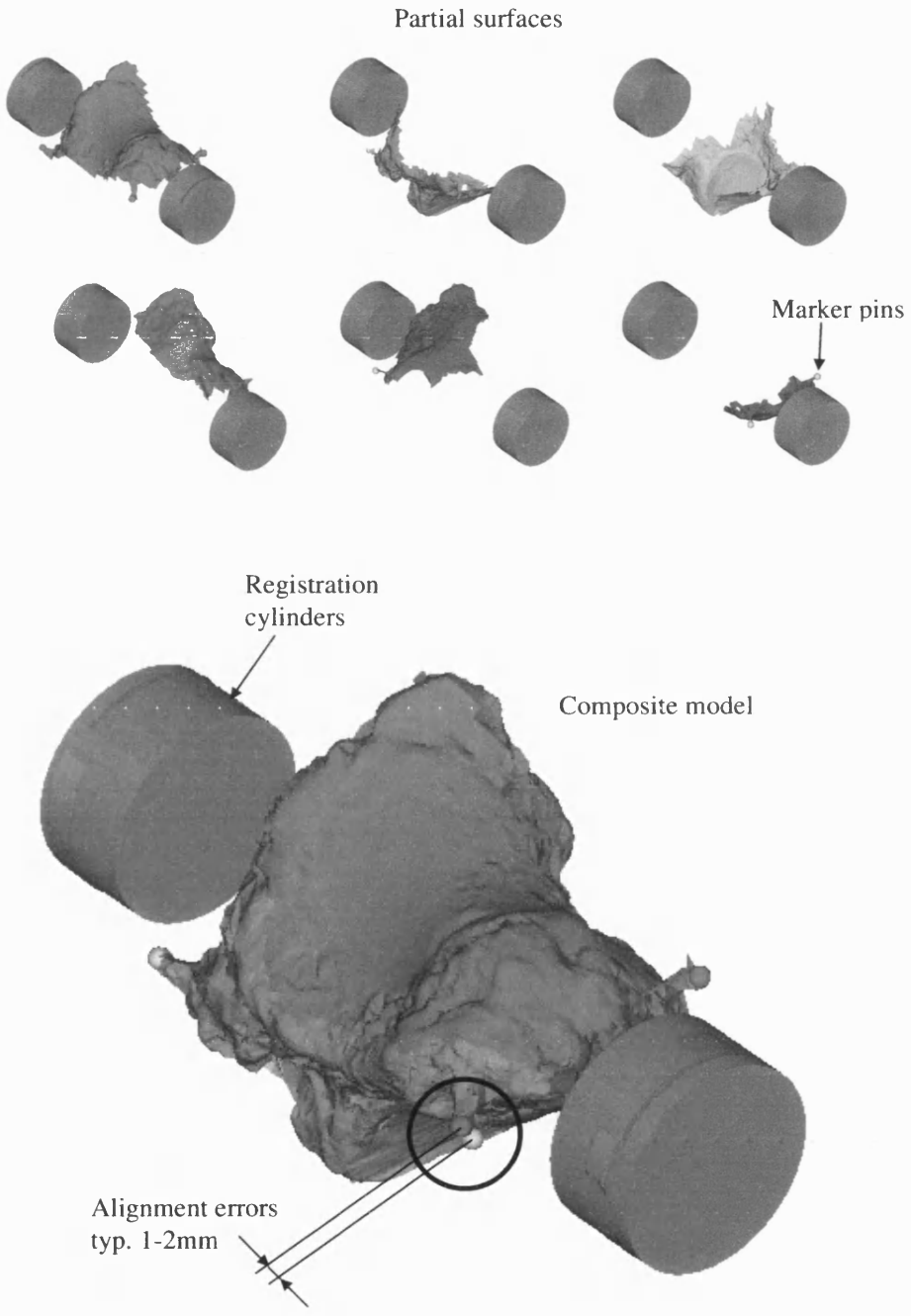

Figure 51 Manual reconstruction of a trapezium bone model from six partial surfaces obtained using a laser profilometer.

5.4 MR Imaging

The feasibility of obtaining 3D models of the wrist bones using magnetic resonance (MR) imaging techniques was investigated. Colleagues at the University of Exeter were consulted with a view to using an experimental MR scanner in the Department of Physics for this study. A cost of £1000 per day was quoted for the use of the equipment, which immediately reduced the attractiveness of this option. In addition, costly specialist software would be required to reconstruct the 3D models from the series of 2D image slices.

There existed the possibility of purchasing a series of MR images of the wrist from a source such as the Visible Human Project. However, this option would still require the use of costly 3D reconstruction software. Internet-based sources of models such as the Vakhum Repository of Morphological Models (http://www.ulb.ac.be/project/vakhum) were also consulted, but there was a scarcity of sufficiently detailed wrist-models.

5.5 Laser Digitisation of Dissected Wrist Bones

The method finally chosen to give accurate 3D models of the carpal bones, complete with articular cartilage, was laser surface digitisation via a bureau service (Archaeoptics Ltd., Glasgow).

5.5.1 Outline of method

Laser surface digitisation has much in common with laser surface profilometry, as outlined in section 5.3. A laser projects a spot of visible red light onto the surface of an object being scanned. The system then calculates the distance from the source to the spot of light. Unlike the profilometry system, where the object moves relative to a fixed laser spot, the laser digitiser sweeps the laser spot over the entire visible surface in a matter of seconds. The object is placed onto a turntable, which is rotated to allow all parts of the surface to be exposed to the scanner. The object is then turned upside-down to allow the bottom to be digitised. The laser digitiser used was a Minolta VI 900 (Minolta Inc.)

The expertise of the bureau lies in the bespoke software developed to align and merge the mosaic of scans. The software performs realignment by recognizing patterns in the surface topography that are common to adjoining sections so that alignment points can be determined from objects of arbitrary shape without the need for physical markers on the object.

Direct digitisation of dissected, disarticulated joints has been used previously to obtain 3D models of the knee (Wilson *et al.*, 2000). However, in these studies, digitisation was achieved using a contacting stylus. The benefit of a laser-based system is that it is non-contacting and allows more rapid sampling in comparison to a stylus-based method. Furthermore, it is believed that this is the first time this approach has been used to digitise the entire carpus since a literature search did not reveal any similar work.

5.5.2 Preparation of Bone Specimens

A fresh-frozen left male human forearm, amputated following brachial plexus injury was dissected to allow digitisation of the carpal bones. Full patient and ethical committee approval was obtained for the study. The wrist was normal, with no history of disease or injury. Dissection was performed by a consultant hand surgeon (Mr. G.E.B. Giddins) with assistance from the author.

Skin, muscles, tendons and fingers were removed from the forearm until the joint capsule surrounding the wrist was visible. Small incisions into the capsule were made to allow visual identification of the carpal bones. The incisions were small enough that normal wrist kinematics were not grossly altered (although it is impossible to tell if this was indeed the case).

All the carpal bones were identified by a combination of palpation and inspection. Into each carpal (with the exception of the pisiform, which was removed) and the radius and ulna, were inserted three conical-headed marker pins (Figure 54). The wrist was then held in the neutral position while the positions of the 24 marker pins were obtained using a digitising stylus (Fastrak system, Polhemus Inc.) (Figure 55). The digitisation process was performed twice, revealing a maximum repeatability error of 1mm. The mean values of the two sets of readings were recorded.

Following digitisation of the marker positions, the carpus was dissected to reveal the individual bones. Great care was taken during this procedure to avoid damaging the articular surfaces. Despite these efforts, some minor pin-prick damage resulted from failed attempts at insertion of the marker pins in some regions of very hard bone. The radius and ulna were resected 20mm from their distal ends and extraneous soft tissue was removed from the carpals. The bones were transported to the scanning bureau in a vessel of saline to maintain hydration of the articular surfaces. Total scanning time was around one hour for all bones and computer models were delivered within three weeks. The resulting 3D models are shown in Figure 57.

Figure 52 Fresh frozen left human forearm.

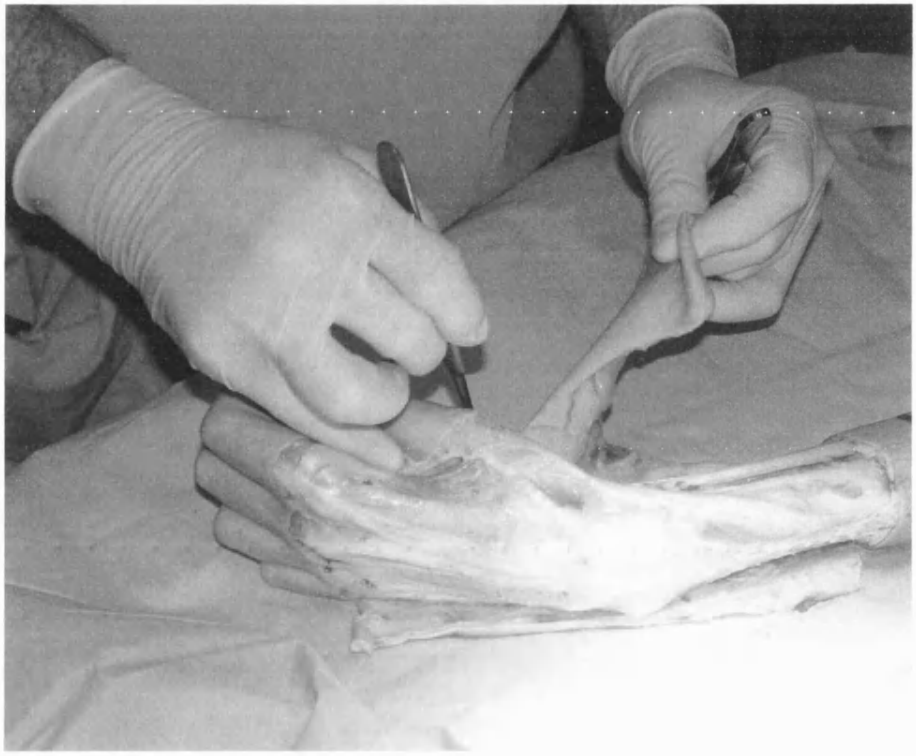

Figure 53 Tissue removal.

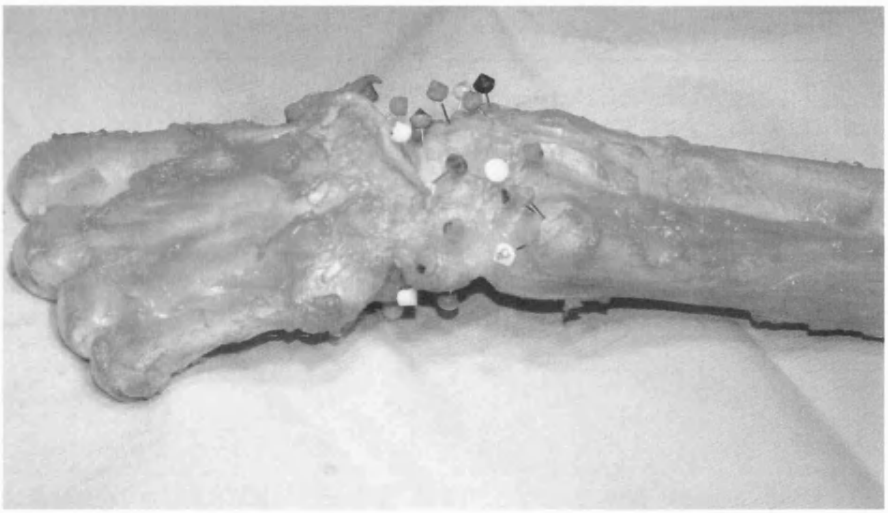

(a)

(b)

Figure 54 Dissection continued until the joint capsule was exposed. Bones were located by palpation through the joint capsule and three marker pins were inserted into each. (a) Dorsal view. (b) Palmar view.

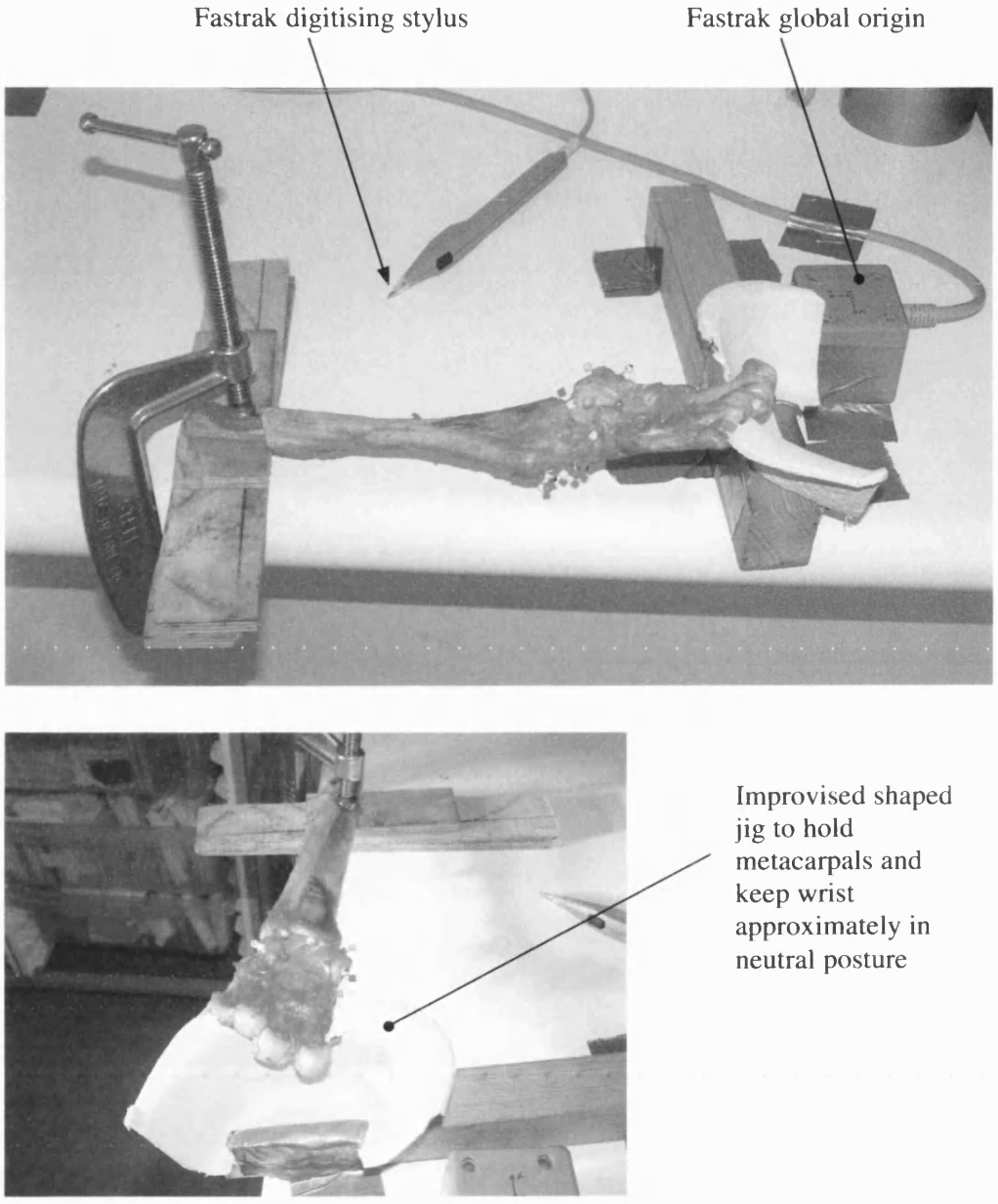

Figure 55 The forearm was held immobile in a jig while the positions of the marker pins were digitised.

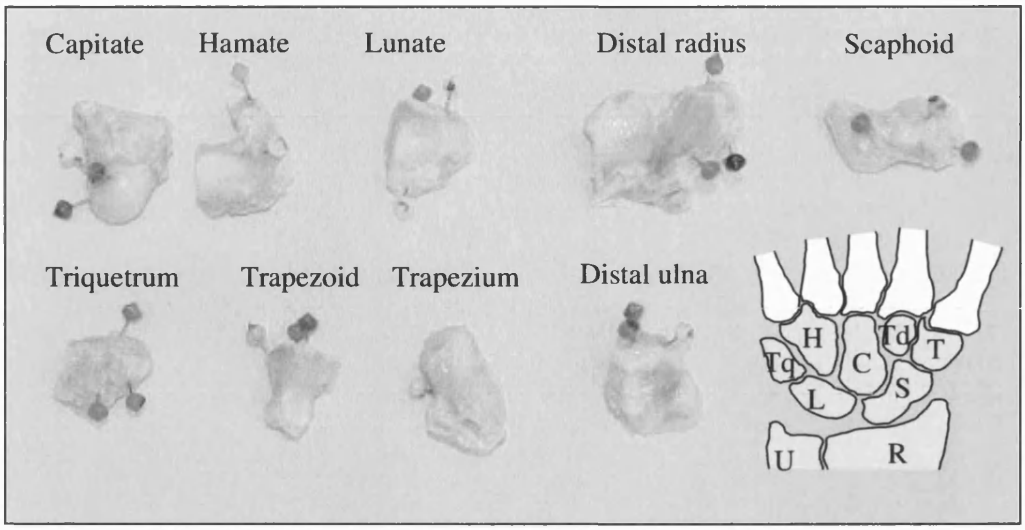

(a)

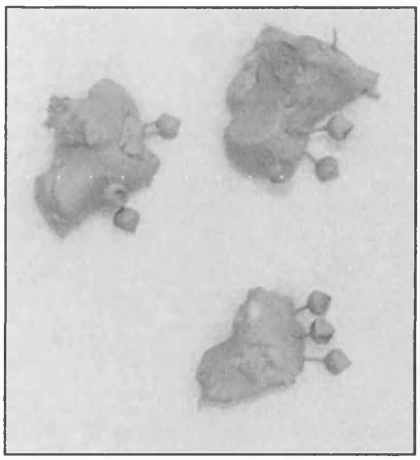

(b)

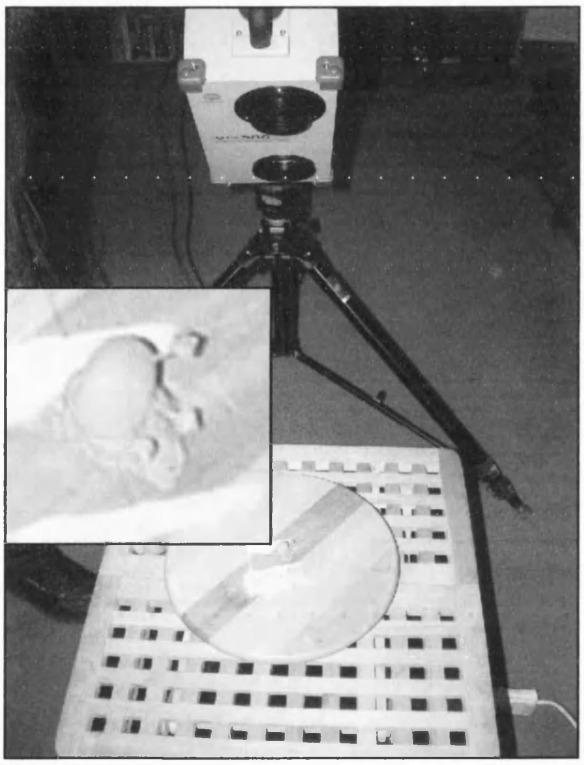

(c)

Figure 56 (a) Individual carpal bones after dissection. (b) Bones spray-painted immediately before scanning to reduce reading errors due to cartilage translucency. (c) Laser scanning with bone mounted on a turntable.

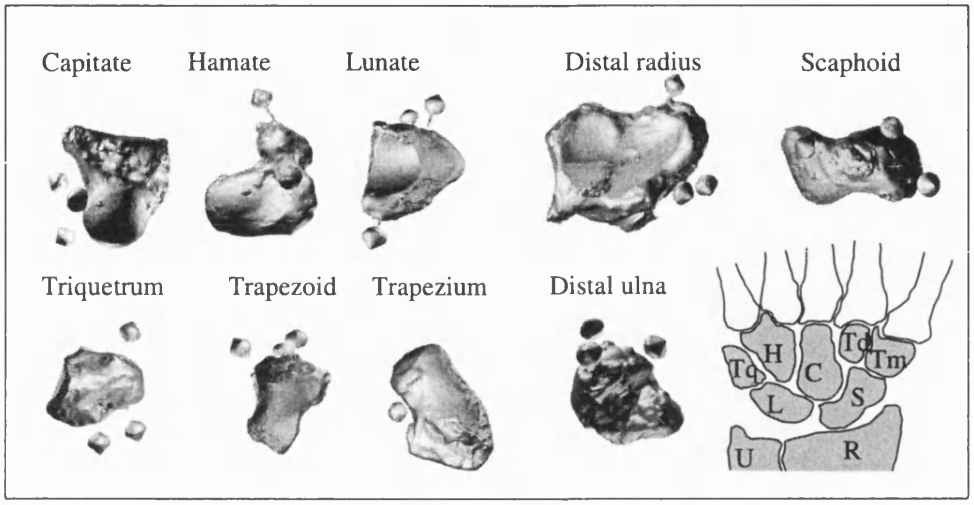

Figure 57 Three-dimensional models of the carpal bones.

5.5.3 Mesh reduction

Before any further operations were performed, the models were mirrored to create a right wrist. In order to reduce computational expense of subsequent operations, the resolution of the models was reduced by 90% using Points2Polys. An investigation into the effects of mesh resolution on computational expense is described in section 5.15. The resolution of the entire ulna and the non-articular surface region of the radius were reduced still further since there was no need to maintain high detail in these regions as they are not involved in the contact area calculation (Figure 58). The original models were highly detailed, having a surface resolution of 0.17mm and it is regrettable that much of this detail was removed. However, it is envisioned that it may eventually be feasible to use the full resolution models, provided the efficiency of the computer program is improved sufficiently. This is discussed further in section 8.1.4.

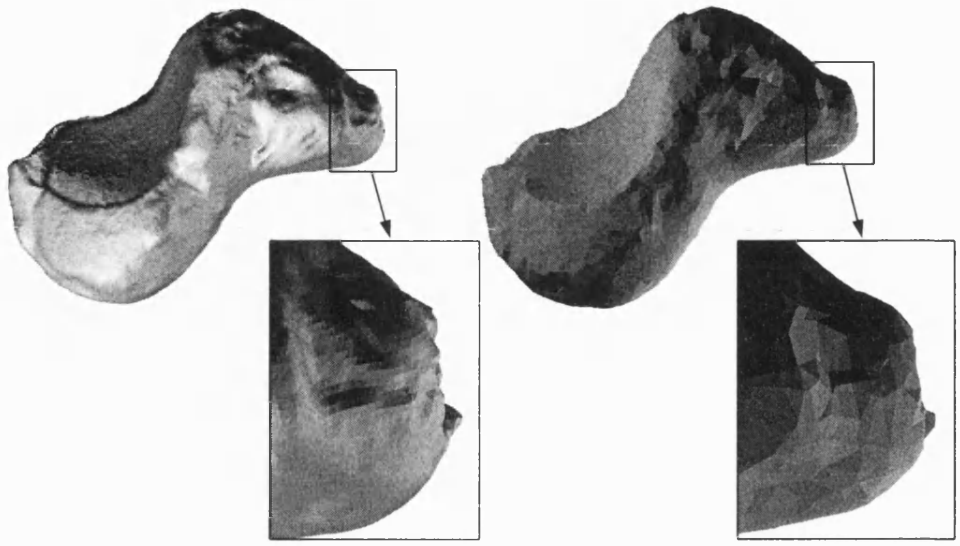

(a) (b)

Figure 58 The mesh resolution for all bones was reduced by 90% to reduce computational expense. (a) Scaphoid bone at full resolution. (b) Scaphoid bone after reduction.

5.5.4 Reconstruction of the Carpus

The carpal bone models exported from Points2Polys were converted into a compatible file format (3DS) using "Deep Exploration" (Right Hemisphere Inc.) The 3DS meshes were imported into a CAD system (AutoCAD, Autodesk Inc.) and realigned into their anatomical positions. This was achieved by repositioning the models so that the tips of all three markers coincided with the digitised coordinates obtained prior to dissection using the three-point alignment command. The markers were then removed from the models. Hole filling was performed on the mesh defects resulting from removal of the shafts. These two operations were performed using Points2Polys. The entire carpus was shifted to align with the coordinate system described in section 5.1.

5.5.5 Alignment Errors

From observing the reconstructed carpus, It became clear that some of the carpal bones were wrongly positioned (Figure 59). There are two possible explanations for the errors:

1. Digitisation errors – the Fastrak stylus was not placed exactly at the tip of one or more marker cones. The magnifying effect of the length of the marker shafts and the fact that some pins were clustered closely together would have meant that the 1mm digitisation errors could produce greater overall positional errors.

2. Carpal separation – It is possible that the positions of the carpal bones could have shifted within the joint capsule because of disturbances during the dissection. In this case, the observed positional errors could be reflective of the actual situation.

5.5.6 Manual Repositioning

The bone models were manually repositioned within AutoCAD with the assistance of the practiced eye of a consultant hand surgeon (Mr. G.E.B. Giddins). This was a painstaking task, since it was necessary to ensure that the surfaces were as close together as possible without actually intersecting. Once the bones were in the best configuration obtainable by visual inspection alone, the arrangement was optimised using the SWORDS algorithm described later. The adjustments made at this stage were of the order of 0.5mm / 1.0°. Figure 61 shows overall dimensions of the assembled wrist.

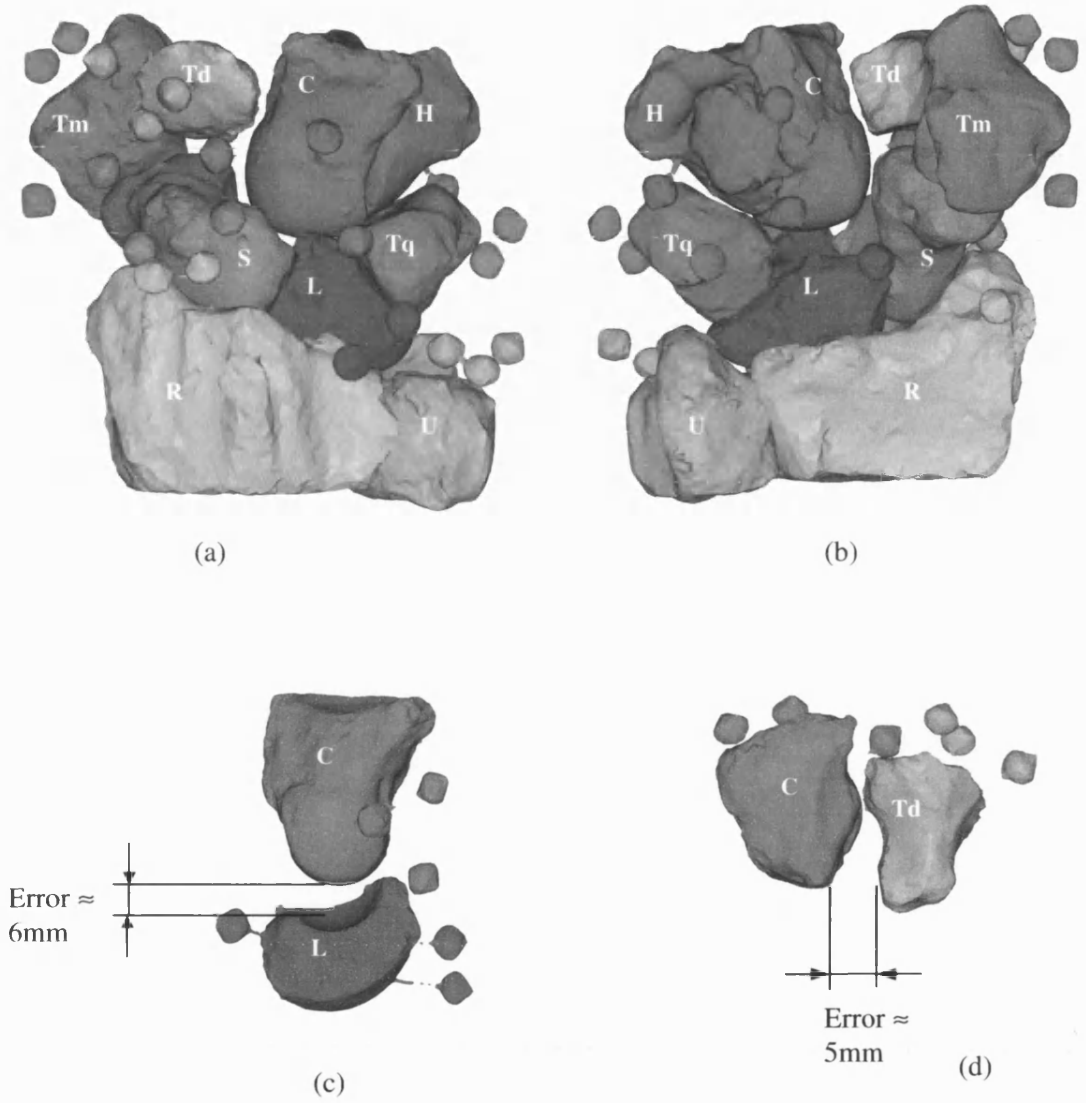

Figure 59 Positions of the carpal bones following realignment of markers on models to recorded coordinates. (a) Dorsal view. (b) Palmar View. (c) Radial view. (d) Distal view. Positional errors of up to 6mm were observed.

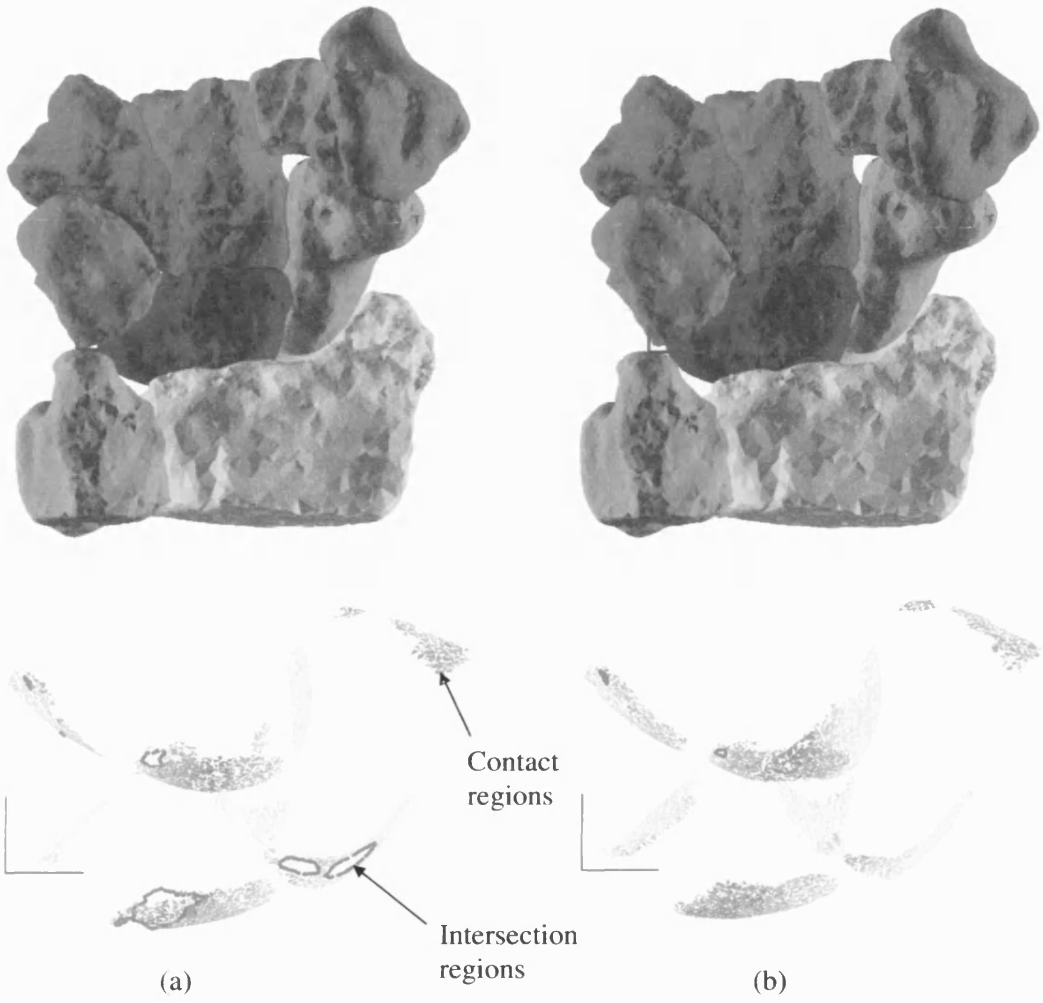

Figure 60 Two further levels of re-alignment were necessary. (a) The bones were manually adjusted in AutoCAD to remove the gross errors shown in Figure 59. (b) Fine-tuning of positions was performed by the SWORDS algorithm in order to eliminate intersection between bones and maximise contact area.

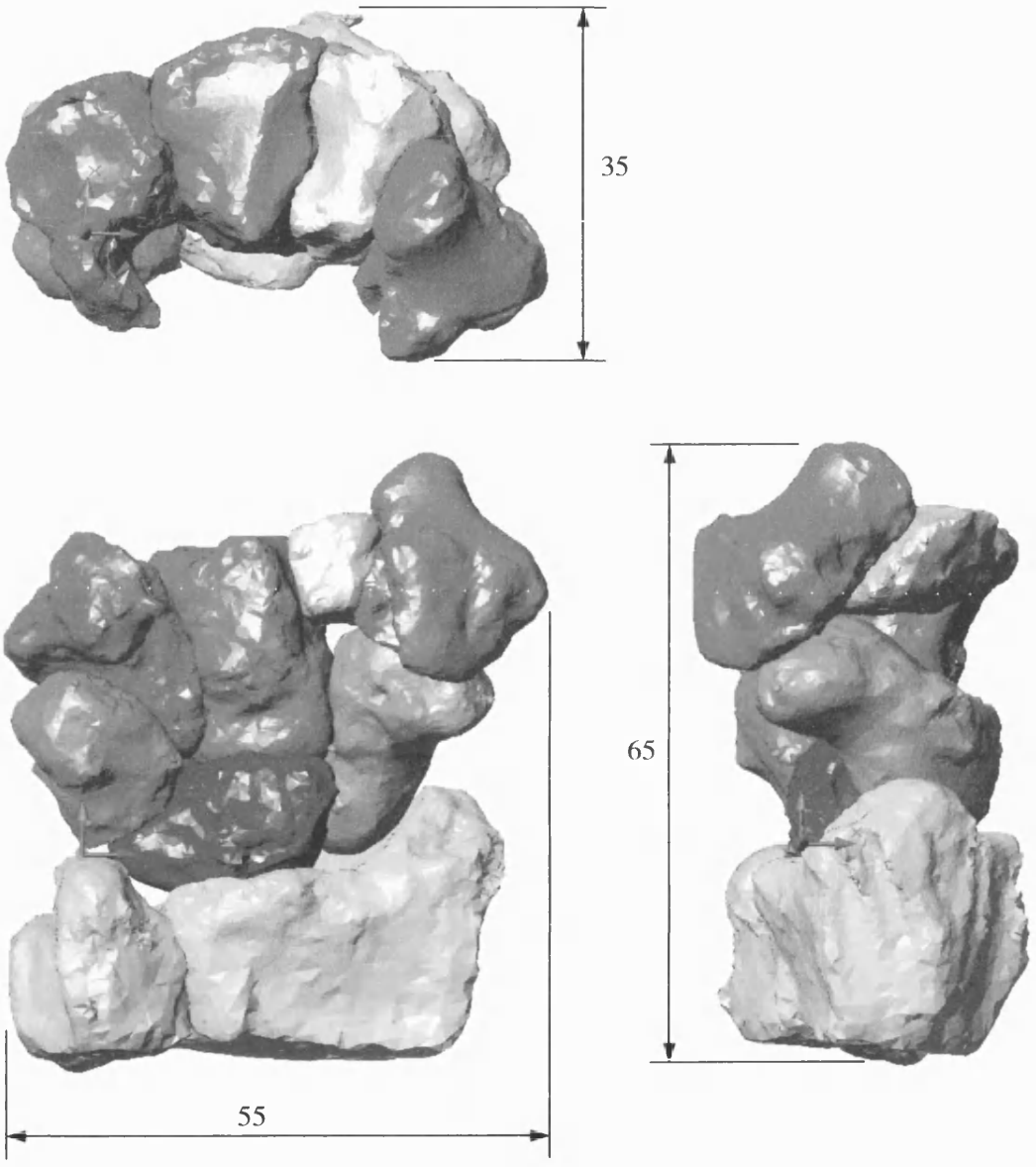

Figure 61 Overall dimensions (millimetres) of the assembled wrist bones.

5.6 Indirect Estimation of Total Joint Surface Contact Area

This section will discuss alternative strategies for evaluating the tightness of packing of the carpals that were considered or tested during the study.

5.6.1 Convex Hull Volume Minimisation

An indirect method was considered based upon the convex hull.

The convex hull is the smallest fully convex three-dimensional shape into which an object or group of objects can fit (Figure 62). Experiments were performed using the "Qhull" (Barber *et al.*, 1996) freeware application. This program computes the shape of the convex hull and its volume from a set of three-dimensional points on the surface of the object or group of objects.

By moving the carpal bones in such a way as to minimise the volume of the convex hull, it was initially thought that the packing density, and so the total contact area, would be maximised. This approach was used in conjunction with a Boolean solid intersection test to check for collisions. Frames from an animation of the minimisation process for three conforming shapes are shown in Figure 63. The animation itself is included on the CD ROM accompanying this thesis. This idea was ultimately rejected because the lunate bone was found to be entirely within the convex hull of the carpus and radius at all hand positions, with the result that its movements had no effect whatsoever on the hull volume (Figure 64, Figure 65).

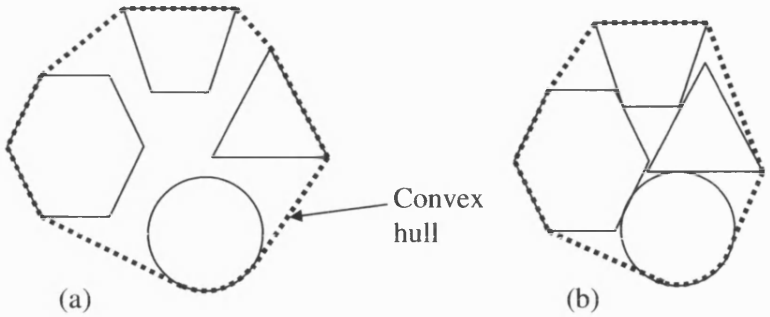

Figure 62 The volume of the convex hull was considered as an indicator of packing density. (a) Low packing density. (b) Maximum packing density gives minimum convex hull volume.

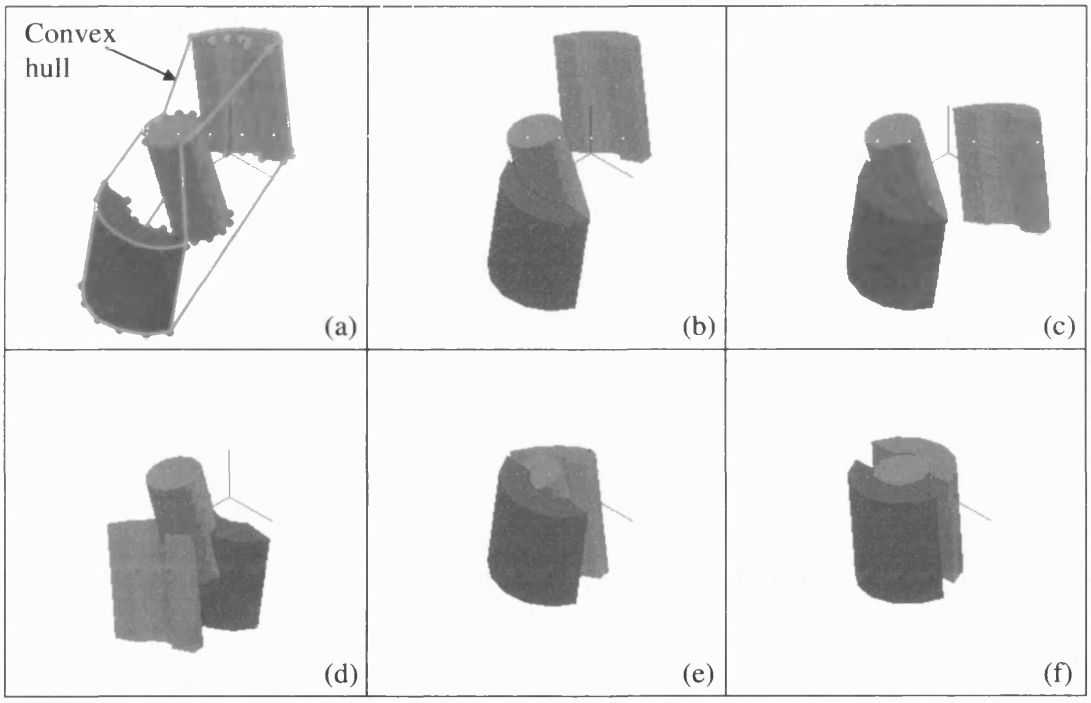

Figure 63 Frames from an animation illustrating convex hull minimisation. Frame (a) shows the points input to the Qhull program to generate the convex hull containing all three objects. Each half-cylinder was given six degrees of freedom. 492 iterations were required for convergence (frame (f)).

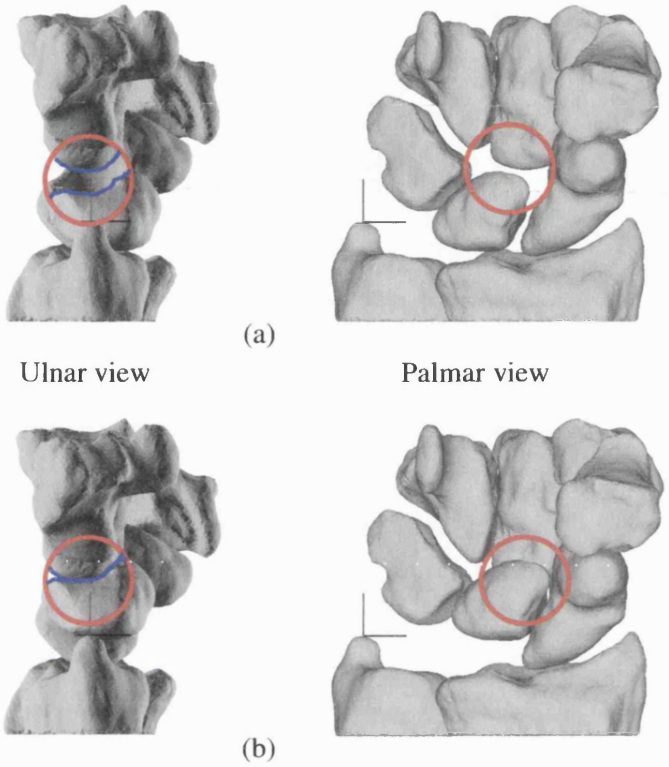

Figure 64 Convex hull volume was rejected as an indicator of surface contact area because of insensitivity to movements of lunate. (a) Lunate separated from capitate and scaphoid, convex hull volume=48075.957168mm^3. (b) lunate in close contact with capitate and scaphoid, convex hull volume=48075.957168mm^3. i.e. no difference.

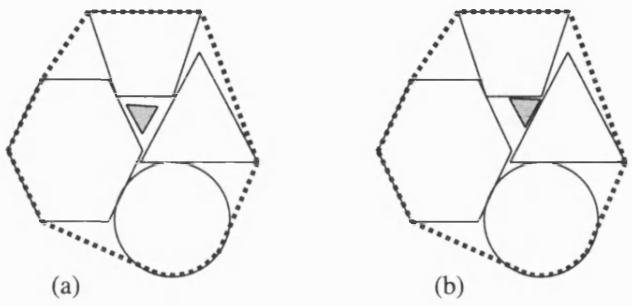

Figure 65 The volume of the convex hull is insensitive to the position of any object that is entirely contained within it. Configuration (b) gives a greater contact between the objects yet the hull volume is the same as for configuration (a).

5.6.2 Inter-Centroid Distance

Minimisation of the distance between centroids of contacting bones was considered as a means of indicating the level of contact area between the bones.

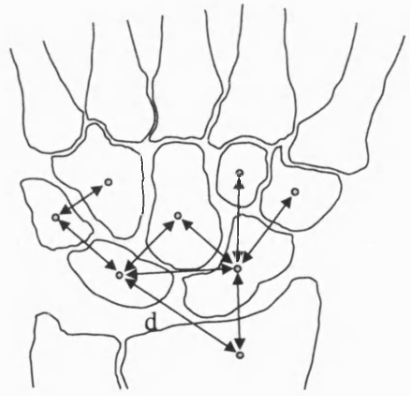

Figure 66 Distance between centroids of contacting bones indicates closeness of packing, which relates to total contact area.

In attempting to minimise the total of all inter-centroid distances, the SWORDS algorithm adjusted the positions and orientations of the carpal bones. If one bone was moved by pure translation closer to its neighbour, then the resulting increase in contact area was reflected in the smaller inter-centroid distance for that pair of bones. However, since the centre of rotation for angular adjustments was the centroid, any gains in contact area resulting from pure rotation did not cause a drop in the inter-centroid distance. However, when combined with an intersection test, this method could be more useful.

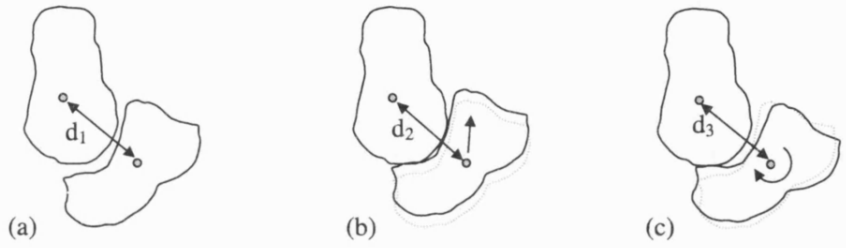

Figure 67 Inter-centroid distance does not indicate increased contact area for pure rotation. (a) original configuration, no contact. (b) Increased contact due to pure translation: $d_2<d_1$. (c) Increased contact due to pure rotation: $d_3 = d_1$.

5.7 Direct Estimation of Contact Area

Due to shortcomings in the indirect methods of computing contact area, the method finally adopted for the study was to estimate contact area at the level of individual facets. This section describes the computational procedure.

5.7.1 Projected Area

An effective method of estimating contact area is to consider the projection of a facet from one surface onto its nearest counterpart on the opposite surface (Figure 68). Those facets separated by more than a threshold distance (0.5mm in this case) are excluded from the calculation. The process is repeated for all pairs of neighbouring facets and the projected area summed to give an estimate the total contact area.

It should be noted that since the 3D bone models are non-deformable, the interface between articular surfaces is point contact and cannot, strictly speaking, produce a contact *area*. However, point contact will not yield sufficient information for the optimisation process to improve the closeness of packing of the bones. Therefore, in the lack of a deformable model, the method described in this section is a compromise that gives merely an indication of the actual contact area. Since the optimisation scheme aims to maximise this quantity, it does not matter that it is not the actual contact area. What is important is that the quantity varies in some proportion with the actual contact area. Experiments to test this idea are presented in section 5.7.1.6.

A C++ computer program was written to perform the contact area estimation, the details of which follow.

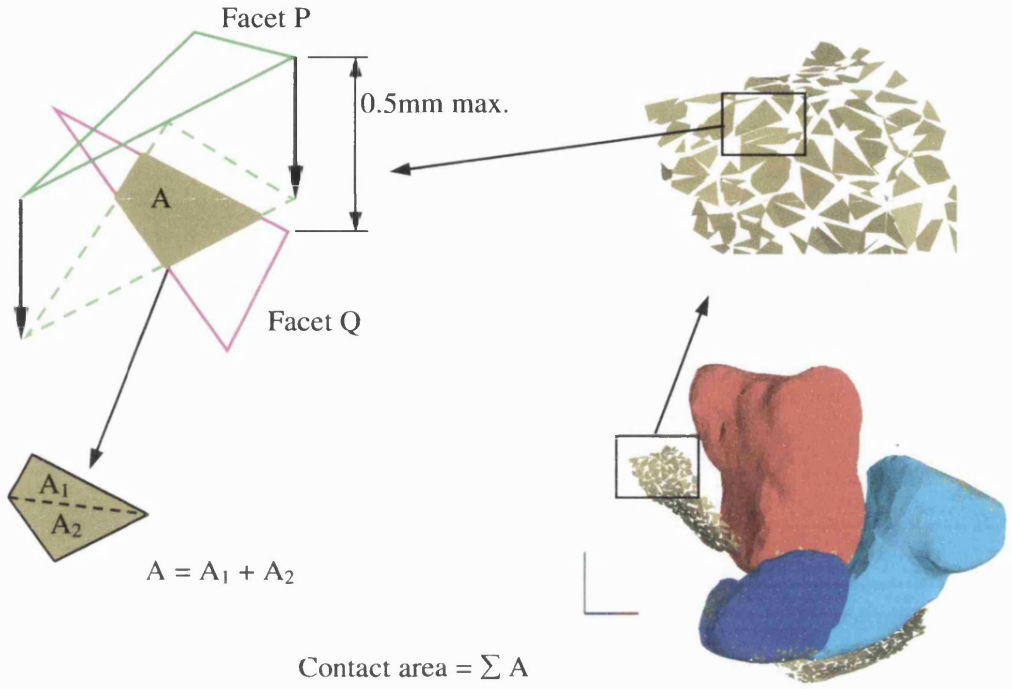

Figure 68 Contact was defined as the projection of facets from one articular surface onto the other. A maximum separation distance of 0.5mm was specified.

5.7.1.1 Vertex Numbering Convention

SWORDS is capable of displaying both solid and surface models. Surface models were used in the estimation of contact area. The models were stored as a list of vertices and a mesh of triangular facets running through the vertices. In order to define "inside" and "outside" surfaces of the models, the vertices were numbered anticlockwise when viewed from the outside surface (Figure 69).

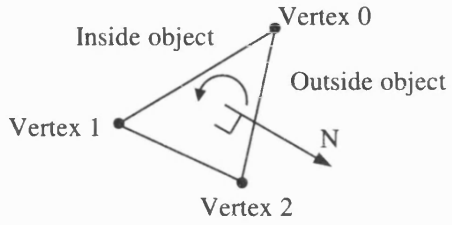

Figure 69 The anticlockwise vertex-numbering convention used by SWORDS to display surface models.

5.7.1.2 Finding Nearest Neighbours

The first step in the process was to calculate the nearest neighbour of each facet on the opposing surface. This was achieved by comparing distances between facet centroids (Figure 70). The pair of facets identified in this way will be referred to as "P" and "Q". Minimum and maximum distance thresholds were set from a menu option in SWORDS.

5.7.1.3 Projection

The next step was to project facet P onto the plane of facet Q (Figure 71). This was achieved by forming a triangle (denoted P') from the three points marking the intersection of surface normal vectors from the vertices of facet P onto the plane of facet Q. If fewer than three points of intersection were found then the process for that pair of facets was terminated. Surface normals and points of intersection were found using methods described in calculations 11.1.1 and 11.1.2 respectively.

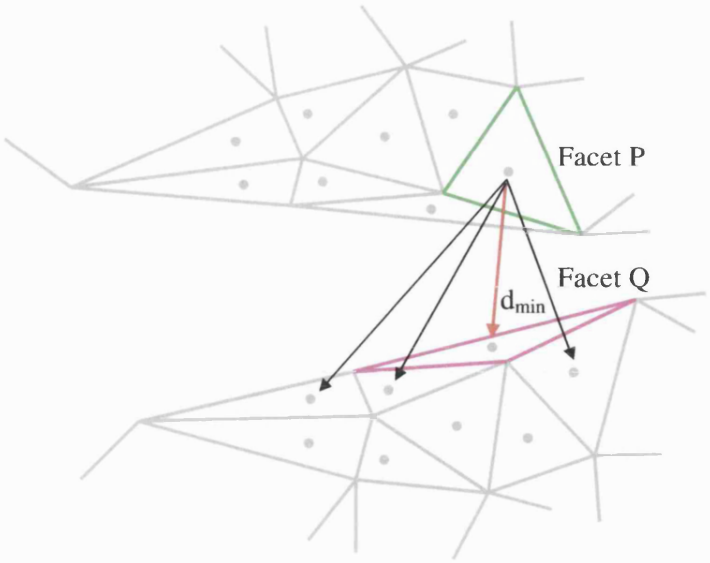

Figure 70 The nearest facet on the opposite surface was that having the minimum inter-centroid distance.

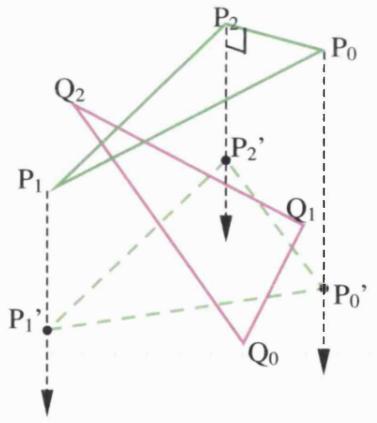

Figure 71 Facet P was projected onto the plane of facet Q to form P'.

5.7.1.4 Overlap Modes

The region of overlap between Q and P' was described by a polygon having between three and six vertices, depending upon the mode of overlap. There are also the special cases where P' is entirely within Q or vice versa (Figure 72).

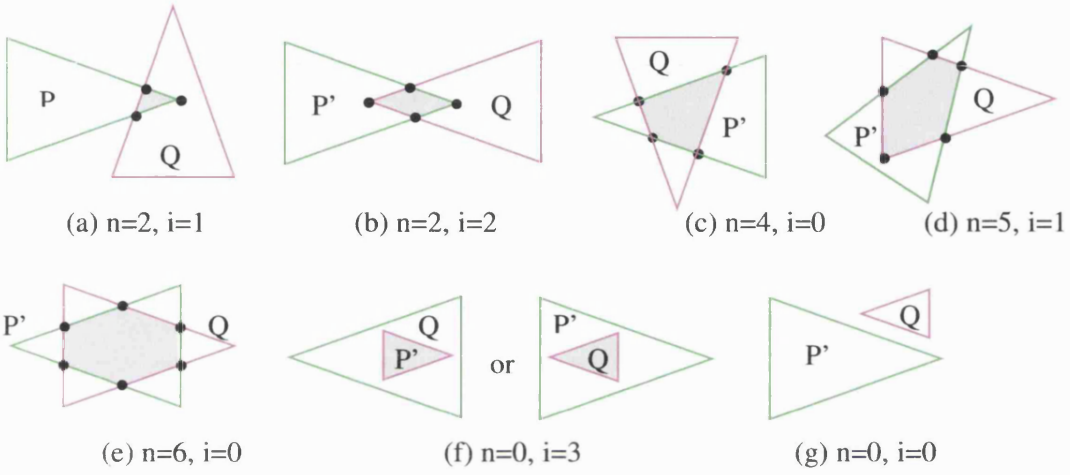

Figure 72 There are seven possible modes of overlap between P' and Q (including the null case, (g)), defined by the number of intersections between lines, n, and the number of internal triangle vertices, i.

It was necessary to determine which of the seven overlap modes illustrated in Figure 72 was applicable. This was achieved by finding the number of points of intersection (n) between edges of triangles P' and Q using calculation 11.1.3 and the number of internal triangle vertices (i) using calculation 11.1.5. Once these two values were known, the overlap mode was categorised according to Table 2. In practice, the process was performed on a decision-tree basis to minimise the number of calculations. For example if six intersection points were found, then the check on internal points was not necessary since overlap mode was automatically (e).

		Number of edge-edge intersections (n)						
		0	**1**	**2**	**3**	**4**	**5**	**6**
No. of vertices (i)	**0**	g	-	-	-	c	-	e
	1	-	-	a	-	d	-	-
	2	-	-	b	-	-	-	-
	3	f	-	-	-	-	-	-

Table 2 Categorization of overlap mode.

5.7.1.5 Region Triangulation

Once the points defining the region of overlap had been determined, it was necessary to calculate the area of the polygonal shape. In order to do this, the polygonal region was divided into one, two, three or four triangles, depending upon the number of vertices (Figure 73). The areas of these triangles were then computed using calculation 11.1.6.

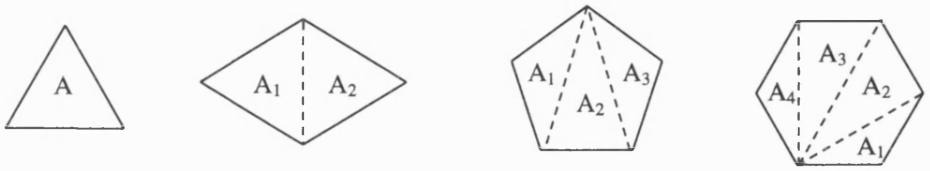

Figure 73 The area of the overlap region was found by splitting it into triangles and summing their areas.

Dividing the polygonal regions into triangles presented a challenge. First, it was necessary to number the vertices sequentially around the perimeter of the polygon. This problem was solved by measuring the angle subtended between lines running from a "root" vertex and all the others using the method described in calculation 11.1.4. Vertices were ordered according to the magnitude of this angle (Figure 74a). Once the vertices were sequentially numbered, the region was divided into triangles sharing a common vertex at the root. The other vertices were found by counting around the perimeter (Figure 74b). The vertices and surface normal vector for each triangle were saved to a DSP file (see section 3.13.1), so that the contact region could be displayed in SWORDS.

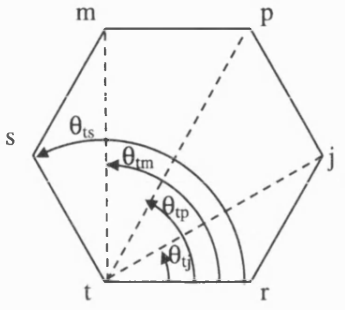

Vertex Ordering:

$\theta_{ts} > \theta_{tm} > \theta_{tp} > \theta_{tj}$

t = vertex #0
r = vertex #1
j = vertex #2
p = vertex #3
m = vertex #4
s = vertex #5

(a)

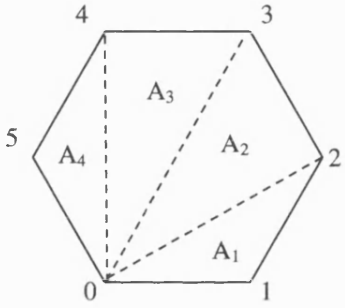

Triangle assignation:

A_1 = Triangle 0,1,2
A_2 = Triangle 0,2,3
A_3 = Triangle 0,3,4
A_4 = Triangle 0,4,5

(b)

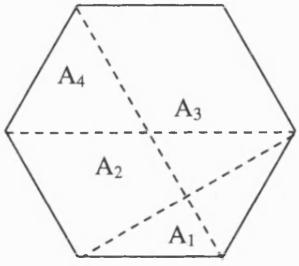

Reasons for Ordering Vertices:

If the triangle vertices are assigned arbitrarily, then confusion results:

The regions may not be triangular.
The regions may intersect.

⇒ The result is meaningless

(c)

Figure 74 Steps taken to divide the overlap region into triangles so that the area could be calculated.

5.7.1.6 Testing

The ability of the method to calculate contact area was tested using a ball and socket joint created in AutoCAD. A 14.9mm diameter ball was placed at the centre of a 15.0mm diameter hemispherical socket. The 0.05mm clearance was introduced to prevent contact occurring at asperities.

In calculating contact area, facets from the ball were projected onto the socket surface. Therefore, the theoretical maximum contact area was that given by the surface area of a hemisphere of 7.5mm radius:

$$A = 2\pi r^2$$
$$= 2 \times \pi \times 7.5^2$$
$$= 353.43\text{mm}^2$$

The maximum value computed by the program was 318.54mm^2. The discrepancy between the two values is because there were gaps in the projected surface (see Figure 75). The cause of these missing areas is explained in section 5.7.2. However, it is not essential that the program return the actual value of contact area, merely that the value is proportional to the closeness of fit between the two surfaces. To test this ability, the contact area was calculated for increasing displacements of the ball out of the socket. The results show that the area returned by the program is a continuous function of the separation between the two surfaces, so the method was considered suitable for directing the optimisation process.

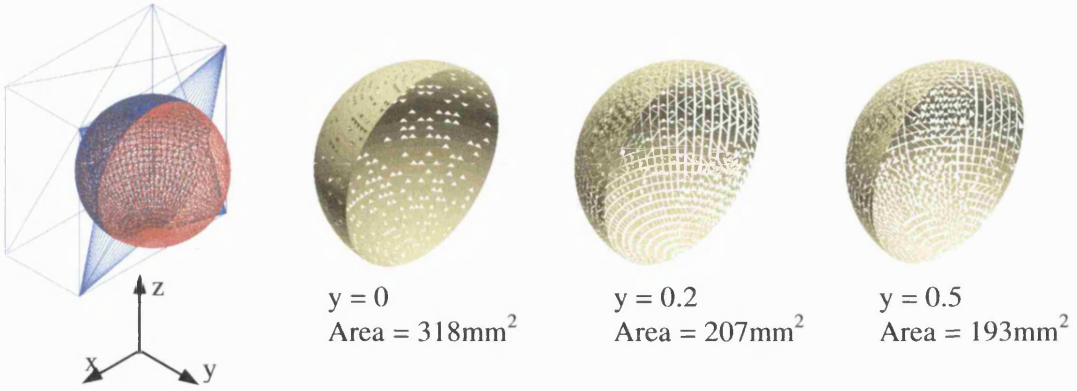

Figure 75 Testing contact area calculation on a ball and socket joint.

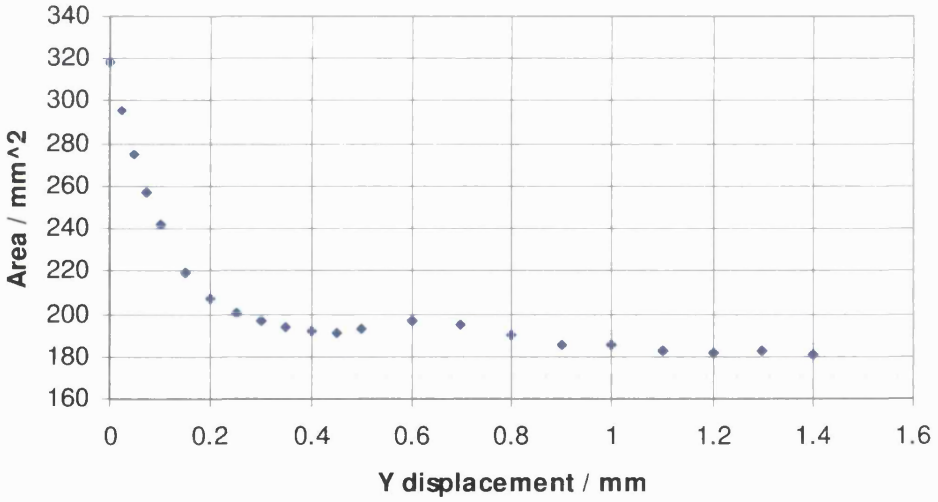

Figure 76 Graph showing variation in contact area as the ball is removed from the socket.

5.7.2 Summary

This section has described the method used to indicate the level of contact area between two articulating surfaces.

The value returned by the method is a function of both the distance between the surfaces and the angle of contact. Since facets are projected in a normal direction, this ensures that the maximum contact area will be returned if the two facets are parallel.

Note that the summation of all the polygonal areas of overlap does not equal the actual contact area between the two surfaces, but provides an indication of the level of contact. This is because each facet from one surface is projected onto a *single counterpart* on the opposite surface, thereby causing areas of overlap to be separated by regions of void instead of forming a continuous surface. In order to eliminate the voids, it would be necessary to consider additionally the area of overlap with all neighbouring facets onto which the projection falls. To do this, it would be necessary to dispense with the proximity test (see section 5.7.1.2) used to find a single nearest counterpart, and attempt to project every facet from one surface onto every facet on the opposite surface. This would increase the computational expense significantly. Furthermore, the contact area could be over-estimated by multiple facets from one surface being projected onto the same region on the opposite surface. A brief investigation revealed a tenfold increase in the computation time (Figure 77).

It is hypothesised that so long as the value output from the contact area computation exhibits some correlation to the actual contact area then this will provide sufficient indication.

Figure 77 By accepting voids in the contact surface, the computation time was significantly reduced but there was still sufficient information to indicate the level of contact. (a) Projection of each facet from one surface onto *all* facets on the opposite surface, time taken= 83.92s. (b) Projection of each facet from one surface onto only its nearest neigbhour on the opposite surface, time taken= 8.34s. (Times are for 4.8% resolution bones).

5.8 Intersection Detection and Evaluation

When moving three-dimensional models, it is possible for two or more objects to occupy the same region of space. Therefore, a test for intersection must be introduced. Intersection detection is the process by which one can determine if two objects are intersecting with each other. Interference evaluation quantifies the "degree" of intersection (Kolli *et al.*, 1996) and was required in the present study. Interference evaluation is a well-known problem in the field of packing theory, with which this study has much in common. It has been described by one author in the field as *"a major computational bottleneck"* (Lin and Gottschalk, 1998). Another study states, *"It seems very hard to solve this problem due to its computational complexity"* (Dai and Cha, 1994). Another author makes the following comment about the problem:

> *"Of the primary terms considered, the single most computationally expensive one to evaluate is interference detection and quantification between components. Thus, to minimize overall run time, we must minimize the complexity associated with this operation"* (Cagan *et al.*, 1998).

This section discusses different approaches to solving the collision detection problem.

5.8.1 Boolean Volume of Intersection

The ACIS geometric modeller used within SWORDS is capable of performing Boolean operations on solid models. Therefore, the volume of the region formed from the Boolean intersection of one object and another is convenient to implement and gives an accurate indication of the degree of interference. Tests showed that Boolean operations could be performed satisfactorily upon solid models that had been converted from surface format using the program created by G. Mullineux (see section 5.2.2). The Boolean intersection method was applied to the full resolution bone models described in section 5.2 and the time taken to return a volume was measured for three degrees of interference. The results are illustrated in Figure 86.

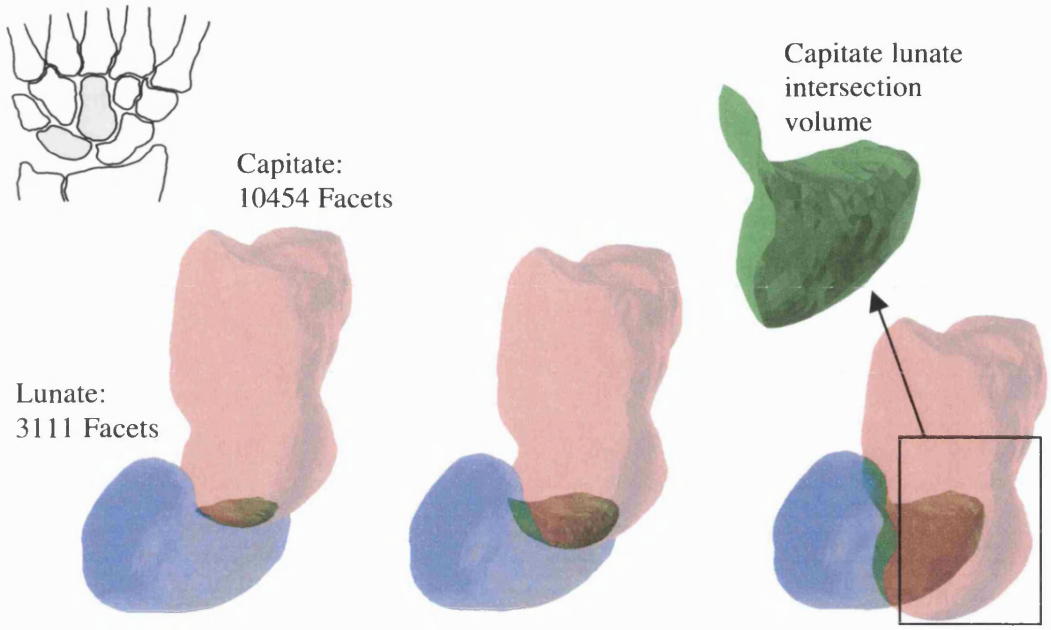

Penetration/mm:	2.00	4.00	10.00
Volume/mm^3:	10.66	99.53	267.56
Time/s:	7.45	8.33	7.52

Figure 78 Testing the ability of the ACIS solid modeller within SWORDS to evaluate three degrees of interference.

5.8.2 Perimeter of Intersection

All that was required for the collision detection was some *indication* of the level of intersection. The *volume* of intersection is the ultimate indicator, but its calculation is computationally expensive. In order to increase the speed of the test, it was necessary to trade off some accuracy in return for increased speed. The perimeter of intersection was considered as an alternative to the volume of intersection.

The overall aim was to compute the perimeter of the closed polygon marking points of intersection between edges and facets of two intersecting bones (Figure 86). Surface facetted models were again used for the method, which was integrated into the same C++ computer program used for the contact area calculation described in section 5.7.

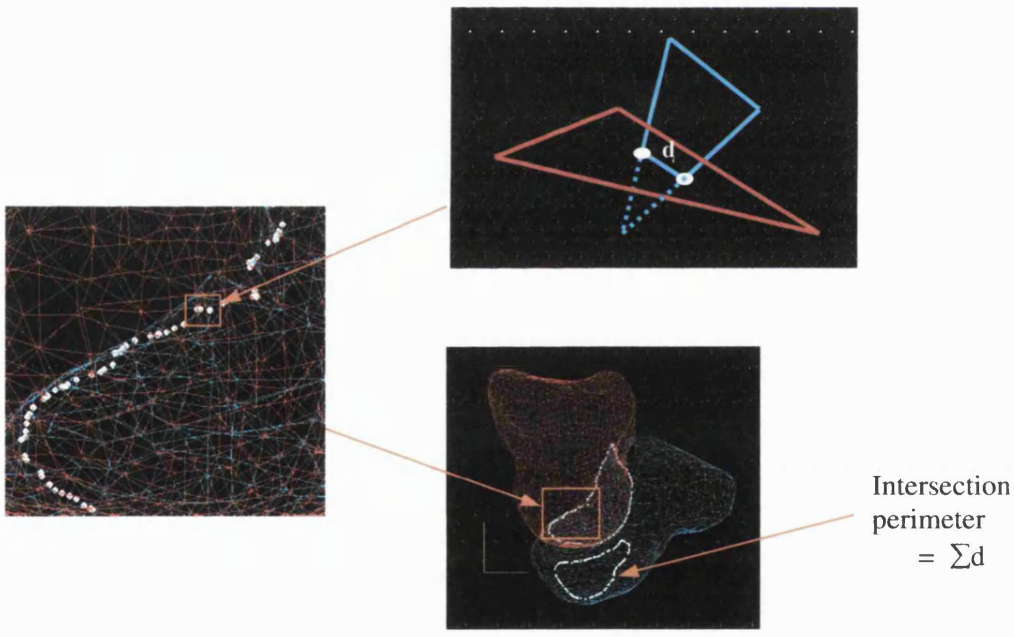

Figure 79 Computing the perimeter of intersection.

5.8.2.1 Bounding Box Overlap Test

The calculation was broken into several pass/fail tests in order to minimise computational requirements. The first stage in this process was to check for overlap between the bounding boxes of the bones. If overlap was detected then the calculation proceeded to the next test, otherwise it terminated.

Figure 86 illustrates nine overlap configurations for the 2D case. The 3D case yields even more combinations and an effective overlap test must be able to detect all of these. An expression was developed which compared the six defining values (Xmin, Ymin, Zmin, Xmax, Ymax, Zmax) of bounding boxes A and B:

IF
(

$(((Xmin_B \geq Xmin_A) \text{ AND } (Xmin_B < Xmax_A) \text{ OR } (Xmax_B > Xmin_A) \text{ AND } (Xmax_B \leq Xmax_A))$
$\text{OR } ((Xmin_B \leq Xmin_A) \text{ AND } (Xmax_B \geq Xmax_A) \text{ OR } (Xmin_A \leq Xmin_B) \text{ AND } (Xmax_A \geq XmAx_B)))$
AND
$(((Ymin_B \geq Ymin_A) \text{ AND } (Ymin_B < Ymax_A) \text{ OR } (Ymax_B > Ymin_A) \text{ AND } (Ymax_B \leq Ymax_A))$
$\text{OR } ((Ymin_B \leq Ymin_A) \text{ AND } (Ym_Ax_B \geq Ymax_A) \text{ OR } (Ymin_A \leq Ymin_B) \text{ AND } (Ymax_A \geq Ymax_B)))$
AND
$(((Zmin_B \geq Zmin_A) \text{ AND } (Zmin_B < Zmax_A) \text{ OR } (Zmax_B > Zmin_A) \text{ AND } (Zmax_B \leq Zmax_A))$
$\text{OR } ((Zmin_B \leq Zmin_A) \text{ AND } (Zm_Ax_B \geq Zmax_A) \text{ OR } (Zmin_A \leq Zmin_B) \text{ AND } (Zmax_A \geq Zmax_B)))$

) = 1

THEN overlap exists

(5.8.2-1)

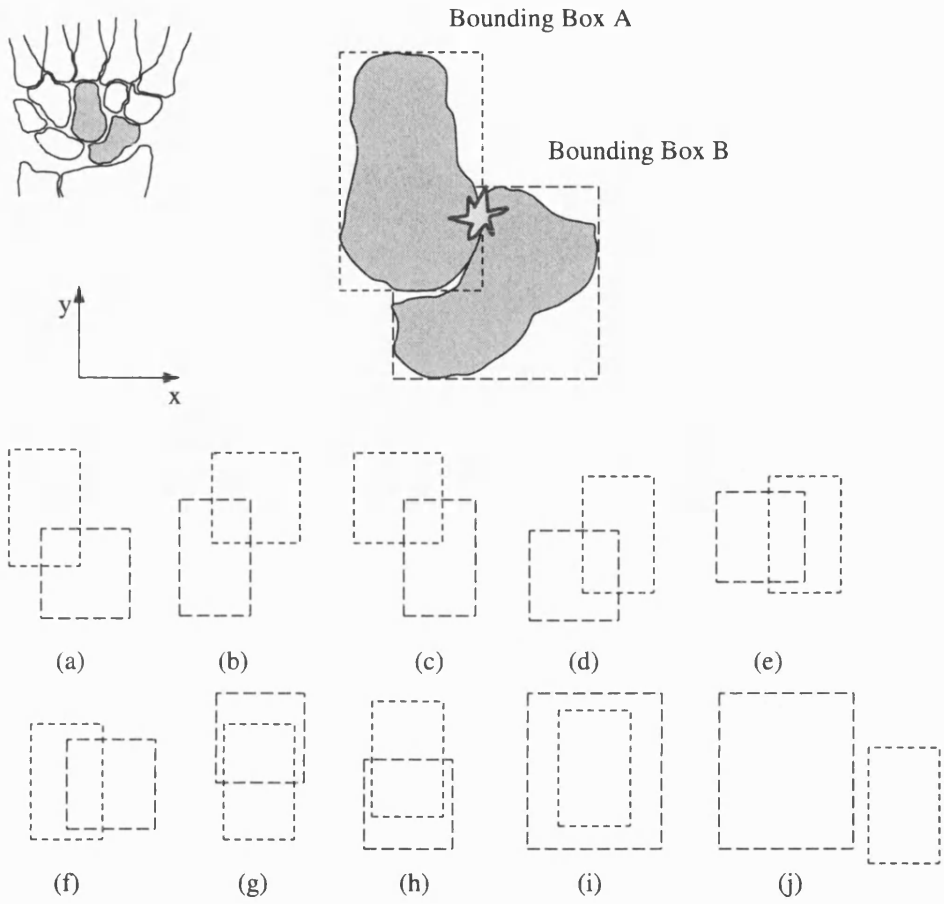

Figure 80 Checking for overlap between bone bounding boxes was the first step in evaluating interference. Diagrams (a) to (j) illustrate the many overlap configurations that must be tested for the 2D case; the 3D case yields even more configurations.

5.8.2.2 Facet Bounding Box Overlap Test

If the bounding boxes of two bones were found to overlap, then the bounding boxes of all facets in each bone were tested for overlap using equation (5.8.2-1).

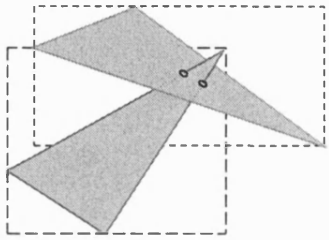

Figure 81 Testing for overlap between facet bounding boxes.

5.8.2.3 Edge-Facet Intersection Points

If two facet bounding-boxes were found to overlap then all points of intersection between edges of one facet and the plane of the other were calculated using calculation 11.1.2. There were four possible outcomes from this calculation, as illustrated in Figure 86: Only outcome (d) resulted in termination of the calculation for that pair of facets.

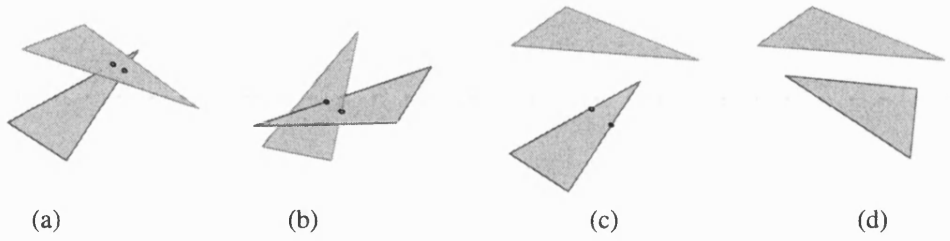

Figure 82 Four modes of edge-facet intersection. (a) Two intersections in the same facet. (b) Intersection in each facet. (c) Edges intersect plane of facet, but outside its boundary. (d) No intersection - facets are parallel.

5.8.2.4 Distance Between Intersection Points

The next process was to determine, using calculation 11.1.5, whether the intersection points found in section 5.8.2.3 were inside a facet boundary in order to eliminate outcome (c) from Figure 82.

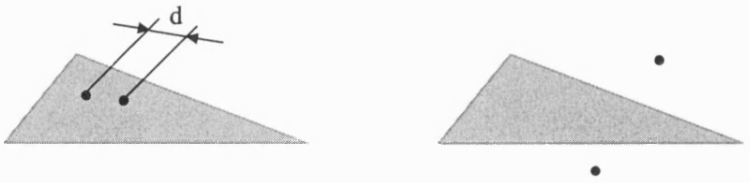

(a) (b)

Figure 83 Testing whether the intersection points lay within the boundary of a facet. (a) Accepted. (b) Rejected.

If one of the points of intersection was on, or very close to an edge, then it was rejected. This was achieved by specifying a tolerance for angle-sum test described in calculation 11.1.5.

If two points were returned, and each was inside the boundary of a facet then the distance between them was calculated and added to a cumulative total for the pair of bones. The chain of points making up the intersection perimeter were written to a text file, which was read by SWORDS and displayed in the graphics window.

5.8.2.5 Testing

The method was demonstrated on the same ball and socket used to test the surface calculation program (see section 5.7.1.6). The level of interference between the two components was gradually increased by moving the ball towards the socket in the y direction. Figure 85 shows that the intersection perimeter is a continuous function that rises steeply to a peak of 45mm before settling at around 40mm. At this point, the intersection perimeter forms a band around the equator of the sphere. The actual circumference of the sphere is $\pi \times 14.9 = 46.8$mm, so the method is reasonably accurate and is considered suitable for directing the optimisation process.

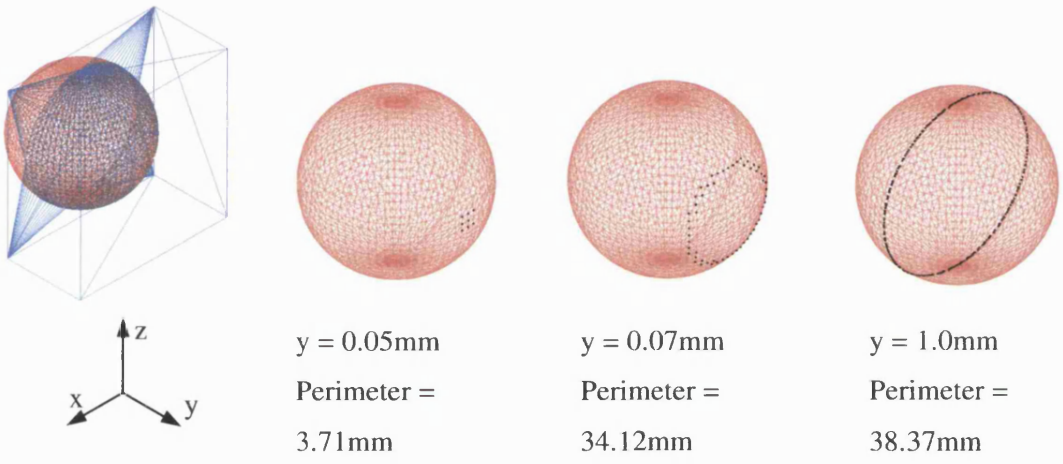

Figure 84 Testing the interference evaluation method. Black dots indicate the growth in the intersection perimeter as the ball is pushed further into the socket.

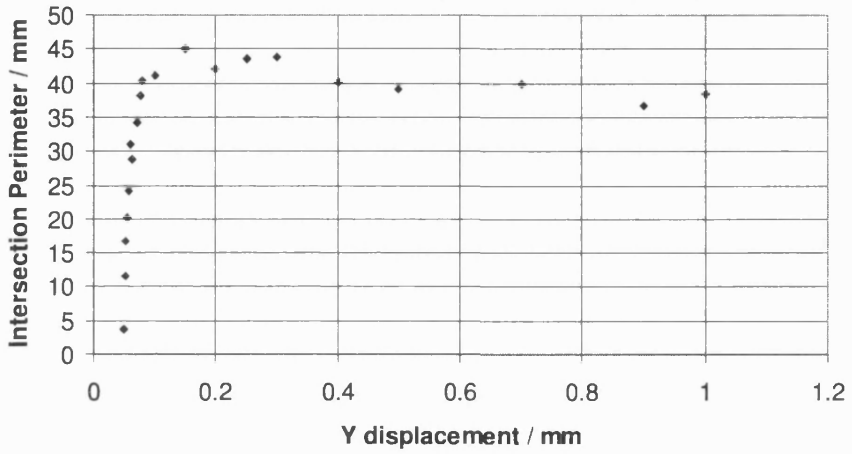

Figure 85 Graph showing the variation in interference perimeter as the ball is moved deeper into the socket.

The speed of the method was compared with the Boolean volume of intersection method (see Figure 78). Faceted surface models of the same resolution as those used for the test with solids were used. The results showed that the perimeter of evaluation could be found in almost half the time taken to find the volume of intersection. However, it should be noted that computation speed was increased using a pre-processing stage (described in section 5.12.2), which was not possible for the volume calculation.

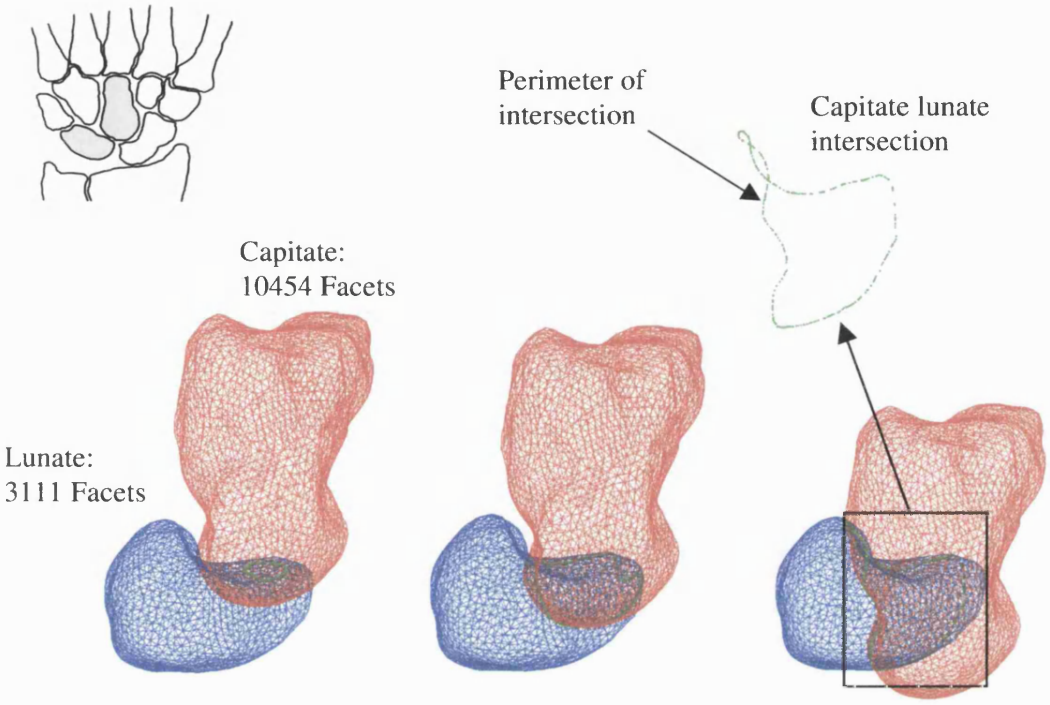

Penetration/mm:	2.00	4.00	10.00
Perimeter/mm^3:	49.80	70.75	99.67
Time for perimeter/s:	**1.98**	**3.79**	**4.42**
Time for Boolean/s:	7.45	8.33	7.52

Figure 86 The intersection perimeter calculation was almost twice as fast as the Boolean intersection volume calculation (Figure 79).

5.9 Transformation

The calculation of intersection perimeter and contact area was performed in a C++ program that was executed each time SWORDS repositioned one of the bone models. This program will henceforth be referred to as CIEP (Contact and Intersection Evaluation Program). Since it was difficult for another program to access the data held by SWORDS in the system memory, a means of communicating the positional adjustments to CIEP was required. The simplest method to implement would have been for SWORDS to save the models to a file on the hard disk after each repositioning. Then CIEP would simply read the new models into its own memory. However, the time taken for SWORDS to save files was almost twice that taken for CIEP to read them (Figure 87a). Therefore, it was decided that SWORDS would save to file only the transformations applied to the models. This file contained just a few tens of numbers, representing translations and orientations, instead of the hundreds of thousands contained in the model file. Therefore, the writing time was trivial. CIEP reads the original model files followed by the transformation file and then re-creates the transformation, before storing the result in its own system memory (Figure 87b). This was a laboured method of transforming the models, but given the constraints imposed by the use of two separate programs, it provided a workable solution.

The three-dimensional transformation procedure is described in calculation 11.1.7.

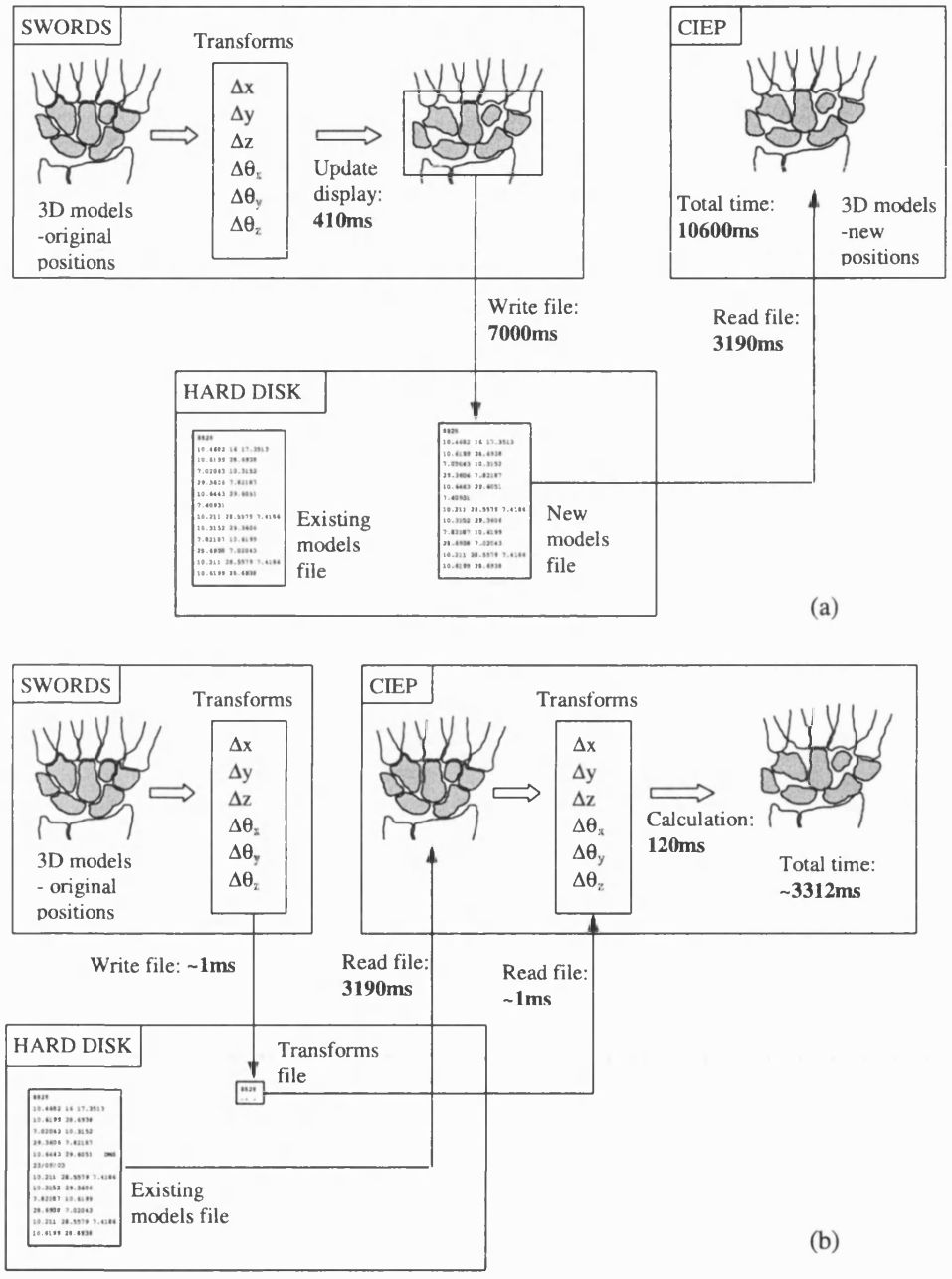

Figure 87 Comparing the time requirements of two methods for applying transformations. Method (b) was implemented because it was around three times as fast as method (a).

5.10 Model Spaces

This section introduces the concept of "model spaces" and describes the way in which they were used in SWORDS to manipulate the bone models.

A model space may be thought of as a region of three-dimensional space inside which geometric entities are placed. The principal defining parameters are the location of its origin relative to the "world space" origin, its orientation about each of the principal axes and its "parent" model space (Figure 88). Model spaces may be arranged hierarchically so that when a parent model space is moved, all its "children" move with it. SWORDS does not allow the positions and orientations of surface models to be moved relative to their model spaces, although this is possible with solid models. Therefore, it was necessary to move the model spaces containing the bones instead.

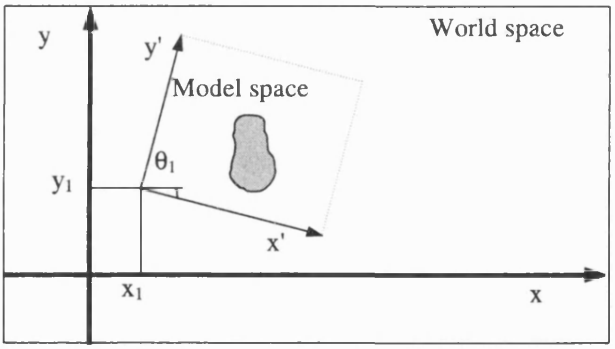

Figure 88 Objects are contained within model spaces defined by the position and orientation (x_1, y_1, θ_1) of the origin relative to a parent model space.

5.10.1 Centres of Rotation

It was decided that rotations of the carpal bones should be performed about their centroid point. This required each bone to be within a parent model space having its origin at the centroid. Therefore, each bone was contained in nested model spaces as illustrated in Figure 89.

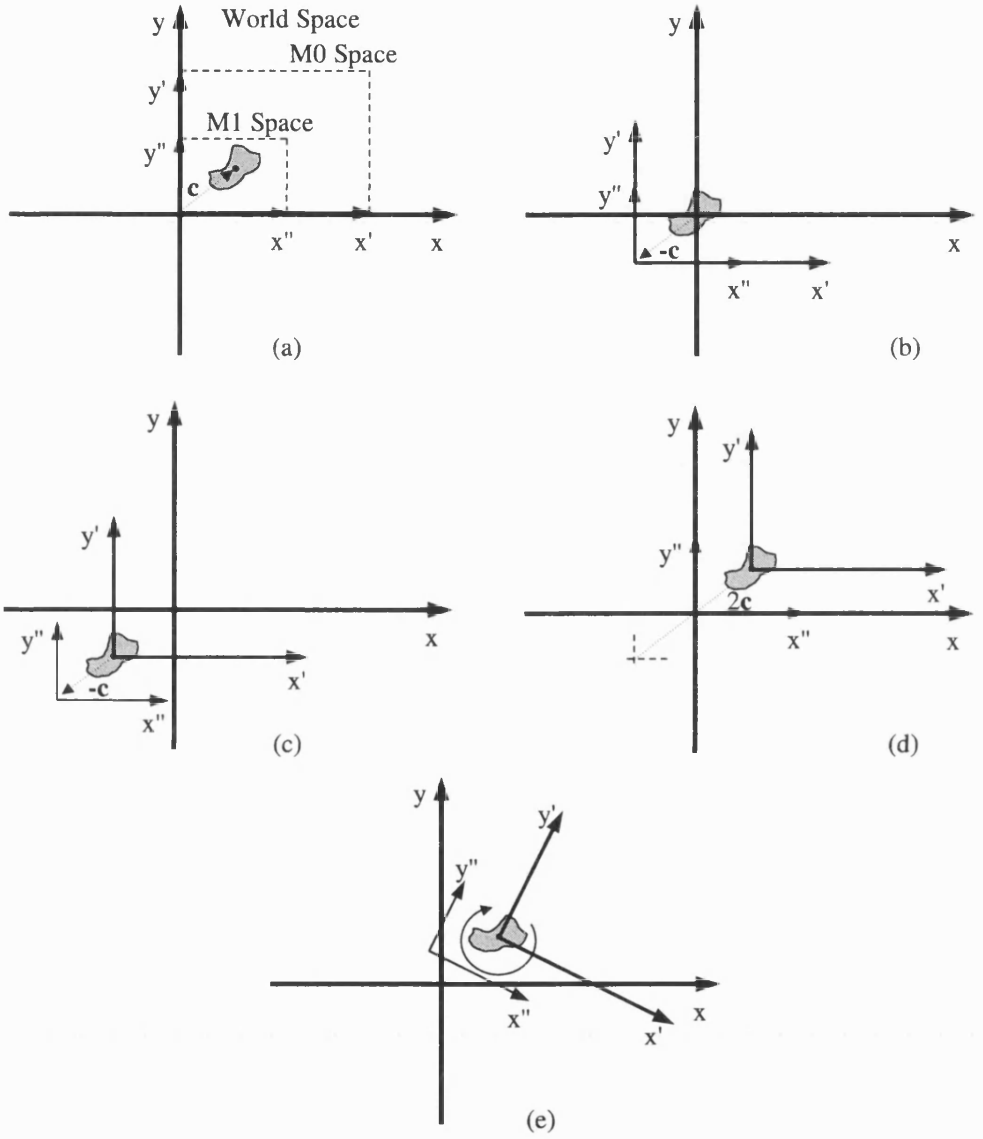

Figure 89 Setting up model spaces to allow rotation about centroids of bones. (a) The bone is inserted into model space M1 (x'', y''), whose parent is model space M0 (x', y') (b) M0 is offset so the bone centroid lies at the world-space origin. (c) M1 is offset so the bone centroid lies at the origin of M0. (d) M0 is moved so the bone returns to its original position with respect to world space. (e) The bone is rotated about its origin by rotating M0.

5.11 Bone Pairs

This section explains why the nine pairs of joint surfaces were chosen to represent total contact area.

The capitate was chosen as the "output" bone representing overall wrist posture. To simplify calculations, the four bones of the distal row were locked together and moved as a fixed, rigid unit. The rationale behind these decisions is explained in section 3.8. With four bones of the seven carpals moving as one, the number of joint surfaces was reduced to nine. For convenience, each bone was assigned a number based upon the alphabetical order of the three-letter abbreviation of its name. Similarly, pairs were numbered 0-8. The arrangement is illustrated in Figure 90.

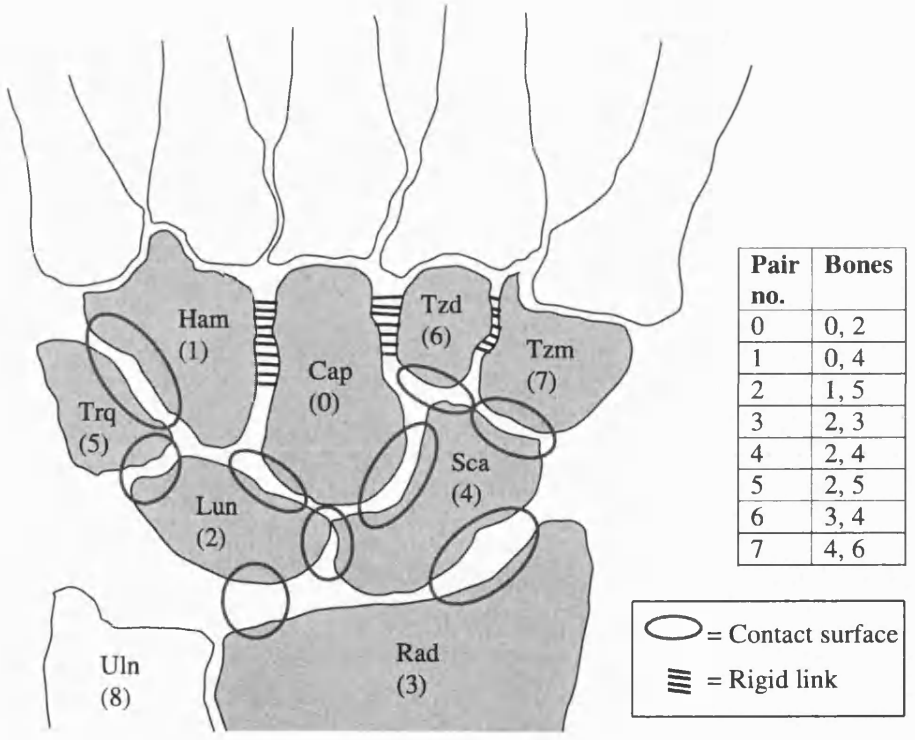

Pair no.	Bones
0	0, 2
1	0, 4
2	1, 5
3	2, 3
4	2, 4
5	2, 5
6	3, 4
7	4, 6

Figure 90 The nine pairs of contact surfaces. Bones 0, 1, 6 and 7 were fixed together. Bones 3 was fixed in space. Bones 2, 4 and 5 were free to move in six degrees of freedom.

5.12 Efficiency Improvements

This section describes the various ways in which the run-time of CIEP was reduced.

5.12.1 RAMdisk

Since system memory could not easily be shared between SWORDS and CIEP, communication was through files saved to and read from the hard disk. In order to reduce the time taken for these operations and to reduce wear from continually accessing the hard disk, a 32Mb portion of the system memory (RAM) was reserved for use as a virtual hard disk, also known as a RAM disk. The nominal usage was only around 5Mb (4.9Mb of which was accounted for by the bone models) but an overhead was required to cope with the large temporary files that were created by the pre-processing program described in section 5.12.2. The RAM disk was created using the RAMdisk (Winsoft Ltd.) application.

5.12.2 Pre-processing to find Nearest Facets

When adjusting the position of the bones to maximise contact area, it was only necessary for the optimisation scheme to apply small translations and rotations since there existed good initial conditions. Consequently, there were large areas of each bone surface that would never come into contact and time was being wasted checking for contact in these regions. It was therefore decided that the redundant facets from the data set should be removed using a separate C++ program. This program will henceforth be referred to as FFRP (Far Facet Removal Program).

The distance from the centroid of each facet to each other facet on the neighbouring bone was calculated. Those pairs of facets separated by less than a threshold value were recorded to a list. Facets outside the threshold distance were not recorded. Many facets appeared more than once on the list. Therefore, upon completion of the test duplicate entries were detected and removed. The result was a list of integers denoting the facet numbers in each bone that were amongst the nearest to the neighbouring bone. This list was read by CIEP before commencing calculations. The process is illustrated in Figure 91.

The savings in terms of facet-count and computation time afforded by the method are illustrated in Figure 93.

FFRP was executed only once for each increment of wrist position prior to commencing the iterative search for maximum contact area.

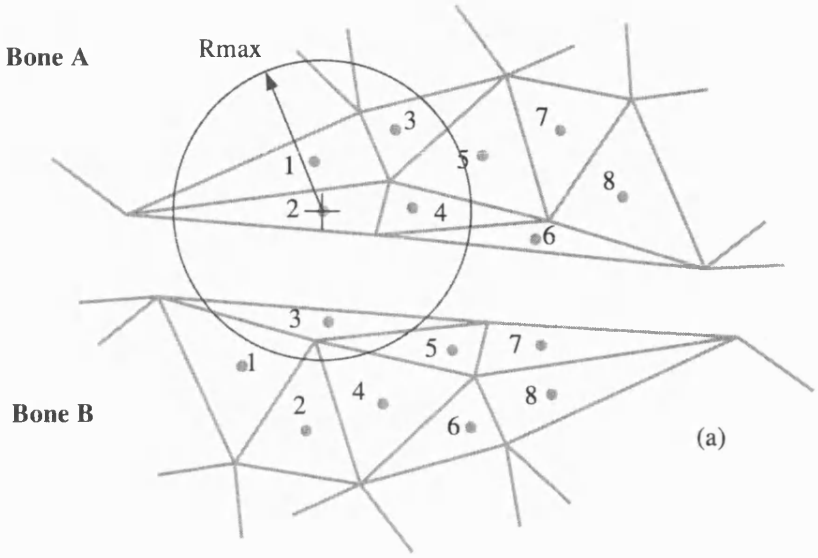

Bone A facet #	Bone B facets within Rmax
1	-
2	3
3	-
4	3,5
5	-
6	5,7
7	-
8	-

(b)

Bone A facets	Bone B facets
2,4,6	3,5,7

(c)

Figure 91 Preprocessing to remove facets that were unlikely ever to come into contact. (a) Each facet of bone B is tested to see whether its centroid lies within a circle of radius Rmax centred on a facet in bone A. (b) Facets within the circle are logged. (c) Duplicate entries are removed from the list.

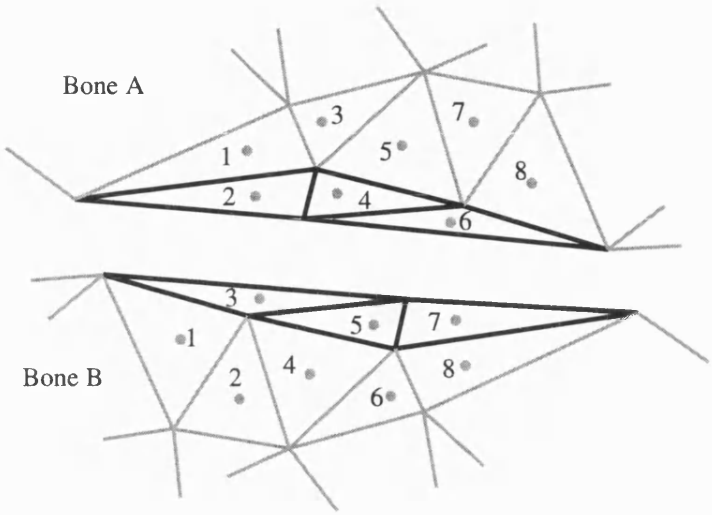

Figure 92 The nearest facets are highlighted.

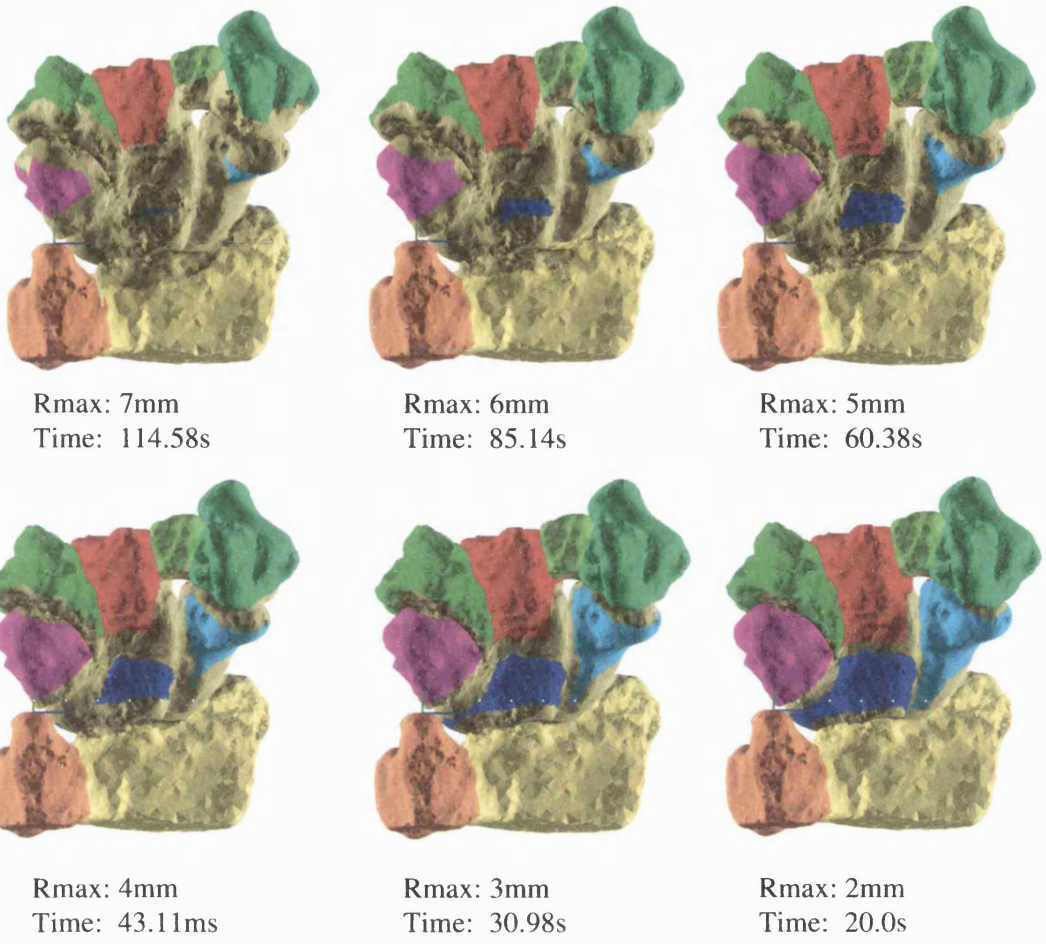

Figure 93 By determining which facets were near articular surfaces (gold coloured regions) prior to starting each iteration, the time taken to execute CIEP was markedly reduced. Times are for models having 10% of the full mesh resolution.

5.12.3 Change Detection

CIEP was originally performing calculations on *all* pairs of bones at every iteration. However, the optimisation scheme in SWORDS altered only one degree of freedom (translation or rotation) of one model space at a time. Therefore, time was being wasted repeating calculations on pairs of bones that had not moved. To improve efficiency, a means of detecting which bones had moved was introduced. Then only those pairs affected by the moves were re-calculated by CIEP, according to Table 3.

Movement of bone	Impact on pairs
0	0, 1
1	2
2	0, 3, 4, 5
3	3, 6
4	1, 4, 6, 7, 8
5	2, 5
6	7
7	8
8	-

Table 3 Deciding which pairs should be recalculated for movements of each bone. Bones/pairs are numbered according to Figure 90.

5.13 Cost Function

When an exact method is used to solve a problem, the requirements are simply the input variables and the mathematical equation that gives a solution as a function of these variables. However, when attempting to solve problems in which the relationship between input parameters and the solution is not explicitly known, an alternative approach is to use numerical optimisation (described in section 3.13.2). So long as there is some means of assessing the "fitness" of the result, a good solution (but not necessarily the best – see section 8.4.1) can be arrived at by varying the input parameters on a trial and improvement basis. The fitness of a trial solution is assessed using an expression known as the "cost function". The lower the "cost", the better is the trial solution.

In the present study, the elements of the cost function were the contact area and the intersection perimeter values. The objective of the optimisation algorithm was to minimise the cost. The *cost function* took the form:

$$\text{cost} = k_1 - a + k_2 i \qquad (5.12.3\text{-}1)$$

Where a = contact area, i = intersection perimeter k_1 and k_2 were constants.

k_1 was set sufficiently high that the cost could never be negative. The value of k_2 was adjusted so that the penalty for intersection was just high enough to avoid collisions but not so high as to introduce too sharp a change in the cost function that the optimisation process was disrupted.

In (5.12.3-1) it is observed that the two elements in the cost function have different units. While area is expressed in mm^2, the intersection perimeter is a linear distance measured in mm. The latter is the "penalty" quantity and the former is the "reward". Ideally, both quantities would be measured in mm^2 to ensure dimensional uniformity. However, since i increases rapidly as the depth of intersection increases, it was decided to leave the units in mm. Provided k_2 is chosen to ensure that the two quantities are of a similar order of magnitude when intersection first occurs, the optimisation scheme will be able to recognise an increasing cost and act accordingly to lower it.

Another point to remember when considering (5.12.3-1) is that where intersection occurs, contact area is not calculated within the region defined by the intersection perimeter (see Figure 94. This means that when one bone model interpenetrates another, the reward part of the cost function falls *and* the penalty part increases. One could argue that since the reward falls when intersection happens, this alone should provide sufficient indication of a poor solution, thereby making the intersection perimeter value redundant. However, if reward alone is used then the system would have no way of differentiating between a configuration in which a bone is making partial contact, partial intersection, and one in which there is simply a low level of contact. With a reward-penalty system, there is less room for ambiguity.

5.13.1 Cost Plot for Ball and Socket

The cost function for the ball and socket was investigated. For variations in the x and z displacement of the ball, the contact area, intersection perimeter and cost were evaluated (Figure 94). Displacement was varied from –0.2 to +0.2 in 0.01mm increments. The values of k_1 and k_2 were set to 1000 and 1 respectively. The results were displayed on three-dimensional surface plots (Figure 95, Figure 96, Figure 97).

The graph of contact area has a smooth distribution and shows a single, well-defined peak when the ball is centred in the socket (x=0, z=0). By contrast, the surface of the intersection perimeter plot is less smooth, although the overall trend is for the value to decrease as the ball is moved towards the central point. The cost function combines both quantities to produce a single minimum point.

The ability of the optimisation scheme to move the ball to the maximum contact area position was investigated. The ball was initially displaced by 0.15mm in the x and z directions. The values of k_1 and k_2 were set to 1000 and 1 respectively. The optimisation method used by SWORDS was set to Hooke and Jeeves, with two degrees of freedom (x and z displacements), a starting step-size of 0.05 and a termination step-size of 0.002. After 22 iterations, the cost function was minimised and the ball was re-located in the central point. Figure 98 shows how the cost decreases. This experiment was an extreme simplification of the problem of the wrist, but for the first time, all the components of the method were shown to work to achieve the desired goal.

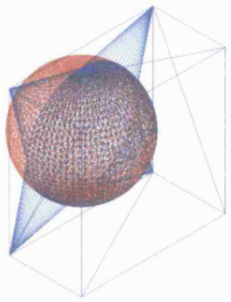

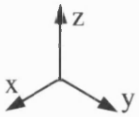

x = 0.06, z = 0.06mm
Perimeter = 20.51mm
Area = 197.34mm^2
Cost = 823.17

x = 0.00, z = 0.06mm
Perimeter = 15.91mm
Area = 229.60mm^2
Cost = 786.31

x = 0.05, z = 0.02mm
Perimeter = 1.63mm
Area = 274.43mm^2
Cost = 727.2

Figure 94 Variation in the cost for three positions of the ball.

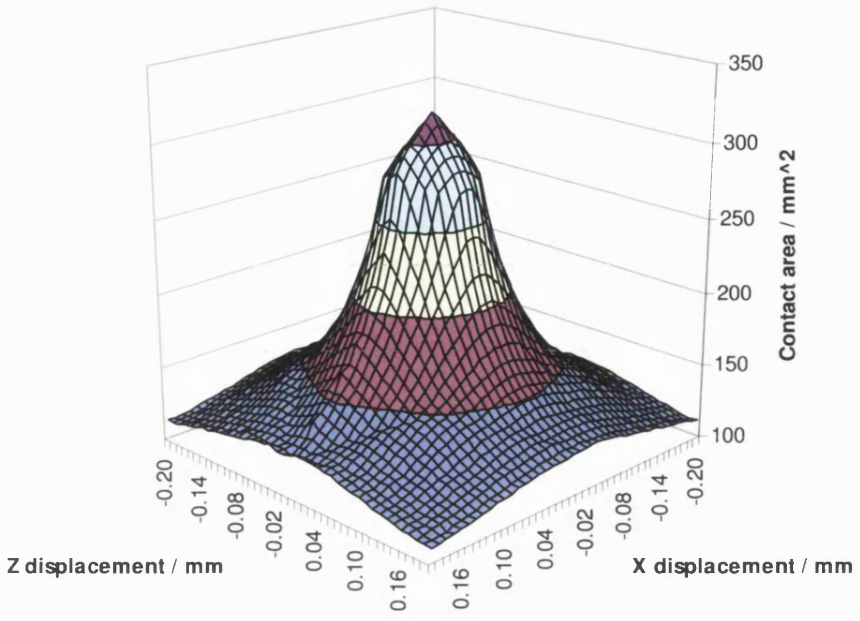

Figure 95 Graph showing the variation in contact area with ball position.

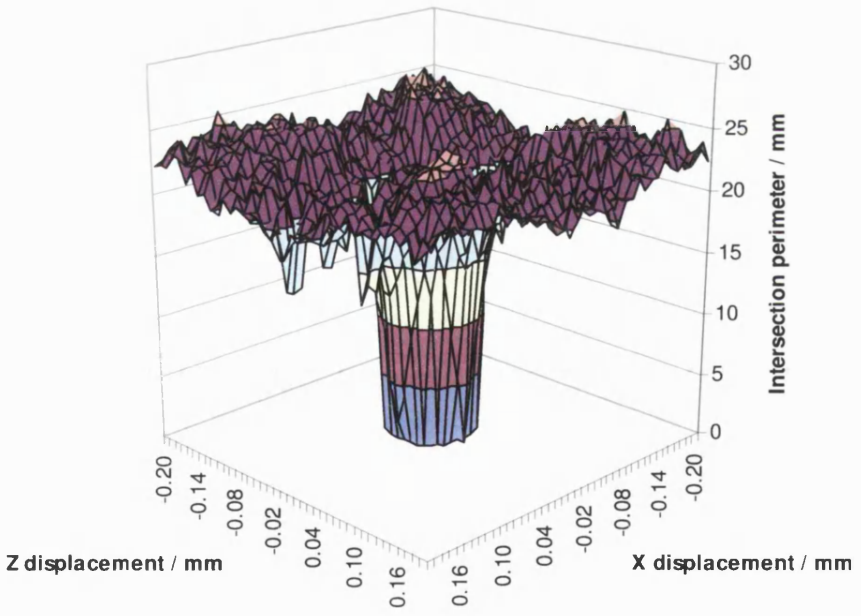

Figure 96 Graph showing variation in intersection perimeter with ball position.

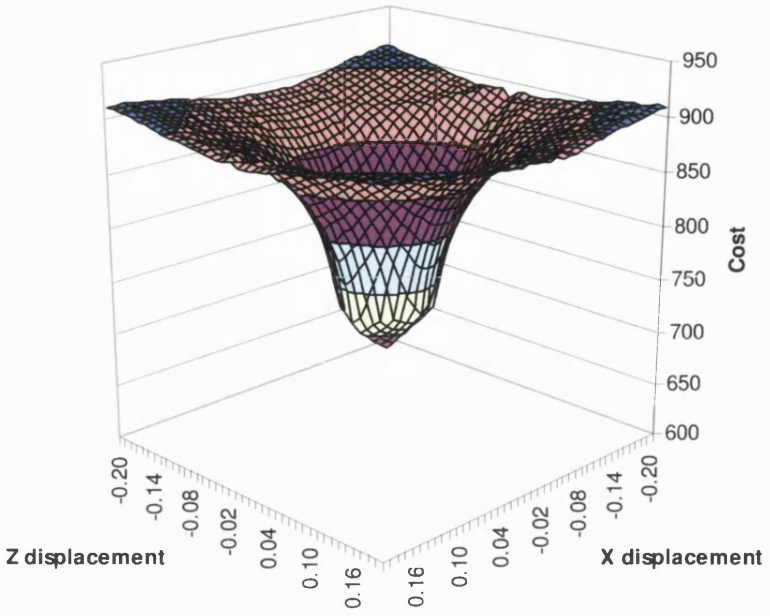

Figure 97 Graph showing variation in cost function with ball displacement.

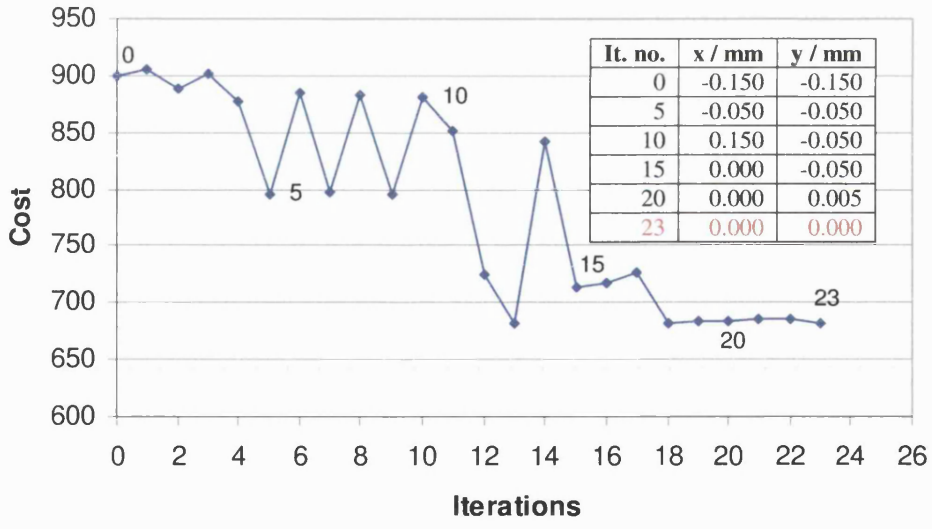

Figure 98 Optimisation progress for ball initially perturbed by -0.15mm in each direction from the central position. The ball has been returned to the centre of the socket after 23 iterations.

5.13.2 Cost Plot for Lunate on Radius

The cost plot for the lunate moving in the x and z direction over the radius was investigated. The lunate was initially perturbed by –1.0mm in x and z directions from its optimum position (x=0, z=0) (defined in 5.5.6). The bone was moved in increments of 0.05mm until x and z values were 1.0mm each. The shape of the contact region and intersection perimeter for three bone positions is illustrated in Figure 99.

A plot of the cost function for the lunate position is shown in Figure 102. The cost was derived according to (5.12.3-1) with k_1 and k_2 set to 1000 and 1 respectively. Note that the minimum cost does not occur at x=0, z=0. This is because the optimum position of the lunate was determined by the algorithm when all bones of the wrist were present. Therefore, the minimum cost arrangement of the lunate upon the radius in isolation will not necessarily coincide with the minimum cost when all bones are present.

5.14 Testing Optimisation

This section describes experiments that were carried out in order to assess the various factors determining the performance of the optimisation process.

5.14.1 Two Degrees of Freedom

The ability of the optimisation algorithm to move the lunate to the global minimum cost position was tested for two degrees of freedom. The starting position was set to x= –0.75mm, z= –0.75mm. For a starting step-size of 0.05mm and termination step-size of 0.002mm, the optimisation algorithm required 29 iterations to converge (see Figure 103, Figure 104). At convergence, the position of the lunate does not quite coincide with the global minimum cost position. However, the errors in x and z are only 0.2 and 0.15mm respectively. The minimum cost obtained was 889.431, while the global minimum was 888.151mm, a difference of less than 0.15%. It is possible that if the termination step-size was set smaller than 0.002, then the algorithm would have finished even closer to the true minimum. In practice however, the small increase in accuracy would come at the expense of longer computation time.

Figure 99 Images of contact and intersection with resulting variation in cost factors for three positions of the lunate.

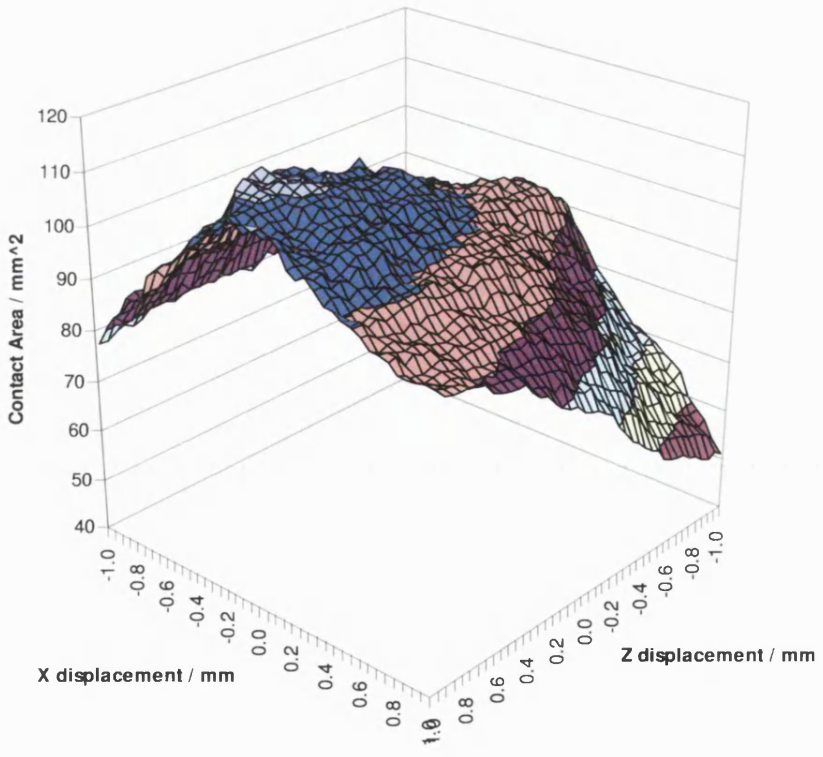

Figure 100 Variation in contact area as the lunate is moved over the radius.

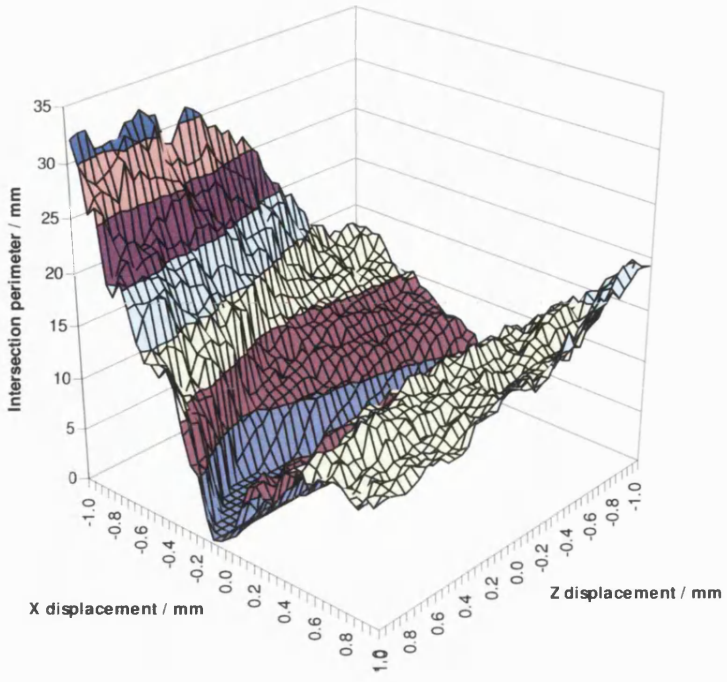

Figure 101 Variation in intersection perimeter as the lunate is moved over the radius.

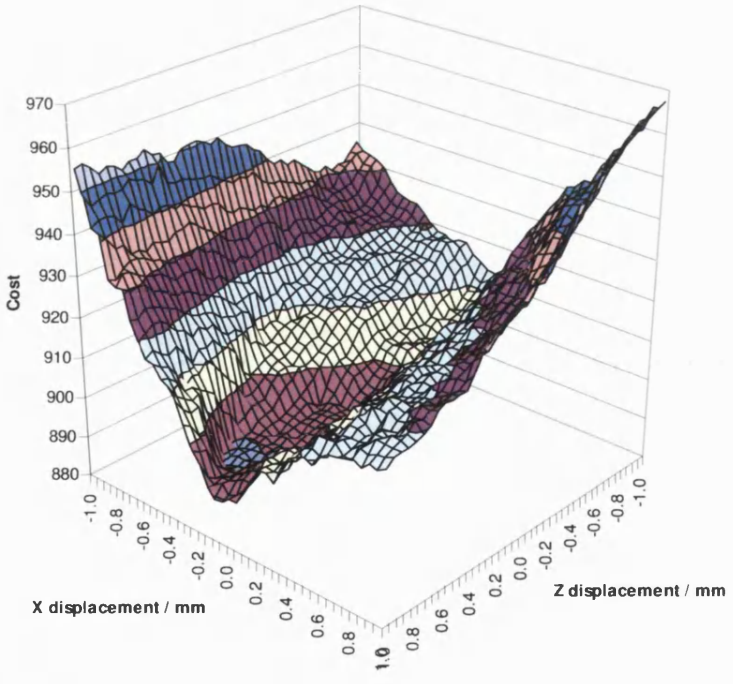

Figure 102 Variation in cost as the lunate is moved over the radius.

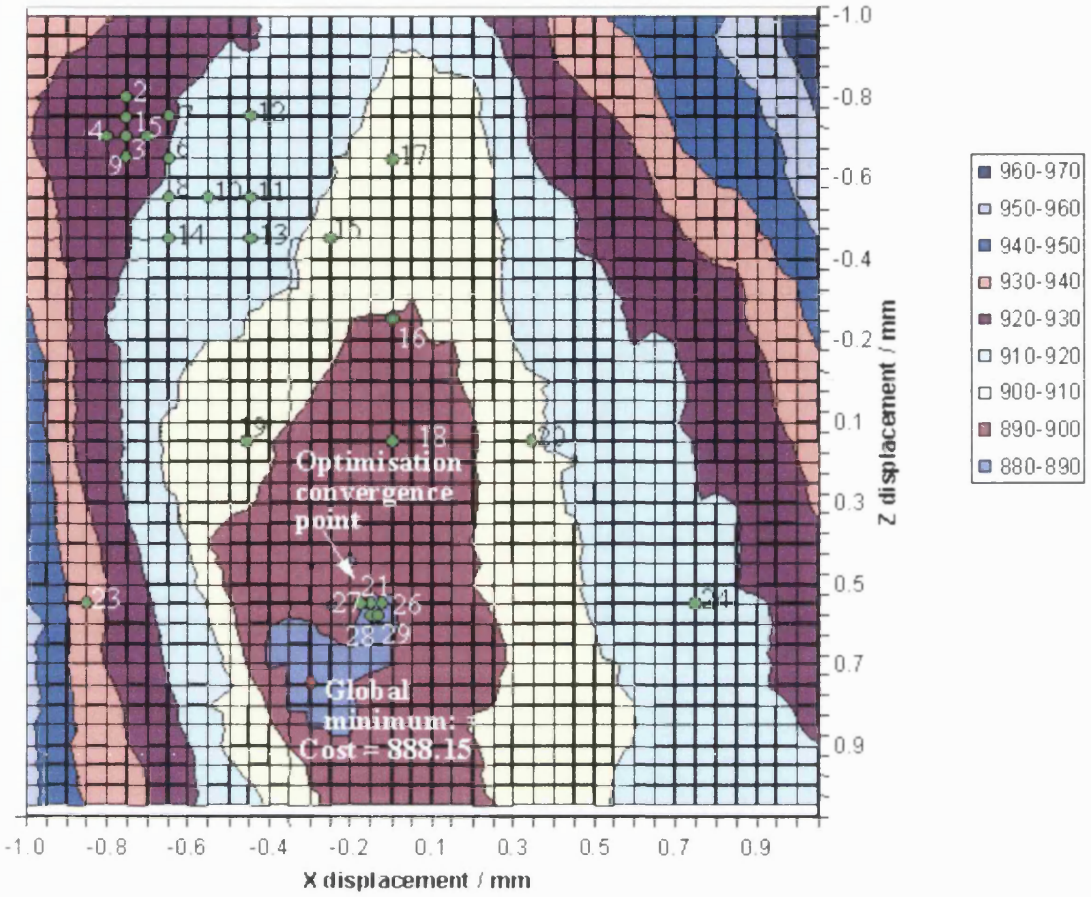

Figure 103 Cost plot for movement of the lunate over the radius using the Hooke and Jeeves method with initial step size of 0.05mm. Markers show iteration number (missing numbers are outside boundaries of graph). Solution has converged to within 0.15% of the global minimum after 29 iterations.

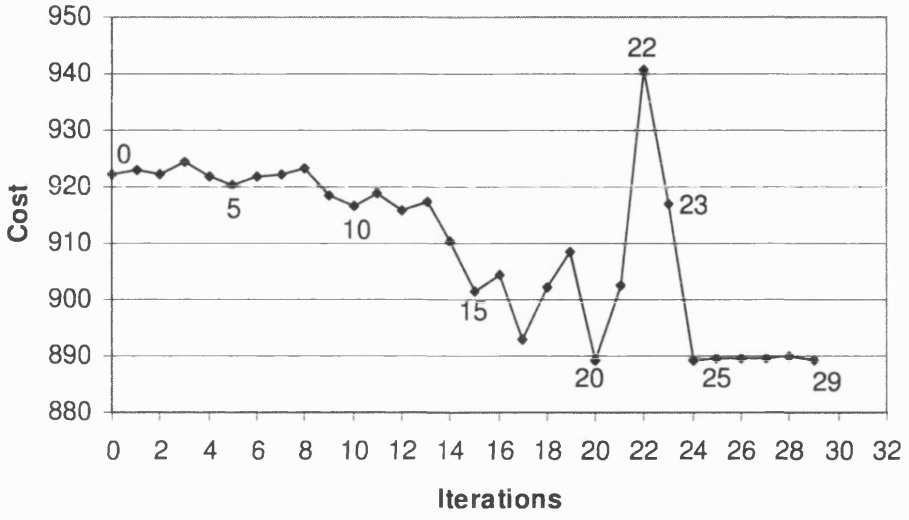

Figure 104 Optimisation progress for lunate positioning on radius. Selected iteration numbers highlighted.

5.14.2 Six Degrees of Freedom

The ability of the algorithm to determine the global minimum cost was tested for six degrees of freedom.

A graphical display of the cost-function for the lunate-radius was not possible if there were more than two degrees of freedom. Therefore, it was difficult to visualise the global minimum cost position and so verify that it had been attained by the optimisation algorithm. Without a definite target to aim for, the most meaningful alternative was to investigate whether the bone always returned to approximately the same position regardless of initial disturbance. This test was performed on the radius-lunate pair of bones with all six degrees of freedom. Three different starting positions were used (see Table 4). The test was performed using the Hooke and Jeeves optimisation method with an initial step size of 0.1 and final step-size of 0.002. The results are shown in Table 5.

It is clear from the results shown in Table 5 that the algorithm does not converge to a common minimum regardless of initial conditions. If this were the case then the translation, rotation and cost values would be the same for all three conditions. This suggests that the algorithm is finding local minima instead of the global minimum (Figure 105).

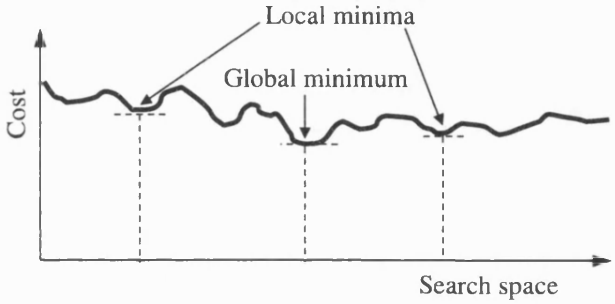

Figure 105 The algorithm may be finding local minima instead of the global minimum.

IC #	x	y	z	θ_x	θ_y	θ_z
1	-0.5	-0.5	0.5	-2	-2	2
2	0.5	0.5	-0.5	2	2	-2
3	-0.5	0.5	-0.5	-2	2	-2

Table 4 Three sets of initial conditions for the lunate bone.

IC#	Initial cost	x	y	z	θ_x	θ_y	θ_z	Its	Final cost
1	989.755	-0.090	0.000	0.900	-1.410	-2.700	1.800	108	889.460
2	967.382	-0.290	-0.110	0.310	2.190	2.200	-1.600	75	881.820
3	952.180	-0.300	-0.100	0.310	-0.790	1.220	-2.000	112	899.348

Table 5 Final positions for three different initial conditions. The final solutions are different, which indicates that local minima are being found.

5.14.3 Optimisation Method Selection

It was necessary to decide which optimisation method contained in SWORDS was most suitable for the present study. These algorithms are described in section 3.13.2. The performance of the three algorithms was compared in a simple test involving the optimisation of the lunate position upon the radius with two degrees of freedom. The task was to minimise the cost function described in section 5.13.2.

Powell's method (old) was found to require almost three times as many iterations as the Hooke and Jeeves method and Powell's method (new). So to save time, bones having just 4.8% of the original resolution were used for this experiment. The algorithms were compared using the three sets of different initial conditions shown in Table 4. The lunate was given six degrees of freedom. With a starting step of 0.1mm and final step of 0.002mm, the ability of each optimisation method to reduce the cost of the solution was investigated.

Of the three methods tested, it is clear from Figure 106 that the Hooke and Jeeves algorithm consistently gives the lowest cost in the smallest number of iterations. It is worrying to note that for identical initial conditions, neither of the methods appears to converge to a common minimum. This provides further evidence to support the results from section 5.14.2 that suggest the methods are only finding local minima and not the global minimum.

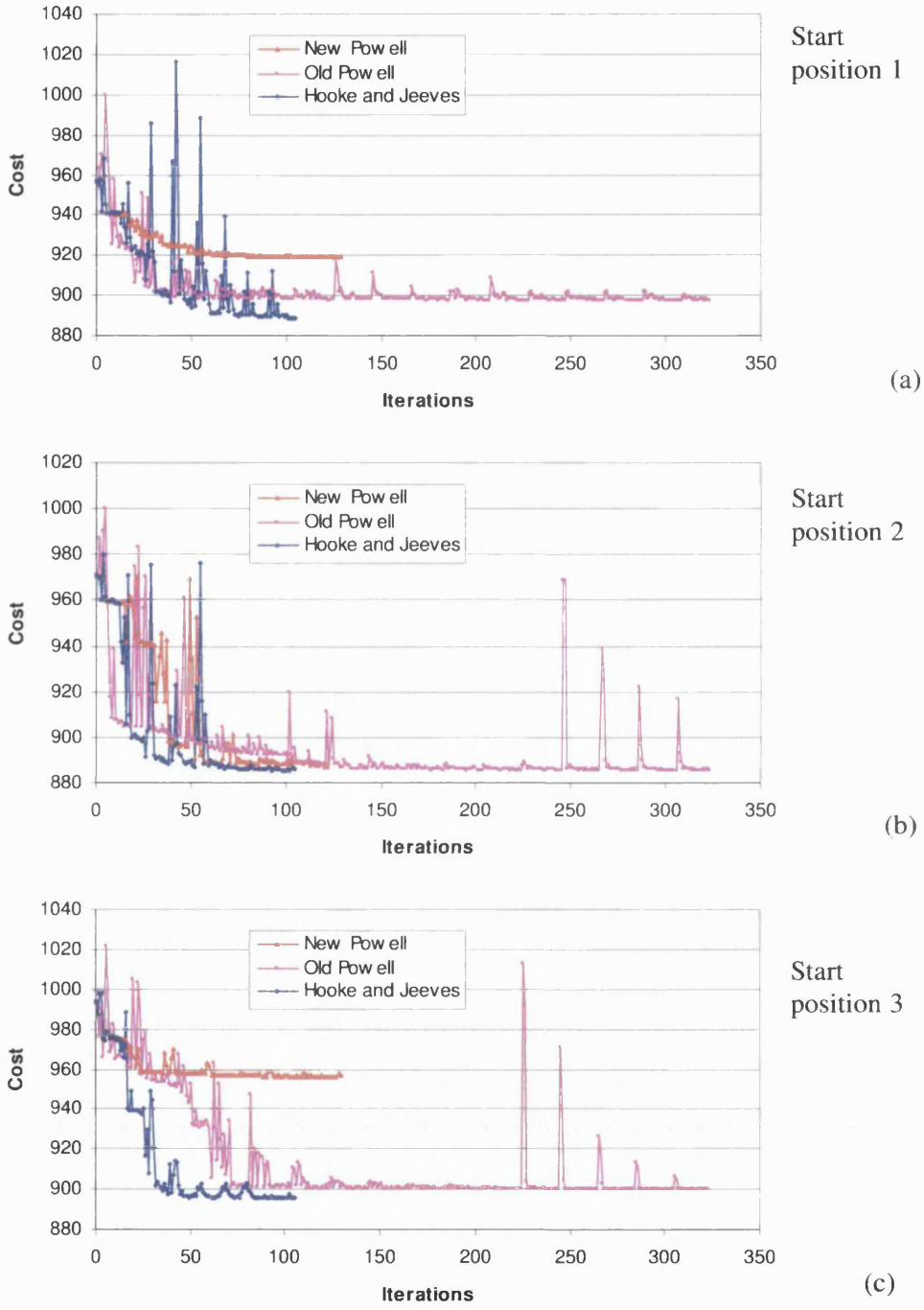

Figure 106 Comparing the performance of three optimisation methods with three different sets of initial conditions. The Hooke and Jeeves Method consistently converged to a superior solution in fewer iterations.

5.15 Mesh Resolution Revisited

The relationship between mesh resolution and speed of computation was investigated in order to determine an appropriate level of detail for the bone models. The experiments were performed on the computer that was used to run the tests. This was a Pentium 4 1.4GHz machine with 512Mb of RAM, 32Mb of which was used for the RAM disk. The bus speed was 400MHz.

5.15.1 Methods

The resolution of the models was varied from 1 to 10% of the original number of facets (Figure 107) using the Points2Polys application and the time taken to perform three key stages of the computation was recorded.

The following stages of computation were investigated:

1. Time taken to read the models from the RAM disk.
2. Time taken to perform furthest facet removal (execute FFRP).
3. Time taken to compute contact area and intersection perimeter (execute CIEP).

All results were recorded with the bones in the neutral position with maximum contact area. For (3) above, times were recorded for the "worst-case" and "best-case" scenarios:

Worst case:	All nine contacting pairs calculated.
Best case:	Only one contacting pair calculated (radius-lunate).

The results were extrapolated to give the total run-time to produce an animation of wrist motion covering 20 degrees of movement in 1.0 degree increments, assuming 400 iterations per increment. The figure of 400 was based upon the fact that around 100 iterations were required for convergence using the Hooke and Jeeves algorithm with six degrees of freedom (see Figure 106). There are 23 degrees of freedom for the wrist as a whole and so this gives (23/6)×100=383 iterations in total, which was rounded to 400 for convenience.

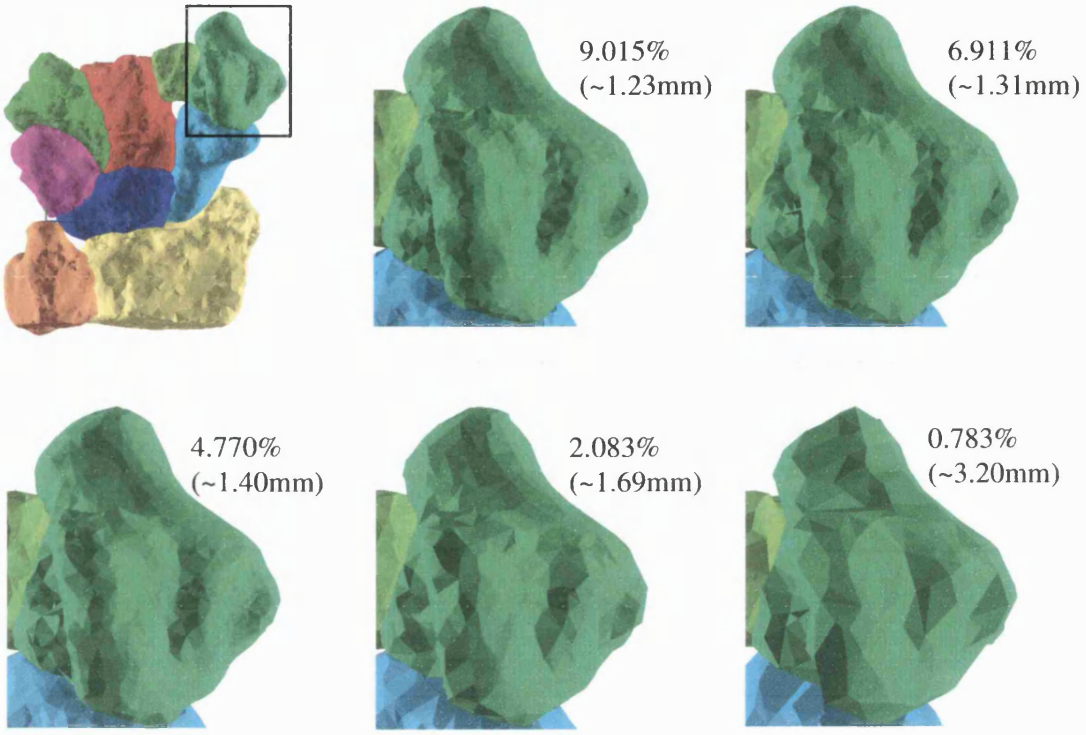

Figure 107 The trapezium bone illustrating five of the ten levels of resolution expressed as a percentage of the original number of facets, with approximate spatial resolution in parentheses.

5.15.2 Results and Discussion

5.15.2.1 Reading Models

Figure 108 shows that the time taken to read the models is a linear function of the mesh resolution. This is because the file-size is directly proportional to the number of facets in the models and the speed at which the system can read characters from an ASCII text file (approximately 1.33 million characters per second in this case) is a constant. It is possible that this time could be reduced if the models were written in binary instead of ASCII but this would not make a significant impact on the overall run-time given the much greater time needed for the other processes.

5.15.2.2 Removing Far Away Facets

Figure 109 shows that the time taken to execute FFRP (far facet removal program) appears to be a quadratic function of mesh resolution. This is because the process compares every entry on one list with every entry on another. If x is the number of entries on each list, then the total number of pairs that can be made from the two lists is x^2-x. This is the form of the equation of the line fitted through the data points.

Despite being the slowest process by far, the FFRP run-time does not significantly affect the total process time because it is only executed once per increment of hand motion (20 times in total). Contrarily, the CIEP is executed once per iteration (20000 in this case).

5.15.2.3 Contact and Intersection Evaluation

At the heart of the CIEP (contact and intersection evaluation program) there is also a pair wise comparison of two lists of facets. Therefore, the time taken to perform this process is also related to the x^2-x relation described above. However, since the number of facets has been significantly reduced by removing a large number of facets (see section 5.12.2), the process is around ten times faster.

Since the number of pairs of articulating surfaces to which the calculations are applied varies according to which bones are moved at each iteration, two sets of data are plotted on Figure 110 representing the best case (a single pair) and worst case (all nine pairs) scenarios.

5.15.2.4 Total Run Time

The data recorded for the FFRP and CIEP processes were used to estimate the time taken to produce a complete animation of wrist movement over a range of 20 degrees in increments of 1 degree. The total time was calculated as follows:

$$\text{Total time} = n_{inc}(t_{FFRP} + n_{it}t_{CIEP}) \qquad (5.15.2\text{-}1)$$

where:
- n_{in} = number of increments of hand movement = 20
- t_{FFRP} = time taken to remove far facets
- t_{CIEP} = time taken to evaluate contact and intersection
- n_{it} = number of iterations required to solve for each increment = 400

Note that (5.15.2-1) does not include the time taken to perform operations within SWORDS before and after each execution of CIEP, as this was negligible in comparison. Figure 111 shows that the total time is again a quadratic function of the level of detail in the models. The equation of the line fitted through the worst-case data points is:

$$\text{Total time (hours)} = 0.53x^2 + 1.53x \qquad (5.15.2\text{-}2)$$

where x = mesh resolution in percentage of original number of facets.

The resolution finally settled on was 4.8% since this allowed even a worst-case solution to be found within 20 hours. This allowed one complete set of results to be obtained each day by leaving the process running overnight.

5.15.2.5 Total Time for Full-Resolution Models

The time taken to run the algorithm if the full resolution models were used was estimated using the worst-case projection from (5.15.2-2):

$$\begin{aligned}\text{Total time} &= 0.53\times100^2 + 1.53\times100 \\ &= 5453 \text{ hours} \\ &= 227 \text{ days}\end{aligned}$$

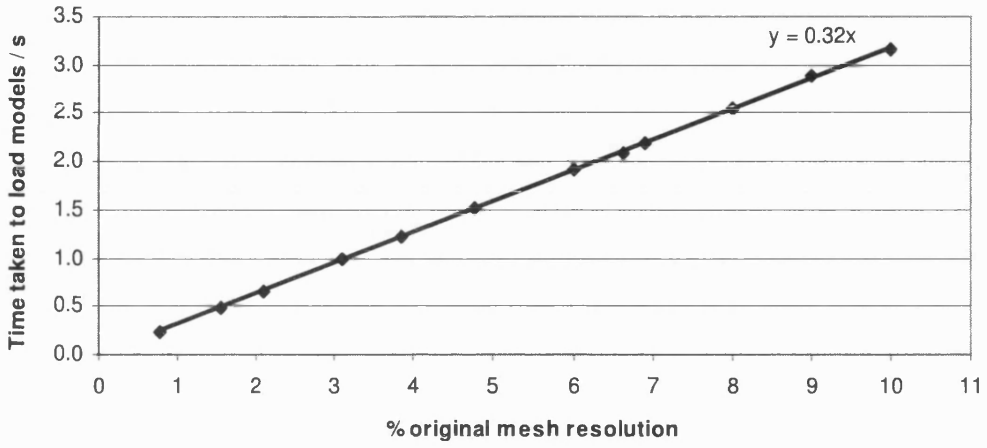

Figure 108 Time taken to read models as a function of mesh resolution.

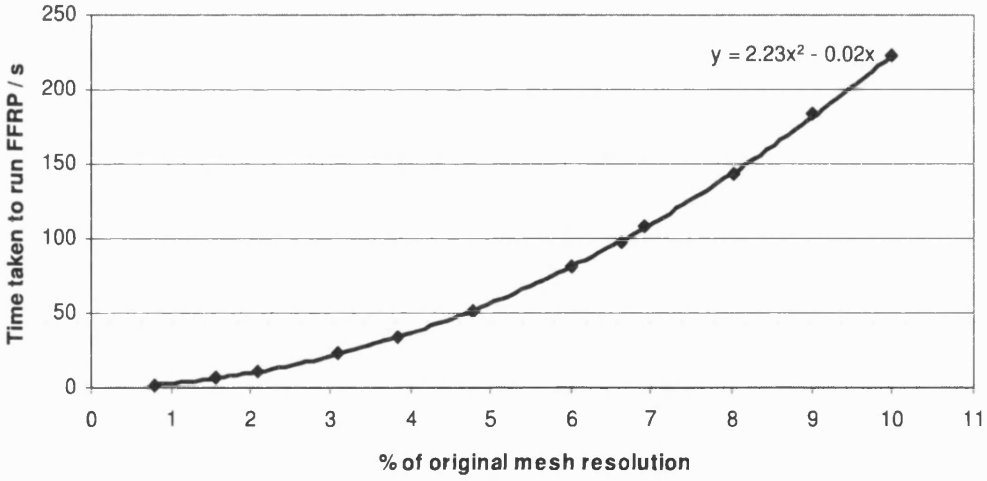

Figure 109 Time taken to perform far-away facet removal as a function of mesh resolution.

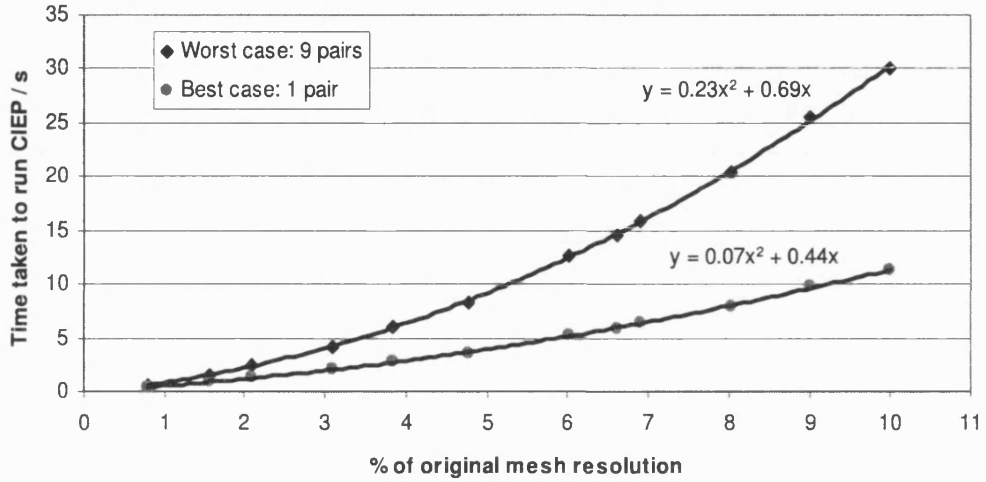

Figure 110 Time taken to calculate contact area and intersection as a function of mesh resolution for best case and worst-case scenarios.

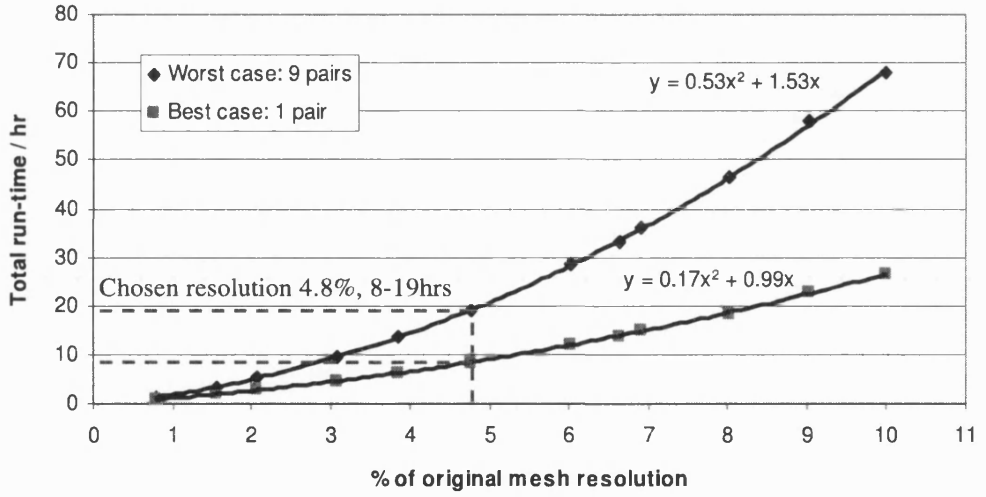

Figure 111 Total run-time as a function of mesh resolution for 20 increments of hand posture, assuming 400 iterations per increment.

5.16 Replay

For each increment of capitate position, the optimised positions of all bones were saved to a file. By reading the file back into SWORDS, and applying the transformations to the model spaces containing the bones, it was possible to create a real-time animation of the predicted motion.

5.17 Describing Movement with Finite Helical Axes

It is convenient to describe the movement of biological joints using the finite helical axis (FHA) method (An and Chao, 1984; Spoor and Veldpaus, 1980; Woltring *et al.*, 1985). Except for the case of pure translation, the movement of a body from one position to the next can be defined by rotation about and translation along an axis in space. The axis is termed finite because its position is only valid over a particular increment of movement. When the body moves in a series of small increments, there will be a corresponding number of finite helical axes whose positions and directions may vary. When describing overall joint movement it is sometimes convenient to determine the mean position of all the finite helical axes.

The movements of the carpal bones predicted by the SWORDS algorithm lend themselves well to FHA analysis. The position and direction of the axes will provide visual confirmation that the bones are moving in the manner expected. The method should also allow the movement to be quantified so that comparisons can be made with experimental studies.

A standalone C++ program was written by G. Mullineux to calculate the FHA for movement of a body between one position and the next (Mullineux, 2003). The mathematical method used is described in calculation 11.1.8.

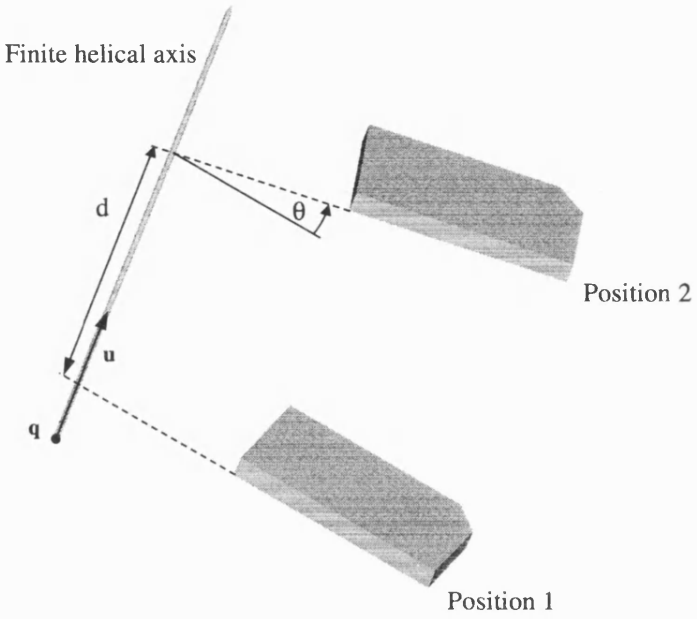

Figure 112 The movement of an object from one position to another may be described by a rotation about (θ) and a translation along (d) a finite helical axis. The axis is defined by a point on the axis (q) and a direction vector (u).

5.17.1.1 Graphical Representation

The file of FHA parameters produced by the program described in 11.1.8 was read by SWORDS at each increment of movement. Each axis was depicted on the screen as a cylinder with a cone at one end to indicate the direction of rotation, using a clockwise convention. The mean axis was calculated from the data and represented as a slightly larger diameter cylinder in a different colour (Figure 113).

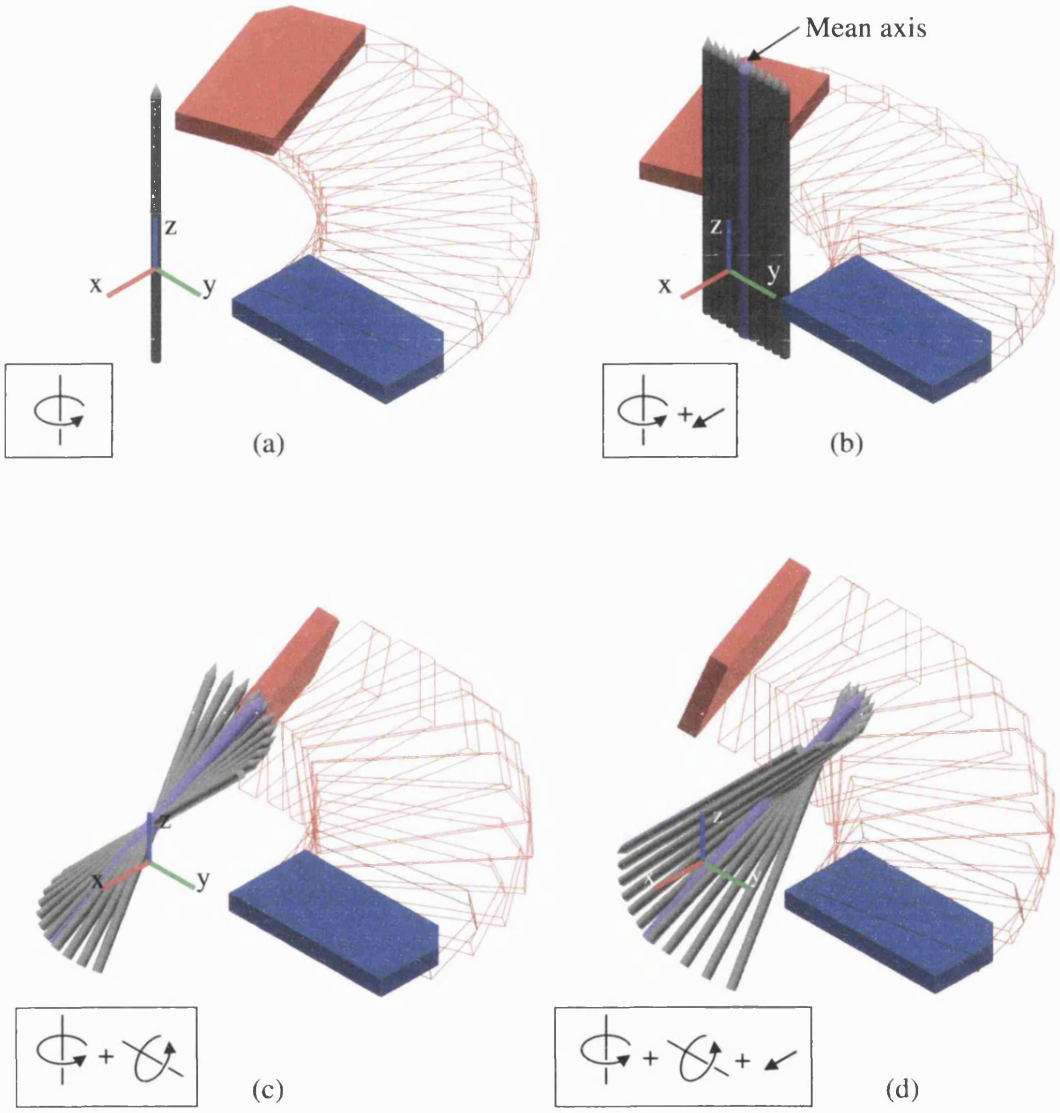

Figure 113 Graphical representation of finite helical axes produced by C++ program for ten increments of movement. (a) Pure rotation about x-axis. (b) Rotation about x-axis and movement in positive x direction. (c) Rotation about x and y axes. (d) Rotation about x and y-axes and movement in positive x direction.

5.18 Predicting the Kinematics of a Biaxial Joint

The ability of the method to predict the kinematics of a joint was tested on three-dimensional computer models of a biaxial-type wrist joint prosthesis. The surfaces of this joint are toroidal in shape and are highly conforming. The prosthesis functions as a two-hinge joint, having axes for radial-ulnar deviation and flexion-extension. The axes are perpendicular to one another with the radial-ulnar deviation axis 5mm distal to the flexion-extension axis. The aim of this test was to ascertain whether the algorithm could predict the movement of the joint, and in so doing, determine its axes of rotation.

5.18.1.1 Method

By eliminating all non-articular surfaces from the computer models, the functionality of the joint was distilled to two toroidal surfaces (see Figure 114). These were converted to facetted models with 2530 facets in the distal component and 2198 in the proximal component.

The proximal component was fixed while the distal component was rotated about the x-axis in one-degree increments from 0 to 35 degrees of radial deviation The centre of rotation was set to the centroid point of the mesh, which was not located near the axes of rotation of the joint itself. The remaining five degrees of freedom of the distal component were varied by the algorithm in order to maximise the contact area at each increment of motion. The process was repeated for rotation about the y-axis in one-degree increments from 0 to 60 degrees of flexion. The initial and final step-lengths were set to 0.1 and 0.002 respectively.

5.18.1.2 Results

Observation of the resulting animations in both directions showed that the distal component moved very close to the surface of the proximal component, indicating that the contact area was being used effectively to control its path. The movement was not perfectly smooth and there were many small deviations away from the correct path. This gave the motion a slightly erratic quality. In both cases, it was clear that overall movement

was taking place about a fixed axis located far from the centroid of the distal component mesh, which was the axis about which initial rotations were applied.

Ulnar Deviation

The results are illustrated in Figure 115(a). Finite helical axes were calculated for every 5th degree of movement. It is clear from the figure that there is variation in the position and to a lesser extent, the direction of the axes. From Figure 116 it can be seen that the predicted axis coincides with the actual axis at the origin, but it is skewed by 3.9° about the z-axis.

Flexion

Figure 115(b) shows the results for flexion. There is considerable variation in the positions of the finite helical axes, which were computed at five-degree intervals of movement. The mean axis was located in approximately the correct position (Figure 116). The error on the axis position was +0.87 mm in the x-direction and +1.57mm in the z direction compared with the geometrical axes of the joint.

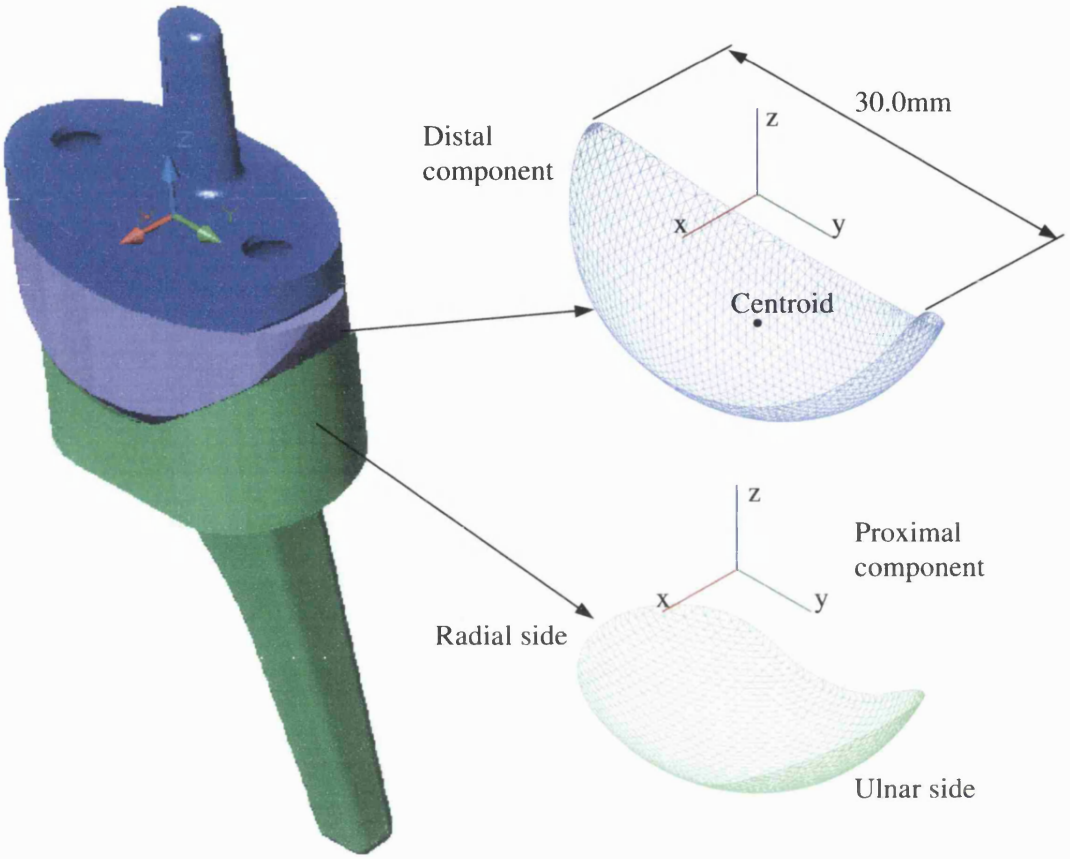

Figure 114 The two toroidal surfaces were extracted from the biaxial joint and imported into the SWORDS model.

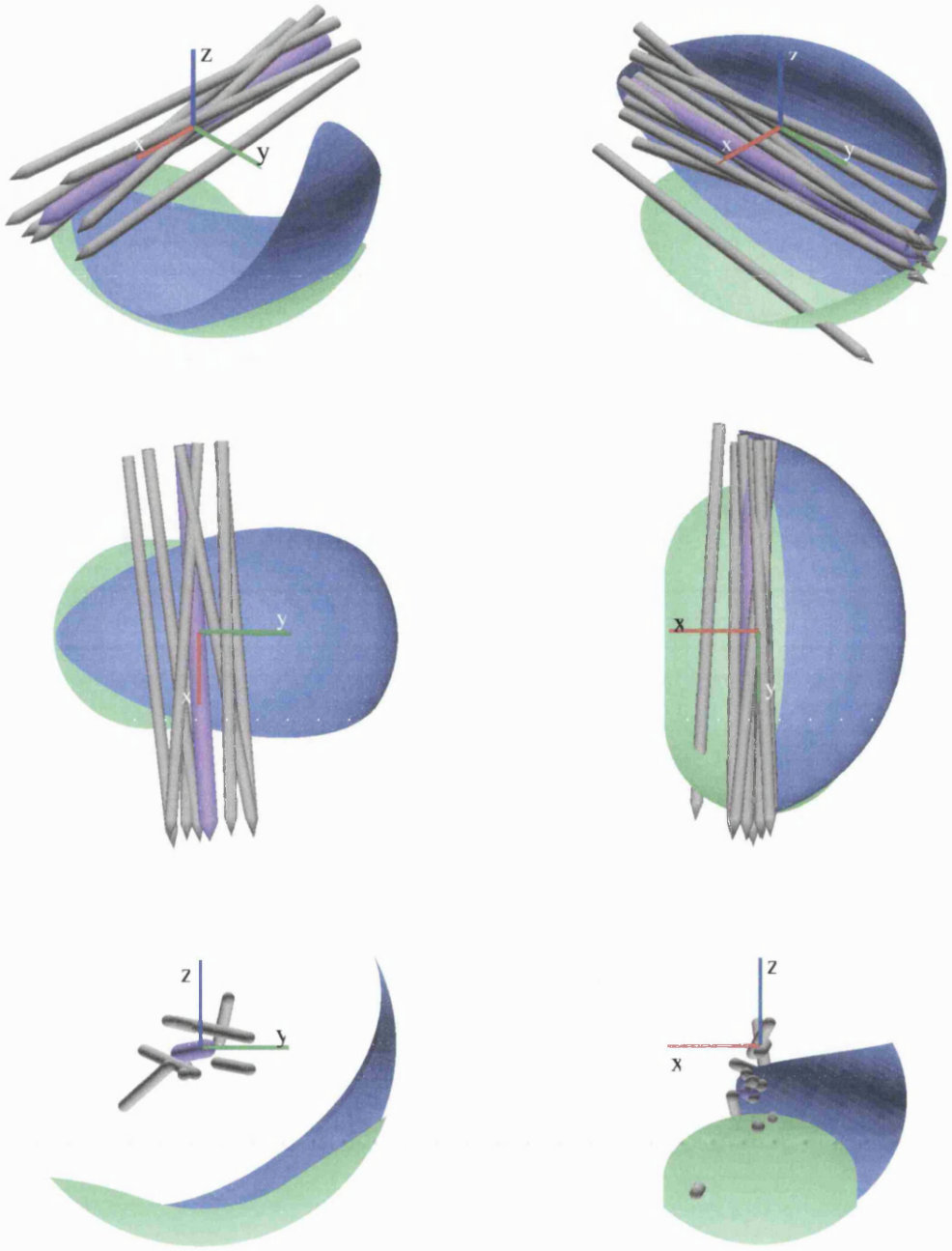

(a) (b

Figure 115 Positions of finite helical axes for every 5th degree of movement. (a) Ulnar deviation. (b) Flexion.

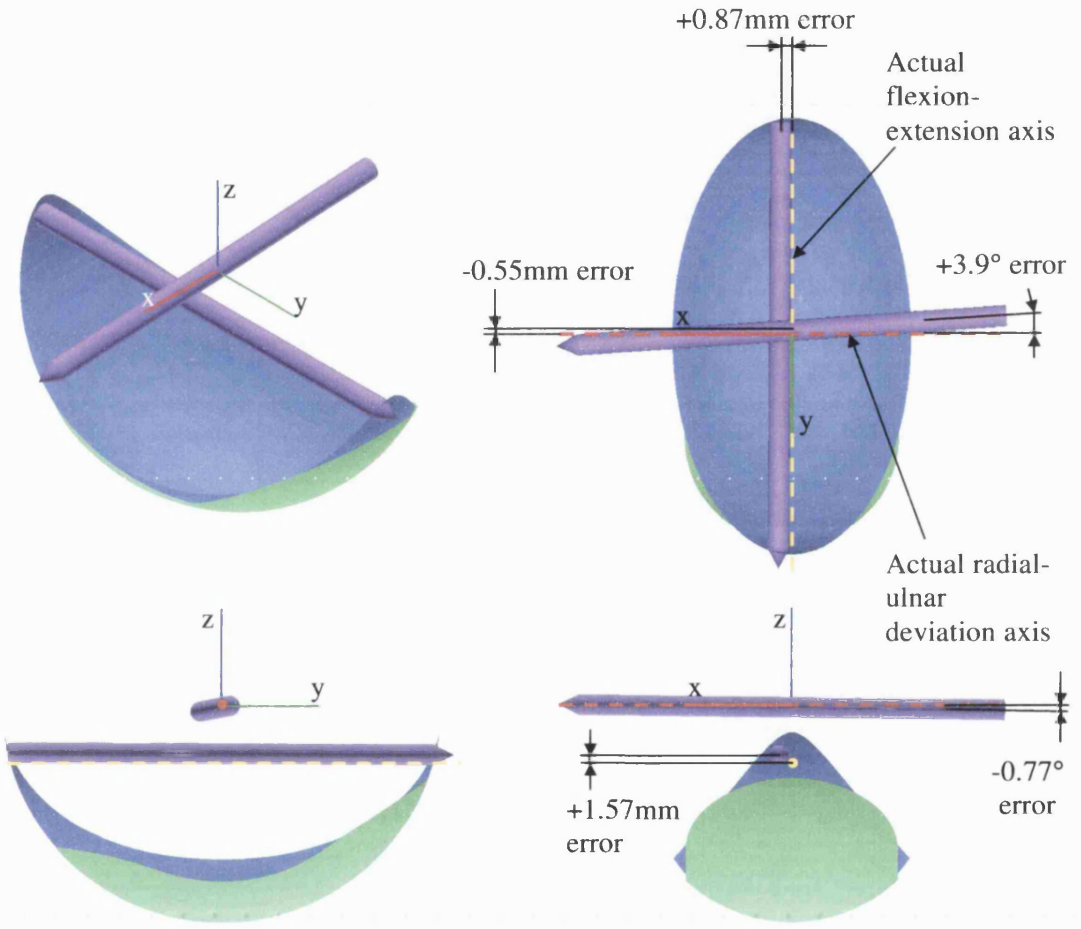

Figure 116 Comparing actual and predicted axes of motion for the biaxial joint.

5.19 Operation and Appearance

This section describes the process of interaction between CIEP (Contact and Intersection Evaluation Program), the SWORDS macro and FFRP (Far Facet Removal Program). The macro written to control SWORDS will henceforth be referred to as CARPAC (*Car*pal *Pac*king).

5.19.1 Interface Appearance

The appearance of the SWORDS window when running CARPAC is illustrated in Figure 117.

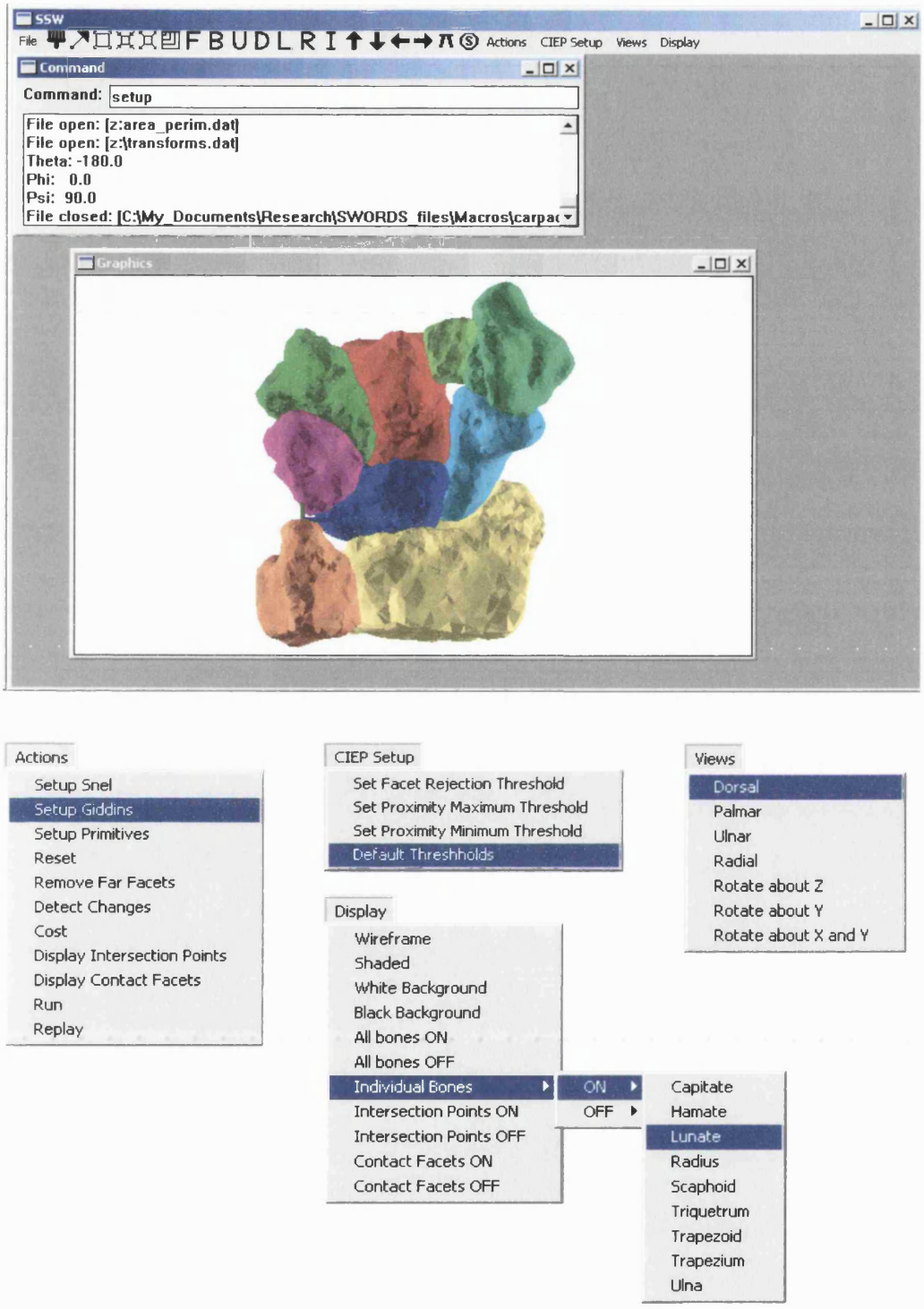

Figure 117 The appearance of SWORDS and the command menu when running the CARPAC macro.

5.19.2 Operation Sequence

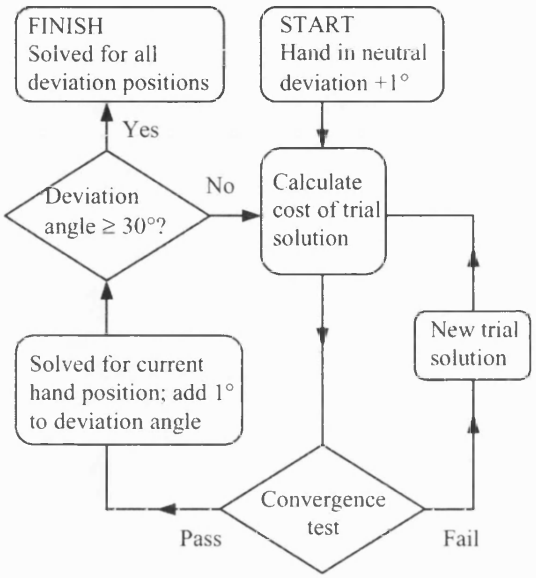

Figure 118 Flowchart illustrating CARPAC operation

A more detailed breakdown of the CARPAC operation sequence follows:

Initiation:

CARPAC macro read into SWORDS.

Individual bone models read into SWORDS.

Bone models written to a single file on RAMdisk for use by CIEP and FFRP.

User selects threshold for far-away facet removal.

User selects maximum and minimum distance threshold for contact area calculation.

User selects minimum and maximum angles of wrist deviation.

Running:

Repeat for 1 degree increments of capitate position from e.g. 0 to 20 degrees ulnar deviation:

(

Execute FFRP; a file listing which facets in each bone are nearest to another bone is written to RAMdisk.

Repeat until the step size used by the optimisation algorithm is smaller than the termination step size:

(

Optimisation algorithm varies one or more of the 23 degrees of freedom.

A file containing the transformations is written from CARPAC to the RAMdisk.

Change detection routine within CARPAC reads the transforms file, detects which bone pairs will need to be re-calculated and writes these as a list to the RAMdisk.

CARPAC executes CIEP.

CIEP reads in the models file from RAMdisk.

CIEP reads in the list of nearest facets from RAMdisk and only performs calculations on these facets.

CIEP reads in the list of affected bone-pairs and only recalculates these.

CIEP writes a file containing the contact area and intersection perimeter for each bone pair.

CARPAC reads the results file from the RAMdisk and calculates the cost of the current solution.

)

Record converged positions of all bones to final results file.

)

Replay:

CARPAC reads the final results file and animates the bones.

Finite helical axes are calculated.

5.20 Method Summary

This section presents a concise outline of the methods adopted for this study.

5.20.1 Software

The theoretical model was created using SWORDS, a constraint modelling program created by colleagues at Bath. In addition to a geometric modeller, SWORDS also contains an optimisation algorithm and so was the ideal choice of software for the project. In order to increase the speed of certain calculations, bespoke C++ programs were written and these communicated with SWORDS via small input and results files.

5.20.2 Bone Models

Three-dimensional computer models of the carpal bones were obtained by laser-digitisation of bones dissected from a disarticulated cadaveric human wrist. The positions of three markers on each bone were digitised prior to disarticulation to allow the computer models to be realigned into their anatomical positions. The bones were scanned at a resolution of ~0.17mm, but at this resolution, it was calculated that computation times would exceed 220 days. Therefore, the resolution was reduced to ~1.40mm to allow run times of 24-48 hours to be achieved.

5.20.3 Output Bones

The capitate was chosen to represent overall wrist posture. The hamate, trapezium and trapezoid bones were fixed to the capitate and moved as single, rigid unit. Rotations were applied to this complex in 1.0 and 0.5 degree increments to advance the wrist into radial or ulnar deviation. The centre of rotation was set at the point representing the mean of all vertex coordinates in the capitate bone model.

5.20.4 Degrees of Freedom

The hamate-capitate-trapezium-trapezoid complex was allowed five degrees of freedom since its rotations in the radial-ulnar deviation plane were fixed for each increment. The scaphoid, lunate and triquetrum were allowed all six degrees of freedom. The radius and ulna were fixed at all times. The total number of degrees of freedom was therefore 23.

5.20.5 Cost function

The aim of the algorithm was to maximise the contact area occurring between nine selected pairs of surfaces at each increment of output bone position by adjusting the 23 degrees of freedom (rotation and translation) of the bones. The nine pairs were as follows: Capitate-lunate, capitate-scaphoid, hamate-triquetrum, lunate-radius, lunate-scaphoid, lunate-triquetrum, radius-scaphoid, scaphoid-trapezoid and scaphoid-trapezium.

The cost function contained a "reward" component and a "penalty" component. The reward was the contact area between bones and the penalty was the level of intersection occurring between bones. Contact area was found by projecting facets from one surface onto their nearest neighbours on the opposite surface and calculating the area of overlap. Intersection was evaluated as the length of the chain of points marking intersections between edges and facets.

5.20.6 Optimisation Method

The Hooke and Jeeves direct search optimisation algorithm contained within SWORDS was used to minimise the cost function. This algorithm works by trial and improvement and adjusts one degree of freedom at a time.

6 RESULTS

Results

The purpose of this section is to present a series of test-runs of the CARPAC algorithm. The reason for the test-runs was to understand the effect of various adjustments and modifications that were made to the configuration. In this section, the performance of the algorithm is judged qualitatively by comparing the results to known results of experimental studies.

It is difficult to appreciate the movement of the bones on the printed page. Therefore, included at the end of this document is a CD ROM containing all the animations described on the following pages.

6.1 Laser-Scanned Bone Models

The CARPAC algorithm was applied to the laser-scanned bone models (see section 5.5) in radial and ulnar deviation. Rotations about the x-axis were applied to the output bone complex (capitate-hamate-trapezoid-trapezium). The centre of rotation was initially set to the point marking the mean of all vertex coordinates in the capitate model. The starting position for all runs was the neutral position. For all tests with the laser-scanned bones, the far-away facet removal threshold was set at 3.0mm. The maximum and minimum distance thresholds for the contact calculation were set to 1.0 and 0.01mm respectively. The computation time for each run varied between 11h 40m and 19h 43m. This agrees well with the 8-19h projections made in Figure 111.

In order to test the effect of various factors on the outcome, tests were initially performed in ulnar deviation only. The runs were repeated with one parameter changing each time in order to isolate its effect. During this phase of testing, the results were assessed qualitatively to see whether the predicted movement patterns demonstrated similar characteristics to experimental results.

Once a satisfactory configuration had been found, it was applied to the radial deviation case and a more quantitative analysis of the results was performed.

Runs are numbered sequentially, with the prefix "U" denoting ulnar deviation and "R" radial deviation. In order to avoid repetition, the starting position of the carpal bones common to all runs is shown in Figure 119.

6.1.1 Modification of the Cost-Function

The first run was made with movement occurring in 1.0 degree increments and with a cost function as follows:

$$\text{Cost} = k_1 - a + k_2 i \qquad (6.1.1\text{-}1)$$

Where a=contact area, i = intersection perimeter, $k_1 = 1000$ and $k_2 = 1.0$

Frames from the animation are shown in Figure 120. A result that is immediately obvious from this run is the separation of the scaphoid from the trapezium and trapezoid. From equation (6.1.1-1) it can be seen that there is no penalty for gross separation of the bones, only for intersection between them. Similarly, since contact is not calculated if surfaces are further than 1.0mm apart, the optimisation algorithm has no information regarding the "fitness" of a trial solution if the bones are grossly separated. Therefore an additional term was introduced into the cost function in an attempt to rectify this problem. The point of closest approach between two surfaces, r, was calculated and used as an additional penalty function as follows:

$$\text{Cost} = k_1 - a + k_2 i + k_3 r^2 \qquad (6.1.1\text{-}2)$$

Where k_3 is a weighting factor, initially set to 5.

Note that if the surfaces were further apart than the far-away facet removal distance threshold (3.0mm in this case) then r was not calculated. However, it was not envisaged that such a large error would occur.

The run was repeated with the modified cost function and the separation observed previously was greatly reduced (see Figure 121). However, there was noticeable intersection between the capitate and scaphoid and, to a lesser extent, between hamate and triquetrum at the +20° ulnarly deviated position (see Figure 122). This suggests the penalty factor for intersection, k_2, was not set sufficiently high.

+0° UD

(a) (b) (c)

Figure 119 The starting positions of the carpal bones common to all runs. (a) Ulnar view. (b) Palmar view. (c) Radial view.

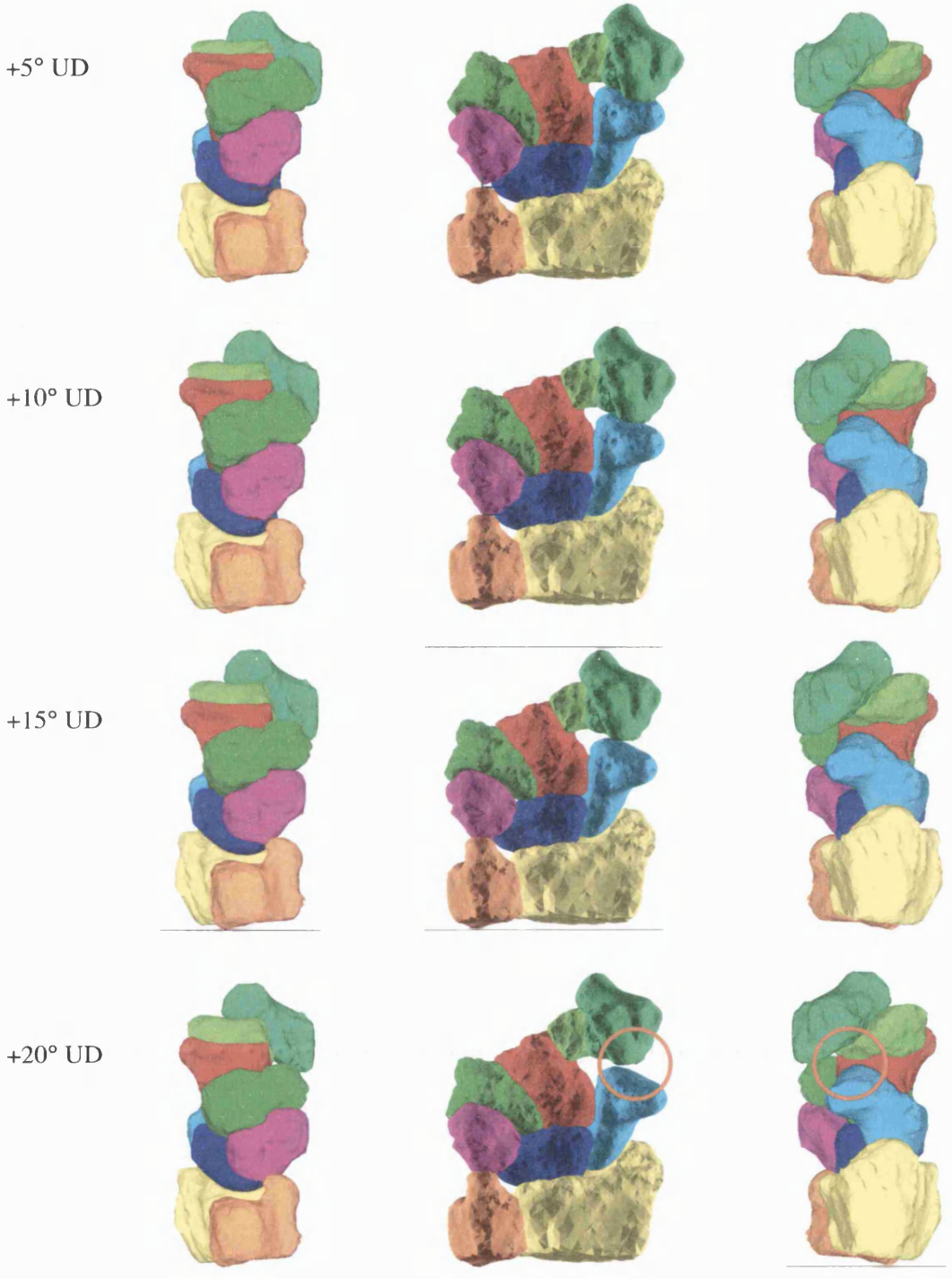

Figure 120 Run #U1 showing separation of the scaphoid from the trapezium and trapezoid. Run time: 13h 16m.

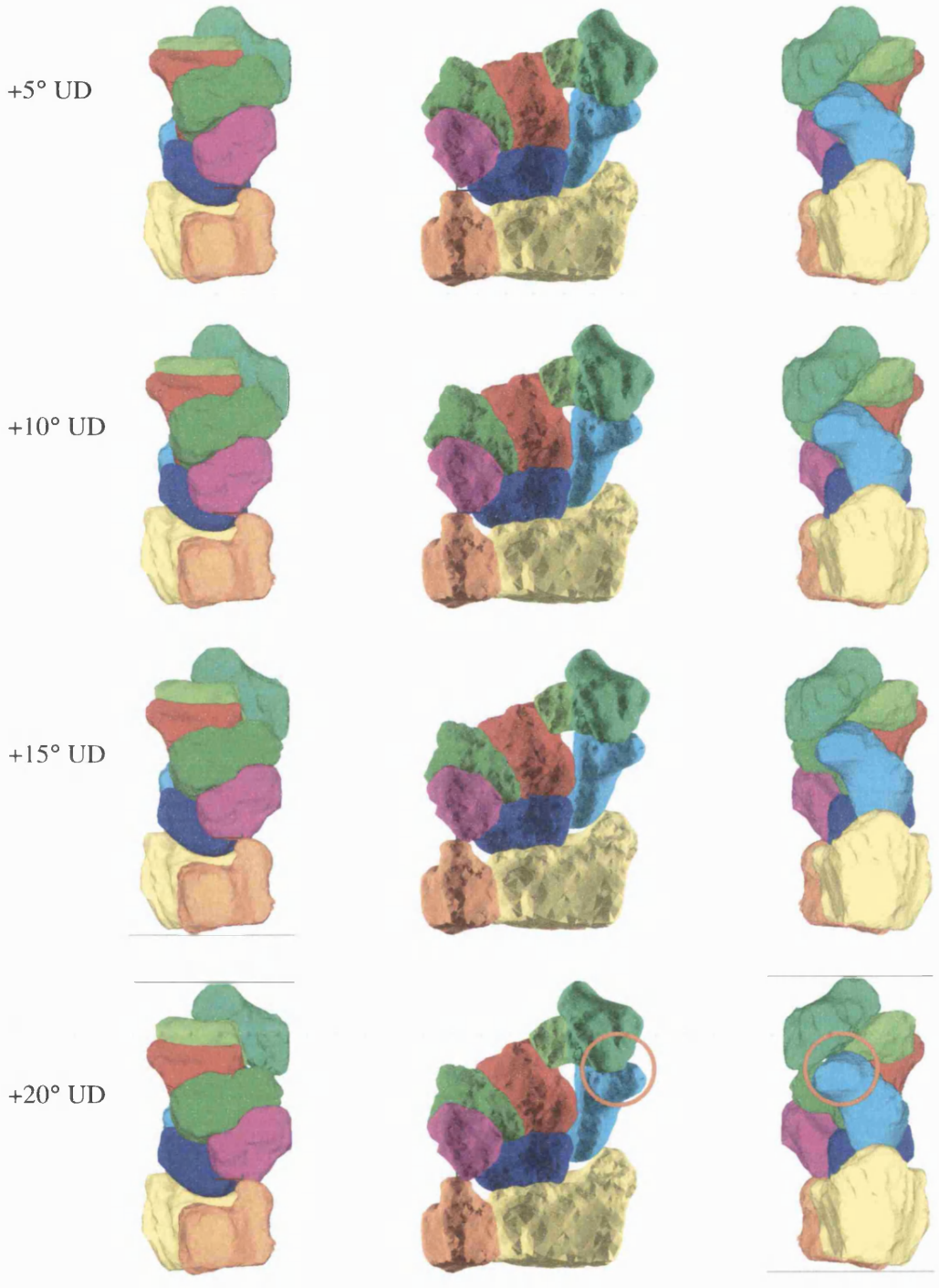

Figure 121 Run #U2 following modification of the cost function to include a penalty for gross separation. Scaphoid no longer separates from the trapezium and trapezoid. Run time: 15h 32m.

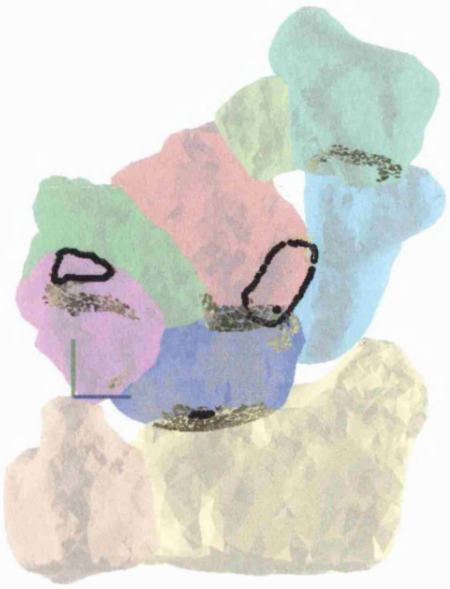

Figure 122 Contact patches and intersection for run #U2 at +20° ulnar deviation. High levels of intersection suggest the penalty factor, k_2, was not sufficiently high.

6.1.2 Weighting Adjustments

6.1.2.1 Run #U3

In an attempt to rectify the problems observed in Figure 122, the penalty factor for intersection was increased from 1.0 to 10.0. The results are shown in Figure 123. While this adjustment helped reduce the intersection levels (see Figure 124), they were not eliminated. Furthermore, there was a recurrence of the scaphoid separation problem although it was not as pronounced as that observed in Figure 120. Of these two problems, it was decided that the priority was the separation of the scaphoid since the actual interpenetration distance represented by the chain of intersection points was quite small and could conceivably be accommodated by compression of the articular cartilage. Therefore, for run #U4, the intersection penalty factor, k_2, was kept at 10.0 while the separation distance penalty, k_3, was increased from 5.0 to 10.0.

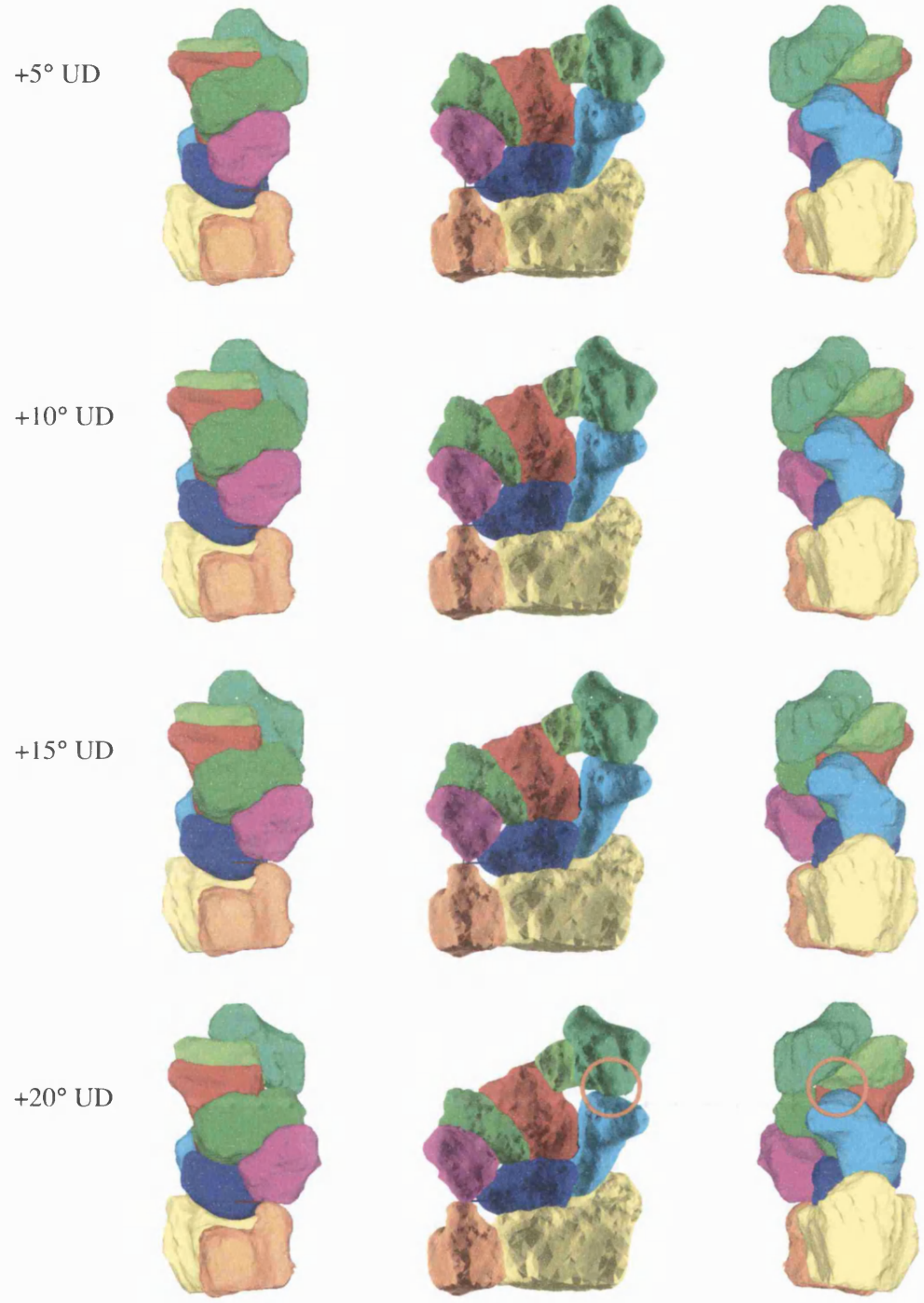

Figure 123 Run #U3 showing the effect of an increased intersection penalty factor. While intersection was reduced, there was a recurrence of the scaphoid separation problem. Run time: 15h 08m.

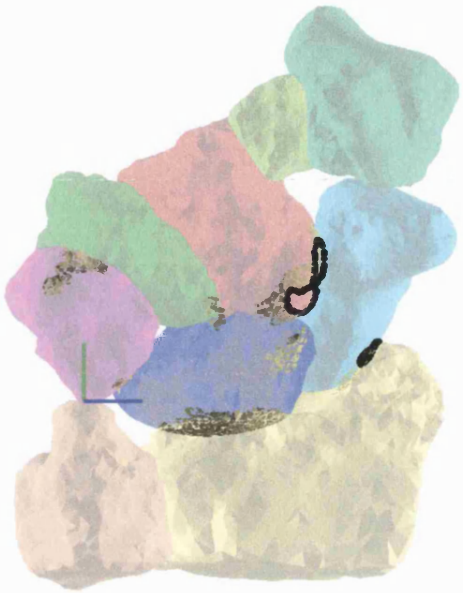

Figure 124 Contact patches and intersection for run #3 at +20° ulnar deviation. The level of intersection has been markedly reduced compared with Figure 122, but the scaphoid has separated from the trapezium and trapezoid.

6.1.2.2 Runs #U4, U5 and U6

In an attempt to overcome the scaphoid separation problem observed in Figure 123, the separation penalty factor, k_3, was increased from 5.0 to 10.0 for run #U4. This reduced the separation between scaphoid and trapezium, but there was still a gap (see Figure 125). Furthermore, the scaphoid lost contact with the radius for the first time in any test thus far. The large region of intersection between scaphoid and capitate, identified as the second priority problem in run #U3, persisted (see Figure 126). It was hypothesised that the scaphoid was becoming impaled on the capitate, thereby losing mobility. Therefore, for run #U5, the separation penalty remained at 10.0 while the intersection penalty was increased to 20.0 in an attempt to eliminate the intersection. The full set of images for run #U5 is shown in Figure 127, and the final position is shown in Figure 128.

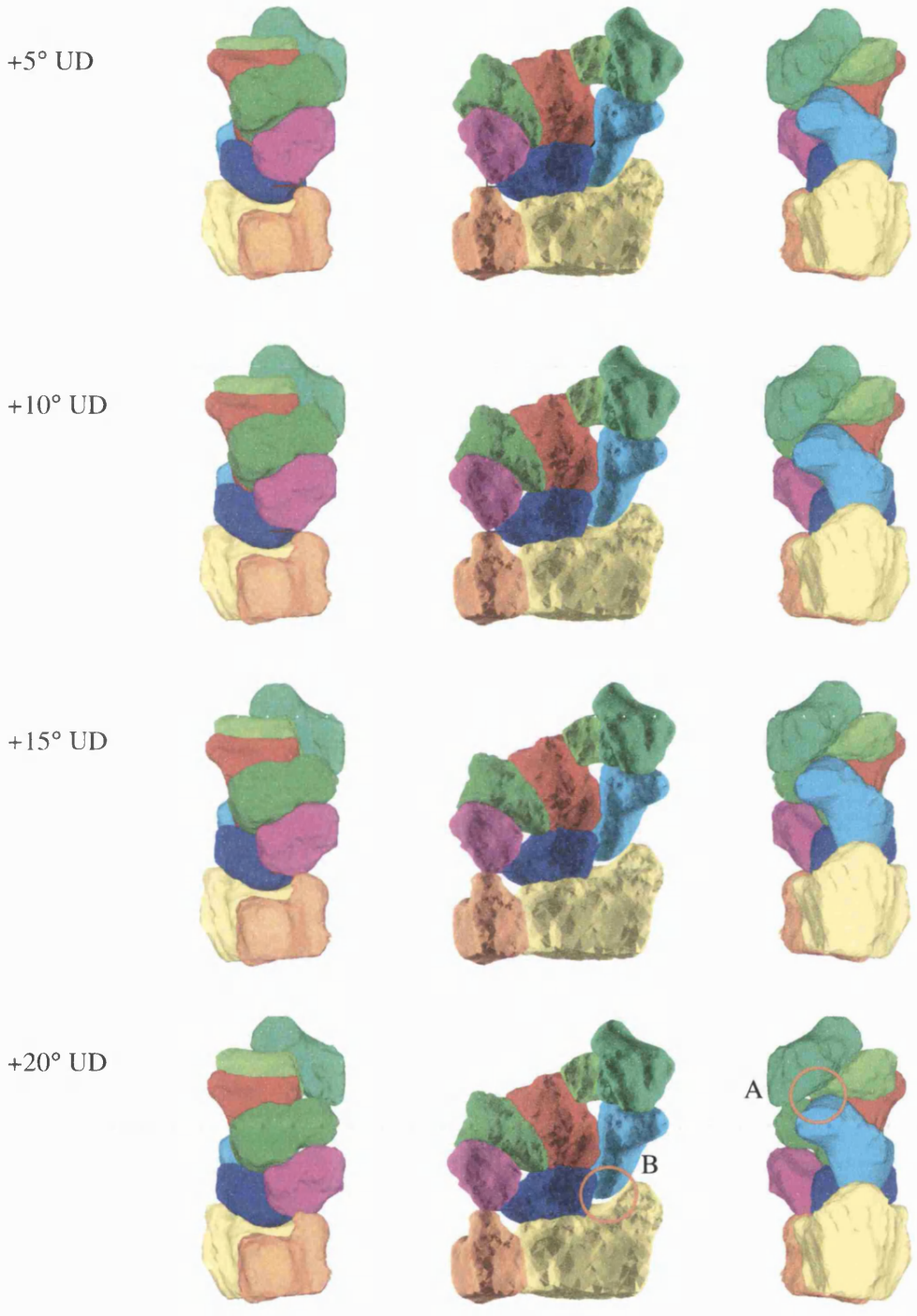

Figure 125 Run #U4 showing the effect of an increased separation distance penalty factor. Separation between scaphoid and trapezium was reduced (A), but the scaphoid lost contact with the radius (B). Run time: 12h 49m.

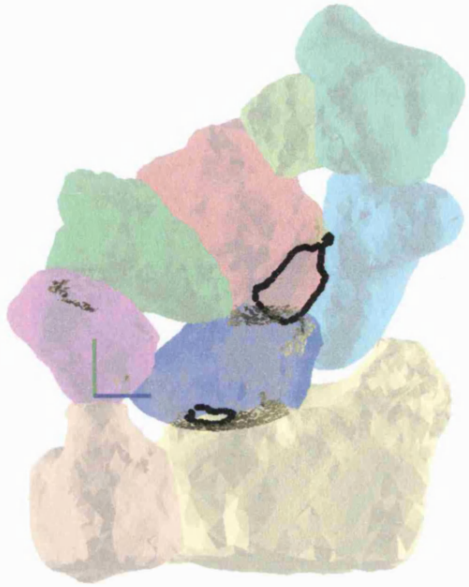

Figure 126 Contact patches and intersection for run #U4 at +20° ulnar deviation with an intersection penalty of 10.0. The scaphoid no longer separates from the trapezium and trapezoid, but the intersection problem persists.

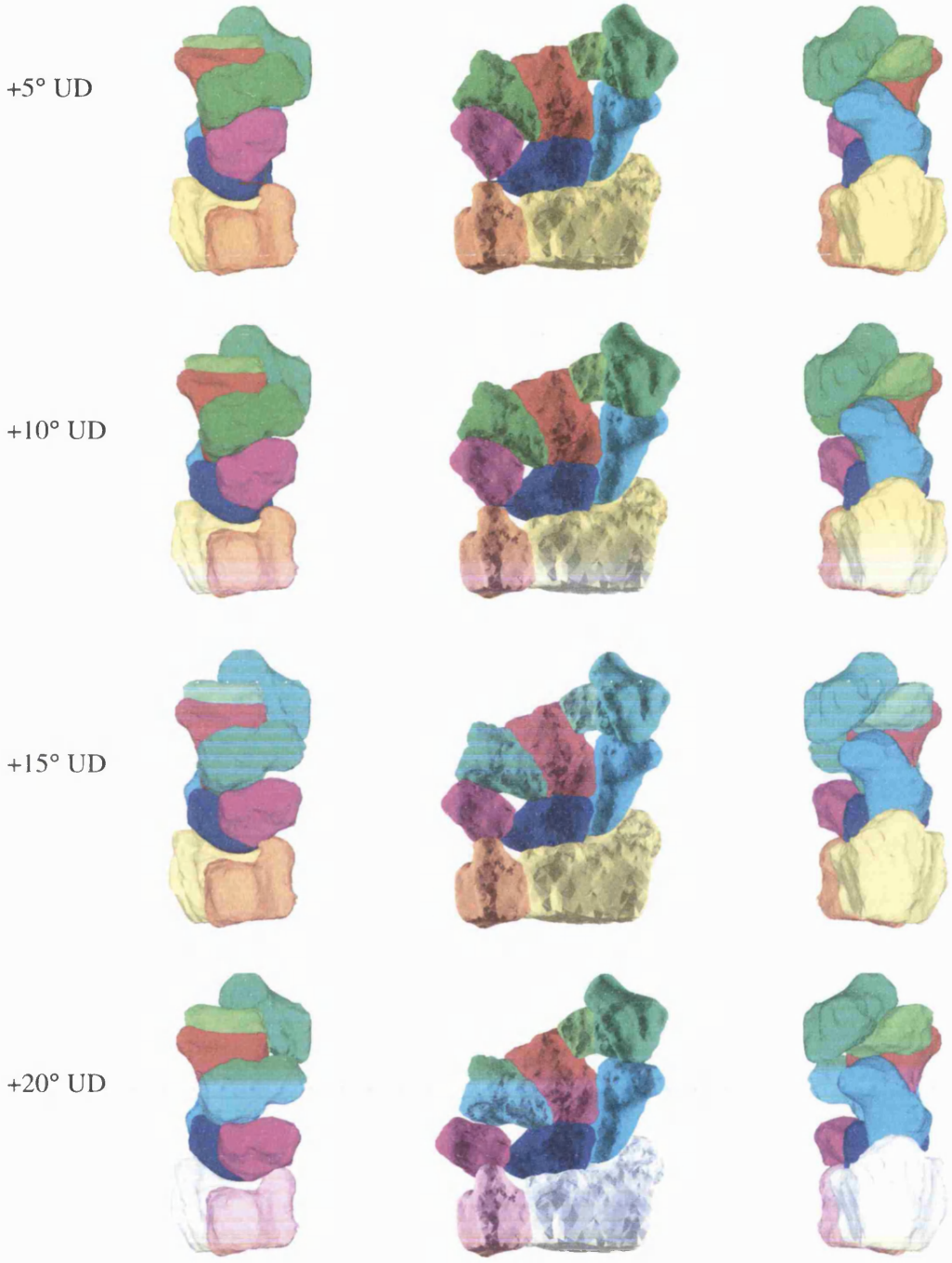

Figure 127 Run #U5 showing the effect of increasing the intersection penalty from 10.0 to 20.0. Note that the scaphoid entirely ceases to move at +15°. Run time: 19h 43m.

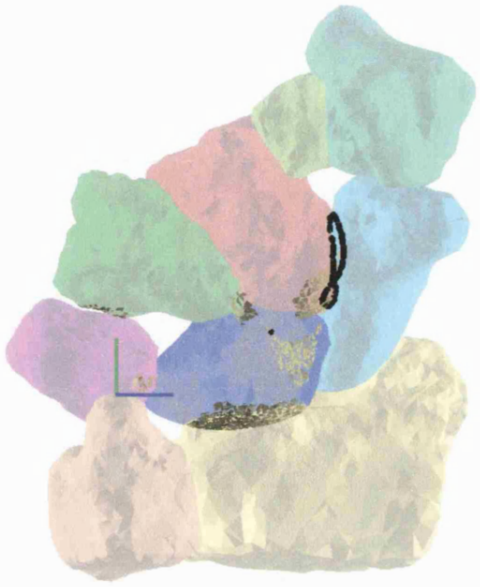

Figure 128 Contact patches and intersection for run #U5 at +20° ulnar deviation with an intersection penalty of 20.0. Intersection persists between the scaphoid and capitate but is less than that for run #U4 (see Figure 126).

In Figure 127, the scaphoid is observed to cease moving entirely at +10° of ulnar deviation, resulting in the recurrence of separation between the distal pole of the bone and the trapezium. This behaviour had not been observed in any previous run and was considered a one-off. Furthermore, Figure 128 shows that, even with a doubled penalty factor, intersection between the capitate and scaphoid persisted, but was less than for the previous run (see Figure 126). For run #U6, the penalty factor was increased from 20.0 to 50.0. The results are shown in Figure 129. The surprising outcome from this run was that the scaphoid remained motionless throughout and the intersection actually increased (see Figure 130 vs. Figure 128).

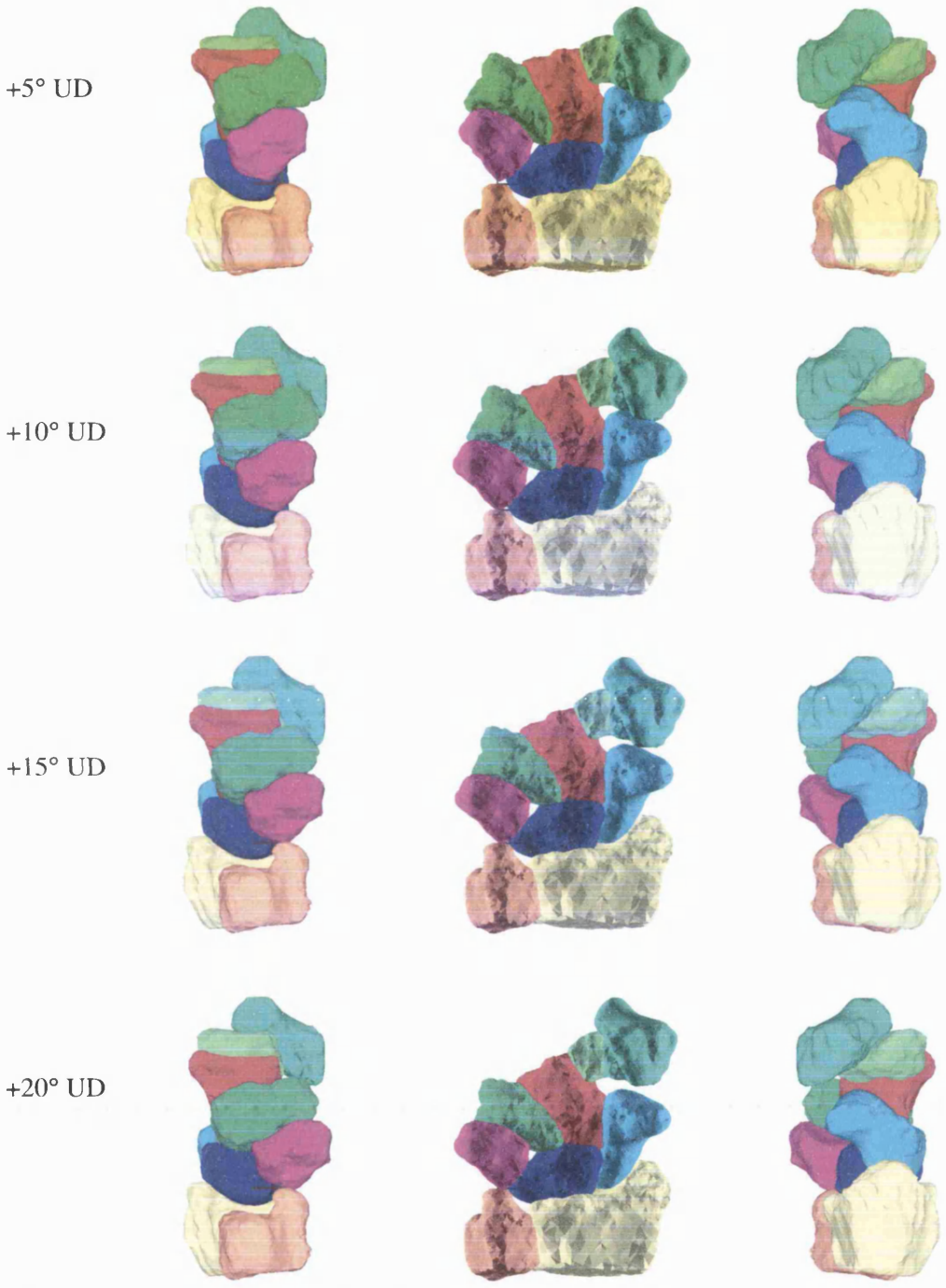

Figure 129 Run #U6 showing the effect of increasing the intersection penalty from 20.0 to 50.0. Note that the scaphoid remains stationary throughout resulting in a large gap between its distal surface and the trapezium. The reason for this behaviour is unclear. Run time: 16h 09m.

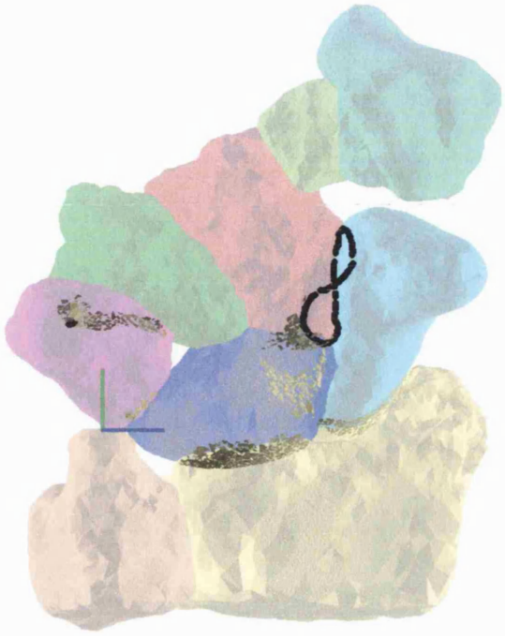

Figure 130 Contact patches and intersection for run #U6 at +20° ulnar deviation with an intersection penalty of 50.0. Intersection persists between the scaphoid and capitate and paradoxically is greater than for run #5 (see Figure 128).

6.1.2.3 Cost History

In order to gain some understanding of the processes that may have led to the unusual results for runs #U5 and #U6, the "cost" of each increment of motion at convergence was plotted against the angle of deviation from the starting position for each run (see Figure 131). The graph shows that for runs #U1 and #U2, there was comparatively little variation in cost from the starting position to the +20° ulnarly deviated position. This suggests that the algorithm was finding similar levels of contact at each increment. The upward trend of the data indicated that contact area was falling as the wrist moved further into ulnar deviation. This could be representative of the physical situation, but more likely represents a build-up of errors since the start position at each increment is based upon the final position from the previous increment. As the penalty factors were increased for runs #U3, #U4, #U5 and #U6, the graph lines became more irregular as the penalty components were magnified. While runs #U3 and #U4 have similar points of inflection to runs #U1 and

#U2, the shapes of lines #U5 and #U6 are markedly different. At point "A" on run #U5, the cost rapidly rises. This coincides with the point at which the scaphoid was seen to become motionless while the capitate impinged upon it increasingly with each additional increment. From reviewing the animation for run #U6, however, it is difficult to ascertain the reason for the sharp drop in cost at point "B".

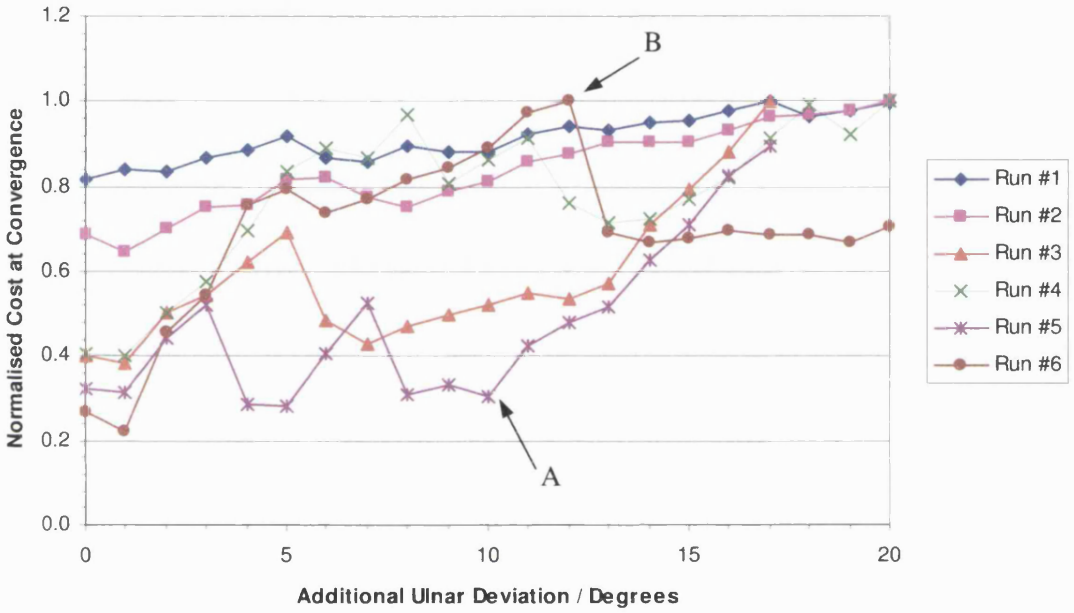

Figure 131 Graph showing normalised cost at convergence against wrist position for six runs. All runs exhibit greater cost towards the end of the range of movement, but the effect becomes more pronounced as larger penalty factors are used for the later runs. A: The point at which the scaphoid became motionless during run #U5.

6.1.2.4 Final Weightings

Following the results of six runs with differing intersection and separation penalty factors, it became apparent that no amount of adjustment would entirely remove the separation and intersection problems. Therefore, it was decided to revert to the configuration used to obtain run #U2. Of all the runs tested, the overall characteristics of the movement predicted during this run bore the closest resemblance to the actual movement of the carpals. These characteristics will be discussed in detail in section 7, once the optimum run conditions have been described.

6.1.3 Centre of Rotation Position Adjustment.

The centre of rotation for the movement imposed on the capitate-hamate-trapezoid-trapezium output complex was initially set at the centroid point of the capitate bone (see section 5.10.1). This point does not coincide with the region in which the actual centre of rotation for this bone is known to lie, since one of the goals of the study was for the algorithm to find this for itself.

It was assumed that the translation variables for the output complex would change during optimisation so as to reposition the effective centre of rotation at a location closer to its true anatomical position for that particular increment of movement. However, there was little if any adjustment of the translation variables for the capitate and so the expected repositioning did not occur (see section 7.1 for a full discussion of the observed kinematics).

In an attempt to assist the progress of the CARPAC algorithm, the centre of rotation for imposed movements was deliberately moved, in two steps, from the centroid point towards a point within the proximal pole of the capitate. This is where the centre of rotation has been shown to lie (see section 3.3). For runs #U7 and #U8, the CARPAC algorithm was re-run with centres of rotation B and C respectively, as illustrated in Figure 132. The remaining parameters were kept the same as for run #U2.

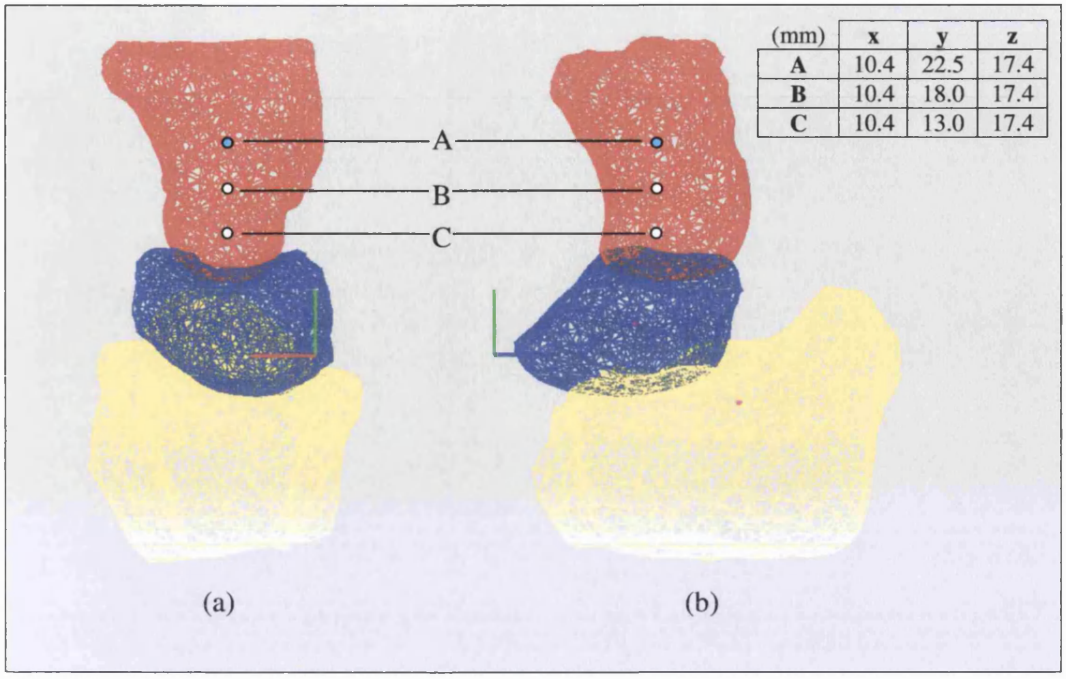

(mm)	x	y	z
A	10.4	22.5	17.4
B	10.4	18.0	17.4
C	10.4	13.0	17.4

Figure 132 The centre of rotation for applied movement of the capitate was moved to two new positions, "B" and "C" in order to investigate its effect on the predicted movements of the bones. "A" is the centroid of the capitate bone, as used for all previous runs. (a) Ulnar view. (b) Palmar view.

The results of repositioning the applied centre of rotation to points "B" and "C" are shown in Figure 133 and Figure 134 respectively. With the centre of applied rotation moved to point "B", the scaphoid remained in contact with both the radius and trapezium throughout the range of motion. In addition, the triquetrum maintained intimate contact with the lunate and hamate throughout the range of movement. However, while the lunate had exhibited 1.8mm of translation in a medial to lateral direction across the face of the radius in run #U2, for run #U7 the movement was only 0.7mm. This meant that there was insufficient space for the triquetrum to clear the ulnar styloid and so a small degree of impingement occurred. When the centre of rotation was set to point "C" (run #U8, Figure 134), the lunate remained motionless throughout the run. In common with all previous runs, very little migration of the centre of rotation for the capitate was observed for either run. Therefore, it was ultimately decided that the centre of applied rotations should remain at the geometrical centroid of the bone.

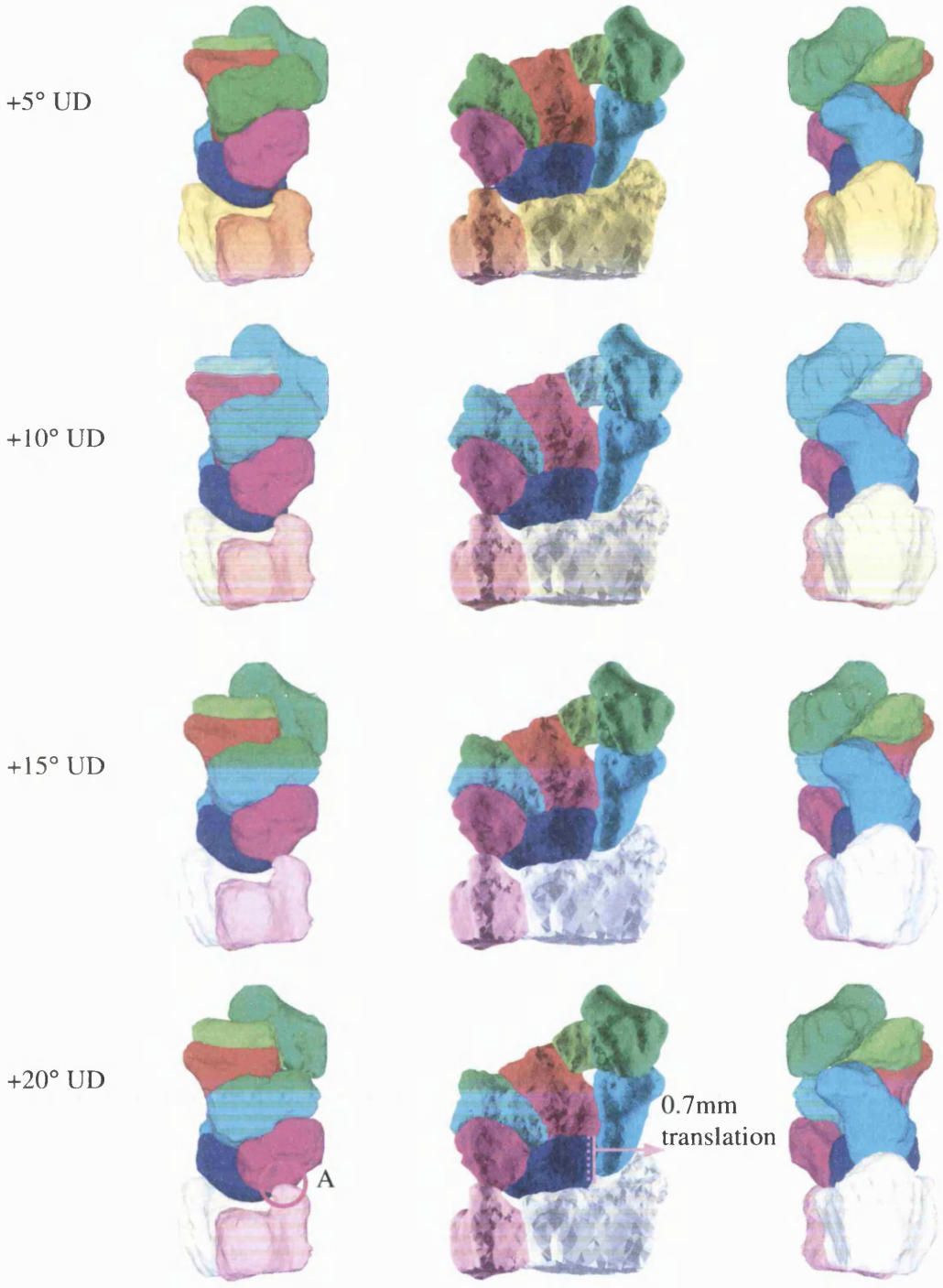

Figure 133 Run #U7 showing the effect of moving the centre of applied rotation to point "B" (see Figure 132). The lunate underwent small perturbations but its total excursion laterally across the face of the radius was just 0.7mm. A: Triquetrum collides into ulnar styloid. Run time: 11h 40m.

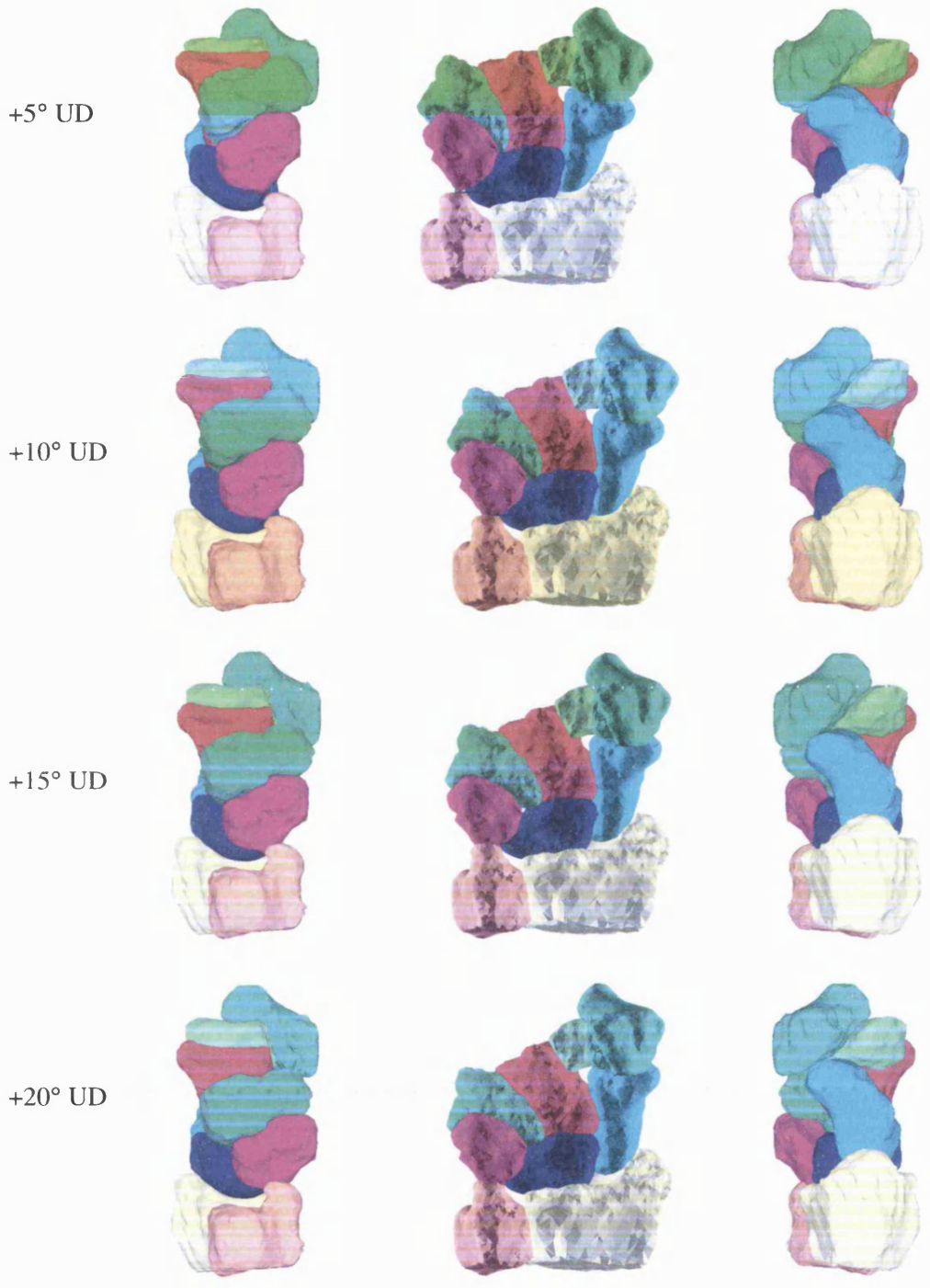

Figure 134 Run #U8 showing the effects of moving the centre of applied rotations to point "C" (see Figure 132). The lunate was found to remain motionless throughout the run. Run time: 11h 50m.

6.1.4 Movement Increment Adjustments

The effect of applying smaller increments of rotation to the output bone complex on the predicted movements was investigated. While all previous runs used a 1.0° increment, for run #U9, the increment was halved to 0.5°. All other parameters except the initial step-size were set to those used for run #U2. The initial step-size was set to 0.25 degrees, i.e. half the movement increment.

The motion for run #U9 (see Figure 135) was generally smoother than for all previous runs on account of the smaller increments of movement. The movement patterns were generally the same as for run #U2, except that the lunate translated further across the face of the radius, in a medial to lateral direction, than for any previous run. The distance translated was 2.2mm as opposed to 1.8mm for run #U2. However, this movement was still not sufficient to prevent the triquetrum becoming impaled upon the distal ulnar styloid.

The time taken for run #U9 was around 30 hours continuous and it was felt that the small improvements in performance over the 1.0 degree case did not justify repeating the run with 0.25° increments.

6.1.5 Model Resolution Adjustments

A single run was made using the bone models having maximum (10%) resolution, after the best configuration had been obtained following runs with the 4.8% resolution bones. The increment of applied movement was returned to 1.0°. The results, shown in Figure 136 were the best obtained thus far. The scaphoid clearly demonstrated out-of-plane motion and maintained firm contact with both the radius and trapezium, the lunate translated further across the face of the radius than for any previous run, and this allowed more space for the triquetrum to pass the ulnar styloid.

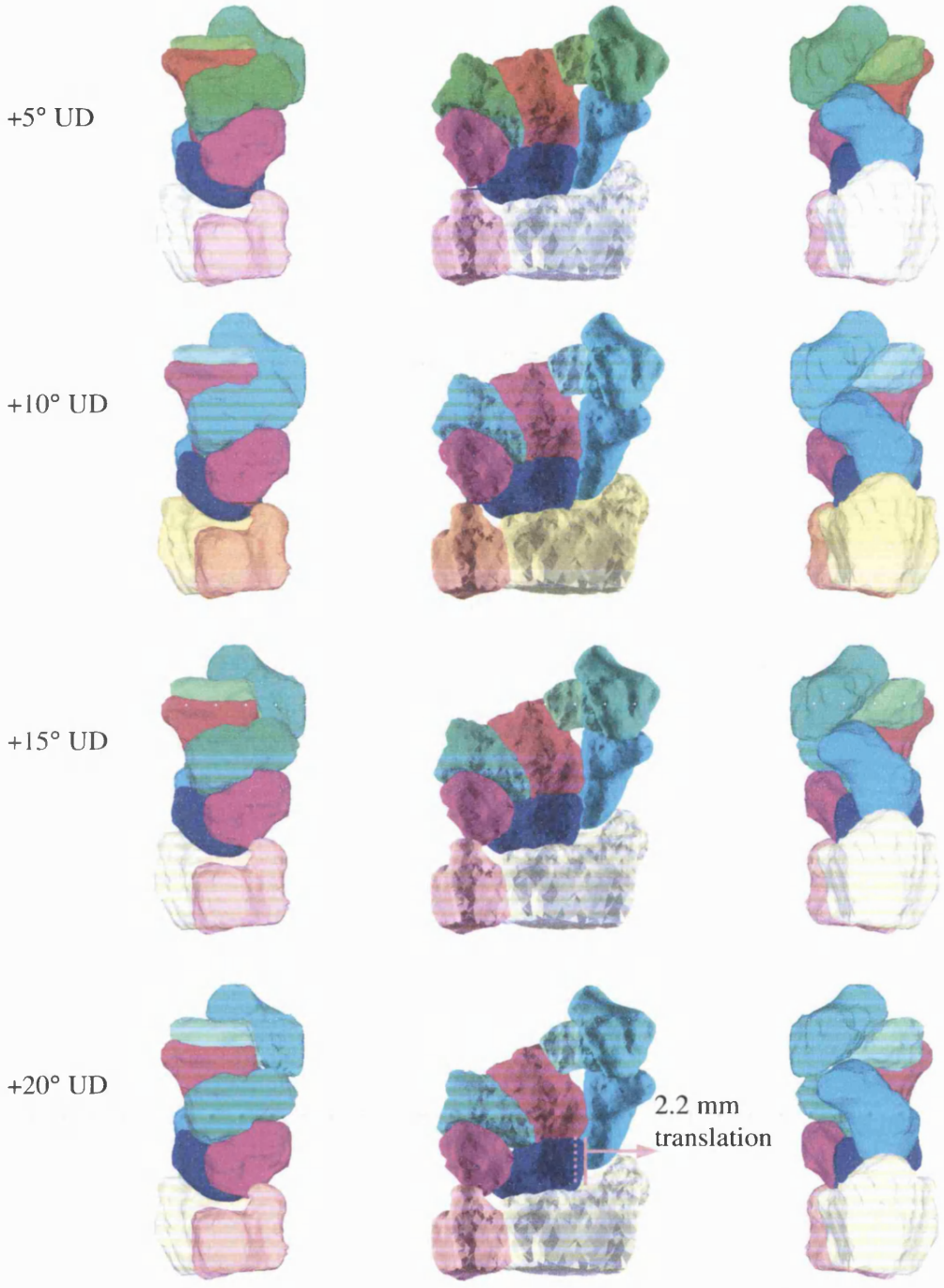

Figure 135 Run #U9 showing the effect of using 0.5° instead of 1.0° increments. The improvement in performance was slight, but the lunate translated further across the face of the radius than for any previous run. Run time: 30h 08m.

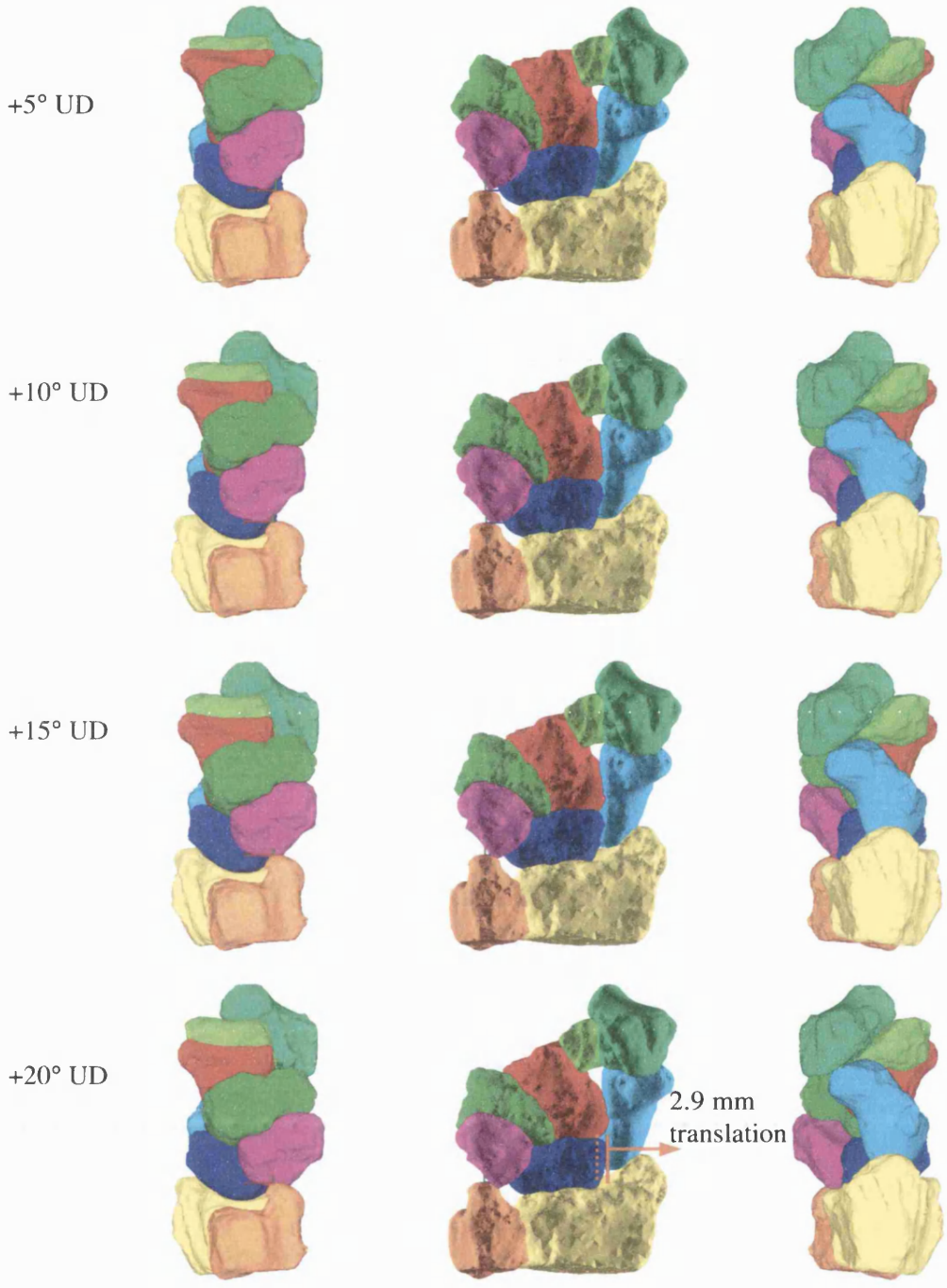

Figure 136 Run #U10 showing the effect of increasing the resolution of the models from 4.8% to 10.0%. The lunate translated by 2.9mm across the radius, which allowed the triquetrum to avoid impinging upon the distal ulnar styloid. Run time: 36h 43m.

6.1.6 Radial Deviation

The CARPAC algorithm was tested in 0 to 30° of radial deviation using the 4.8% resolution bone models. The increment of movement was set to 1.0 degrees and the cost function weightings were the same as those used for run #U2. The results are shown in Figure 138.

6.1.6.1 Run #R1

Despite performing well in ulnar deviation, the algorithm was not initially as successful for the radial deviation case. During the first run (see Figure 138), the scaphoid exhibited very little out-of plane movement and therefore, the trapezium and trapezoid collided with its distal pole. The extent of the impingement is shown in Figure 137, where the chains of intersection points have been superimposed onto the final frame from the animation. Furthermore, the lunate translated just 0.4mm in the lateral to medial direction across the face of the radius.

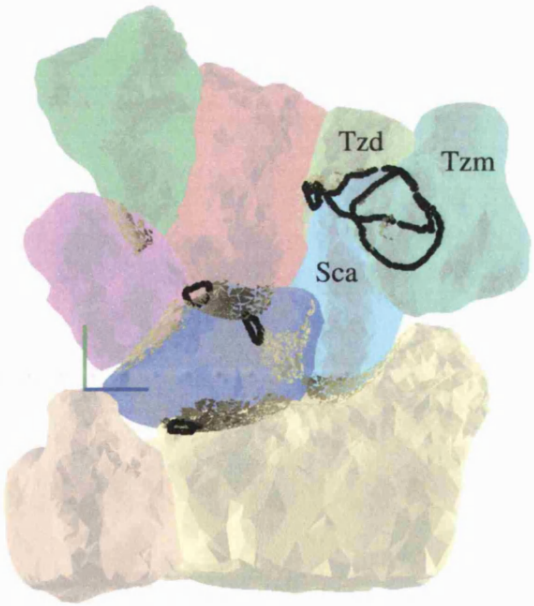

Figure 137 Contact patches and intersection for run #R1 at +30° ulnar deviation showing the high level of intersection between the scaphoid and the trapezium and trapezoid.

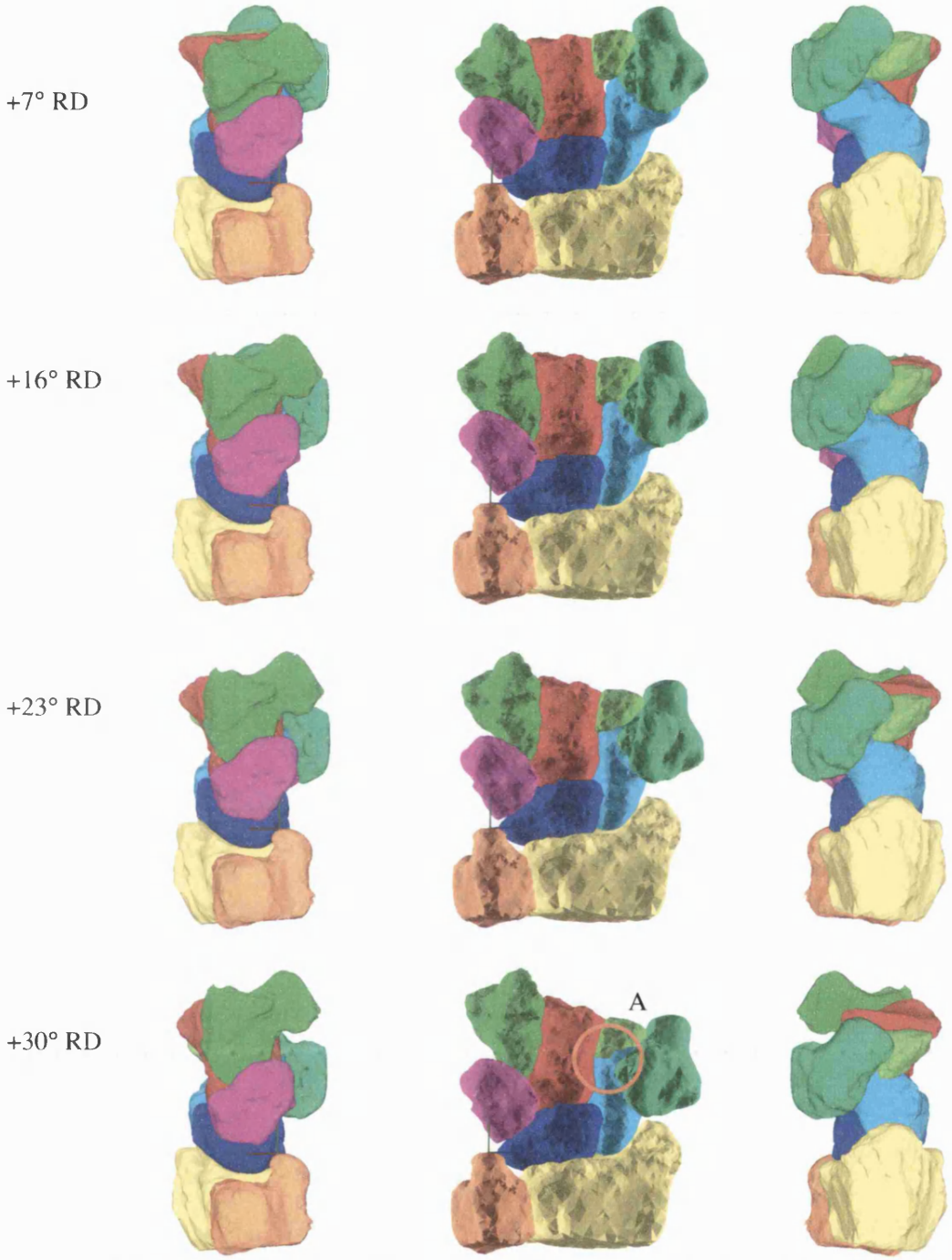

Figure 138 Run #R1 showing performance of the algorithm in radial deviation. There was no out-of-plane rotation of the scaphoid, as is shown to occur in experimental studies. A: The scaphoid interfered heavily with the trapezium and trapezoid. Run time: 23h 13m.

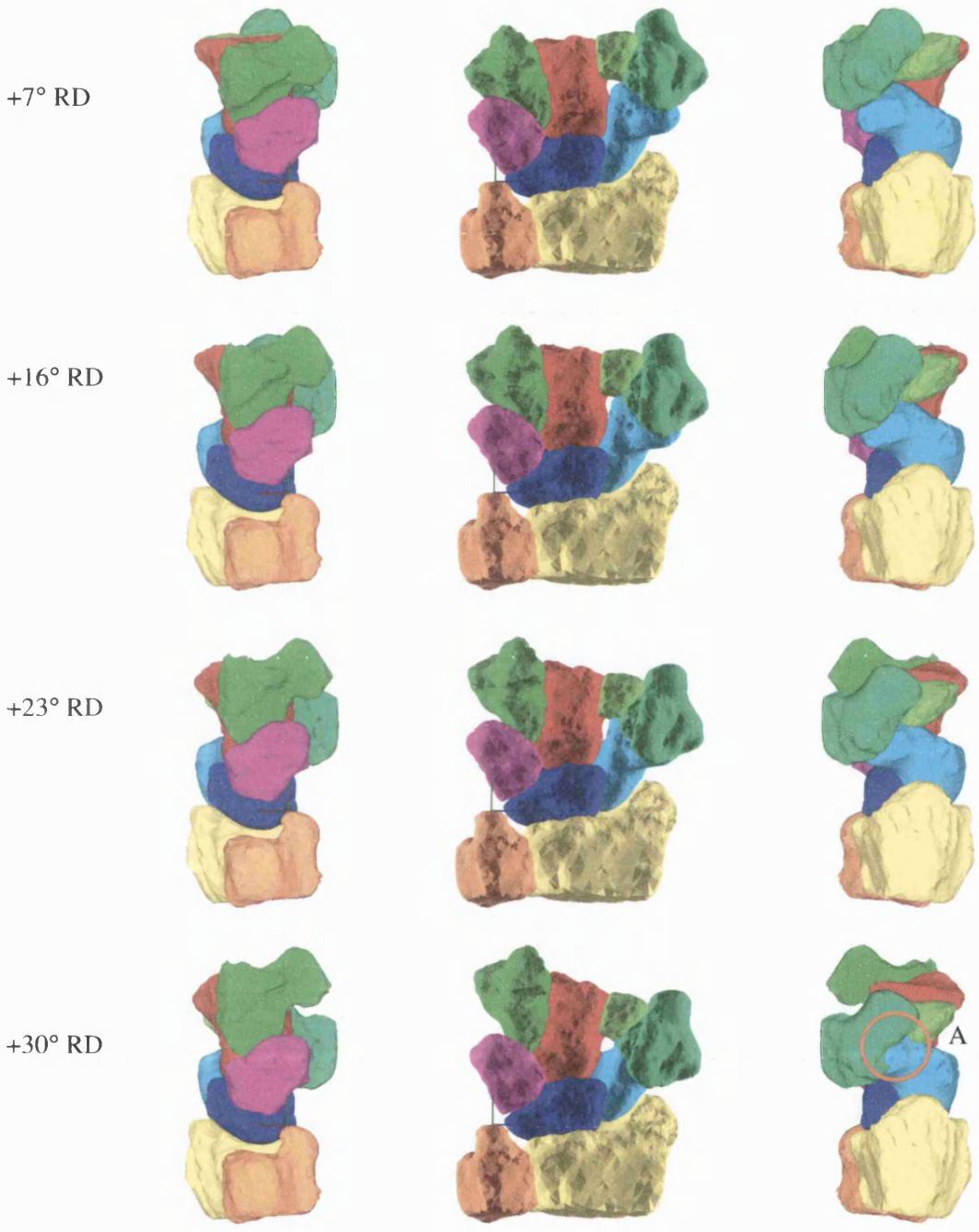

Figure 139 Run #R2 showing the effect of increasing the intersection penalty from 1.0 to 10.0. The distal pole of the scaphoid still penetrated the trapezium (A), but this only occurred after +12°. Prior to this point, the scaphoid was displaying the expected out-of-plane rotation. Run time: 26h 35m.

6.1.6.2 Run #R2

For run #R2, the intersection penalty was increased from 1.0 to 10.0 (see Figure 139). For the first 10 degrees of movement, the scaphoid was seen to rotate out of the plane of the page to avoid the trapezium descending towards its distal pole. However, after this point, its smooth out-of plane rotation ceased and the distal pole became embedded in the trapezium as was observed in run #R1. During the ulnar deviation runs, increasing the resolution of the model (both in terms of decreasing the step-size and using more detailed models) was found to be more effective in reducing intersection and improving performance generally. Therefore, the weighting-adjustment strategy was abandoned in favour of resolution increase.

6.1.6.3 Run #R3

For run #R3, the cost-function values were kept the same as for run #R1, but the movement increment was reduced from 1.0° to 0.5° (see Figure 140). While the scaphoid still collided with the trapezium and trapezoid, this only occurred after around 30 increments of movement. Up until this point, the behaviour was closer to the actual movement of the bone than for run #R2. This is because the concave region of the scaphoid maintained a much closer level of contact with the proximal ball of the capitate than for the previous runs. However, the characteristic lateral to medial sliding of the lunate across the face of the radius was entirely absent.

6.1.6.4 Run #R4

Given that the best results of all ulnar deviation runs were obtained using the higher resolution bone-models, for run #R4, the model resolution was set to 10.0% instead of 4.8% (see Figure 141). The increment of movement was returned to 1.0 degree and all cost-function weightings were as per run #U2. Despite the improvements afforded by this strategy in the ulnar deviation case, no improvement was found for radial deviation. The scaphoid exhibited very little out-of plane movement and collided with the trapezium and trapezoid at around +15° of radial deviation.

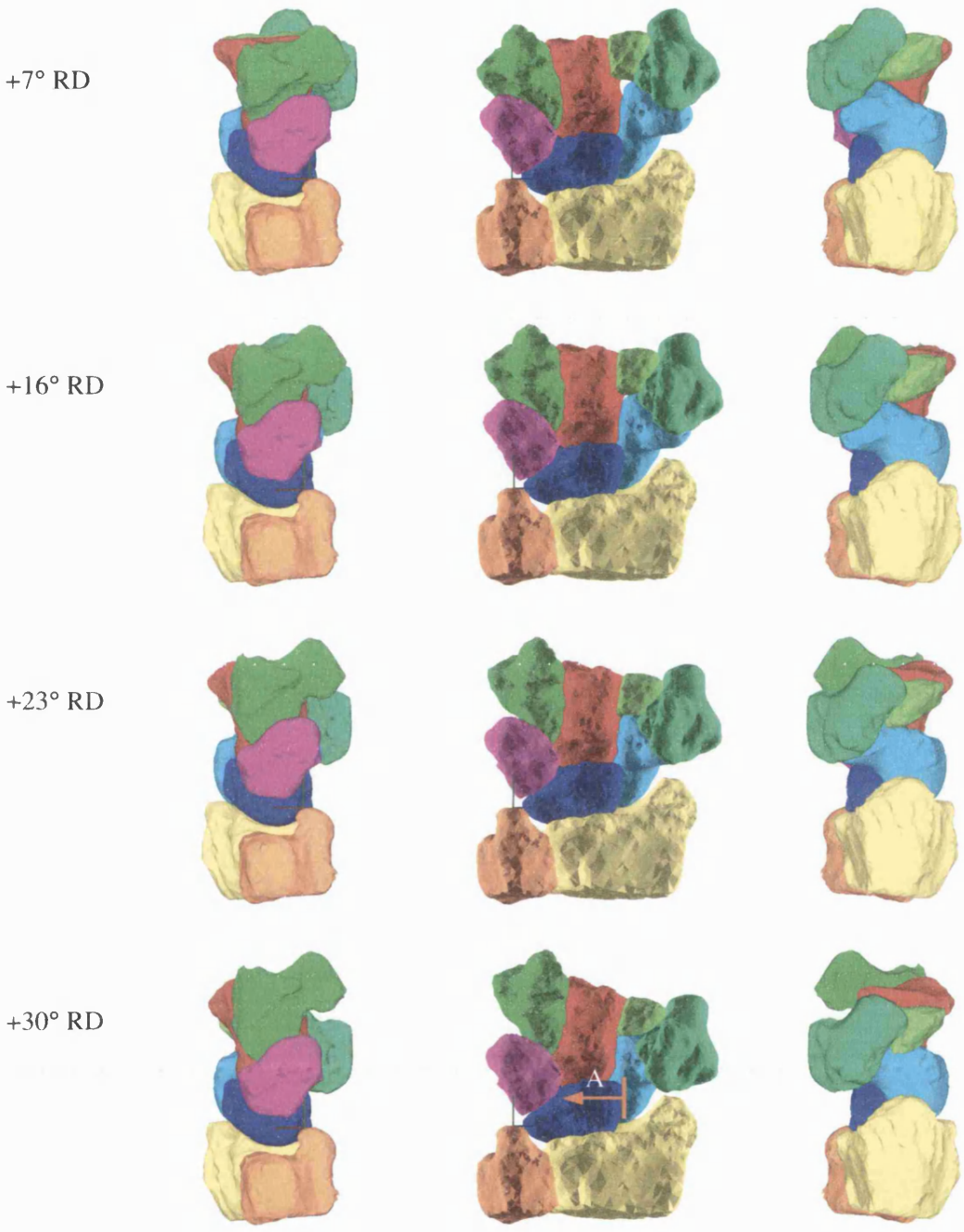

Figure 140 Run #R3 showing the effect of reducing the increment of applied motion from 1.0 to 0.5 degrees. The scaphoid flexed correctly out of the page, but after 15°, collided with the trapezium as in run #R2. The scaphoid remained in closer contact with the capitate throughout than in run #R2. A: No overall lateral to medial sliding of the lunate occurred. Run time: 41h 43m.

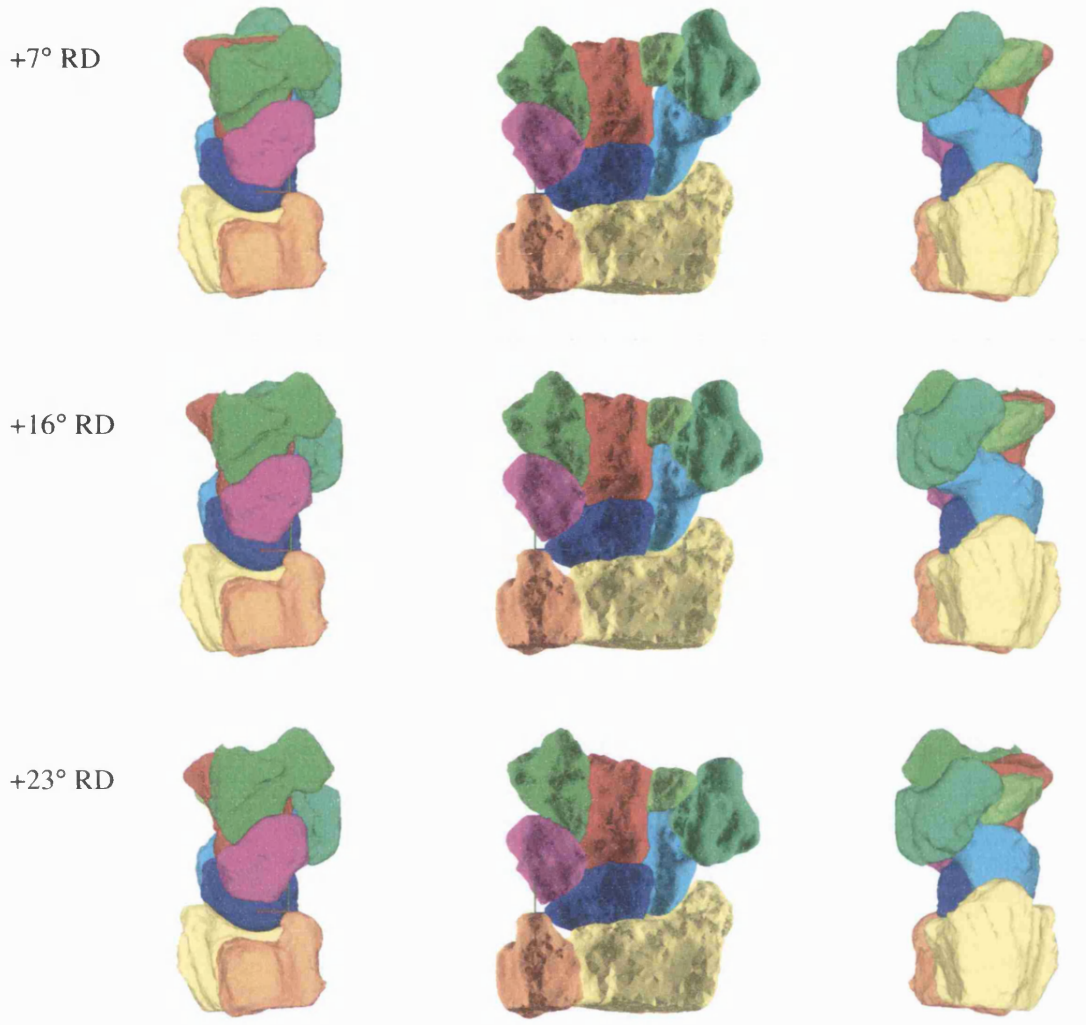

Figure 141 Run #R4 showing the effect of using 10% instead of 4.8% resolution models. The lunate did not translate along the radius and the scaphoid-trapezium collision problem persisted. The run was aborted at +27°. Run time: 62h 49m.

6.1.6.5 Run #R5

In attempting to improve performance of the model in radial deviation, several strategies involving minor adjustments to the CARPAC algorithm were tried, but with limited success. Therefore a more radical idea was tested for run #R5.

The Lunate Problem

A possible cause for the problems encountered was identified as the lunate-radius interface. The lunate is known to translate in a lateral-to-medial direction across the face of the radius during radial deviation (see Figure 22). In so doing, its contact with the radius diminishes. However, as the lunate slides off the medial side of the radius, it slides onto a soft-tissue structure known as the triangular fibrocartilage complex (TFCC) (see section 3.8.3.6 and Figure 27 for further explanation).

The TFCC was not initially included in the CARPAC model. Consequently, as the lunate slides across the radius towards the ulna, its area of contact with the radius diminishes and there is no compensatory support from a TFCC analogue. This may explain why none of the predicted results so far have shown ulnarward sliding of the lunate.

It was reasoned that if the surface of the radius were extended on the ulnar side to simulate the TFCC contact, then the reluctance of the lunate to slide ulnarward would be overcome. To this end, the radius bone model was modified. Working in AutoCAD, the non-articular regions of the model were erased and a section of the surface was copied twice to create the extension ledge. This was performed on the 4.8% resolution models only. The gaps between original surface and extensions were filled using Points2Polys to form a continuous surface (see Figure 142, Figure 143). The results of run #R5 are shown in Figure 144.

The results from run #R5 were much the same as for previous runs. Despite the additional surface on the radius, the lunate did not slide ulnarward as was hoped and the scaphoid-trapezium collision problem remained. Even with the intersection penalty increased from 1.0 to 10.0 (run #R6, see Figure 145), the problem persisted. At this point, it was decided to cease testing because all reasonable approaches had been tested without success.

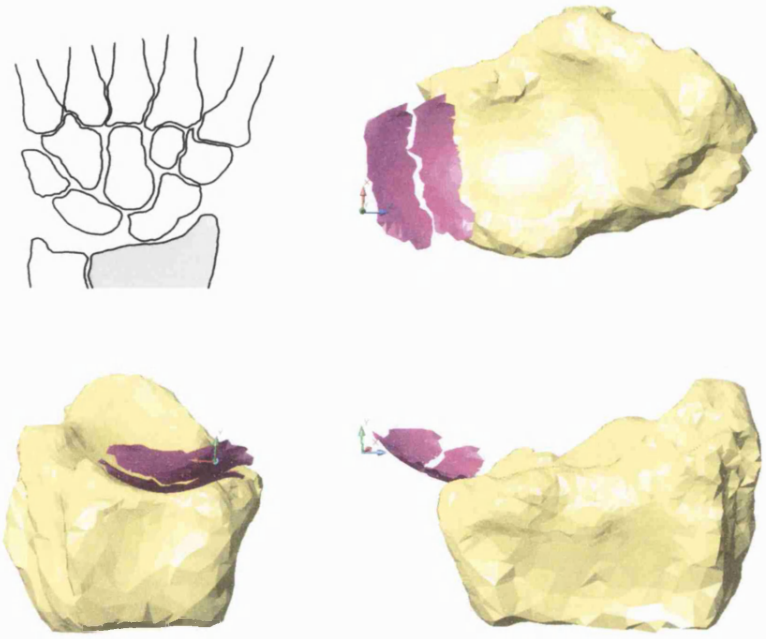

Figure 142 The radius was modified to simulate the triangular fibrocartilage complex. Its medial surface was extended by copying a section of the existing surface.

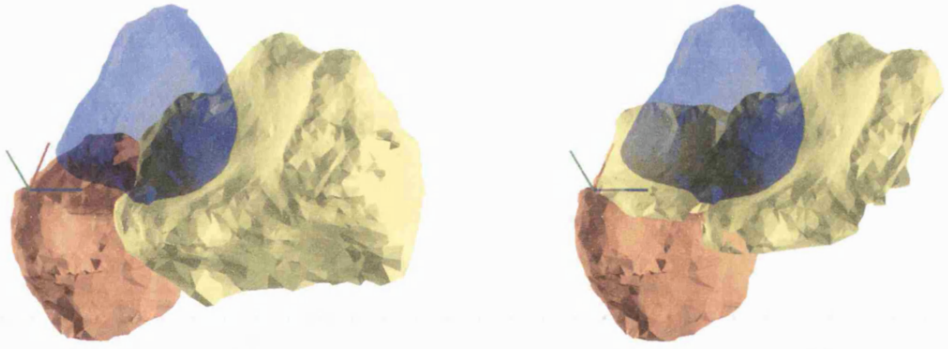

Figure 143 Appearance of the original (a) and modified (b) radius in SWORDS. The non-articular surface regions of the radius were removed and the gaps between the extensions were removed.

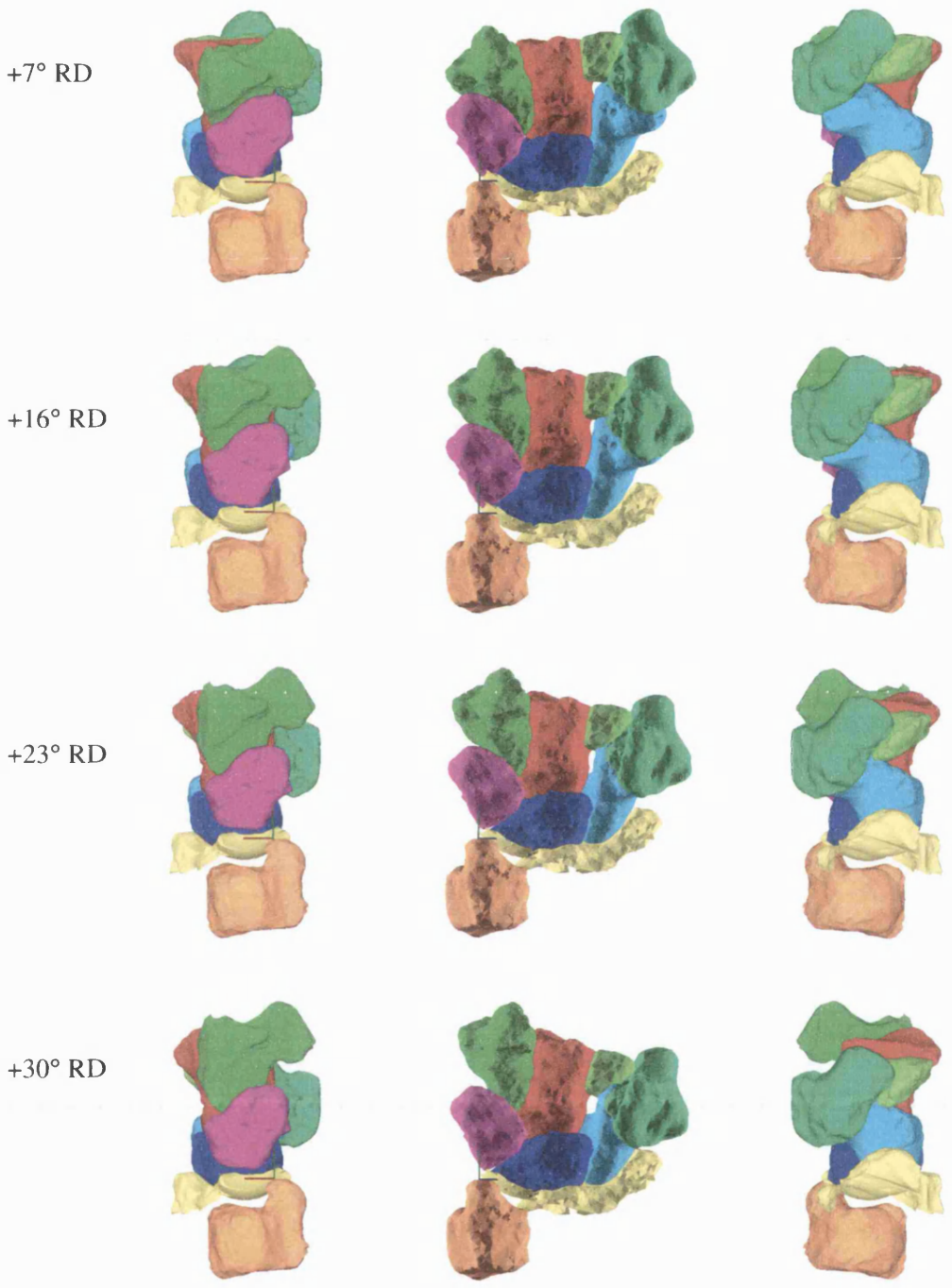

Figure 144 Run #R5 showing the effect of replacing the original radius model with the medially-extended version. Run time: 18h 57m.

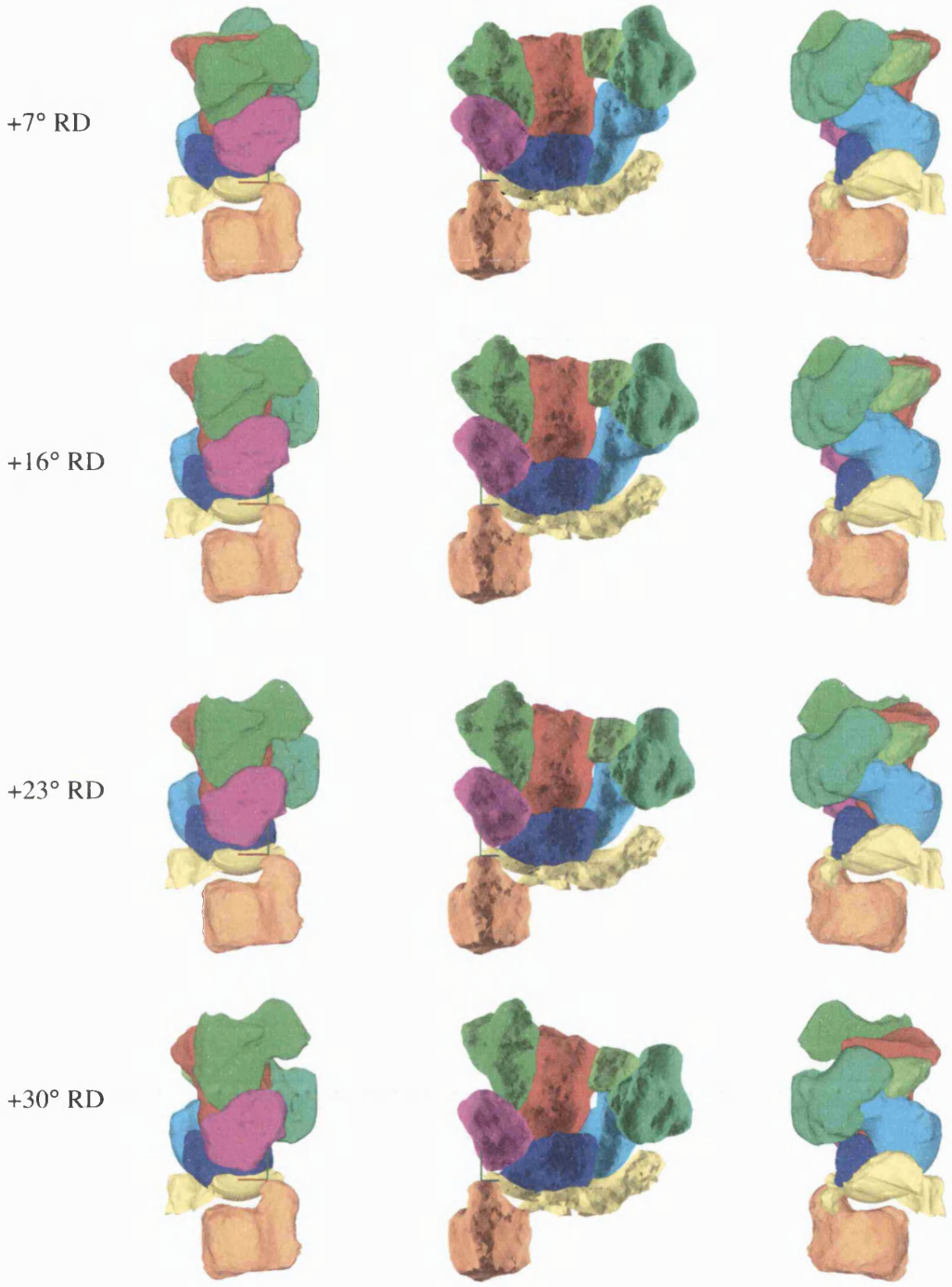

Figure 145 Run #R6 - as run #R5 but with intersection penalty increased from 1.0 to 10.0. The scaphoid still collided with the trapezium. Run time: 17h 15m.

6.2 CT Reconstructed Bones

The CARPAC algorithm was applied to the bones obtained from a reconstructive CT study (see 5.2) (Snel *et al.*, 2000).

In order to account for the variation in cartilage thickness, the results of the separation distance study (see Table 1, section 5.2.3) were used to individually weight all pairs of contacting surfaces.

The starting position common to both radial and ulnar deviation runs is shown in Figure 146.

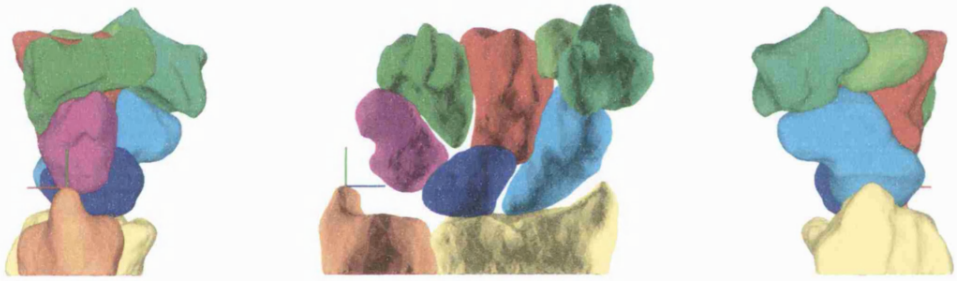

(a) (b) (c)

Figure 146 The starting position common to all runs with the CT reconstructed bones.

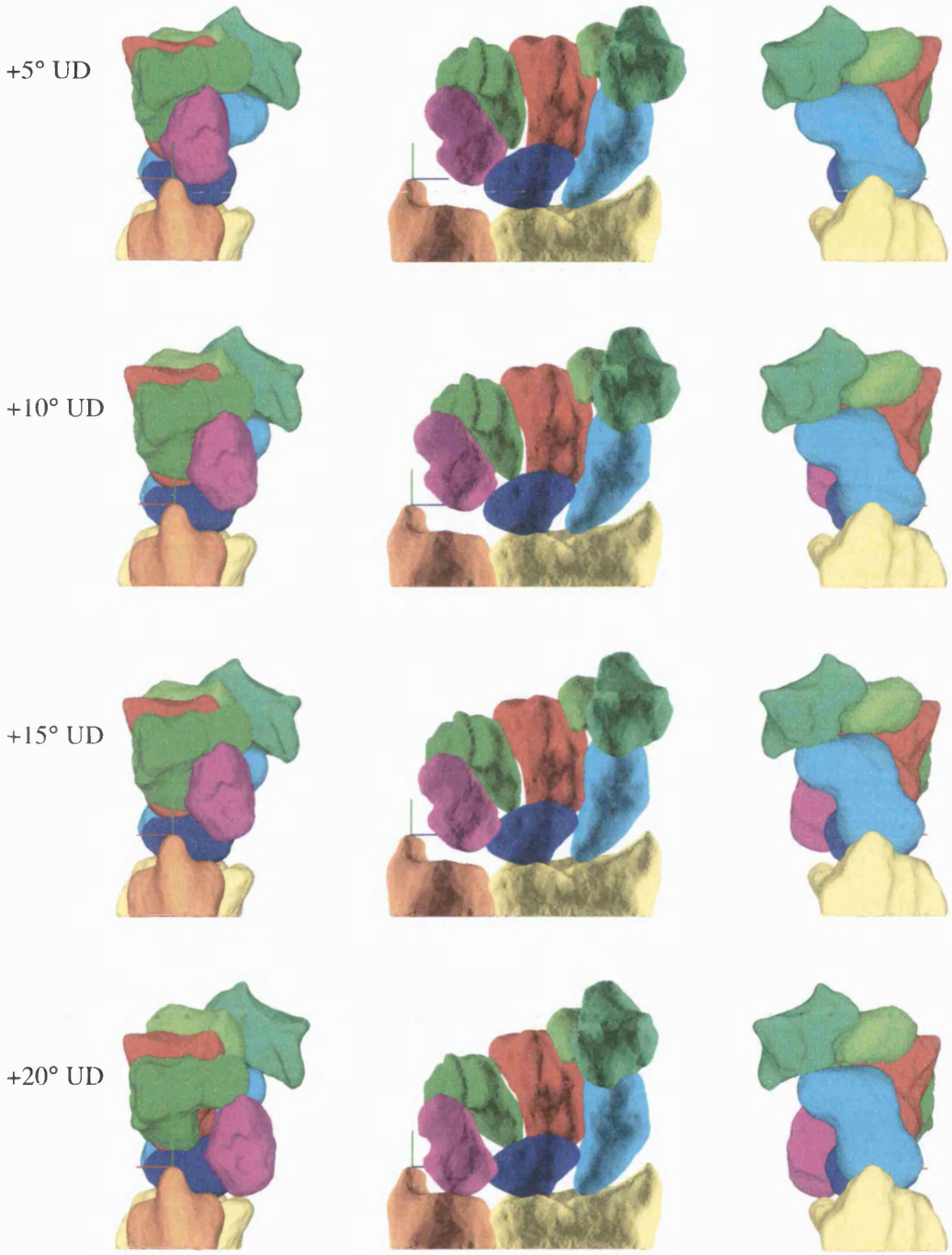

Figure 147 Run #U1 showing predicted movement of the CT reconstructed bones for 0-20 degrees ulnar deviation.

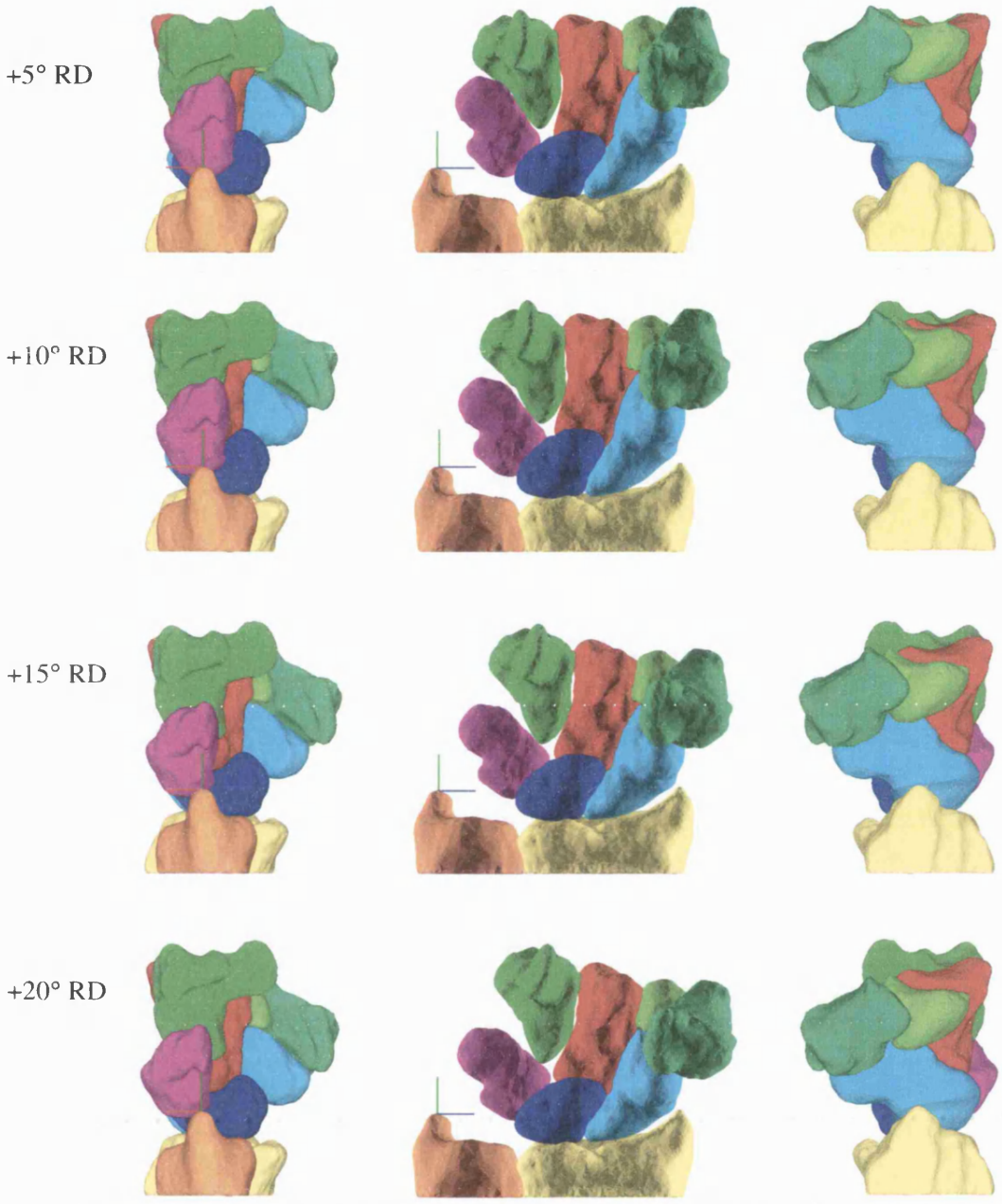

Figure 148 Run #R1 showing predicted movement of the CT reconstructed bones for 0-20 degrees of radial deviation.

The results of these runs were generally not as good as good as for the laser-scanned bones.

6.2.1 Ulnar Deviation

In ulnar deviation, the scaphoid was seen to extend correctly. However, the air-gap between capitate and scaphoid expanded from around 1.0mm at the start of the run to nearer 3mm at the end. Conversely, the gap between the trapezium and the distal end of the scaphoid decreased until the two surfaces were almost touching.

The lunate underwent very little sliding across the face of the radius and did not appreciably alter its orientation. Consequently, poor contact was made with the proximal scaphoid where the two surfaces should have remained parallel to one another.

The triquetrum migrated by around 10mm in a dorsal-to-palmar direction and maintained only very poor contact with the hamate and lunate. Furthermore, it impinged upon the ulna and did not undergo any significant reorientation.

6.2.2 Radial Deviation

In radial deviation, the scaphoid flexed as expected and made good contact with the lunate. The lunate did not change its position or orientation appreciably. The triquetrum maintained contact with the lunate, but became detached from the hamate.

6.2.3 Summary

It was ultimately decided to abandon testing on the CT reconstructed bones due to the poor quality of the results in comparison to the laser-scanned bones. When models that included cartilage were available, it was considered fruitless persevering with a set of models without cartilage.

7 RESULTS ANALYSIS

Results Analysis

This section describes, using finite helical axis analysis, the predicted movement-patterns resulting from the best two runs with the laser-scanned bone models. These were run #U10 in ulnar deviation and run #R3 in radial deviation. For run #R3, only the first 10° of movement were analysed because after this point, collision between scaphoid and trapezium increased markedly.

The key results are summarised and compared to experimental findings in section 7.5. When comparing the results quantitatively, it is worth bearing in mind the naturally high level of scatter associated with biological data (see Figure 15 for an example of this).

7.1 Capitate-Hamate-Trapezium-Trapezoid Complex

7.1.1 Ulnar Deviation

In ulnar deviation, the output complex showed little motion other than the rotation that was applied about the x-axis, despite having five degrees of freedom. Finite helical axes were computed for the movement. These are illustrated in Figure 149. With the exception of three increments of movement, all the FHAs pass through the centroid of the bone. This is the point about which rotations were applied. The results do not agree with experimental studies, which tend to place the axes nearer the proximal end of the bone. For comparison, the positions of the FHAs from an experimental study (Neu *et al.*, 2001) are shown in Figure 151.

The three axes that do not pass through the centroid point occurred at 4.0, 7.0 and 17.0 degrees of ulnar deviation. At these points, the bone was undergoing small amounts of supination in addition to ulnar deviation. The total amount of supination was 2.5°. However, the experimental results from Moojen *et al.* (2002a) reveal 8.9° (SD 3.3°) of pronation of the capitate at 20° ulnar deviation.

7.1.2 Radial Deviation

In radial deviation, there was no movement of the output complex except the applied rotations. This is indicated in Figure 150, which shows all FHAs passing through the centroid point.

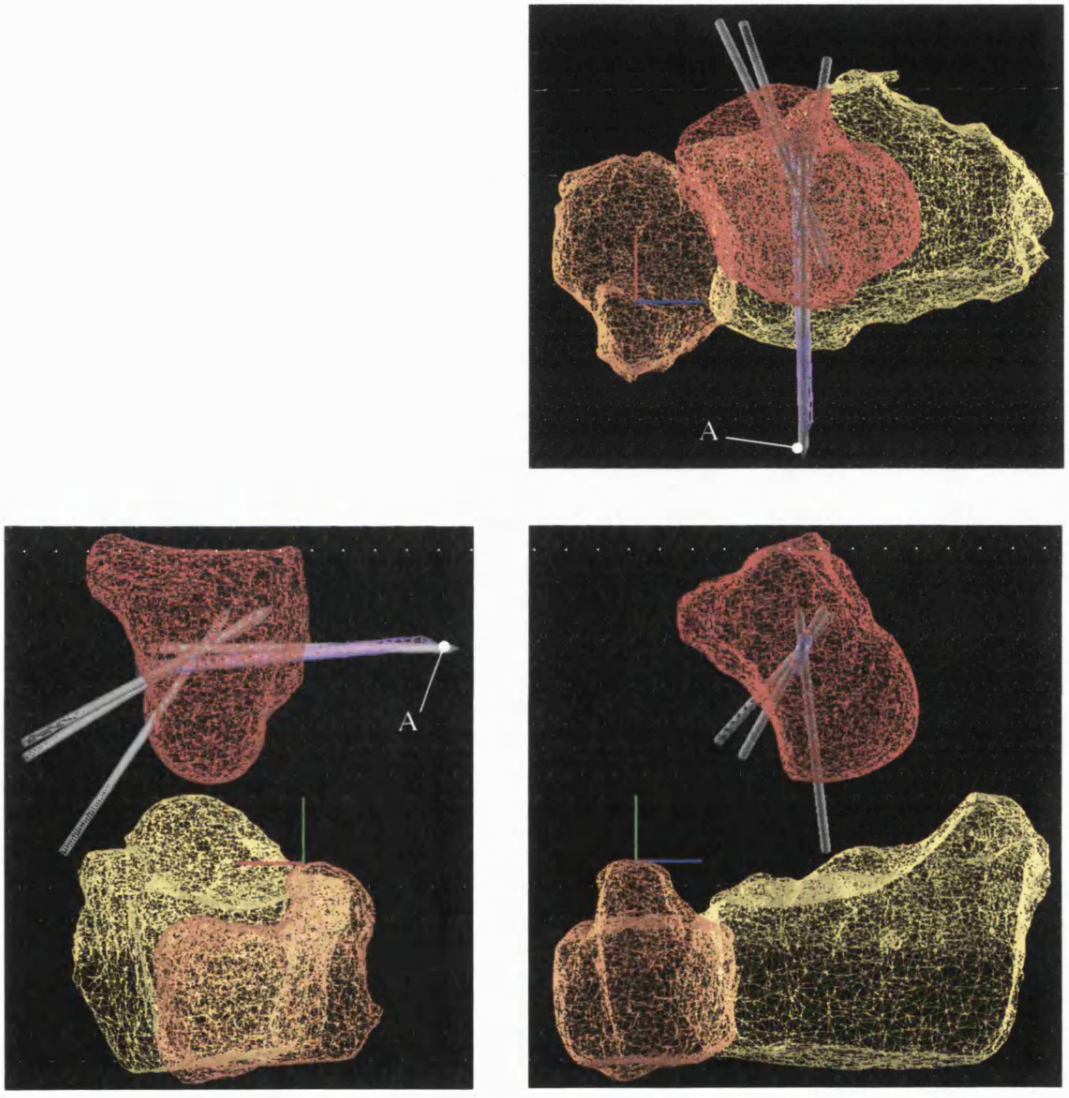

Figure 149 Movement of the capitate in ulnar deviation showing finite helical axis locations computed at 1.0° increments of movement (grey) and mean finite helical axis (magenta). A: Multiple FHAs located here.

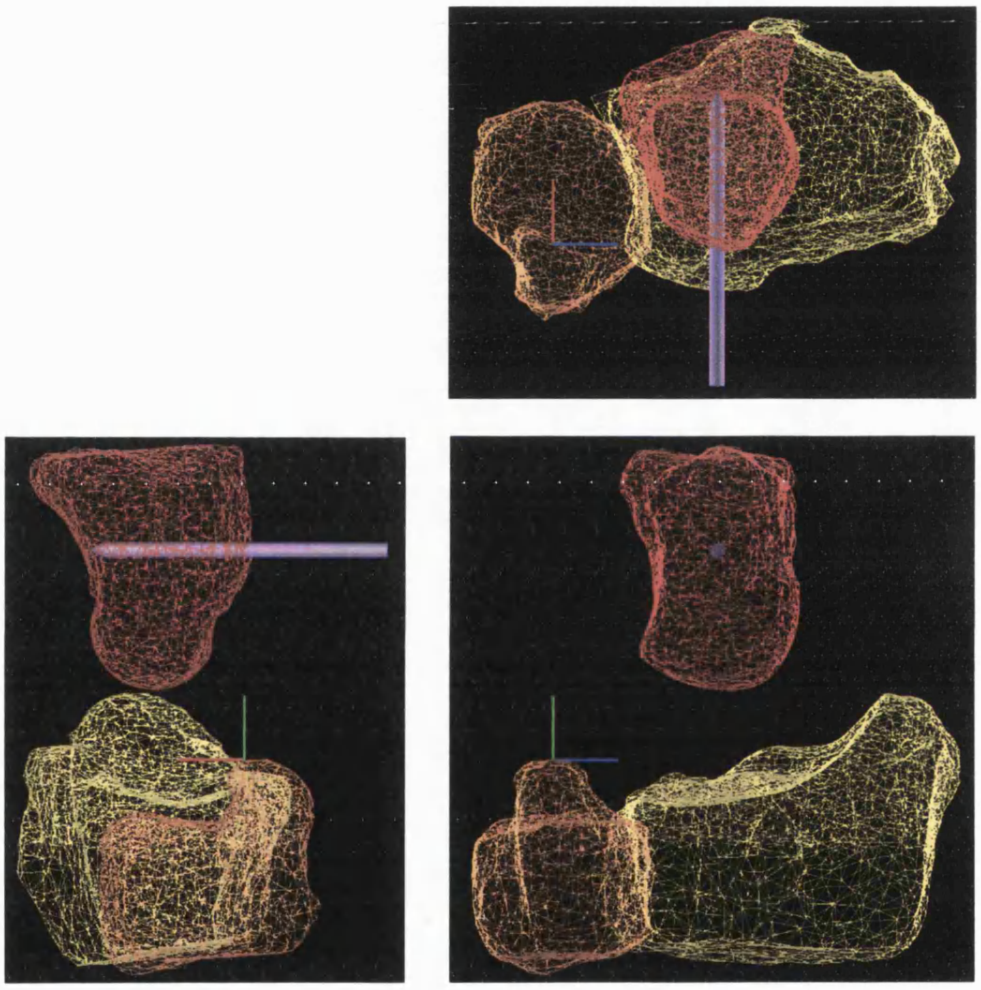

Figure 150 Finite helical axis positions for 0-10 radial deviation. There was no movement of the output complex except for the applied rotations. Therefore, all axes were coincident.

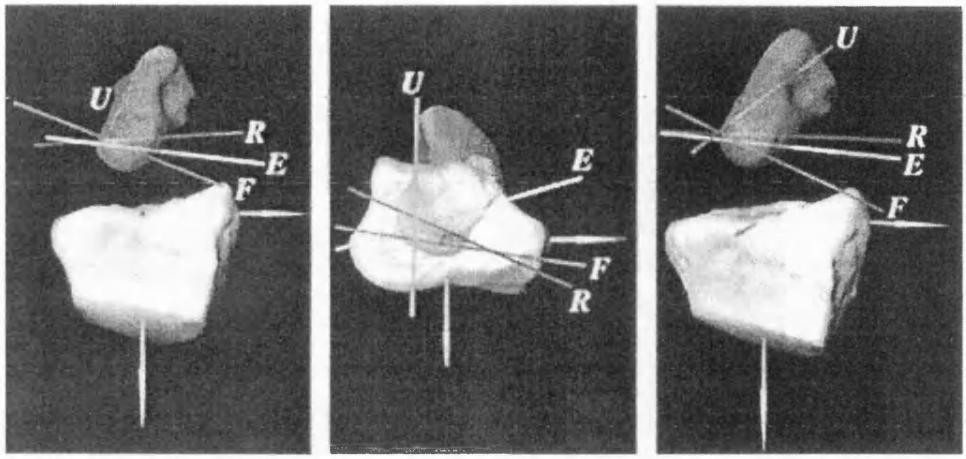

Figure 151 Finite helical axis placement from an experimental study (Neu *et al.*, 2001). U=FHA location for the capitate in ulnar deviation. R=FHA location in radial deviation. The axes pass through the proximal pole of the bone.

7.2 Lunate

Unlike the capitate, upon which rotations were imposed, movement of the lunate was entirely under the control of the optimisation algorithm.

7.2.1 Ulnar Deviation

In ulnar deviation, the lunate was observed to slide towards the lateral side of the radius, away from the ulna. This is in agreement with experimental studies. The total lateral displacement was 2.9mm. The lateral sliding reported by Moojen *et al.* (2002a) was also 2.9mm (SD 0.9mm), although it must be stressed that these results came from a different wrist and the fact that these two figures are identical is likely to be pure coincidence. In addition to sliding, the lunate underwent 2.4° of flexion. This is in the opposite direction to that in which the lunate is known to move. Moojen *et al.* reported that the lunate extended by 24.2° (SD 11.2°) during a global wrist angle of 20° ulnar deviation. The bone also underwent 5.6° of supination, which does not agree with the 2.6° (SD 6.7°) of pronation reported by Moojen *et al.*

7.2.2 Radial Deviation

As stated in section 6.1.6.3, the lunate remained virtually motionless throughout the run. Small perturbations occurred, but the bone made no overall movement in any direction. The finite helical axis locations are shown in Figure 153. By contrast, Moojen *et al.* reported 8.0° (SD 5.1°) of flexion and 0.5mm (SD 0.7mm) of displacement in the negative-z direction during radial deviation.

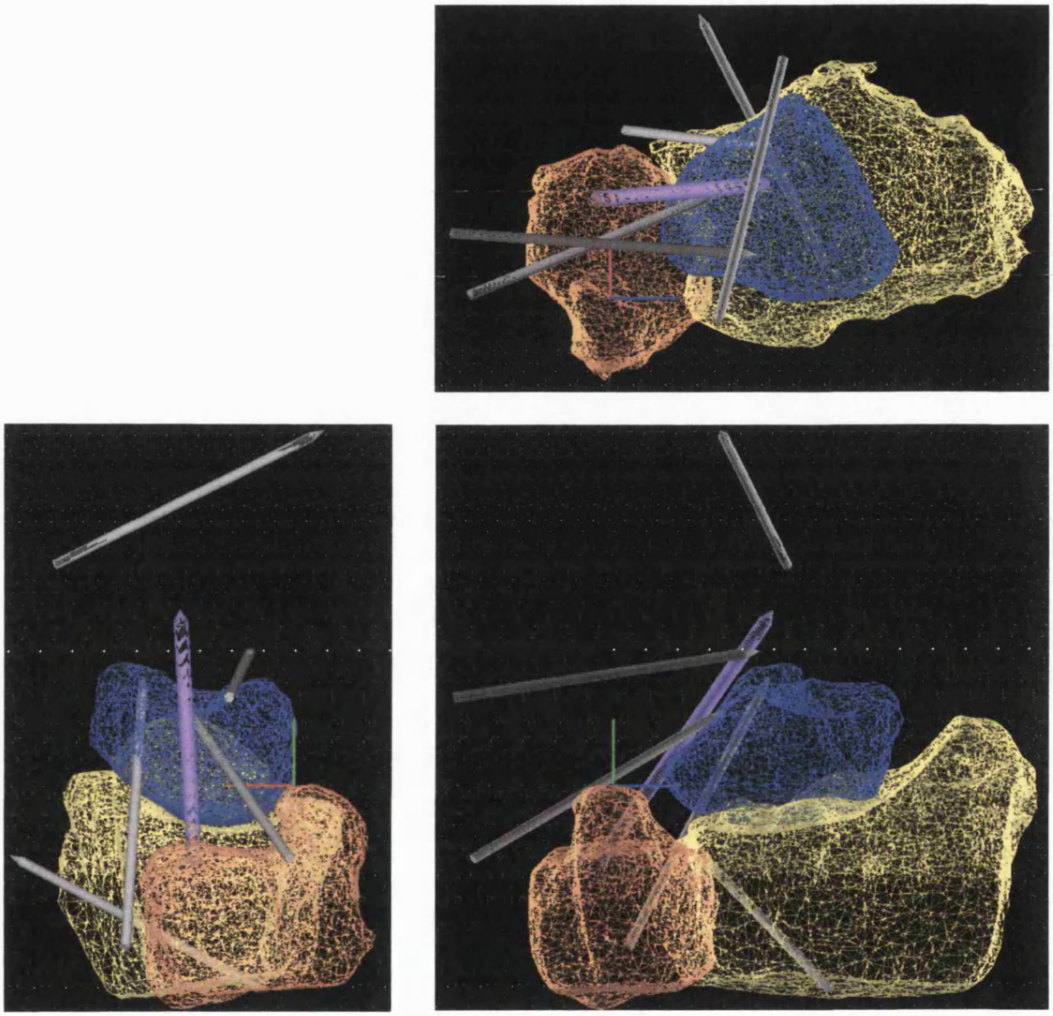

Figure 152 Finite helical axes for lunate motion in ulnar deviation plotted every 4th degree of capitate rotation to obtain an averaging effect. While there is still a great amount of scatter, the axes tend to point in a medial to lateral (positive z) direction, which reflects the sliding of the lunate away from the ulna across the radius and its clockwise rotation about the z-axis.

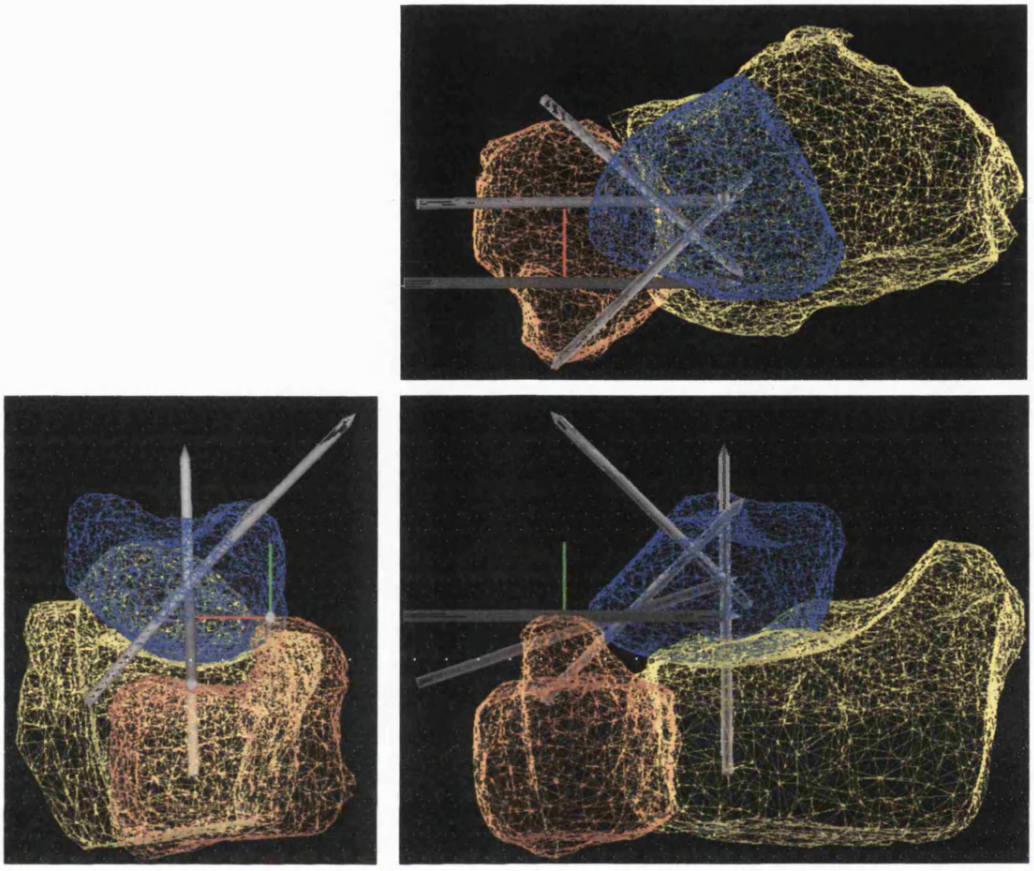

Figure 153 Finite helical axis locations for the lunate during 10° of radial deviation. Axes plotted for every 2nd increment of capitate motion. The axes are highly scattered which reflects the fact that the bone underwent minor positional adjustments in seemingly random directions but made very little overall excursion.

7.3 Scaphoid

The most successful results were obtained for the Scaphoid, especially in ulnar deviation.

7.3.1 Ulnar Deviation

The scaphoid demonstrated continuous extension during ulnar deviation. This is illustrated by the fact that in Figure 154, the FHAs all point in roughly the same direction. The magnitude of extension was 14.3°. An experimental study of scaphoid kinematics in 11 volunteers (Moojen *et al.*, 2002b) showed the scaphoid to extend by 20.4° (SD 10.7°) during 20° of ulnar deviation. Another study observed a mean extension of 12° (SD 29°) in 20 volunteers (Feipel and Rooze, 1999). Given the high level of scatter typical of biological data, the results appear to correlate well with these two studies.

The amount of ulnar deviation of the bone was 7.3°, which is similar to the 10.0° (SD 4.2°) reported by Moojen *et al.*

7.3.2 Radial Deviation

In radial deviation (Figure 155), the scaphoid flexed but the movement was not as smooth as for ulnar deviation. This is reflected by the greater level of scatter between the FHA locations. With the wrist in 10° of radial deviation, the total out-of-plane rotation was 6.4° of flexion, which is similar to the 8.1° (SD 4.8°) reported by Moojen *et al.* at the same point.

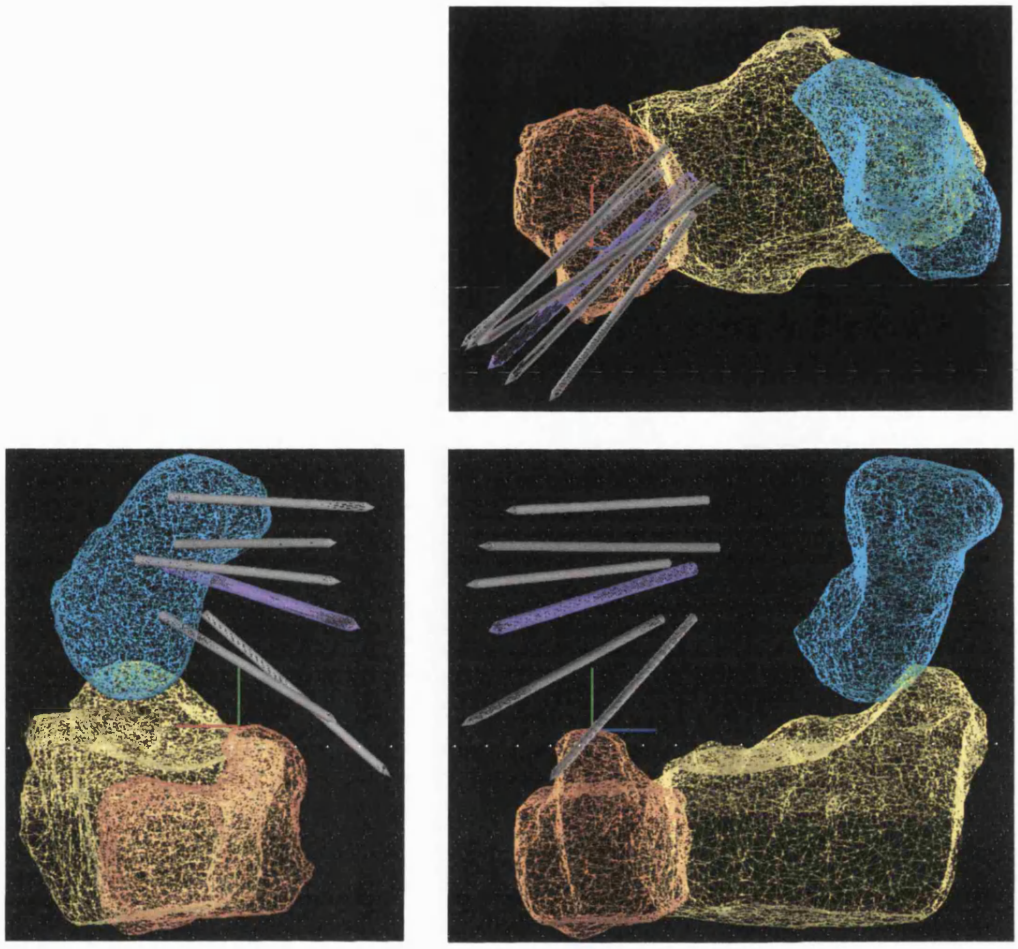

Figure 154 Finite helical axis locations for the scaphoid in ulnar deviation. Axes plotted every fourth increment of movement.

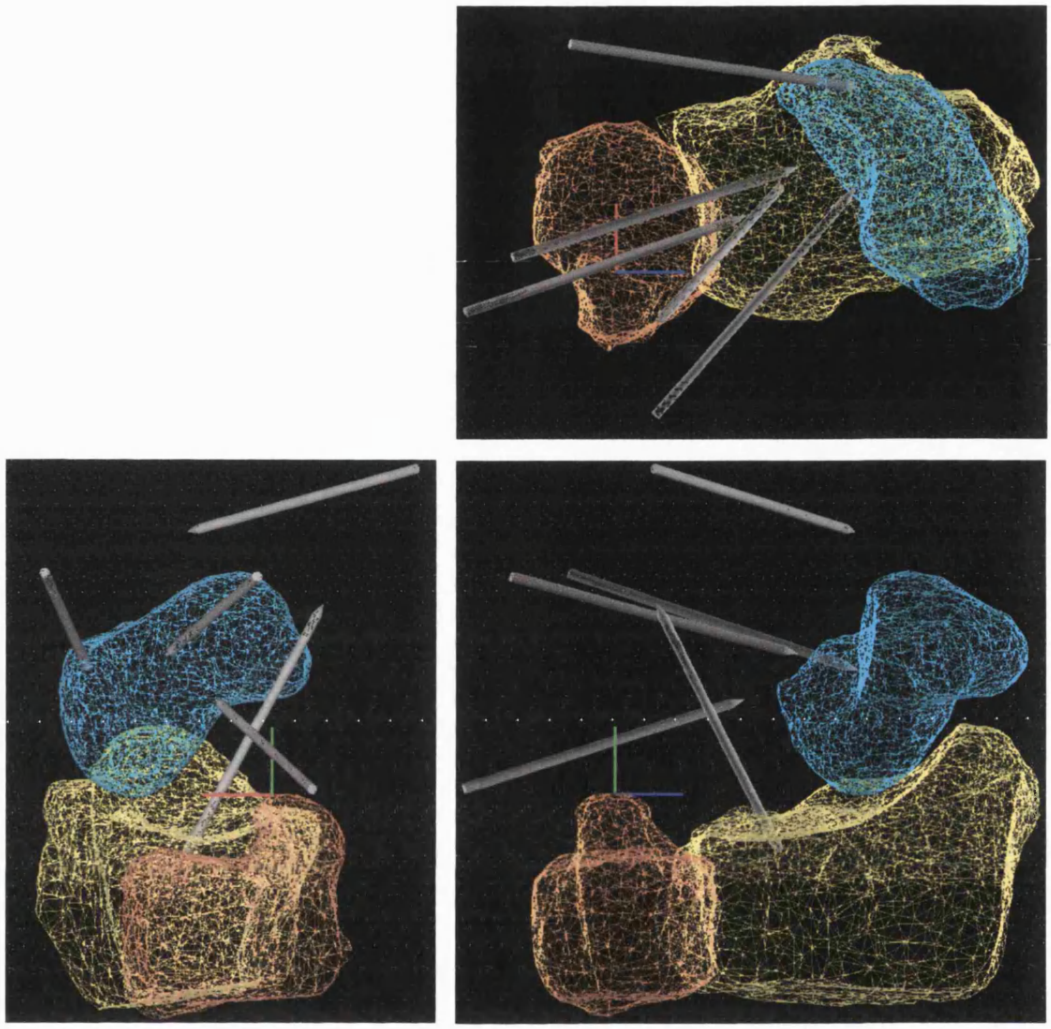

Figure 155 Finite helical axis locations for the scaphoid in 10° of radial deviation. Axes plotted every second increment of capitate rotation.

7.4 Triquetrum

The behaviour of the triquetrum most closely matched experimental results when the output complex was radially deviated.

7.4.1 Ulnar Deviation

The triquetrum underwent rotation in the same sense as the output complex. This is indicated in Figure 156 by the fact that all FHAs have a component pointing in the negative-x direction. The bone underwent 10.6° of ulnar deviation, which compares favourably to the 13.9° reported by Moojen *et al.* (2002b). There was also 3.7° of supination (clockwise rotation about the y-axis), which does not agree with the 2.6° of pronation reported by Moojen *et al.* The bone was also found to slip up the medial surface of the hamate while its absolute position moved in a proximal direction, although it is more difficult to show this from the finite helical axes. The combination of distal-to-proximal sliding with supination indicates a helical movement, which was reported by Weber *et al* (1984).

7.4.2 Radial Deviation

In radial deviation, the triquetrum was seen to undergo 1.8° of pronation, which does not match the 0.6° of supination reported by Moojen *et al.* This is reflected by the fact that four out of five of the FHAs have a strong component in the negative y direction.

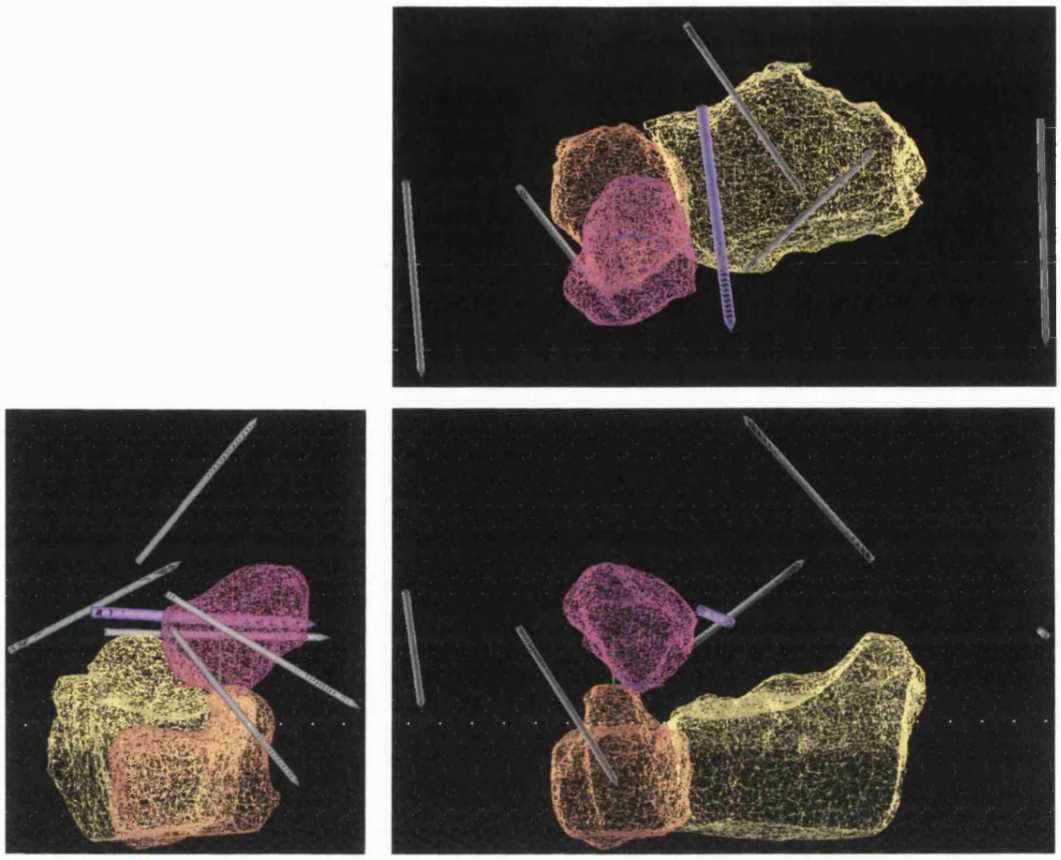

Figure 156 Finite helical axis locations for the triquetrum in ulnar deviation. Axes plotted every fourth increment of movement.

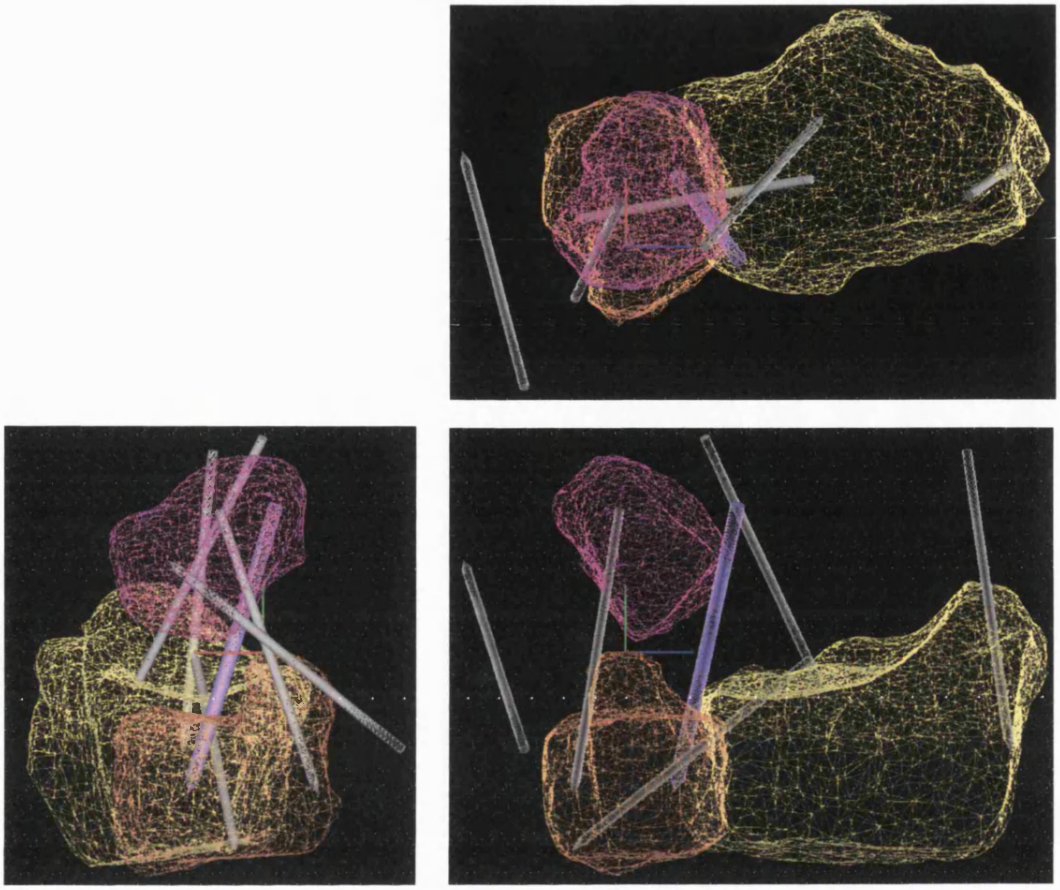

Figure 157 Finite helical axis locations for the triquetrum in radial deviation. Axes plotted every second increment of capitate rotation. Four out of five of the FHAs have a strong component in the negative y direction reflecting the small helical movements of the bone.

7.5 Results Summary

The sign-convention for rotations described in this section is as follows:

Flexion	Extension	Radial-dev	Ulnar-dev	Supination	Pronation
+ve	-ve	+ve	-ve	+ve	-ve

Table 6 Sign convention for carpal bone rotations

	Flexion			Deviation			Pro/Supination		
	P	M	(SD)	P	M	(SD)	P	M	(SD)
Capitate									
20° UD	-0.9	-3.7	(5.1)	-20.0	-20.0	(0.0)	2.5	-8.9	(3.3)
10° RD	0.0	-0.3	(4.2)	10.0	10.0	(0.0)	0.0	3.7	(2.8)
Lunate									
20° UD	2.3	-24.2	(11.2)	0.5	-11.3	(2.8)	5.6	-26.0	(6.7)
10° RD	-1.0	8.0	(5.1)	-1.0	2.9	(1.9)	2.0	0.2	(2.3)
Scaphoid									
20° UD	-14.0	-20.4	(10.7)	-7.1	-10.0	(4.2)	0.3	-4.2	(5.9)
10° RD	6.4	8.1	(4.8)	5.3	3.0	(1.8)	6.4	-0.1	(2.4)
Triquetrum									
20° UD	1.1	-20.1	(9.8)	-10.5	-13.9	(4.1)	3.8	-2.6	(6.5)
10° RD	-1.3	5.0	(4.5)	-1.8	6.1	(1.5)	-1.9	0.6	(2.0)

Table 7 Comparing the predicted results (P) with those from a CT study of 11 normal wrists (M) (Moojen *et al.*, 2002a). UD = ulnar deviation, RD = radial deviation.

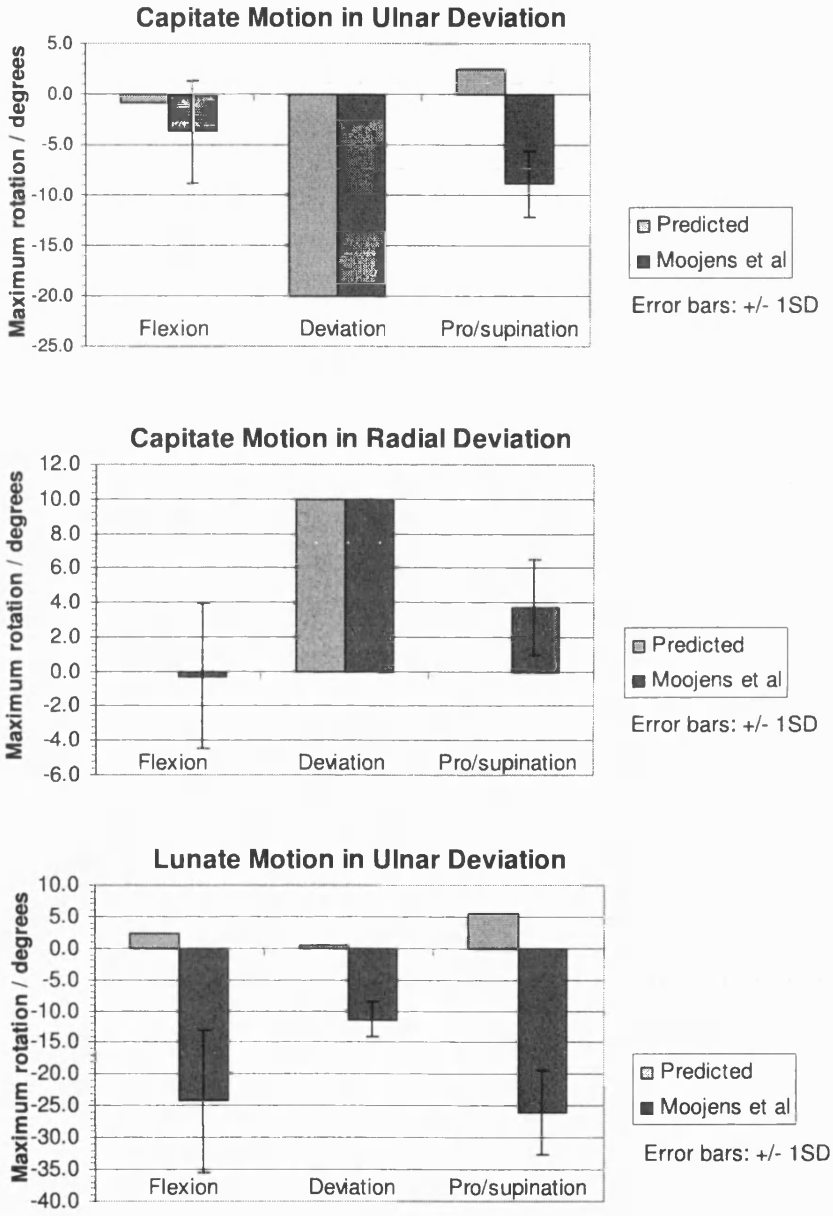
Capitate Motion in Ulnar Deviation
Maximum rotation / degrees
5.0
0.0
-5.0
-10.0
-15.0
-20.0
-25.0
Flexion
Deviation
Pro/supination
Predicted
Moojens et al
Error bars: +/- 1SD
Capitate Motion in Radial Deviation
Maximum rotation / degrees
12.0
10.0
8.0
6.0
4.0
2.0
0.0
-2.0
-4.0
-6.0
Flexion
Deviation
Pro/supination
Predicted
Moojens et al
Error bars: +/- 1SD
Lunate Motion in Ulnar Deviation
Maximum rotation / degrees
10.0
5.0
0.0
-5.0
-10.0
-15.0
-20.0
-25.0
-30.0
-35.0
-40.0
Flexion
Deviation
Pro/supination
Predicted
Moojens et al
Error bars: +/- 1SD

Figure 158

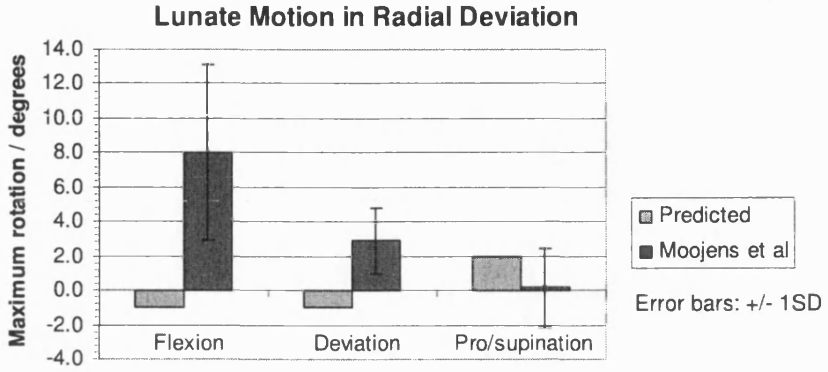
Lunate Motion in Radial Deviation
Maximum rotation / degrees
14.0
12.0
10.0
8.0
6.0
4.0
2.0
0.0
-2.0
-4.0
Flexion
Deviation
Pro/supination
Predicted
Moojens et al
Error bars: +/- 1SD

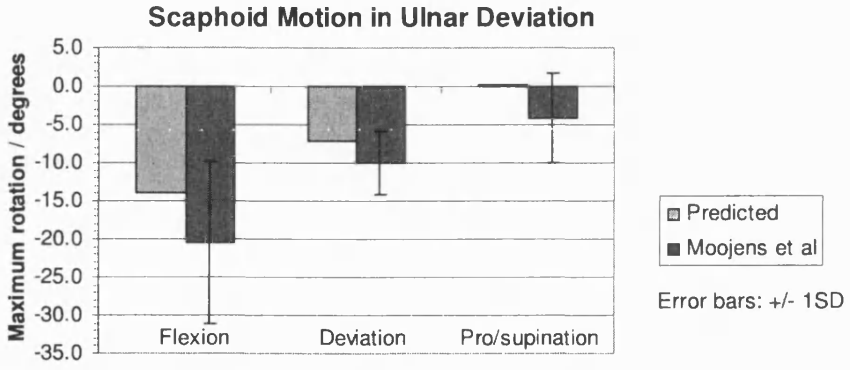
Scaphoid Motion in Ulnar Deviation
Maximum rotation / degrees
5.0
0.0
-5.0
-10.0
-15.0
-20.0
-25.0
-30.0
-35.0
Flexion
Deviation
Pro/supination
Predicted
Moojens et al
Error bars: +/- 1SD

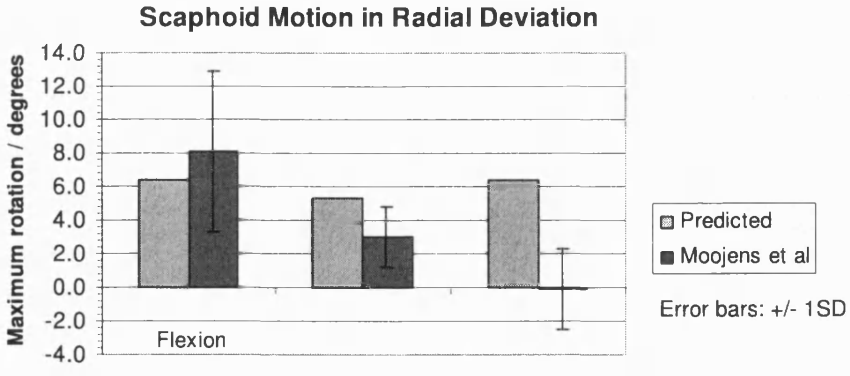
Scaphoid Motion in Radial Deviation
Maximum rotation / degrees
14.0
12.0
10.0
8.0
6.0
4.0
2.0
0.0
-2.0
-4.0
Flexion
Predicted
Moojens et al
Error bars: +/- 1SD

Figure 159

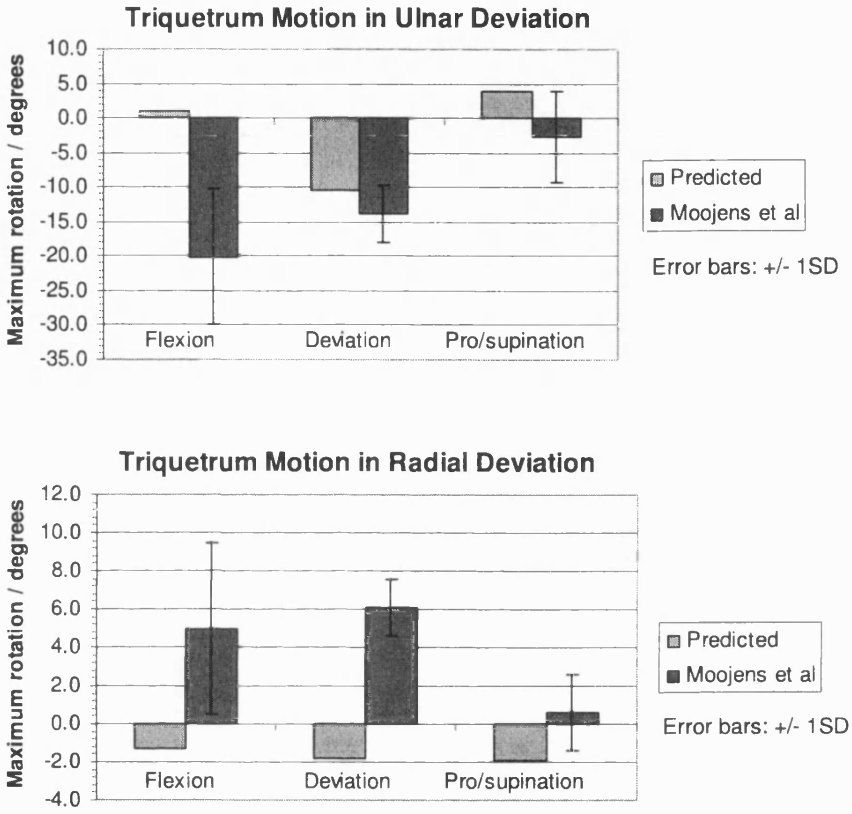
Triquetrum Motion in Ulnar Deviation
Maximum rotation / degrees
10.0
5.0
0.0
-5.0
-10.0
-15.0
-20.0
-25.0
-30.0
-35.0
Flexion
Deviation
Pro/supination
Predicted
Moojens et al
Error bars: +/- 1SD
Triquetrum Motion in Radial Deviation
Maximum rotation / degrees
12.0
10.0
8.0
6.0
4.0
2.0
0.0
-2.0
-4.0
Flexion
Deviation
Pro/supination
Predicted
Moojens et al
Error bars: +/- 1SD

Figure 160

8 DISCUSSION

Discussion

The CARPAC algorithm correctly predicted certain aspects of the complex behaviour of the carpal bones. The results for the scaphoid in particular closely matched the characteristic movements of this bone. Some, but not all aspects of the behaviour of the lunate and triquetrum also matched experimental observations.

Given the fact that the only information available to the algorithm was the shape of the bones (although 90% of the detail was lost), the overall results of the study are encouraging. This was an ambitious piece of research into one of the most complicated and poorly understood of all the joints. Therefore, it is not surprising that certain aspects of carpal behaviour were *not* correctly predicted – indeed this was expected.

The purpose of this section is to critically assess the various stages of the project and to discuss means by which the outcome could be improved. This section also includes suggestions for further work where appropriate.

Areas discussed in this section are categorised in the following broad sections:

- Model acquisition
- Anatomical considerations
- Cost function
- Optimisation
- Kinematics

8.1 Model Acquisition

Several options were available for obtaining the three-dimensional models of the carpal bones. The laser-scanning method was ultimately decided upon because it offered the best ratio of surface detail to cost of acquisition. However, there were several disadvantages associated with this method and these are discussed below.

8.1.1 Marker Pins

Three pins were inserted into each bone to enable anatomical positions to be recorded. While care was taken to place these in regions away from the main articular surfaces, it was inevitable that some would lie in sensitive locations. Removal of the pins from the computer models left holes in the triangular mesh where the shafts had entered the body of the bone. It is possible that some artefacts were introduced during the closure of these holes.

An alternative approach to using three discrete pins would have been to use a single structure having three separate reference points (Figure 161). This would have reduced by two thirds the number of holes in the mesh. However, in order to avoid misalignment errors, it would have been crucial to obtain a firm, immobile anchorage point in the bone. This may have required a larger-diameter shaft. So in effect, three small holes would have been replaced by a single larger one.

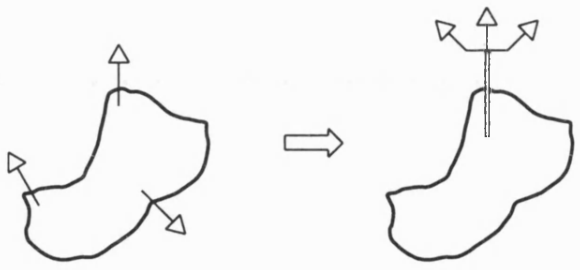

Figure 161 Replacing three discrete marker pins with a single three-pronged structure would minimise loss of surface detail but a firm anchor would be essential to maintain accuracy.

Marker digitisation was performed twice and mean values were taken. The error in the digitised location of marker tips was found to be +/-1mm. This value is large in comparison to the size of the bones and necessitated some manual re-positioning of the bones (see section 8.1.3). It is possible that this error could be reduced by altering the shape of the tip. The tips were made conical so that they could easily be located in the computer mesh. However, this hindered location of the Fastrak digitising stylus. If the tips were modified to include a concavity, then this could accommodate the stylus tip and reduce the digitisation error (Figure 162).

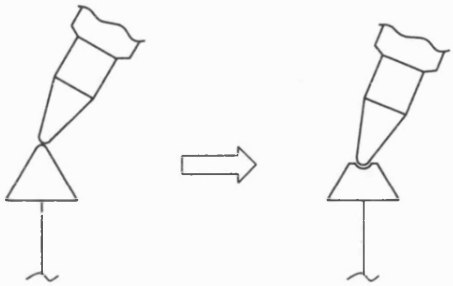

Figure 162 By replacing the sharp tip with a concavity, the errors in marker digitisation would have been reduced.

8.1.2 Carpal Separation

A further source of location error could have resulted from the bones being dislodged from their anatomical positions during dissection. The marker pins were inserted and their positions digitised before the joint capsule and intrinsic ligaments were removed. It was assumed that these precautions would be adequate to keep the wrist intact. However, it is possible that the carpals separated slightly when the tendons that crossed over the joint were removed. Without the use of radiographs, there was no easy way to check for this occurrence.

8.1.3 Realignment

Due to the sources of error mentioned above, the aligned positions of the carpals did not appear fully correct. Therefore, the only available option was to manually reposition the computer models. Since no radiographs of the intact wrist were available prior to

dissection, it is not possible to say whether the positions of the bones following realignment truly reflected their original arrangement.

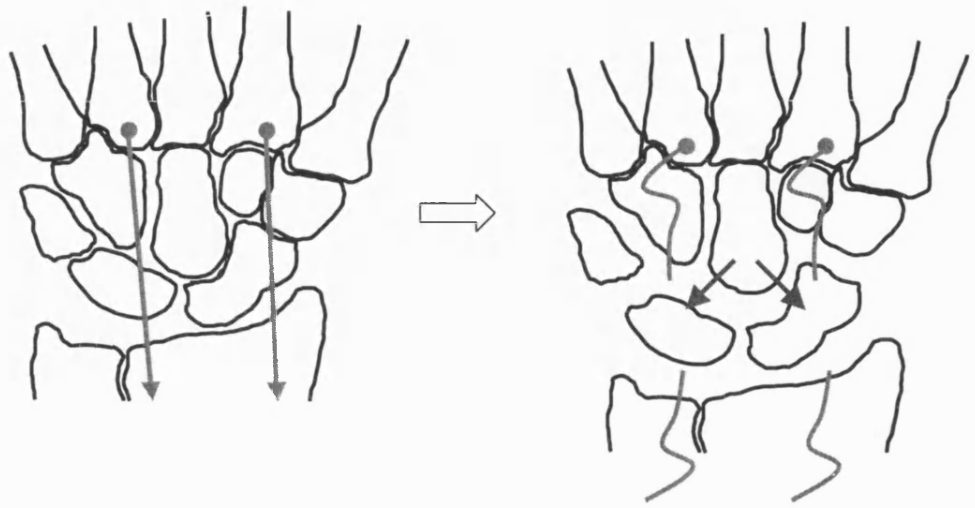

Figure 163 It is possible that the carpus could have separated to an extent when the tendons crossing the joint were removed. This may account for the large gaps between the bones following realignment with the digitised marker positions.

8.1.4 Resolution vs. Time

Due to the high computational requirements of the CARPAC algorithm, it was only possible to use 4.8% of the original detail in the laser-scanned bones (although a single run was made at 10% in ulnar deviation). On the 1.4GHz Pentium 4 (400MHz bus speed) desktop used to run the model, the time taken for a run using the full resolution available in the models was estimated as 227 days.

The performance of computers can be measured using industry-standard tests. One such test is the Whetstone benchmark, which was devised in England by Curnow and Wichman in the February 1976 issue of the Computer Journal. This benchmark contains linear arrays to which addition, subtraction, multiplication, division and complex operations. The speed of a computer may be represented in terms of millions of Whetstone instructions per second or MWIPS. Higher Whetstone ratings mean more powerful machines. The speed of the computer used for the work described in this thesis was 554.8 MWIPS (for double-

precision operations). The Whetstone benchmark program is included on the CD ROM that accompanies this thesis.

8.1.4.1 Moore's Law

Moore's Law is named after Intel co-founder Gordon Moore. In 1965, Moore noticed that the number of transistors on a silicon chip, and therefore its processing power, was doubling every 18 months (see Figure 164) (Moore, 1965). This relation has held true since the first central processor units (CPUs) were developed in the early 1970s. Assuming the relation continues to apply, it will take around 12 years (from the start-date of the present study, i.e. 2000) for CPU power to increase sufficiently to allow the run-time to be reduced to less than 24 hours. However, by this time it will also be possible to run the 4.8% resolution models in 4.7 minutes as opposed to 20 hours! The Whetstone rating of such a machine will be around 142000 MWIPS.

The memory requirements of using larger models must also be considered. Holding the present (4.8% resolution) models in the system memory occupies 15Mb of RAM. The full-resolution models would occupy $20 \times 15 = 300$Mb of RAM, but at least this much again must be set aside for operating system requirements. Fortunately, the capacity vs. price ratio for RAM follows an inverse Moore's Law relation, so RAM requirements are not likely to be a major problem.

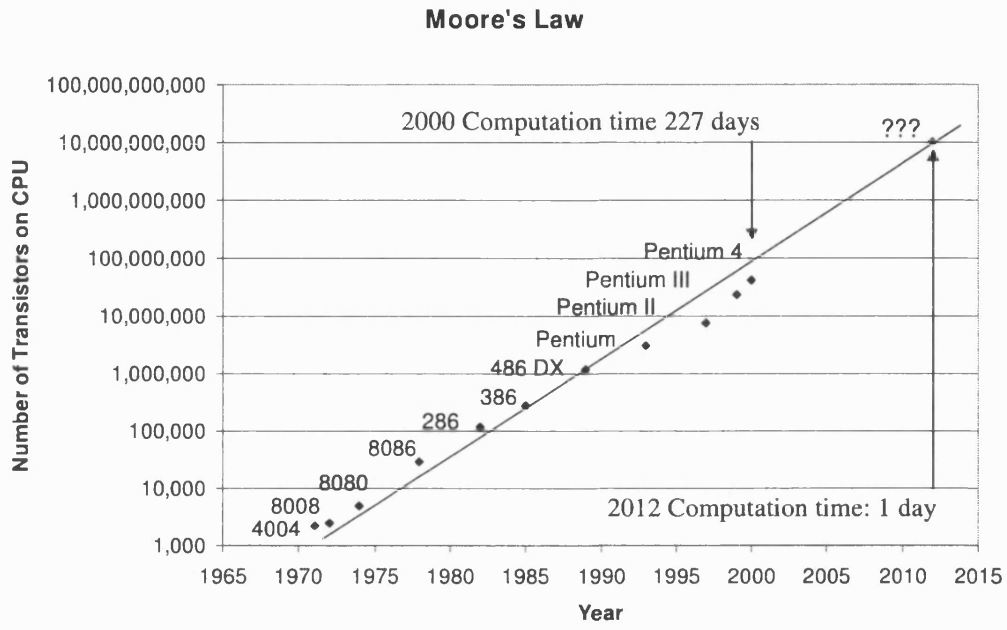

Figure 164 Moore's "Law" states that CPU power doubles every 18-24 months. The relation has held true since the 1970s. If it continues to apply, then by 2012, processor power should be sufficient to allow the full resolution models of the laser-scanned bones to be used. (http://www.Intel.com).

8.1.5 NURBS Representation

The models in the present study were created by connecting together vertices with a mesh of facets. The disadvantage of this method is that the surface is not continuous and smooth like the real thing, but consists of thousands of flat, triangular sections. It is possible that the performance of the CARPAC model could be improved if some means of smoothing the surfaces were implemented. In order to do this, it would be necessary to fit a mathematical surface through the vertices, in the same way that a best-fit curve is fitted to experimental data on graphs. A possible means of achieving this is to replace the triangular meshing with a NURBS representation.

NURBS (non-uniform rational b-spline) is a relatively new technique for displaying 3D objects. Instead of fitting flat triangular patches between mesh vertices, a NURBS modeller fits patches of surface having mathematically-defined curvature. Where two or more patches meet, the method ensures continuity of curvature. The overall effect is to give the impression of a smooth, continuous surface. A 2D curve-fitting algorithm using aspects of NURBS is included with Microsoft Word (Figure 165).

Figure 165 A 2D curve fitted to points using the curve-fitting function in Microsoft Word. The extension to the 3D case would give the bone models a smooth, mathematically continuous surface.

The difficulty of using a NURBS representation would lie in calculating the contact area between surfaces. The mid-point method (see section 8.3.1) could be used to generate a set of points through which a new NURBS surface could be fitted, but a means of finding the area of this surface would still need to be found. This is a soluble problem, but one that is likely to involve greater complexity than the method adopted for the present study.

8.1.6 MRI Study

In order to better validate the results, the bones within the CARPAC model would come from the same wrist as those used for the experimental study. A way to achieve this would be to obtain the experimental results by imaging the wrist in several positions of radial to ulnar deviation using an MR scanner. (An MR scanner would be preferable to a CT scanner because the articular cartilage would be distinguishable from surrounding tissue structures). Three-dimensional models could be extracted from the MR images and used in the CARPAC model. Great improvements have been made to the MR imaging technique in recent years. Image resolution is related to the magnetic field strength of the MR scanner. The typical field-strength of a hospital MR scanner is 1.0 – 1.5 Tesla. In standard form, this allows a voxel-size (3D equivalent of a pixel) of approximately $1.0mm^3$ (Snel *et al.*, 2000). However, a recent study was performed on the wrist using an 8.0 Tesla Scanner capable of resolutions approaching $0.1mm^3$ (Ashman *et al.*, 2002). Alternatively, resolution may be increased by reducing the field of view of the scanner. This is achieved by using a smaller transmit-receive coil. A study using a 1.5 Tesla scanner and a transmit-receive coil optimised for the wrist achieved a spatial resolution of around $0.4mm^3$ (Kocharian *et al.*, 2002).

During writing-up of the present study, a grant was awarded by the British Society for Surgery of the Hand to pay for the use of an MR scanner to achieve the goals stated above.

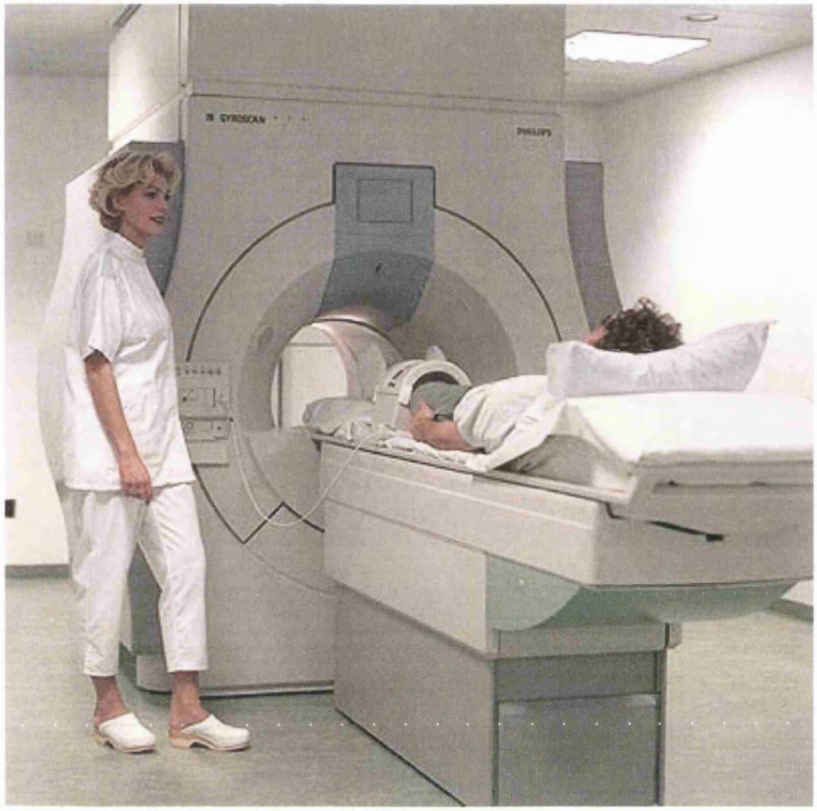

(a)

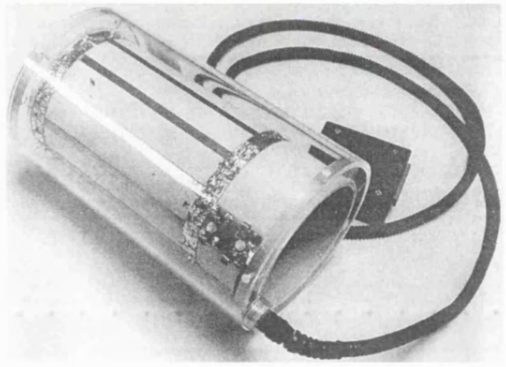

(b)

Figure 166 (a) An MR scanner with a dedicated leg-sized transmit-receive coil (www.lymphomainfo.net/ tests/mri.html). (b) By using a dedicated wrist coil, spatial resolution of up to 0.1mm^3 is possible (Kocharian *et al.*, 2002).

8.2 Anatomical Considerations

Several simplifications were made to the anatomy of the computer wrist model in order to ease the computational workload. Some possible effects of these are discussed in this section.

8.2.1 Rigid Distal Row

It is known that very little movement occurs between the bones of the distal row and consequently these bones were moved as a single rigid unit in the CARPAC model. However, it is possible that the small amount of movement that does occur between the bones is sufficient to influence the movement of the bones of the proximal row.

Close inspection of Figure 20 reveals that the hamate extends by approximately 3 degrees relative to the capitate during maximum ulnar deviation. Weber *et al.* (1984) additionally report a 2mm translation of the bone.

8.2.2 Bone Pairs

In finding the total contact area, between the carpals, nine pairs of interacting surfaces were considered (see section 5.11). However, it was noted that in ulnar deviation, the lunate contacted the hamate and the triquetrum occasionally impinged upon the ulna. The hamate-lunate interaction was not included in the list of bone pairs since the lunate was classified as "type I" (see section 3.5.1), i.e. it did *not* have an additional articulation with the hamate. Collision between the triquetrum and ulna is prevented in the wrist by the triangular fibrocartilage complex. This was omitted from the CARPAC model, so this could explain the impingement between these two bones.

8.2.3 Pisiform

The pisiform bone was omitted from the CARPAC model as it is a sesamoid that rests on the palmar-medial side of the joint rather than interacting within it. However, it is known to have a subtle effect on carpal kinematics. One study comparing kinematics of the wrist following removal of the bone reported a 6-10% loss of wrist motion and 10% loss of grip strength (Lam *et al.*, 2003).

8.2.4 Deformable Joint Surfaces

Articular cartilage deforms under load to help spread the load and minimise contact stress. The CARPAC model did not allow for deformation of the bone-surfaces, so this is an additional source of error. It is possible that some of the minor collisions between bones that were observed in the predicted results could have been accommodated by compression of the cartilage in these regions. It would conceivably be possible to represent deformation of the cartilage by placing spring-elements onto each vertex or facet of the bone models, but this would require a radical change in the structure of the CARPAC algorithm. SWORDS is not ideally suited to kinetics problems, and it would probably be more appropriate to use a dedicated musculoskeletal modelling program such as SIMM (Software for Interactive Musculoskeletal Modelling, Motion Analysis Corp.) for this purpose. If it is possible to integrate the contact area maximisation with the kinetic equilibrium equations of SIMM, then this could represent a fruitful route for further investigation.

8.2.5 TFCC

The triangular fibrocartilage complex (TFCC) is a soft-tissue structure located at the distal tip of the ulna (see section 3.8.3.6). It was excluded from the CARPAC model due to difficulties in modeling deformable structures.

When the lunate was found to remain motionless in radial deviation, it was assumed that this was because the TFCC was not present in the model (see 6.1.6.5). Therefore, the surface of the radius was extended to simulate the support provided by the TFCC. Unfortunately, this did not have the desired effect, as medial motion of the lunate was not induced.

The TFCC is a deformable structure whose function would be difficult to reproduce in the CARPAC model without using kinetic techniques (described in section 3.9). Since the TFCC is subject to the greatest deformity at the extremes of movement, an alternative approach would simply be to continue with the present model but limit the range of movement to a central band of say 15° ulnar to 10° radial deviation.

8.2.6 Anatomical Variation

An animation of wrist movement obtained from multi-position CT imaging of the wrist was used as a yardstick by which to qualitatively compare the results from the CARPAC model. It is accepted that the morphology of the wrist from which this animation was obtained is different to that of the wrist used in this study. Consequently, there undoubtedly were subtle differences between the motion patterns of the two joints. However, all wrists exhibit a similar set of overall characteristics. The objective was for the CARPAC algorithm to demonstrate these. It was not expected to resolve all the subtle nuances of movement. For this reason, it was considered satisfactory to use the patterns of Figure 21 as a reference even though this was not the same wrist as that used in the present study.

8.3 Cost Function

Key to the success of the CARPAC algorithm was the cost function. From the values of 23 variables, the cost function returned a measure of the "fitness" of each trial-solution. The fitness, or cost, of the solution is what guided the iterative search. It was principally defined by the estimated contact area, minus a measure of the intersection, occurring between two bones. Given the simplifications present in the model, this value appeared to represent an intuitive indication of the closeness of packing of the carpals. However, it was not *proven* as the best measure of fitness.

While the approach described in this thesis was shown to improve the closeness of packing of the carpal bones, there is no guarantee that this was the most efficient means of doing this. A limitation of the study was that the performance of the algorithm was not compared objectively to any of the packing algorithms described in section 3.12. That is to say the experiments highlighted in said section were not reproduced in this study. However, it should be noted that the CARPAC algorithm is not strictly a packing algorithm because it does not impose the additional constraint of fitting the objects into a finite volume.

The purpose of this section is to discuss the three components of the cost function used in this study.

8.3.1 Surface Area Evaluation

The present study considered the projected area of facets from one joint surface upon the other in order to evaluate the contact area. This section discusses an alternative method.

Midpoint Method

An alternative method of calculating the contact area between two surfaces is to find the set of points defining the midpoints of lines connecting facets from either bone. The connecting lines are normal to the facet from which they originate. This set of points is then triangulated and the contact area is found by summing the area of the triangles. A similar approach was used to compute contact area in a study of force distribution throughout the wrist (Genda and Horii, 2000).

If the bones used in the study are obtained from reconstructing serial MR image slices, then the midpoints can easily found during the segmentation stage of reconstruction. Points defining the midline between two-dimensional contours of neighbouring bones are found. These points are then stacked along with the outlines of the bones to create three-dimensional surfaces. This approach was used in a study of force distribution in the wrist (Iwasaki *et al.*, 1998). In order to use this particular method for the present study, it would be necessary to first cut the 3D bone models into a series of 2D slices. Slicing would require the bones to be converted from surface to solid format. This would be a highly time-consuming process and wholly unsatisfactory for repetitive application.

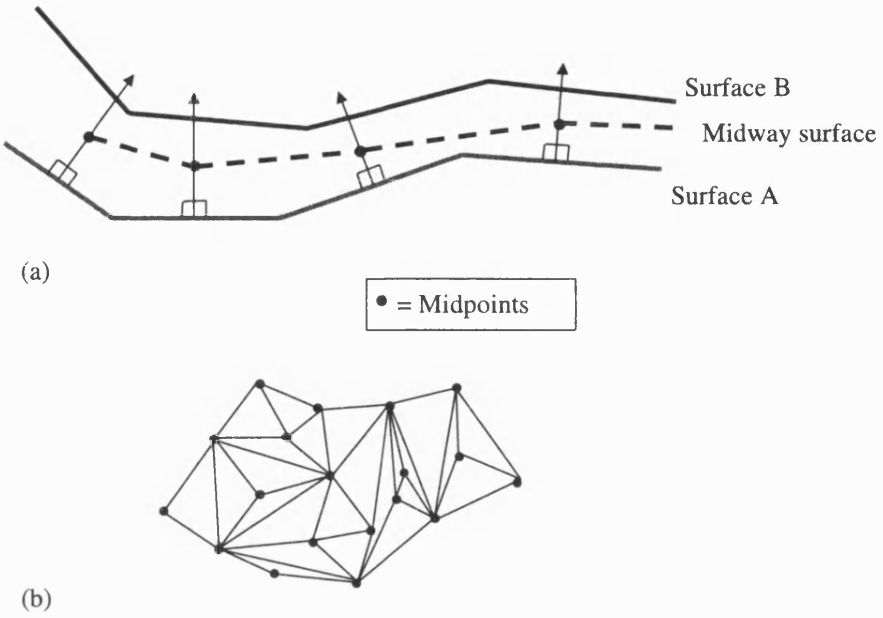

Figure 167 Calculation of contact area by triangulating midpoints between two surfaces (a) 2D view of edge of facets: Finding midpoints (b) Triangulating the points.

The advantage of the midpoint method is that the resulting surface is continuous i.e. it does not consist of isolated polygons of contact as does the projected-facet method. Consequently, the graph of contact area against displacement may be smoother, which would assist a direct-search type optimisation process. However, there are two principal disadvantages of the method:

1. Computational Expense

While it is relatively straightforward to find the set of points defining the midway surface, triangulation, especially in three-dimensions, is a complex and time-consuming mathematical procedure. However, without actually writing code to do this, it is difficult to quantify the time requirements in comparison to the method finally implemented in this study.

2. Holes

Where there are regions of intersection between the two surfaces, it will be desirable for the midway surface to have corresponding "holes". The presence of holes in the mesh will add to the complexity of the triangulation algorithm, although this problem is soluble.

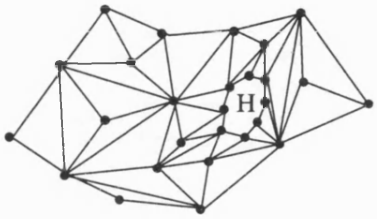

Figure 168 Triangulation is a complex procedure, made more difficult by the presence of holes (H) in the mesh where one surface intersects the other.

8.3.2 Intersection Evaluation

The intersection evaluation algorithm worked efficiently and was relatively robust. The CIEP program suffered only three premature terminations during the 15 runs that are documented. (These merely caused the optimisation process to pause until the CIEP window was manually closed – then the program immediately restarted leaving SWORDS unaffected). Given that during each run, the program executed some 8000 times (20 degrees of movement, 400 iterations per degree), this represents a reliability of 99.9975%. During the early stages of testing when crashes of this kind occurred frequently, the sources were easily identified and appropriate error traps were put into the code. However, as the code became more reliable it became increasingly difficult to find the source of fatal errors. Hence, 100% reliability was not a realistic goal.

8.3.3 Proximity Evaluation

The third component of the cost function was the proximity evaluation. This was introduced into the cost function after the first run and was successful in preventing bones drifting apart. The value returned to the cost function was the squared sum of the minimum distances between each pair of bones. The value was squared to ensure the term only became dominant when the distance between the bones was great. If the term were dominant when the bones were in close proximity, then the priority would be shifted

towards achieving vertex-on-vertex positioning of the two bones, which may have conflicted with the contact area requirement.

8.4 Optimisation

The optimisation procedure used results from the cost function to direct the search for maximum contact area in the most fruitful direction.

8.4.1 Global Minima

In section 5.14.2, it was shown that the optimisation process was not finding a global minimum when six degrees of freedom were available. However, it was assumed that this would not be a major problem providing the increments of applied movement were sufficiently small that the global minimum is close, in the search space, to the initial conditions. Given the nature of the problem (see below), it was not possible to tell whether the algorithm was actually finding the global minimum at each increment. Local minima will always be present with this kind of problem, but by reducing the number of degrees of freedom, the likelihood of finding one instead of the global minimum diminishes. This idea is discussed in section 8.5.1.

8.4.2 NP Completeness

The reason why it is so difficult to find the global minimum is that the three-dimensional packing problem belongs to a class of problems termed "NP complete" (Downsland and Downsland, 1992). Mathematical problems may be loosely classified as "P", "NP" or "NP-Complete". The class P consists of all those decision problems that can be solved on a deterministic sequential machine in an amount of time that is polynomial in the size of the input. The class NP consists of all those decision problems whose positive solutions can be verified in polynomial time given the right information, or equivalently, whose solution can be found in polynomial time on a non-deterministic machine. NP-complete is the hardest of the problems in the NP class. At present, all known algorithms for NP-complete problems require time which is exponential in the problem size and exact solutions cannot be found. Therefore it is necessary to use a heuristic algorithm which

works "reasonably well" on many cases, but for which there is no proof that it is always fast. (from definition of NP-completeness at www.wikidpedia.com).

8.4.3 Alternative Optimisation Methods

One of the objectives of the study was to use SWORDS to make the CARPAC model. This was convenient because SWORDS contains optimisation algorithms that can be used as "black boxes" provided a set of variables and a cost-function are available.

The Hooke and Jeeves direct-search method determines the local gradient of the cost function and moves in the direction of steepest descent. The algorithm works well if the cost function is smooth and has few local minima. If the cost function is particularly "lumpy" and contains discontinuities, as is the case with the present study (see Figure 102), then it is more difficult for the algorithm to find the global minimum.

It was assumed that, since the output bone complex was moved in only very small increments (1.0°), then the global minimum of the cost function at each increment would be fairly close to the initial conditions. Under such circumstances, it was assumed that a direct-search method would suffice to find the global minimum. However, doubts remain, and it is possible that the optimisation stage could be improved by using an alternative technique. This section discusses one such alternative.

"Genetic" Algorithm

Genetic algorithms are search algorithms based on the mechanics of natural selection. A "population" of solutions is generated and aspects of the fitter members are combined, creating two new "offspring" at each generation. These offspring replace those members of the population having lower fitness. The effect is to gradually increase the overall fitness of the population. Occasionally "mutations" are introduced whereby variables are changed at random in order to prevent regions of the search-space being permanently lost. Genetic algorithms are theoretically and empirically proven to provide robust search in complex spaces (Goldberg, 1989).

The advantage that genetic algorithms have over direct-search methods is that they do not consider local variations in the cost function as a means of directing the search into the

most profitable direction. Instead, the search is randomised throughout the search space, and is directed by combining the fittest solutions. Therefore, the method is better able to cope where the cost function is noisy and discontinuous.

The performance of a direct-search method and a genetic algorithm are compared in Figure 169, where a "lumpy" cost function is presented. While the Hooke and Jeeves method succeeds in finding a local maximum, the genetic algorithm locates the global minimum for this particular problem.

Practical Considerations

In order to implement a genetic algorithm for the present study, it would be necessary to modify SWORDS to include such a method in addition to its direct-search algorithms – a major undertaking. Alternatively, the optimisation could be performed by an external program, as has already been done to compute the cost function. However, if both geometric operations and optimisation were to be performed externally, then SWORDS would be used only as a graphics display. Given the inelegant method of communicating to external programs via files saved to the hard disk (see Figure 87), in such a case it may prove more efficient to write the entire program in C++ and not use SWORDS at all. Since this represents such a large undertaking, no attempt was made to try a genetic algorithm in the present study.

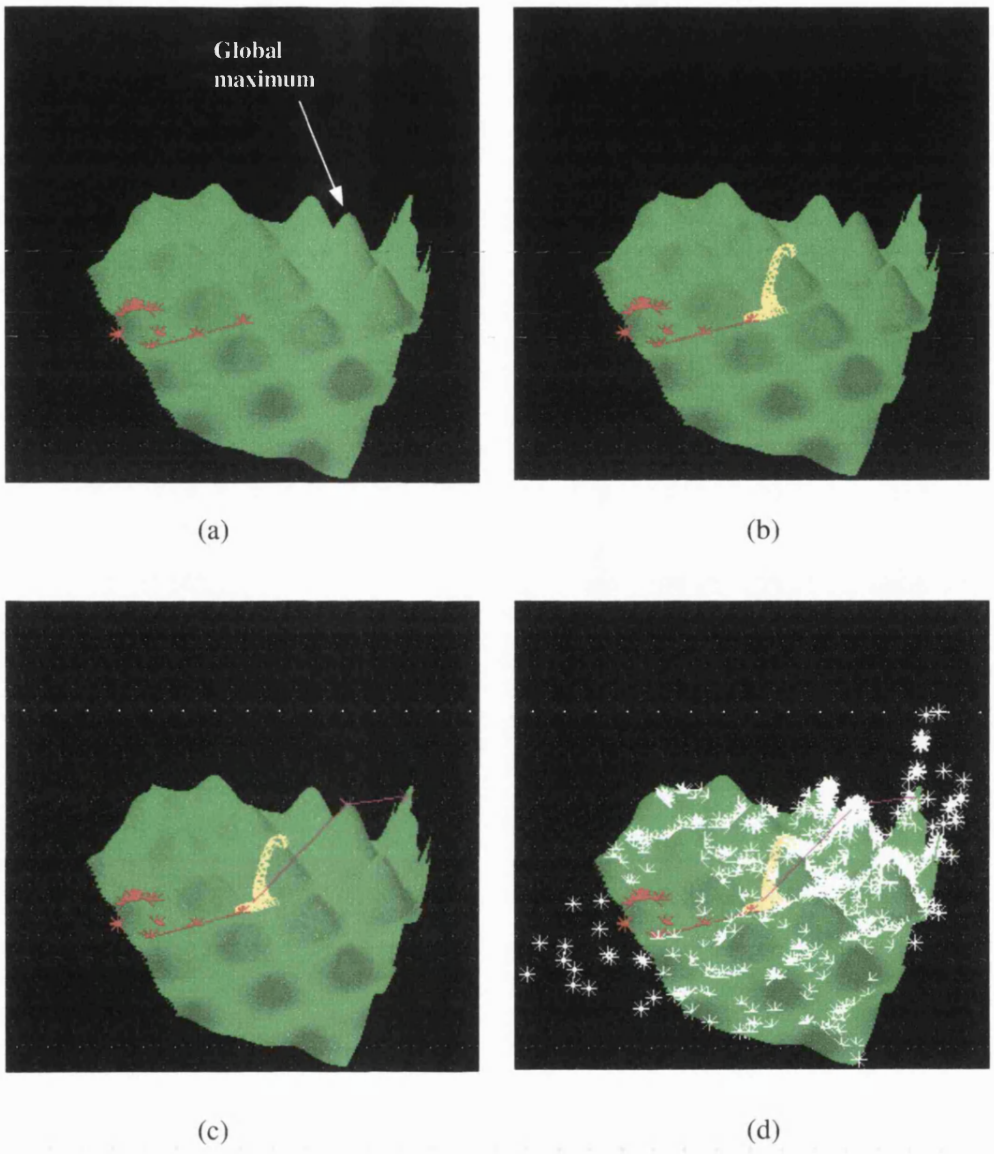

Figure 169 Comparison of four different optimisation methods for a "lumpy" search-space. The objective is to find the global maximum, i.e. the highest point on the terrain. (a) Hill-climber based on local linearization. (b) Hooke and Jeeves. (c) Genetic algorithm after 10 generations. (c) Genetic algorithm after 1000 iterations (http://www.soton.ac.uk/~ajk/opt/welcome.html).

8.5 Kinematics

The only kinematic input to the CARPAC model was the rotation about the x-axis applied to the capitate-hamate-trapezoid-trapezium complex. The movement of the triquetrum, scaphoid, and lunate plus the five remaining degrees of freedom of the output complex were under the control of the optimisation scheme. This section discusses alternative strategies in relation to kinematic input.

8.5.1 Reducing the Unknowns

In the current configuration, the input is applied to the system by rotating the capitate about the x-axis. An alternative means of applying input to the system would be to use the *actual* movement of the capitate. This could be extracted from an MR imaging study of the wrist in several positions of radial and ulnar deviation. (This would, of course necessitate using the same bones for the CARPAC model as the MR study). With the motion of the capitate correct from the outset, the number of degrees of freedom would be reduced by five.

Known kinematics could be applied to other bones in addition to the capitate. For example, if actual movements were applied to the capitate *and* the lunate, say, then the there would be just twelve degrees-of-freedom – six each for the scaphoid and triquetrum. Indeed, applying known movements to the lunate would remove the problem of the TFCC discussed in section 8.2.5. The result would be a much smaller search-space and an increased chance of finding the global minimum. Furthermore, since at each increment of movement the correct positions of two bones would be known, the effect of error build-up (discussed in section 6.1.2.3) would be less pronounced.

8.5.2 Other Movements

The present study considered only radial-ulnar deviation. The wrist is also capable of flexion-extension movement and circumduction, which is a combination of both movements. An obvious extension of the work is to run the CARPAC algorithm in extension and flexion.

The arc of motion in flexion and extension is more than twice that for radial-ulnar deviation (see section 3.2.1). Therefore, the time taken to run the algorithm would have been prohibitive unless the increment of motion was reduced to, say 5°. However, given the problems with local minima, and the fact that increasing the increment of motion demonstrably worsened the performance of the algorithm, it is doubtful whether any meaningful results could have been obtained.

If the scheme for reducing the unknowns described in section 8.5.1 were introduced, then running the algorithm in flexion and extension would possibly be a more viable option.

8.5.3 Finite Helical Axes

The finite helical axis (FHA) analysis was highly beneficial during the testing phase of the algorithm (see section 5.18). However, the erratic movement of the carpals predicted by the CARPAC model meant that it was difficult to obtain any useful information from the resulting FHAs.

If the MR imaging study described in 8.5.1 is carried out, then the FHA computation program will be an essential tool in investigating the actual movements of the bones. Furthermore, it is expected that the results of the CARPAC model will show a marked improvement. An effective way to demonstrate such an improvement will be simply to compare the consistency of the FHA placement with the current set of results.

9 CONCLUSIONS

Conclusions

There is a high incidence of arthritis in the wrist and hand, but joint replacement technology in the wrist and other small joints is still in its infancy compared with the larger joints. The wrist is the most complex of the small joints and there is a need for fundamental research into the way in which it works. At present there is no generally agreed upon satisfactory explanation for the complex movement patterns of the carpal bones.

A search of the literature revealed that research into the functioning of the wrist has been performed using *kinetic* modelling techniques. These models are capable of predicting carpal bone behaviour, but require information about the ligament mechanical properties and insertion sites in addition to the shapes of the carpals. Several authors have suggested that the ligaments play a secondary role in governing the movements of the carpal bones and that the morphology of the bones is what dictates their behaviour. Therefore, the originality of the present study lies in the fact that the model does *not* rely upon ligamentous constraints, but is based solely upon the shapes of the interacting joint surfaces.

The purpose of the work was to test a new hypothesis on wrist kinematics. The hypothesis was based on the assumption that the carpal bones move in such a way as to maximise contact area at all postures. To test the idea, three-dimensional computer models of the wrist bones were created using data obtained by laser-digitisation of a dissected human wrist. A computer program was written to calculate the contact area and this was used to assess the fitness of trial solutions offered by an optimsation scheme. For increments of overall wrist posture, the optimisation scheme adjusted the positions of the bones so that the contact area was maximised. The aim was to see whether certain characteristic behaviour of the carpal bones could be reproduced by comparing the predicted movements to known experimental results.

The CARPAC algorithm correctly predicts certain aspects of the complex behaviour of the carpal bones. Within the wide variation typical of biomechanical data, the results for the scaphoid in particular were similar to the characteristic movements of this bone in both radial and ulnar deviation. During 20° of unlar deviation, the bone demonstrated 14.3° of extension, which, given the wide variation associated with biological data, is near to the 20.4° (SD 10.7°) reported by an experimental study. In 10° of radial deviation, the bone underwent 6.4° of flexion, which again is close to the 8.1° (SD 4.8°) experimental result. In ulnar deviation, the lunate demonstrated medial-to lateral sliding across the radius of 2.9mm, which also agrees with experimental findings. The predicted movement of the triquetrum demonstrated no quantifiable characteristics similar to those of experimental studies. The axis of rotation of the capitate was found to remain fixed throughout the test. Its position did not coincide with the region in which experimental studies have shown it to lie.

Given the fact that the only information available to the algorithm was the shape of the bones, and that it was only possible to use very low-resolution meshes, the overall results of the study are very encouraging.

The four objectives set out in section 4.2 have been accomplished:

1. Obtaining Three-Dimensional Computer Models of the Carpal Bones

Three-dimensional models were successfully obtained for relatively little cost. The detail provided was more than sufficient for the task required. The disadvantage of the method was the error inherent in the realignment procedure.

2. Calculation of Total Surface Contact Area

A method was developed for estimating the contact area based upon the projection of one facet onto its nearest counterpart.

3. Collision Detection and Evaluation

An efficient means of estimating the level of intersection between adjacent surfaces was found based upon the perimeter of the loop of intersection. The method was found to be almost twice as fast as the calculation of the actual volume of intersection.

4. Movement Prediction

Despite doubts over local minima problems, an optimisation scheme within was successfully applied to the bone models with the result that certain overall trends of carpal behaviour were correctly predicted.

In terms of the overall aim, the work has shown that the hypothesis appears to offer a plausible explanation for the behaviour of the scaphoid. While the remaining bones did not conform to the hypothesis, this does not necessarily mean the hypothesis has been disproved. There remain several limitations in the CARPAC model and further work is required to resolve the issue.

9.1 Recommendations for Further Work

In order to continue the work, it would be necessary to perform some alterations to the method. Those ideas believed to have the most potential are now summarised.

1. Obtain Bone Models using MR Imaging

While the present study used laser-digitisation to obtain cartilage-inclusive models of the carpals, the major disadvantage of this method was the problem of realigning the bones into their anatomical positions. By contrast, bone models reconstructed from serial MR images would be in the correct orientation from the outset, thereby eliminating a potential source of error.

2. Reduce Unknowns

With the benefit of hindsight, expecting the CARPAC model to predict the movements of several bones simultaneously from a single rotation input was a very optimistic goal. A more realistic objective for future work would be to apply the actual movements to all but one of the bones and then direct efforts towards predicting the movement of a *single* bone. This would not only reduce the local minima problem, but would also save time, as it would be necessary to consider fewer interacting surfaces. Alternatively, it would be possible to increase the resolution of the bone models. The actual movements of the bones would easily be extracted from MR imaging data of the wrist in several increments of radial and ulnar deviation.

3. Try Different Optimisation Methods

The Hooke and Jeeves optimisation method performed well in the study, but it is unclear whether a direct search method is the most suitable for this application. It would be interesting to try a genetic algorithm for comparison.

4. Create a Standalone Program

This is the first time that SWORDS has been used to model the movement of a biological joint. The complexities of the problem were such that a great deal of the processing was performed by external programs. The method of communicating information between SWORDS and the programs was not particularly efficient. Ultimately, SWORDS was only used for the optimisation process and graphics display. For future implementations, it is recommended that the CARPAC model be created from scratch in C++. This would obviate the requirement for separate programs, which would eliminate the time that is currently being wasted shifting large amounts of data from one location to another prior to processing.

10 REFERENCES

References

An,K.N. and Chao,E.Y. (1984) Kinematic analysis of human movement. *Annals of Biomedical Engineering* **12,** 585-597.

Andrews,J.G. and Youm,Y. (1979) A biomechanical investigation of wrist kinematics. *J.Biomech.* **12,** 83-93.

Arthritis Research Campaign . Arthritis - The Big Picture. http://www.arc.org.uk/about_arth/BigPic.pdf . 2003.
Ref Type: Electronic Citation

Ashman,C.A., Farooki,S., Abduljalil,A.M., and Chakeres,D.W. (2002) In vivo high resolution coronal MRI of the wrist at 8.0 Tesla. *Journal of Computer Assisted Tomography* **26,** 387-391.

Barber,C.B., Dobkin,D.P., and Huhdanpaa,H. (1996) The quickhull algorithm for convex hulls. *ACM Transactions on Mathematical Software (TOMS)* **22,** 469-483.

Berger,R.A. (2001) The anatomy of the ligaments of the wrist and distal radioulnar joints. *Clin.Orthop.* **383,** 32-40.

Bourke,P. Intersection of a plane and a line. http://astronomy.swin.edu.au/~pbourke/geometry/planeline/ . 1991.
Ref Type: Electronic Citation

Bourke,P. Determining whether a line segment intersects a three-vertex facet. http://astronomy.swin.edu.au/~pbourke/geometry/ . 1997.
Ref Type: Electronic Citation

Brumbaugh,R.B., Crowninshield,R.D., Blair,W.F., and Andrews,J.G. (1982) An in-vivo study of normal wrist kinematics. *J.Biomech.Eng* **104,** 176-181.

Cagan,J., Degentesh,D., and Yin,S. (1998) A simulated annealing-based algorithm using hierarchical models for general three-dimensional component layout. *Computer-Aided Design* **30,** 781-790.

Chung,C.B., Lektrakul,N., Gigena,L., and Resnick,D. (2001) Magnetic resonance imaging of the upper extremity: advances in technique and application. *Clin.Orthop.* **383,** 162-174.

Cobb,T.K. and Beckenbaugh,R.D. (1996) Biaxial total-wrist arthroplasty. *J.Hand Surg.[Am.]* **21,** 1011-1021.

Craigen,M.A. and Stanley,J.K. (1995) Wrist kinematics. Row, column or both? *J.Hand Surg.[Br.]* **20,** 165-170.

Crisco,J.J., McGovern,R.D., and Wolfe,S.W. (1999) Noninvasive technique for measuring in vivo three-dimensional carpal bone kinematics. *J.Orthop.Res.* **17,** 96-100.

Dai,Z. and Cha,J. (1994) An octree method for interference detection in computer aided 3D packing. *Advances in Design Automation* **69,** 29-33.

Dai,Z., Cha,J., and Yuan,J. (1994) An octree-based heuristic algorithm for 3-D packing. *Advances in Design Automation* **69,** 125-133.

Downsland,K.A. and Downsland,W.B. (1992) Packing Problems. *European Journal of Operational Research* **56,** 2-14.

Feipel,V. and Rooze,M. (1999) Three-dimensional motion patterns of the carpal bones: an in vivo study using three-dimensional computed tomography and clinical applications. *Surg.Radiol.Anat.* **21,** 125-131.

Ferris,B.D., Stanton,J., and Zamora,J. (2000) Kinematics of the wrist. Evidence for two types of movement. *J.Bone Joint Surg.Br.* **82,** 242-245.

Genda,E. and Horii,E. (2000) Theoretical stress analysis in wrist joint-neutral position and functional position. *J.Hand Surg.[Br.]* **25,** 292-295.

Goldberg,D.E. (1989) *Genetic Algorithms in Search, Optimization and Machine Learning.* Adison Wesley, Reading, Massachusetts.

Hooke,R. and Jeeves,T.A. (1961) "Direct search" solution of numerical and statistical problems. *J.Assoc.Comput.* **8,** 212-229.

Horii,E., Garcia-Elias,M., Bishop,A.T., Cooney,W.P., Linscheid,R.L., and Chao,E.Y. (1990) Effect on force transmission across the carpus in procedures used to treat Kienbock's disease. *J.Hand Surg.[Am.]* **15,** 393-400.

Ikonen,I. (1997) Concept for a genetic algorithm for packing three dimensional objects of complex shape. *1st Online Workshop on Soft Computing* 211-215.

Ikonen,I., Biles,W.E., Kumar,A., and Ragade,R.K. (1997) Genetic algorithm for packing three-dimensional non-convex objects having cavities and holes. *Proceedings of the 7th International Conference on Genetic Algortithms.East Lansing, Michigan* 591-598.

Inglis,A.E. (1982) *American Academy of Orthopaedic Surgeons: Symposium on Total Joint Replacement of the Upper Extremity* . The C.V. Mosby Company., St. Louis.

Iwasaki,N., Genda,E., Barrance,P.J., Minami,A., Kaneda,K., and Chao,E.Y. (1998) Biomechanical analysis of limited intercarpal fusion for the treatment of Kienbock's disease: a three-dimensional theoretical study. *J.Orthop.Res.* **16,** 256-263.

Kapandji,I.A. (1982) The Wrist. In *The Physiology of the Joints* Pp. 132-163. Maloine S.A. Editeur, Paris.

Kocharian,A., Adkins,M.C., Amrami,K.K., McGee,K.P., Rouleau,P.A., Wenger,D.E., Ehman,R.L., and Felmlee,J.P. (2002) Wrist: improved MR imaging with optimized transmit-receive coil design. *Radiology* **223,** 870-876.

Kolli,A., Cagan,J., and Rutenbar,R. (1996) Packing of generic, three-dimensional components based on multi-resolution modeling. *Proceedings of the 1996 ASME Design Engineering Technical Conferences and Computers in Engineering Conference, Irvine, California.*

Kooloos,J.G., Vorstenbosch,M.A.T.M., and Savelberg,H.H. (1994) A Computergraphics Model of the Wrist Joint. In *Advances in the Biomechanics of the Hand and Wrist* (Edited by Schuind,F.) Plenum Press, New York.

Lam,K.S., Woodbridge,S., and Burke,F.D. (2003) Wrist function after excision of the pisiform. *Journal fo Hand Surgery (British and European Volume, 2003)* **28B,** 69-72.

Lin,M.C. and Gottschalk,S. (1998) Collision detection between geometric models: a survey. *Proceedings IMA Conference on Mathematics of Surfaces 1998.*

Linscheid,R.L. (1986) Kinematic considerations of the wrist. *Clinical Orthopaedics* **202,** 27-39.

Lorei,M.P., Figgie,M.P., Chitranjan,R.S., and Inglis,A.E. (1997) Failed total wrist arthroplasty. *Clinical Orthopaedics and Related Research* **342,** 84-93.

Luttgens,K., Deutsch,H., and Hamilton,N. (1992) *Kinesiology : scientific basis of human motion.* Brown and Benchmark, Madison, Wis; Oxford.

Malchau,H., Herberts,P., Soderman,P., and Anders,O. Prognosis of Total Hip Replacement: Update and Validation of Results from the Swedish National Hip Arthroplasty Registry 1979-1998. http://www.jru.orthop.gu.se/archive/AAOS-2000-NHR.pdf . 2000.
Ref Type: Electronic Citation

Manal,K., Lu,X., Nieuwenhuis,M.K., Helders,P.J., and Buchanan,T.S. (2002) Force transmission through the juvenile idiopathic arthritic wrist: a novel approach using a sliding rigid body spring model. *J.Biomech.* **35,** 125-133.

Maupertuis,P.M. Principle of Least Action. 1746.
Ref Type: Generic

Meagher ,D. (1982) Geometric Modelling using octree encoding. *Computer Graphics and Image Processing* **19,** 129-147.

Moojen,T.M., Snel,J., Ritt,M., Kauer,J., Venema,H., and Bos,K. (2002a) Three-dimensional carpal kinematics in vivo. *Clin.Biomech.* **17,** 506-514.

Moojen,T.M., Snel,J.G., Ritt,M.J., Venema,H.W., Kauer,J.M.G., and Bos,K.E. (2002b) Scaphoid kinematics in vivo. *J.Hand Surg.[Am.]* **27A,** 1003-1010.

Moore,G. (1965) Cramming more components onto integrated circuits. *Electronics* **38,** 114-117.

Moore,J.A., Small,C.F., Bryant,J.T., Ellis,R.E., Pichora,D.R., and Hollister,A.M. (1993) A kinematic technique for describing wrist joint motion: analysis of configuration space plots. *Proc.Inst.Mech.Eng [H.]* **207,** 211-218.

Mullineux,G. Notes on finding screw transformations. 2003.
Ref Type: Personal Communication

Neu,C.P., Crisco,J.J., and Wolfe,S.W. (2001) In vivo kinematic behavior of the radio-capitate joint during wrist flexion-extension and radio-ulnar deviation. *J.Biomech.* **34,** 1429-1438.

Nordin,M. and Frankel,V.H. (1989) *Basic Biomechanics of the Musculoskeletal System.* Lea and Febiger, Philadelphia; London.

Patterson,R.M., Nicodemus,C.L., Viegas,S.F., Elder,K.W., and Rosenblatt,J. (1998) High-speed, three-dimensional kinematic analysis of the normal wrist. *J.Hand Surg.[Am.]* **23,** 446-453.

Powell,M.J.D. (1964) An efficient method for finding the minimum of a function of several variables without calculating derivatives. *Computer Journal* **7,** 155-162.

Savelberg,H.H., Kooloos,J.G., De Lange,A., Huiskes,R., and Kauer,J.M. (1991) Human carpal ligament recruitment and three-dimensional carpal motion. *J.Orthop.Res.* **9,** 693-704.

Savelberg,H.H., Kooloos,J.G., Huiskes,R., and Kauer,J.M. (1992) Strains and forces in selected carpal ligaments during in vitro flexion and deviation movements of the hand. *J.Orthop.Res.* **10,** 901-910.

Schuind,F., Cooney,W.P., Linscheid,R.L., An,K.N., and Chao,E.Y. (1995) Force and pressure transmission through the normal wrist. A theoretical two-dimensional study in the posteroanterior plane. *J.Biomech.* **28,** 587-601.

Snel,J.G., Venema,H.W., Moojen,T.M., Ritt,J.P., Grimbergen,C.A., and den Heeten,G.J. (2000) Quantitative in vivo analysis of the kinematics of carpal bones from three-dimensional CT images using a deformable surface model and a three-dimensional matching technique. *Med.Phys.* **27,** 2037-2047.

Spoor,C.W. and Veldpaus,F.E. (1980) Rigid body motion calculated from spatial co-ordinates of markers. *J.Biomech.* **13,** 391-393.

Szykman,S. and Cagan,J. (1997) Constrained three dimsnsional component layout using simulated annealing. *ASME Journal of Mechanical Design* **119,** 28-35.

Udy,J.L., Balling,R., and Benzley,S.E. (1988) Computation of interferences between three-dimsnsional objects and the optimal packing problem. *Advances in Engineering Software* **10,** 8-14.

Viegas,S.F. (2001) Variations in the skeletal morphologic features of the wrist. *Clin.Orthop.* **383,** 21-31.

Viegas,S.F., Yamaguchi,S., Boyd,N.L., and Patterson,R.M. (1999) The dorsal ligaments of the wrist: anatomy, mechanical properties, and function. *J.Hand Surg.[Am.]* **24,** 456-468.

Volz,R.G., Lieb,M., and Benjamin,J. (1979) Biomechanics of the Wrist. *Clinical Orthopaedics and Related Research* **149,** 112-117.

Weber,E.R. (1984) Concepts governing the rotational shift of the intercalated segment of the carpus. *Orthop.Clin.North Am.* **15,** 193-207.

Wilson,D.R., Feikes,J.D., Zavatsky,A.B., and O'Connor,J.J. (2000) The components of passive knee movement are coupled to flexion angle. *J.Biomech.* **33,** 465-473.

Wolff,J., Maquet,P., and Furlong,R. (1986) *The Law of Bone Remodelling*. Springer-Verlag, Berlin.

Woltring,H.J., Huiskes,R., De Lange,A., and Veldpaus,F.E. (1985) Finite centroid and helical axis estimation from noisy landmark measurements in the study of human joint kinematics. *J.Biomech.* **18,** 379-389.

Yin,S. and Cagan,J. (2000) An extended pattern search algorithm for three-dimensional component layout. *Journal of Mechanical Design* **122,** 102-108.

Youm,Y., McMurtry,R.Y., Flatt,T.E., and Gillespie,T.E. (1978) Kinematics of the Wrist I. An experimental study of radial-ulnar deviation and flexion-extension. *J.Bone Joint Surg.Am.* **60-A,** 423-431.

Youm,Y. and Flatt,A.E. (1980) Kinematics of the wrist. *Clin.Orthop.* **149,** 21-32.

11 APPENDICES

11.1 Calculations

11.1.1 Surface Normal Vector

Given a plane defined by vectors $\mathbf{v}_0$ and $\mathbf{v}_1$, the surface normal vector is given by:

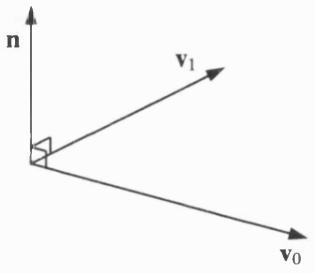

$$\mathbf{n} = \begin{vmatrix} i & j & k \\ x_0 & y_0 & z_0 \\ x_1 & y_1 & z_1 \end{vmatrix}$$

Figure 170

(11.1.1-1)

11.1.2 Intersection Between a Line Segment and a Plane

This calculation from Bourke (Bourke, 1991).

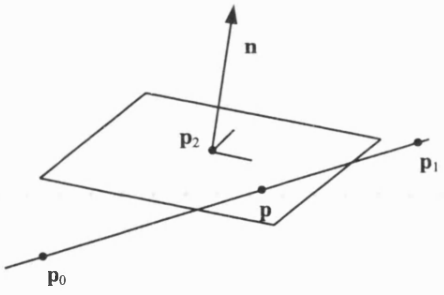

Figure 171

The equation of a plane with normal vector **n** and point $\mathbf{p}_2$ on the plane may be written as:

$$\mathbf{n} \cdot (\mathbf{p} - \mathbf{p}_2) = 0 \qquad (11.1.2\text{-}1)$$

Where P is any point on the plane.

The equation of the line segment joining $\mathbf{p}_0$ and $\mathbf{p}_1$ is given by:

$$\mathbf{p} = \mathbf{p}_0 + \mathbf{u}(\mathbf{p}_1 - \mathbf{p}_0) \qquad (11.1.2\text{-}2)$$

By substituting (11.1.2-2) into (11.1.2-1), the intersection occurs when:

$$\mathbf{n} \cdot (\mathbf{p}_0 + \mathbf{u}(\mathbf{p}_1 - \mathbf{p}_0)) = \mathbf{n} \cdot \mathbf{p}_2 \qquad (11.1.2\text{-}3)$$

Solving for u gives:

$$\mathbf{u} = \frac{\mathbf{n} \cdot (\mathbf{p}_2 - \mathbf{p}_0)}{\mathbf{n} \cdot (\mathbf{p}_1 - \mathbf{p}_0)} \qquad (11.1.2\text{-}4)$$

If the denominator of (11.1.2-4) is zero then the normal to the plane is perpendicular to the line. In this case, the line is parallel to the surface so the test must proceed no further.

For the intersection point to lie between P_0 and P_1, u must be between zero and one.

11.1.3 Point of Intersection Between Two Line Segments

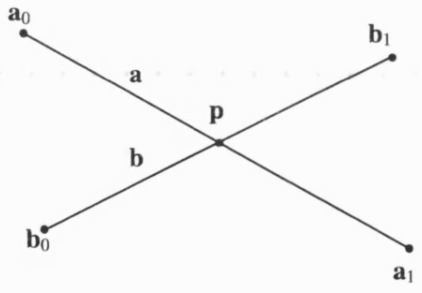

Figure 172

$$\mathbf{\Delta a} = \mathbf{a}_1 - \mathbf{a}_0$$
$$\mathbf{\Delta b} = \mathbf{b}_1 - \mathbf{b}_0 \qquad (11.1.3\text{-}1)$$

$$\mathbf{a} = \mathbf{a}_0 + \alpha\mathbf{\Delta a}$$
$$\mathbf{a} = \mathbf{a}_0 + \beta\mathbf{\Delta a} \qquad (11.1.3\text{-}2)$$

The two line equations are equated to find the point of intersection:

$$\mathbf{p} = \mathbf{a}_0 + \alpha\mathbf{\Delta a} = \mathbf{b}_0 + \beta\mathbf{\Delta b} \qquad (11.1.3\text{-}3)$$

This is split into x, y and z components to produce three simultaneous equations:

$$\mathbf{a}_{0x} + \alpha\Delta\mathbf{a}_x = \mathbf{b}_{0x} + \beta\Delta\mathbf{b}_x \quad (11.1.3\text{-}4)$$

$$\mathbf{a}_{0y} + \alpha\Delta\mathbf{a}_z = \mathbf{b}_{0y} + \beta\Delta\mathbf{b}_y \quad (11.1.3\text{-}5)$$

$$\mathbf{a}_{0z} + \alpha\Delta\mathbf{a}_z = \mathbf{b}_{0z} + \beta\Delta\mathbf{b}_z \quad (11.1.3\text{-}6)$$

From (11.1.3-4), we obtain:

$$\alpha = \frac{\mathbf{b}_{0x} - \mathbf{a}_{0x} + \beta\Delta\mathbf{b}_x}{\Delta\mathbf{a}_x} \quad (11.1.3\text{-}7)$$

Substituting (11.1.3-7) into (11.1.3-5) gives:

$$\mathbf{a}_{0y} + \left[\frac{\mathbf{b}_{0x} - \mathbf{a}_{0x} + \beta\Delta\mathbf{b}_x}{\Delta\mathbf{a}_x}\right]\Delta\mathbf{a}_y = \mathbf{b}_{0y} + \beta\Delta\mathbf{b}_y \quad (11.1.3\text{-}8)$$

From which β is found:

$$\beta = \frac{\Delta\mathbf{a}_x(\mathbf{a}_{0y} - \mathbf{b}_{0y}) + \Delta\mathbf{a}_y(\mathbf{b}_{0x} - \mathbf{a}_{0x})}{\Delta\mathbf{a}_x\Delta\mathbf{b}_y - \Delta\mathbf{b}_x\Delta\mathbf{a}_y} \quad (11.1.3\text{-}9)$$

Substituting (11.1.3-9) into (11.1.3-3) gives the point of intersection, P,:

$$\mathbf{p} = \mathbf{b}_0 + \left[\frac{\Delta\mathbf{a}_x(\mathbf{a}_{0y} - \mathbf{b}_{0y}) + \Delta\mathbf{a}_y(\mathbf{b}_{0x} - \mathbf{a}_{0x})}{\Delta\mathbf{a}_x\Delta\mathbf{b}_y - \Delta\mathbf{b}_x\Delta\mathbf{a}_y}\right]\Delta\mathbf{b} \quad (11.1.3\text{-}10)$$

11.1.4 Angle subtended between two vectors

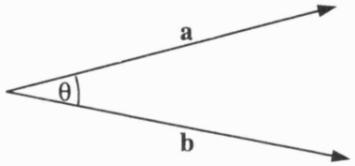

$$\theta = \cos^{-1}\left[\frac{\mathbf{a}\cdot\mathbf{b}}{|\mathbf{ab}|}\right] \qquad (11.1.4\text{-}1)$$

Figure 173

11.1.5 Internal Point Test

This describes how it is possible to tell whether a point lies within the boundary of a triangle. The method relies upon the fact that the sum of the angles subtended between lines joining an internal point to each vertex will always be 2π. Method taken from Bourke (Bourke, 1997).

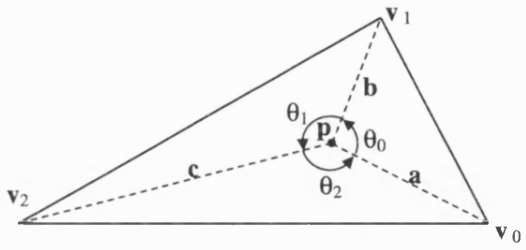

$\theta_0 + \theta_1 + \theta_2 = 2\pi \Rightarrow$ **p** is inside triangle

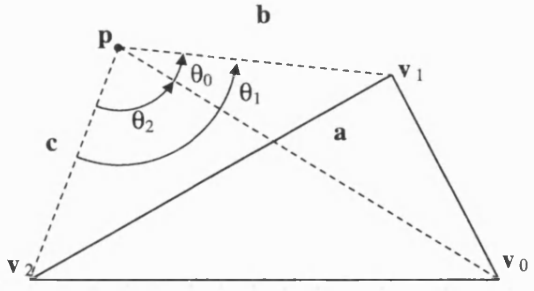

$\theta_0 + \theta_1 + \theta_2 < 2\pi \Rightarrow$ **p** is outside triangle

Where $\theta_0 = \cos^{-1}\left(\frac{\mathbf{a}\cdot\mathbf{b}}{|\mathbf{ab}|}\right)$ $\theta_1 = \cos^{-1}\left(\frac{\mathbf{b}\cdot\mathbf{c}}{|\mathbf{bc}|}\right)$ $\theta_2 = \cos^{-1}\left(\frac{\mathbf{a}\cdot\mathbf{c}}{|\mathbf{ac}|}\right)$

Figure 174

11.1.6 Area of a Triangle

The area of a triangle is calculated using a property of the vector product.

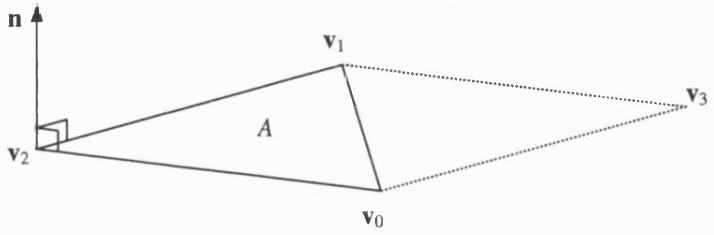

Figure 175

The area of the parallelogram $\mathbf{v}_0$, $\mathbf{v}_3$, $\mathbf{v}_1$, $\mathbf{v}_2$ is given by the magnitude of the vector product of any two edges of triangle $\mathbf{v}_0$, $\mathbf{v}_1$ and $\mathbf{v}_2$. So the area of triangle $\mathbf{v}_0$, $\mathbf{v}_1$, $\mathbf{v}_2$ is given by:

$$A = \frac{\left|\mathbf{v}_2\mathbf{v}_1 \times \mathbf{v}_2\mathbf{v}_0\right|}{2} \qquad (11.1.6\text{-}1)$$

11.1.7 Three-dimensional Coordinate Transformation

This section explains how the coordinates of the vertices of an object change with respect to world space when the model space containing the object is moved.

When a model space is moved, the change in its position may be broken into translation and rotation. In order to find the new positions of the vertices in world space (x_w, y_w, z_w), the translation vector (x_t, y_t, z_t) and initial origin position (x_i, y_i, z_i) are first subtracted from all vertices in the model space (x_m, y_m, z_m), so that its origin coincides with the world-space origin. Then the rotation matrix is applied before adding the translations back on to the rotated coordinates.

The rotation matrices for rotation about each of the principal axes are as follows:

$$R_x = \begin{bmatrix} 1 & 0 & 0 \\ 0 & \cos\theta_x & -\sin\theta_x \\ 0 & \sin\theta_x & \cos\theta_x \end{bmatrix} \quad R_y = \begin{bmatrix} \cos\theta_y & 0 & \sin\theta_y \\ 0 & 1 & 0 \\ -\sin\theta_y & 0 & \cos\theta_y \end{bmatrix} \quad R_z = \begin{bmatrix} \cos\theta_z & -\sin\theta_z & 0 \\ \sin\theta_z & \cos\theta_z & 0 \\ 0 & 0 & 1 \end{bmatrix}$$

(11.1.7-1)

The order in which SWORDS applies rotations to model spaces is: $R_x \rightarrow R_z \rightarrow Ry$. So to obtain the general rotation matrix, the individual rotation matrices are multiplied in sequence. The complete transformation is then given by:

$$\begin{bmatrix} x_w \\ y_w \\ z_w \end{bmatrix} = \left[\begin{bmatrix} x_m - x_t - x_i \\ y_m - y_t - y_i \\ z_m - z_t - z_i \end{bmatrix} \cdot \begin{bmatrix} c\theta_y c\theta_z & -s\theta_z & s\theta_y c\theta_z \\ c\theta_x s\theta_z c\theta_y + s\theta_x s\theta_y & c\theta_x c\theta_z & s\theta_y c\theta_x s\theta_z - c\theta_y s\theta_x \\ s\theta_x s\theta_z c\theta_y - c\theta_x s\theta_y & s\theta_x c\theta_z & s\theta_y s\theta_x s\theta_z + c\theta_x c\theta_y \end{bmatrix} \right] + \begin{bmatrix} x_t + x_i \\ y_t + y_i \\ z_t + z_i \end{bmatrix}$$

$s = \sin$
$c = \cos$

(11.1.7-2)

11.1.8 Calculation of Finite Helical Axis

Suppose that a rigid body occupies one of two positions in space. Let these be labelled as 1 and 2. There is a rigid body transformation which maps from the first position onto the second. Finite helical axis theory states that this transformation can be regarded as a rotation about followed by a translation in a direction parallel to that axis (Woltring *et al.*, 1985).

This section describes the method used by G. Mullinuex to convert model space transforms (movements in x, y and z direction and rotation about x, y and z axes) into finite helical axis representation (Mullineux, 2003).

11.1.8.1 Separating Rotation from Translation

Let $\mathbf{a}^{(1)}$ denote the position vector of some point in the body in the first position. Suppose that this moves to position vector $\mathbf{a}^{(2)}$ in the second position. Suppose that the initial and final positions are changed by translation to bring the position of the given point onto the origin. Then the transform from the initial to the final position is simply a rotation about some axis $\mathbf{u}$ through the origin followed by the addition of vector $\mathbf{a}^{(2)}$ (Figure 112).

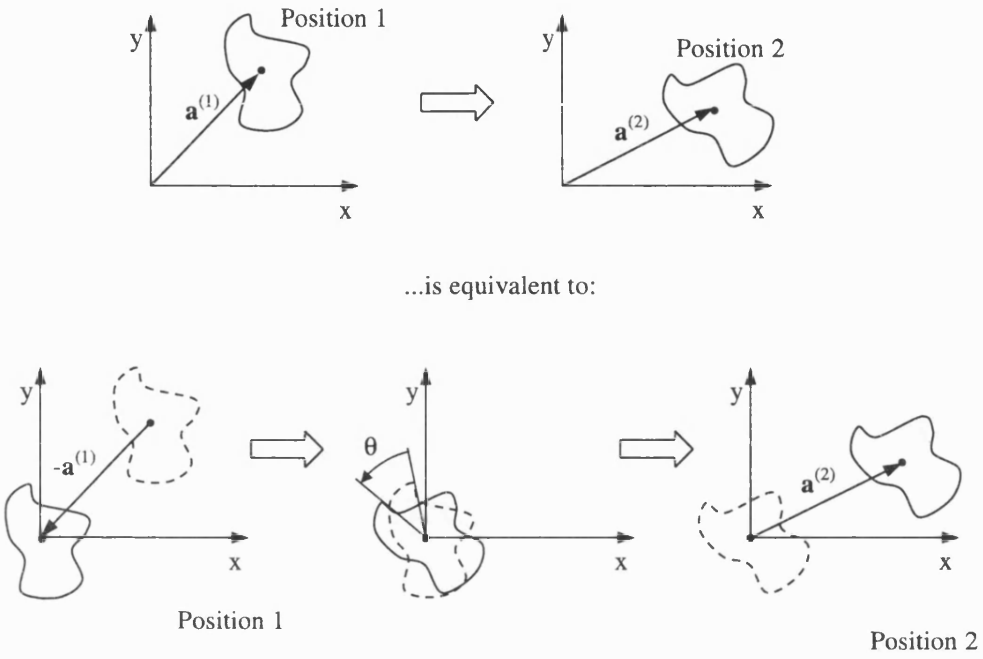

Figure 176 Movement of a body from one position to another.

Suppose that u is a unit vector and let R be the corresponding rotation matrix (see 11.1.7). Then the original transform has the following effect on the general position vector q:

$$\mathbf{q} \mapsto \mathbf{F}(\mathbf{q}) = \mathrm{R}(\mathbf{q} - \mathbf{a}^{(1)}) + \mathbf{a}^{(2)} \qquad (11.1.8\text{-}1)$$

Since **u** represents the axis (through the origin) of rotation, the following relation holds. This also says that **u** is an eigenvector of R with unity as the eigenvalue:

$$\mathrm{R}\mathbf{u} = \lambda\mathbf{u} = \mathbf{u} \qquad (11.1.8\text{-}2)$$

If q is a point on the helical axis, then it only moves along the axis and so:.

$$\mathbf{F}(\mathbf{q}) = \mathbf{q} + \alpha\mathbf{u} \qquad (11.1.8\text{-}3)$$

where α represents the distance travelled along the axis. Using equation (11.1.8-1) this gives:

$$(\mathrm{R} - \mathrm{I})\mathbf{q} = \mathrm{R}\mathbf{a}^{(1)} - \mathbf{a}^{(2)} + \alpha\mathbf{u} \qquad (11.1.8\text{-}4)$$

Unfortunately, this equation cannot be used immediately to find a point **q** on the axis. This is because the matrix $(R\text{-}I)$ is singular (since unity is an eigenvalue of R). Indeed equation (11.1.8-4) is not even consistent for every value of α. However, the equation can be used to determine what α should be. Firstly note that transposing equation (11.1.8-2) gives:

$$\mathbf{u}^{\mathrm{T}}\mathrm{R}^{\mathrm{T}} = \mathrm{u}^{\mathrm{T}} \qquad (11.1.8\text{-}5)$$

Post-multiplying by R and noting that R^T is the inverse of R gives:

$$\mathbf{u}^{\mathrm{T}} = \mathbf{u}^{\mathrm{T}}\mathrm{R} \qquad (11.1.8\text{-}6)$$

Now pre-multiply equation (11.1.8-4) by $\mathbf{u}^T$ to show that:

$$\mathbf{u}^T(R-I)\mathbf{q} = \mathbf{u}^T A\mathbf{a}^{(1)} - \mathbf{u}^T\mathbf{a}^{(2)} + \alpha\mathbf{u}^T\mathbf{u} \qquad (11.1.8\text{-}7)$$

The left-hand side is zero when equation (11.1.8-6) is substituted into this, and hence:

$$\alpha = \frac{\mathbf{u}^T(\mathbf{a}^{(2)} - \mathbf{a}^{(1)})}{\mathbf{u}^T\mathbf{u}} \qquad (11.1.8\text{-}8)$$

With this value of α, the set of equations (11.1.8-4) is consistent. There are however infinitely many solutions. Let $\mathbf{q}_0$ be any solution. Then the transformation of the typical point is given by:

$$\mathbf{q} \mapsto \mathbf{F}(\mathbf{q}) = R(\mathbf{q} - \mathbf{q}_0) + \mathbf{q}_0 + \alpha\mathbf{u} \qquad (11.1.8\text{-}9)$$

11.1.8.2 Points Sets

Suppose the initial position of the body is determined by n points labelled $\mathbf{r}_1^{(1)},\ldots,\mathbf{r}_n^{(1)}$. Similarly, let $\mathbf{r}_1^{(2)},\ldots,\mathbf{r}_n^{(2)}$ be the points in the final position.

Choose $\mathbf{a}^{(1)}$ and $\mathbf{a}^{(2)}$ to be the centroids of the two sets:

$$\mathbf{a}^{(1)} = \frac{1}{n}\sum \mathbf{r}_i^{(1)} \qquad \mathbf{a}^{(2)} = \frac{1}{n}\sum \mathbf{r}_i^{(2)} \qquad (11.1.8\text{-}10)$$

Determination of the helical axis transform takes place over several stages:

Stage 1 – Find *R*

Begin by imagining the points translated so that the centroids lie at the origin (see Figure 177). Define

$$\mathbf{s}_i^{(1)} = \mathbf{r}_i^{(1)} - \mathbf{a}^{(1)} \quad \mathbf{s}_i^{(2)} = \mathbf{r}_i^{(2)} - \mathbf{a}^{(2)} \quad \text{for } 1 \le i \le n \qquad (11.1.8\text{-}11)$$

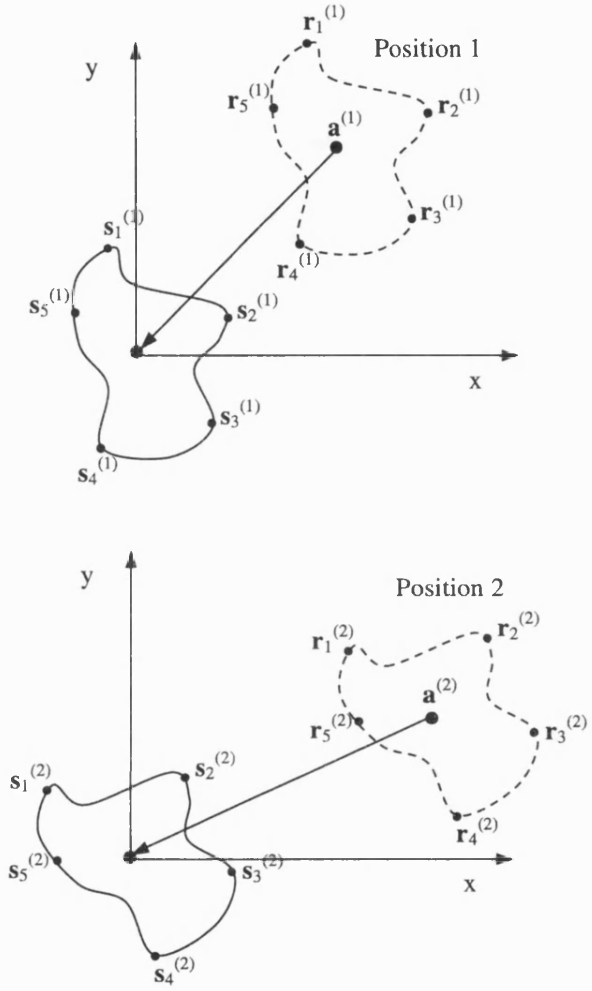

Figure 177 Point sets for postions 1 and 2 are moved so that the origin of each set (a) lies at the origin.

The transform between $\mathbf{s}^{(1)}$ and $\mathbf{s}^{(2)}$ is simply a rotation about an axis through the origin. The difference vector,

$\mathbf{s}_i^{(2)} - \mathbf{s}_i^{(1)}$, is perpendicular to the axis and hence the vector product

$$(\mathbf{s}_i^{(2)} - \mathbf{s}_i^{(1)}) \times (\mathbf{s}_j^{(2)} - \mathbf{s}_j^{(1)})$$

for $i \neq j$ is parallel to the axis. Forming the sum of all these vector products for i>j has an averaging effect. The vector which is the sum, can be divided by its length to give the unit vector **u** which lies along the axis of rotation (see Figure 178).

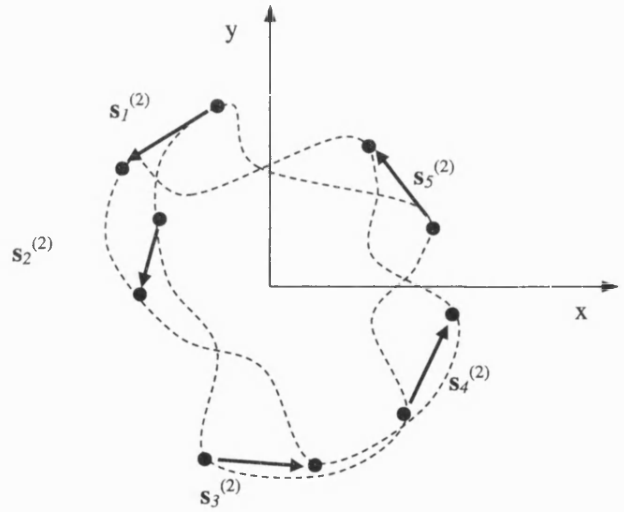

Figure 178 The the vector-product of any pair of vectors shown will be parallel to the axis of rotation. In this case, the direction vector of the axis is out of the page.

The vector

$$\mathbf{s}_i^{(1)} - (\mathbf{s}_i^{(1)}.\mathbf{u})\mathbf{u}$$

is perpendicular to the axis and represents a vector from the axis to the point $\mathbf{s}_i^{(1)}$. Let $\mathbf{v}_i^{(1)}$ be a unit vector in this direction. Define $\mathbf{v}_i^{(2)}$ similarly. The rotation matrix turns the first of these unit vectors onto the second. Hence

$$\cos\theta = \mathbf{v}_i^{(1)}.\mathbf{v}_i^{(2)} \qquad \text{and} \qquad \sin\theta = (\mathbf{v}_i^{(1)} \times \mathbf{v}_i^{(2)}) \cdot \mathbf{u} \qquad (11.1.8\text{-}12)$$

where θ represents the angle of rotation of the body around the axis as it moves from the initial to the final position (see Figure 179). Again these can be averaged over n possible values to determine more exact values for the cosine and sine and hence the value itself.

The rotation has now been obtained. The matrix R is given from Rodrigue's formula

$$R = (\cos\theta)I + (\sin\theta)\begin{bmatrix} 0 & -u_3 & u_2 \\ u_3 & 0 & -u_1 \\ -u_2 & u_1 & 0 \end{bmatrix} + (1-\cos\theta)\mathbf{u}\mathbf{u}^T \qquad (11.1.8\text{-}13)$$

where u_1, u_2, u_3 are the components of $\mathbf{u}$.

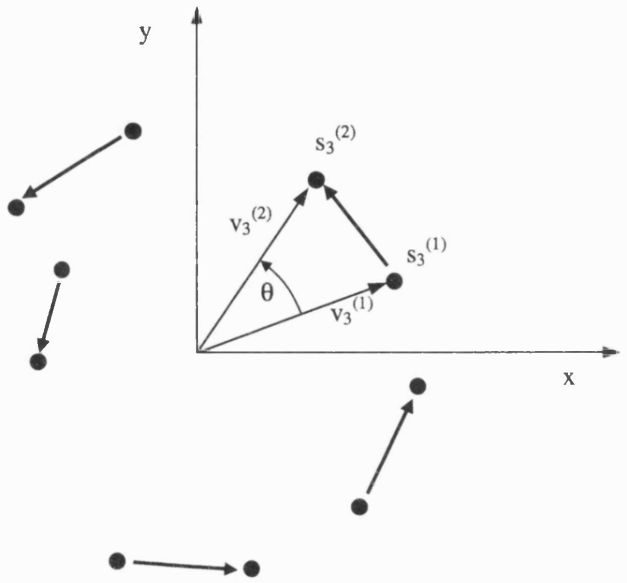

Figure 179 Calculating the angle of rotation about the helical axis. The procedure is performed between each pair of points and an average value is obtained

Stage 2 – Find α

The next stage is to find the distance of translation along the axis. This is obtained directly by inserting **u** into equation (11.1.8-4).

Stage 3 – find $\mathbf{q}_0$

Finally, a point $\mathbf{q}_0$ on the axis needs to be found. This is a solution of equation (11.1.8-4). The difficulty is that the equations are singular and there is no unique solution. The following approach works, but there is probably a more elegant version.

Effectively one of the components of $\mathbf{q}_0$ is set to zero and the other two are found using just two of the three equations. This is the same as removing one row and one column

from the matrix of coefficients (*R-I*). There are nine ways to do this and the one which results in a 2×2 matrix with the largest determinant is chosen.

Solving the 2×2 set of equations and setting the remaining component to zero gives a point on the axis. Other points on the axis take the form

$$\mathbf{q} + t\mathbf{u}$$

where t is a scalar.

The distance, s, of this point from the origin is found from the origin is given by:

$$s = (\mathbf{q} + t\mathbf{u}) \cdot (\mathbf{q} + t\mathbf{u})$$

$$s = \mathbf{q} \cdot \mathbf{q} + 2t(\mathbf{q} \cdot \mathbf{u}) + t^2 \mathbf{u} \cdot \mathbf{u}$$

(11.1.8-14)

Differentiating with respect to t and setting to zero gives:

$$\frac{ds}{dt} = 2t(\mathbf{q} \cdot \mathbf{u}) + 2t\mathbf{u} \cdot \mathbf{u} = 0$$

(11.1.8-15)

The point on the axis nearest the origin occurs

$$t = -(\mathbf{q}.\mathbf{u})$$

(11.1.8-16)

since $\mathbf{u}$ is a unit vector. Hence $\mathbf{q_0}$ can be taken as

$$\mathbf{q}_0 = \mathbf{q} - (\mathbf{q} \cdot \mathbf{u})\mathbf{u}$$

(11.1.8-17)

11.2 Published Conference Papers and Abstracts

Proceedings of the 50th Annual Meeting of the Orthopaedic Research Society, March 7-10 2004, San Francisco, U.S.A.

A HYPOTHESIS OF CARPAL BONE MOTION: DOES FORM GOVERN FUNCTION?

+*Sirkett, DM; *Mullineux, G; *Miles, AW; **Giddins, GEB
+*Centre for Orthopaedic Biomechanics, Department of Mechanical Engineering, University of Bath, UK

ABSTRACT INTRODUCTION

Despite numerous experimental studies, there is still no satisfactory explanation of the factors controlling the complex movement of the wrist, or carpal, bones. A thorough understanding of normal wrist function is essential for surgeons and researchers investigating injuries and pathological conditions that may result in abnormal kinematics.

It has been suggested that the complex movements of the carpal bones are governed primarily by the shapes of their articular surfaces [1,2]. It may be argued that the role of the intrinsic ligaments is to stabilise the joint and maintain its integrity under load rather than to dictate carpal movement patterns.

This project addresses the hypothesis that the morphology of the carpal bones and the manner in which they move are governed by the minimum energy principle. It is assumed that biological structures are formed using the minimum of materials necessary to provide adequate function. In the case of the carpal bones, this suggests their form is such that loading forces are evenly distributed throughout the articular surfaces, thereby minimising contact stress. This is achieved by maximising contact area with conforming joint surfaces. If contact stress is minimised in this manner, then the biological "construction cost" of the bones is minimised, which agrees with the initial hypothesis.

METHODS

Seven carpal bones and the distal radius and ulna were dissected from a fresh-frozen human wrist. Patient consent and ethical committee approval was obtained for the study. Three-dimensional computer models of the bones were obtained using a laser surface digitiser. The coordinates of three marker pins inserted into each bone were digitised prior to dissection to enable the bone models to be realigned into their anatomical positions. The orientation of the capitate bone was chosen to represent overall wrist angle. The hamate, capitate and trapezoid moved as a single unit since it is known that there is very little movement between these bones.

The contact area and intersection between all pairs of interacting joint surfaces were calculated using a C++ program (Fig. 1).

SWORDS, a geometric constraint modeller created at the University of Bath was used to display 3D graphics and maximise contact area using a built-in numerical optimisation algorithm.

For increments of capitate movement, *SWORDS* maximised total contact area occurring between articulating surfaces by adjusting the positions and orientations of the bones. Impingement between neighbouring bones was avoided by introducing the intersection score as a penalty in the optimisation process. There were a total of twenty-nine degrees of freedom (five for the capitate-hamate-trapezoid complex and six each for the hamate, lunate, scaphoid and triquetrum). The radius and ulna were fixed in space.

RESULTS

The method was applied to the carpal bone models for overall joint angles of between 10 and 30 degrees of ulnar deviation in 0.5-degree increments. The optimised positions of the bones at each increment were recorded and collated to form an animation of the predicted carpal motion (Fig. 2). The time taken to maximise the contact area at each increment was approximately one hour on a P4/1.4GHz desktop PC.

The movement patterns of the carpal bones were qualitatively compared to those obtained from a multi-position computed tomographic imaging study of radial and ulnar deviation [11].

The following observations were made when comparing predicted with experimental movement patterns for ulnar deviation: 1) In disagreement to experimental findings, sliding of the lunate and scaphoid against the radius in a medial to lateral direction was not observed. 2) The model did not predict the roll into extension of the lunate, which was observed experimentally. 3) The scaphoid exhibited characteristic out-of-plane movements in agreement with experimental results. It moved into extension as the overall wrist angle moved into ulnar deviation. 4) The triquetrum tucked into and travelled up the medio-dorsal surface of the hamate, as observed experimentally.

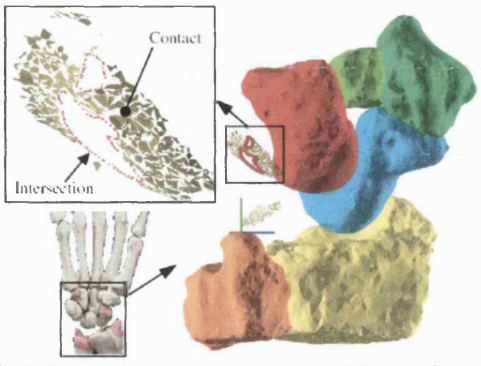

Fig. 1. Contact and intersection between hamate and triquetrum. Palmar view of right wrist. Hand bone image source: www.primalpictures.com

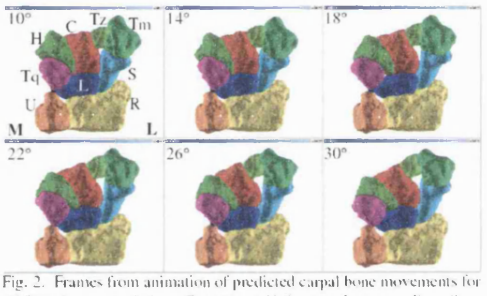

Fig. 2. Frames from animation of predicted carpal bone movements for 10-30° of ulnar deviation. C=capitate, H=hamate, L=lunate, R=radius, S=scaphoid, Tq=triquetrum, Tm=trapezium, Tz=trapezoid, U=ulna, M=medial side, L=lateral side.

DISCUSSION

The study aims to investigate whether the morphology of the articular surfaces alone accounts for the complex kinematics of the carpal bones.

The results predicted by the method in ulnar deviation show agreement with experimental observations in certain aspects of carpal behaviour. Further refinement and testing of the method, including its application to flexion/extension movements will allow a greater understanding of its predictive capability.

The calculation of contact area and intersection is a computationally intensive task that must be performed repetitively on a trial and improvement basis. Therefore, the principal limitation of the method is its computational expense. Furthermore, it is difficult to ascertain whether the optimisation algorithm is delivering a global or a local maximum solution.

Since to our knowledge there exists no predictive model of the wrist that fully explains the laws governing its function, development of the work will yield valuable insight into this poorly understood joint.

REFERENCES

[1] Savelberg et al, *J. Orth. Res 10*, 1992, 901-910.
[2] Kooloos et al, *Advances in the Biomechanics of the Hand*. Plenum Press, 1994.
[3] Snel et al, *Medical Physics*, 27, 2000, 2037-2047.

**Royal United Hospital, Combe Park, Bath, UK

Proceedings of the Institute of Physics and Engineering in Medicine
Annual Scientific Meeting, 15-17 September 2003, Bath, UK. pp114-115.

Can Wrist Motion be predicted by Maximising Contact Area ?

DM Sirkett[1], G Mullineux, AW Miles, GEB Giddins[2]
[1] Centre for Orthopaedic Biomechanics, Department of Mechanical Engineering, University of Bath, UK
[2] Royal United Hospital, Coombe Park, Bath, UK

Background and Purpose Despite numerous experimental studies there is still no satisfactory explanation of how the wrist works. A thorough understanding of wrist function is essential for surgeons involved in the treatment of injuries and disease, and for the design of prosthetic wrist joints.

The aim of the work is to develop a three-dimensional computer model of the wrist that will predict movement patterns of the carpal bones based upon maximisation of contact area. This paper outlines the details of our method.

The underlying premise is that the shape of the carpal bones and the manner in which they move are governed by the minimum energy principle. It is assumed that biological structures are formed using the minimum of materials necessary to provide adequate function. In the case of the carpal bones, this suggests their form is such that loading forces are evenly distributed throughout the joint surfaces, thereby minimising peak local loading. This is achieved by maximising contact area through the use of conforming joint surfaces. If peak loading is reduced in this way, then the material used to create the bones is minimised, which agrees with our initial assumption.

Methods The carpal bones are represented as three-dimensional faceted models obtained by laser surface digitisation of carpal bones dissected from a fresh-frozen left human forearm.

A C++ computer program was written to calculate the contact area and level of intersection between the 3D computer models of the carpal bones (see figure 1). Contact area was determined by summing the projected area of each facet upon its nearest neighbour on the opposing articular surface. Intersection was evaluated as the perimeter of the closed loop of points marking intersections between edges and facets of overlapping bones.

SWORDS [1], a geometric constraint modeller created by colleagues at Bath was used to display 3D graphics and maximise contact area using a built-in numerical optimisation algorithm [2].

The capitate was chosen as the output bone after a study reported only 1.1° of movement relative to the third metacarpal [3].

For increments of capitate movement, *SWORDS* maximises total contact area between all bones by adjusting translation and rotation parameters.

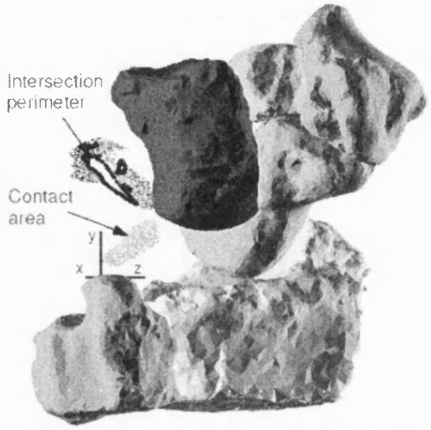

Figure 1 Contact between lunate and triquetrum; contact *and* intersection between hamate and triquetrum. For clarity, triquetrum, hamate and lunate are not displayed.

Results The algorithm was tested with two conforming toroidal surfaces representing a biaxial type wrist replacement. By maximising contact area for increments of radial and ulnar deviation, the algorithm correctly computed the path taken by the distal joint component as it articulated against the proximal component.

Conclusions We have outlined a new method for predicting carpal bone movement. The method has been successfully applied to a pair of conforming articular surfaces. Three-dimensional models of the carpal bones were obtained by digitisation of a dissected cadaveric wrist. The next step in the work is to apply the method to the computer models of the carpal bones.

References

[1] Mullineux G. Constraint resolution using optimization techniques. Computers and Graphics, 2001: 25: 483-492.

[2] Hooke R and Jeeves TA. Direct search solution of numerical and statistical problems. J. Assoc. Comput. Mach., 1961: 8: 212-229.

[3] Patterson RM *et. al.* High-speed three-dimensional kinematic analysis of the normal wrist. Journal of Hand Surgery [Am]. 1998: 23: 446-453.

Proceedings of the IASTED International Conference
BIOMECHANICS
June 30-July 2, 2003, Rhodes, Greece
pp241-246

DOES THE MINIMUM ENERGY PRINCIPLE GOVERN WRIST KINEMATICS?

DM Sirkett, G Mullineux, AW Miles, GEB Giddins
Centre for Orthopaedic Biomechanics, Department of Mechanical Engineering, University of Bath, UK

Abstract
While theoretical and computer models describing kinematics of the larger joints have been developed, there is still no generally agreed upon satisfactory explanation of how the wrist works.

A new explanation of the underlying rules that may govern the motion of the carpal bones has been outlined. We propose that the carpal bones move in such as way as to maximise the total contact area between all pairs of articular surfaces. This would minimise contact stress, thereby minimising in biological terms the "construction cost" of the carpal bones. This agrees with the principle of minimum energy, which governs many natural processes.

Carpal bones from a fresh frozen cadaveric forearm were dissected and their shapes converted into three-dimensional computer models using non-contact laser digitisation. A computer program was developed to measure contact area between neighbouring articular surfaces and to maximise this quantity by adjusting the six degrees of freedom of the carpal bones. The program is able to avoid impingement of bones upon one another through the use of collision detection.

The method has been applied to a pair of articulating surfaces that may be found in biaxial type wrist prostheses and correctly computed the kinematics of the joint.

Key Words
Kinematics and Kinematic Assessment, Computational Biomechanics

1. Introduction
The wrist is the most complex joint in the human body and is essential for optimal hand function. Despite numerous experimental studies there is still no satisfactory explanation of how it works. A thorough understanding of wrist function is essential for surgeons involved in the treatment of injuries and disease, and for the design of prosthetic wrist joints.

The purpose of the work is to test a new theory of wrist kinematics. The underlying premise is that the shape of the carpal bones and the manner in which they move are governed by the minimum energy principle. It is assumed that biological structures are formed using the minimum of materials necessary to provide adequate function. In the case of the carpal bones, this may suggest that their form is such that loading forces are evenly distributed throughout the joint surfaces, thereby minimising peak local loading. This is achieved by maximising contact area through the use of conforming joint surfaces. If peak loading is reduced in this way, then the material used to create the bones is minimised, which agrees with our initial assumption.

To date, investigations into wrist kinematics have been primarily observational in nature. The movement patterns of the individual carpal bones have been recorded using cadaveric wrists [1,2,3] and with live subjects using imaging methods with three-dimensional computer reconstructions [4,5,6]. There is variation in the movement patterns of carpal bones between individuals [7,8,9] but there is no general rule that can be applied to explain the movement patterns of carpal bones, taking into account morphological variations. This hampers understanding of normal carpal mechanics.

2. Aims and Objectives
The aim of the work is to develop a three-dimensional computer model of the wrist that will predict movement patterns of the carpal bones based upon maximisation of contact area. Specific objectives for the work are i) to develop the computer algorithm used to calculate contact area, ii) to find a suitable numerical optimisation scheme to maximise the contact area for increments of hand position, iii) to obtain a set of three-dimensional computer models of the carpal bones, including the articular surfaces and iv) to validate the method by comparing the results to those obtained from an experimental study of normal wrist kinematics. This paper covers objectives (i) to (iii).

3. Materials and Methods

3.1. Computer representation of carpal bones

The carpal bones are represented as three-dimensional faceted models. Three-dimensional models of bones may be obtained by reconstruction of a series of cross-sectional images from tomographic (CT) or magnetic resonance (MR) scans. While CT imaging is capable of producing detailed models with typical voxel sizes of 0.2 mm [10] it cannot reliably differentiate articular cartilage surfaces from surrounding soft tissue. In this respect, MR imaging is more discriminating but unless multiple scans and custom-sized coils are used, the resolution is limited to around 1.0 mm [6]. Therefore, it was decided to use direct surface digitisation. The particular method decided upon was non-contact laser-digitisation. A fresh-frozen cadaveric left human forearm, amputated above the elbow following brachial plexus injury was used for the study. There was no history of wrist injury or disease in the specimen. Written consent was obtained from the donor and the local ethics committee approved the study.

Tissue was resected from around the wrist capsule and the extrinsic ligaments were removed. The carpal bones were held in their correct anatomical positions by the intrinsic ligaments. Three conical-headed marker pins were inserted into each carpal bone (see Figure 1) and their three-dimensional coordinates recorded using a Fastrak (Polhemus Inc.) digitising stylus. The digitisation was performed twice, revealing a maximum repeatability error of +/-1.0 mm. The intrinsic ligaments were then removed and extraneous tissue was removed from the carpal bones. The pisiform was excluded from the study, as it is a sesamoid bone.

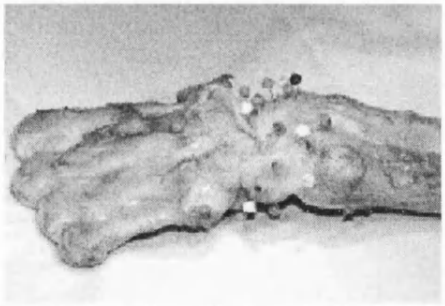

Figure 1 Three marker pins inserted into each bone

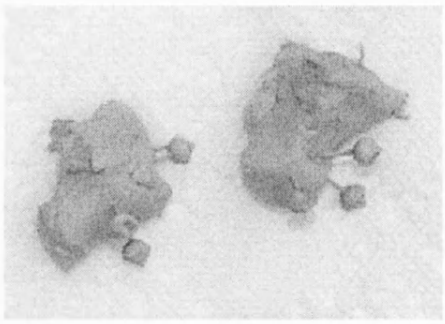

Figure 2 Bones spray-painted matt grey prior to laser-digitisation: trapezium (left), capitate (right)

The dissected carpal bones, including the distal 20 mm of the radius and ulna were transported in cooled saline to maintain hydration of the articular cartilage. Laser scanning was performed at a specialist bureau (Archaeoptics Ltd., Glasgow). All bones were spray-painted matt grey immediately prior to scanning in order to negate reflection errors resulting from cartilage translucency.

The surface resolution of the models was 0.17 mm, which yielded around 100,000 facets per bone. However, in order to reduce computational expense during the initial stages of the study, mesh resolution was reduced by 90%.

The bone models were moved into their correct anatomical orientations using the recorded positions of the three marker pins. The intact wrist was then mirrored to create a right-hand joint. These operations were performed within AutoCAD 2000 (Autodesk inc.). Some manual re-positioning of the bones was required due to errors in the digitised marker positions. The aligned carpal bones are shown in Figure 3.

Once imported into the computer model, the approximate geometrical centroid of each bone was found. These points were positioned at the mean X, Y and Z coordinates of all vertices and were used as the centres of rotation for each bone for adjustments of orientation during the subsequent optimisation process.

Figure 3 Three-dimensional bones after alignment.

3.2. Overview of Computer Model

A simplified block diagram for the method is shown in Figure 4. In the first instance, we are only considering the movement of the carpals during pure radial-ulnar deviation. A study found that there was less than 1.1 ° of motion between the third metacarpal and the capitate [11]. Therefore the capitate has been chosen to represent the overall wrist angle with respect to the fixed radius. The four bones of the distal row (hamate, capitate, trapezoid and trapezium) are firmly connected by the intrinsic ligaments, with little relative movement. Therefore, these bones were considered to move as a single, rigid body in the computer model.

Starting at zero degrees radial-ulnar deviation, the six degrees of freedom of the lunate, scaphoid, triquetrum, trapezoid and trapezium and five degrees of freedom of the capitate (since its radial-ulnar deviation angle is fixed) are adjusted by the optimisation algorithm until the "cost" of the solution is minimised. The cost is defined as the level of intersection between all bones minus the total contact area. Contact area was calculated between nine pairs of bones, these were: capitate-lunate, capitate-scaphoid, hamate-triquetrum, lunate-radius, lunate-scaphoid, lunate-triquetrum, radius-scaphoid, scaphoid-trapezoid, scaphoid-trapezium.

The computer model was created in two sections. The *SWORDS* geometric constraint modelling software [12] created at Bath, was used for 3D graphics display. A numerical optimisation algorithm [13] within *SWORDS* was used to minimise the cost function, which was calculated within a standalone C++ program.

The operation of the C++ cost calculation program will be broken into three stages: i) subdivision, ii) intersection evaluation, iii) contact area calculation.

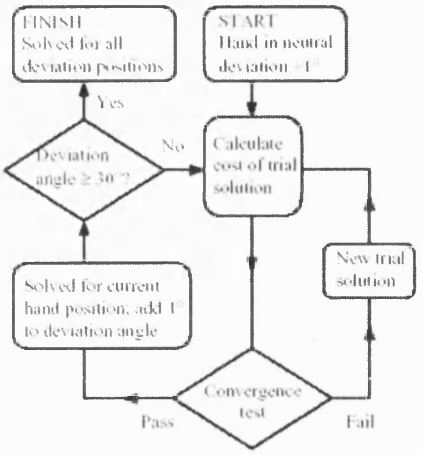

Figure 4 Flowchart outlining operation of computer model

• **Subdivision:** In order to minimise computational expense, the number of facets involved is reduced according to a simple proximity test. At each new increment of hand posture, those facets whose centroids are not within 3.0 mm of any facet on the opposite articular surface are eliminated from the data set. This procedure reduced the total number of facets involved in the problem by more than 50 % (see Figure 5.1).

• **Collision Detection:** Since the optimisation process relies on trial and improvement when moving the bones, an intersection test must be introduced into the cost function so that collisions may be avoided.

Ideally, the *volume* of intersection between overlapping bones would be calculated. However, since this is a computationally expensive task, described by one author as a "major computational bottleneck" [14], an alternative

indicator of intersection was used. This was chosen as the perimeter of the closed loop formed by the series of points marking intersections between edges and facets of the overlapping bones.

Figure 5. Facets further apart than 3.0 mm are eliminated from the data set

• **Contact area:** The aim of this stage was to calculate the area of the 2D polygon defining the region of intersection between facet A and the projection of facet B upon facet A. This process was repeated for all pairs of facets until the total area of contact was calculated. Figure 6 illustrates the appearance of regions of contact occurring between the lunate and triquetrum. The triquetrum has been deliberately made to mildly overlap the hamate so as to demonstrate the appearance of the intersection perimeter. So as to make these features clear, the aforementioned three bones are displayed semi-transparent.

• **Optimisation:** The values of contact area and intersection perimeter were calculated by a standalone C++ program and returned to the optimisation algorithm in *SIFORDS*. A total of 23 degrees of freedom were available to the algorithm. The Hooke and Jeeves algorithm does not require the cost function to be continuous or differentiable and so it is well suited to this particular problem.

The optimisation algorithm minimises the value of the "cost" of the solution. This is defined in (1).

$$\text{Cost} = k_1 - \text{contact area} + k_2 \times \text{intersection perimeter} \quad (1)$$

Where k_1 and k_2 are set to ensure Cost > 0.

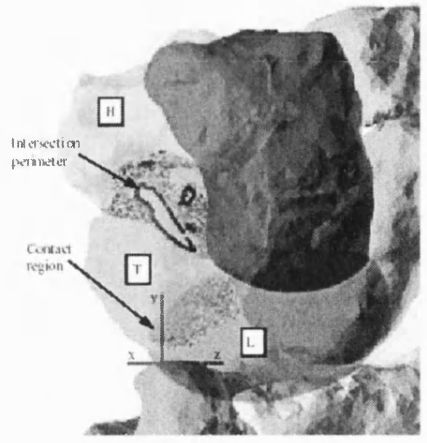

Figure 6. Contact between lunate (L) and triquetrum (T); contact *and* intersection between hamate (H) and triquetrum.

Once the contact area has been maximised, the radial-ulnar deviation angle is incremented and the optimisation process is performed once more.

4. Results

The principal purpose of this paper is to outline the approach used for the computer model of the wrist. Therefore, results for the laser-digitised bones are not yet available. However, the method has been tested on a pair of conforming geometrical surfaces.

4.1. Testing

The algorithm was tested with two conforming toroidal surfaces representing the geometry of a biaxial type joint prosthesis. By maximising contact area for increments of radial and ulnar deviation, the algorithm was able to correctly compute the path taken by the mobile distal joint component as it articulated against the fixed proximal component. Results are illustrated in Figure 7. A small amount of axis positioning error was observed from one increment of movement to the next. This could be due to

discontinuity in curvature of the joint surfaces associated with the faceted representation.

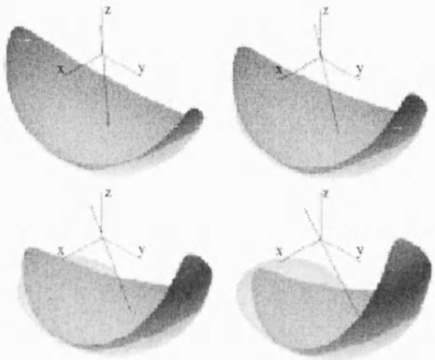

Figure 7 Four frames taken from the animation of predicted movement for a biaxial toroidal joint. The actual axis of rotation is the global x-axis.

6. Concluding Remarks

We have outlined a new method for predicting carpal bone movement. The method has been shown to work for a pair of articulating surfaces with fully conforming surfaces. Three-dimensional models of the carpal bones have been obtained by digitisation of cadaveric material. The next step in the work is to apply the method to the new models.

At present, the four bones of the distal row are fixed together and move as a single, rigid unit. However, if the results look encouraging, these can be easily separated and moved independently.

The method relies upon a good starting position to predict the positions of the bones adopted at the next increment of overall wrist angle. Therefore, positional errors will tend to accumulate as the output angle deviates further from the neutral position.

We are proposing that movement of the bones is determined solely by the interaction of joint surfaces. Without the additional constraints of ligaments, it is therefore essential that the surfaces are very accurately defined. Some of the articular surfaces on the digitised carpal bones suffered minor damage during dissection. While most of these defects were rectified by manual editing of the three-dimensional mesh, it remains to be seen how the remainder will affect the results. Furthermore, the reduction in mesh resolution in the interests of computational efficiency may introduce additional errors due to increased non-linearity of surface curvature.

If the method can be shown to work then we will gain a new explanation of the laws governing the kinematics of the wrist joint, which are not fully understood at present. This will provide invaluable information for surgical applications, where a thorough understanding of normal kinematics is essential for the treatment of joint injury and instability.

References

[1] Y. Youm, R.Y. McMurtry, A.E. Flatt & T.E. Gillespie, Kinematics of the wrist, an experimental study of radial-ulnar deviation and flexion-extension. *The Journal of Bone and Joint Surgery, 60-A*, 1978, 423-431.

[2] J.G. Andrews & Y. Youm, A biomechanical investigation of wrist kinematics. *Journal of Biomechanics, 12*, 1979, 83-93.

[3] R.B Brumbaugh, R.D. Crowninshield, W.F. Blair, J.G. Andrews, An in-vivo study of normal wrist kinematics, *Journal of Biomechanical Engineering, 104*, 1982, 176-181.

[4] V. Feipel & M. Rooze, Three-dimensional motion patterns of the carpal bones: an in-vivo study using three-dimensional computed tomography and clinical applications. *Surgical Radiological Anatomy, 21*, 1999, 125-131.

[5] J.J. Crisco, R.D. McGovern, S.W. Wolfe, Noninvasive technique for measuring in-vivo three-dimensional carpal bone kinematics. *Journal of Orthopaedic Research, 17*, 1999, 96-100.

[6] J.G. Snel, H.W. Venema, T.M. Mooijen, J.P. Rijt, C.A. Grimbergen & G.J. den Heeten, Quantitative in-vivo analysis of the kinematics of carpal bones from three-dimensional CT images using a deformable surface model and a three-dimensional matching technique. *Medical Physics, 27*, 2000, 2037-2047.

[7] B.D. Ferris, J. Stanton, J. Zamora, Kinematics of the wrist. Evidence for two types of movement. *Journal of Bone and Joint Surgery Br., 82*, 2000, 242-245.

[8] M.A. Craigen, J.K. Stanley, Wrist Kinematics. Row, column or both? *Journal of Hand Surgery Br., 20*, 1995, 165-170.